Modelling of Mechanical Properties of Ferritic Weld Metals

By
Sree Harsha Lalam
Sidney Sussex College
Cambridge

Department of Materials Science and Metallurgy
Pembroke Street
Cambridge
CB2 3QZ

A dissertation submitted for the degree of Doctor of Philosophy at University of Cambridge

October 2000

This thesis is dedicated
to my mother, *Sree Devi Lalam*

PREFACE

This dissertation is submitted for the degree of Doctor of Philosophy at the University of Cambridge. The research described herein was conducted under the supervision of Professor H. K. D. H. Bhadeshia in the Department of Materials Science and Metallurgy, University of Cambridge, between October 1997 and September 2000.

Except where acknowledgement and reference is specifically made to the contrary, this work is, to the best of my knowledge, original and has been carried out without collaboration. Neither this thesis, nor any substantially similar dissertation has been or is being submitted for any degree, diploma or other qualification at any other university. Part of this work has been presented in the following publications;

Lalam, S. H., Bhadeshia, H. K. D. H. and MacKay, D. J. C .,*Estimation of mechanical properties of ferritic steel welds. Part 1: Yield and tensile strength*, Science and Technology of Welding and Joining, **5(3)**, 135–147, 2000.

Lalam, S. H., Bhadeshia, H. K. D. H. and MacKay, D. J. C ., *Estimation of mechanical properties of ferritic steel welds. Part 2: Elongation and Charpy toughness*, Science and Technology of Welding and Joining, **5(3)**, 149–160, 2000.

Lalam, S. H., Bhadeshia, H. K. D. H. and MacKay, D. J. C ., *Short communication: The Bruscato factor in the temper embrittlement of welds*, Science and Technology of Welding and Joining, accepted and to be published in volume **5**, 2000.

Lalam, S. H., Bhadeshia, H. K. D. H. and MacKay, D. J. C ., *The Charpy impact transition temperature for some ferritic steel welds*, Australasian Welding Journal, **45**, 33–37, 2000.

Sree Harsha Lalam
October 2000

ACKNOWLEDGEMENTS

I would like to thank Professor A. H. Windle for the provision of laboratory facilities in the Department of Materials Science and Metallurgy at the University of Cambridge. I would like to express my sincere gratitude to my supervisor Professor H. K. D. H. Bhadeshia for his encouragement and inspirational guidance throughout this work. His enthusiasm and encouragement have been a great motivation to me.

I am extremely grateful to my friends Mr. Thomas, Mr. Miguel, Dr. Carlos, Dr. Francisca, Mrs. Dorothy, Mr. Hiroshi and Dr. Nobu for their help and useful discussions during the course of my research. My special thanks to Miss. Vicky for her help.

I sincerely thank my housemate Chandra Sekhar and my CCT parent Dr. Sridhar for their moral support and encouragement during my stay in Cambridge. I appreciate the friendship showed by Phase Transformations group members. I would like to thank Dr. Ichikawa for his enthusiasm and help.

Thanks also due to my friends in my bachelors degree for their encouragement. I am highly grateful to the Cambridge Commonwealth Trust for a scholarship and Committee of Vice–chancellors and Principles for ORS award. I would like to thank National Power, UK for their financial support for my project.

ABSTRACT

Welding is a key technology in the manufacture of engineering components and is of particular importance in the context of steels. The complexity of welding alloys has in the past prevented the development of generalised models capable of giving quantitative estimates of anything other than the most simple mechanical properties. It has been possible in the present work, using a neural network technique within a Bayesian framework in combination with physical properties, to develop a set of models dealing with the yield strength, ultimate tensile strength, the ductility and impact toughness of weld metals as a function of the chemical composition and heat treatment. The models are based on a vast quantity of published experimental data which were all digitised and assessed for model development.

Neural networks are used in circumstances where the complexity is difficult to deal with using only scientific principles. For this same reason, the trained networks cannot ever be fully tested since it is hard to imagine how multi–fold interactions between the inputs can affect the outcome. Nevertheless, an attempt was made to assess whether the networks reproduce the known physical metallurgy. For example, the effect of carbon and manganese on the yield strength of low–alloy weld deposits. In almost all cases considered, the networks could be shown to recognise known trends, taking into account the error estimates. Where possible, the network predictions were compared against physical models. For example, the yield strength of carbon–manganese welds can be estimated using deformation theory; this was shown to compare well against predictions using the neural network models. However, in some cases, such as when considering the effect of tungsten on the strength of low–alloy steel welds, it was evident that the models lacked knowledge to such an extent as to make the predictions unphysical. The situation was corrected by adapting steel data to represent welds, and the resulting model was demonstrated to behave properly. This example illustrates that the networks should not be used blindly but rather as an aid to design.

The combined set of models, together with experience from physical metallurgy, were then used to propose a new tungsten–containing welding alloy for use in circumstances where post–weld heat treatments are not practical. This proved to be successful at the first attempt; subsequently, the models have been used successfully by others in a similar way, to invent welding alloys without doing experiments.

The tempering resistance of the tungsten–containing weld has been studied experimentally and compared against a number of alloys. This work indicates that the replacement of molybdenum by tungsten in creep–resistant alloys leads to a lower as–deposited hardness which can be exploited to eliminate post–weld heat treatments. The creep strength can nevertheless (probably) be maintained by the use of vanadium.

Contents

Chapter 1

INTRODUCTION

Steels are used in the construction and fabrication of engineering structures, with service temperatures ranging from subzero to about 600 °C over long periods of time. The vast majority of iron alloys are ferritic because they are cheap and it is easy to modify their microstructures to obtain an impressive range of desirable properties.

The fabrication of steels unavoidably involves welding, a complex process incorporating numerous metallurgical phenomena. It is not surprising therefore, that the final microstructure both inside the weld metal and in all adjacent regions affected by the welding heat, is remarkably varied. Many of the important features of weld microstructure can now be calculated using a combination of thermodynamics and kinetic theory [1]. Such calculations are now being performed routinely in industry during the course of alloy design or when investigating customer queries.

Naturally, it is the mechanical properties of the weld which enter the final design procedures. There has been some progress in estimating the yield strength from the microstructure using combinations of solution strengthening, grain size effects, precipitation hardening and dislocation strengthening [1]. The ultimate tensile strength can in a limited number of cases be calculated empirically from the yield strength [2]. However, there has been no progress at all in creating models for vital properties such as ductility, toughness, creep and fatigue strength [3].

The failure of previous work [4, 5, 2] to create models with wide applicability comes largely from constraints due to the linear or pseudo–linear regression methods used, with poor error assessments and most importantly from the very limited variables and data considered in the analysis.

The purpose of the work presented in this thesis was to create quantitative models for the yield and ultimate tensile strength, ductility and toughness, using the special method of neural networks within a Bayesian framework [6]. This is non–linear regression analysis with many advantages which will be described later in the thesis. It was at the same time the intention to exploit the thousands of data in the published literature so that the models created are of

the widest possible applicability. Model validation is a key feature of the work; this involves the design and experimental assessment of novel alloys which have never before been conceived, validation of a large variety of published data and testing against the known principles of physical metallurgy. The flow of the research is illustrated in Fig. 1.1.

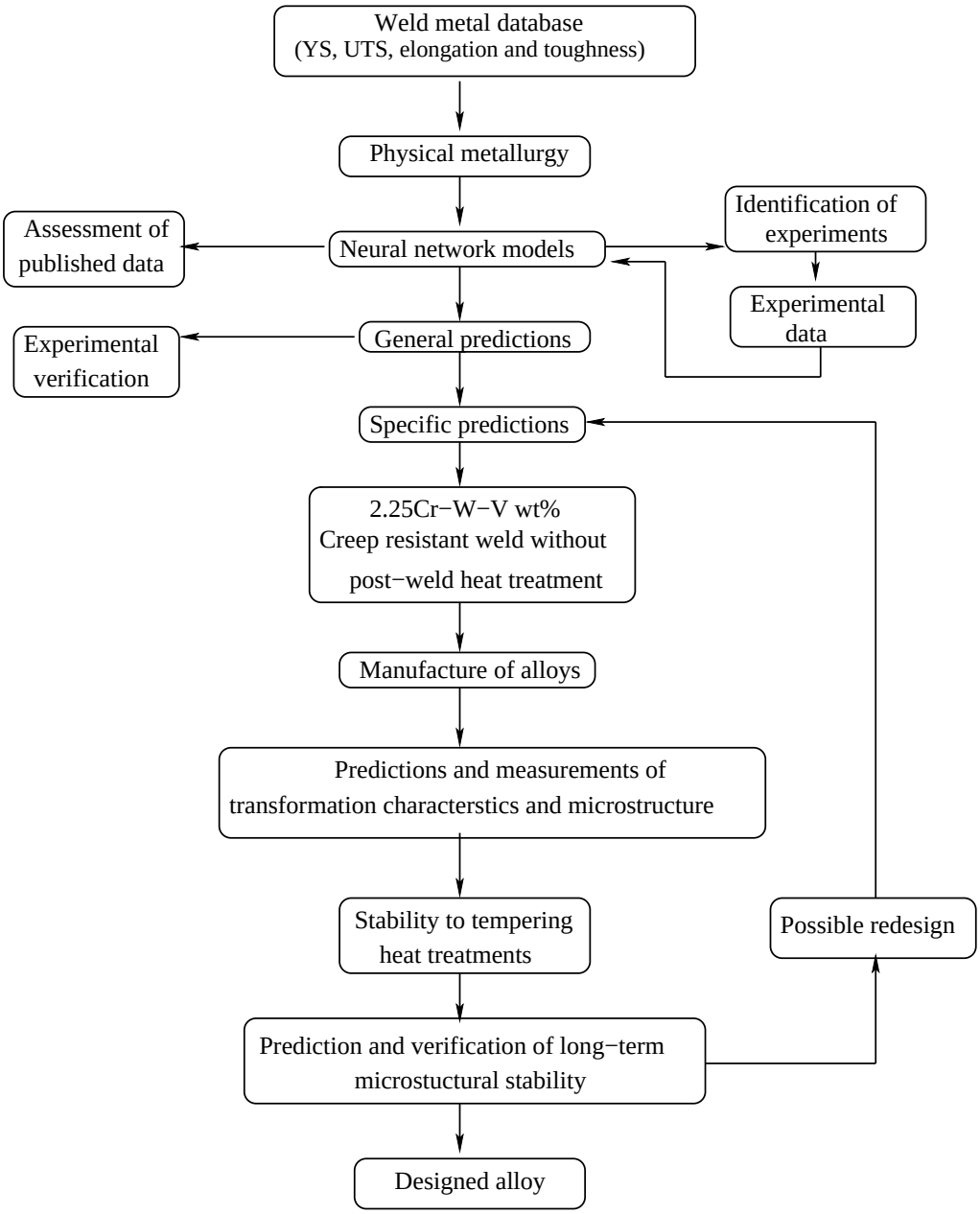

Figure 1.1: Flow diagram illustrating the research.

1.1 Welding Processes

Welding is one of the most popular joining methods for steels. The joining of two alloys can be done by melting the two surfaces to be joined by heat, with or without the help of a filler wire. The method by which heat is generated in order to fuse the base metal and filler wire defines the nature of the welding process: electric arc welding, electron beam welding, friction welding. The work presented in this thesis focuses on arc welds which are now described in some more detail.

1.1.1 Arc Welding

An electric arc is the source of heat to melt and join metals. As shown in Fig 1.2, an electric arc is struck between the work piece and the electrode which is manually or mechanically moved along the joint or electrode remains stationary while the work piece can be moved. The electrode may or may not be consumed during the process. The molten weld pool is protected by an inert or active gas shroud generated using flux or via an external supply of gases.

Manual Metal Arc Welding

This is also called the shielded metal arc welding (SMAW) process. Its simplicity and versatility makes it popular. A consumable electrode coated with flux (silicates, minerals and metals) is used as shown in Fig 1.3. The coating provides elements which act as arc stabilizers, generate gases and a slag cover to protect the weld pool from the environment and add alloying elements to the weld deposit. The electrode and workpiece are connected to a power source; usually the electrode is connected to the positive terminal of the power source. The arc is initiated by touching the electrode tip to the base metal and then forming an air gap. The heat generated as a consequence melts the base metal, the electrode core and its covering.

Gas Tungsten Arc (TIG) Welding

A non-consumable tungsten electrode is used together with an inert shroud. The key advantage of this process over manual metal arc welding is that higher quality welds can be produced. The equipment used in this process is portable and usable with all metals, for a wide range of thicknesses and in all welding positions.

Gas Metal Arc Welding

Gas metal arc welding (GMAW) uses a continuous wire which is consumed to form the weld metal together with an inert gas shield. The mode of liquid metal transfer from electrode to the base metal can be varied by choosing different types of gases. All metals can be welded by

using argon or carbon dioxide. This process gives high weld metal deposition rates and can be automated.

Submerged Arc Welding

As the name indicates, the electric arc and molten weld metal are submerged under a layer of molten flux and unfused granular flux. The tip of a continuously fed consumable wire is the electrode. Because the arc is submerged under molten flux the radiation losses are minimised giving maximum energy efficiency. This is an automated process which can be used with the base metal in the horizontal position.

1.2 Variables Associated with Welding

The most important variables are the process, chemical composition of the weld deposit, heat input, the initial temperature of the base metal at the region to be welded (pre–heating), temperature of the weld deposit during multirun welding (interpass temperature) and heat treatment given to the weld metal after welding (post–weld heat treatment). The type of joint (Fig 1.4) and the material thickness have to be considered in selecting a weld process. The primary function of the heat source is to generate heat to melt the base metal and consumable electrode. The rate of melting is controlled by amount of heat input, defined as:

$$\text{Net heat input(J mm}^{-1}) = \frac{fIV}{S}$$

where I is the electric current in amperes, V is the voltage applied between power source terminal and electrode expressed in volts, S is the travel speed of the heat source in mm s^{-1} and f is the arc transfer efficiency. In most of the arc welding processes the efficiency is between 0.8 and 0.99. The weld metal composition plays a vital role in determining the mechanical properties of the weld joint and the microstructure of weld metal. A post–weld heat treatment is often given to the as–deposited weld to lower the hardness and restore the toughness.

1.3 Weld Microstructure

When a molten metal solidifies in the gap between components to be joined, this welds the components together. The basic metallurgy of the welded joint can be divided into two major regions: the fusion zone and heat affected zone (HAZ). The fusion zone experiences temperatures above the melting point of the material and represents both the deposited metal and the parts of the base metal melted during welding. The heat affected zone, (Fig. 1.5) on the other hand, represents the close proximity to the weld, where the temperatures experienced are below the melting point and there is a change in the microstructure of the base metal.

1.3.1 Weld Metal Solidification

In steels weld metal solidification starts at edge of the fusion zone into the weld metal with δ–ferrite as the initial phase (Fig 1.10). As it cools, δ–ferrite transforms into austenite and with further lowering of the weld metal temperature austenite decomposes to ferrite. Most steels contain small quantities of alloying elements and hence show similar crystal structure changes as pure iron. Therefore in weld metal solidification, weld deposits begin solidification with the epitaxial growth of columnar δ–ferrite from the hot grains of the base metal at fusion surface. The grains grow rapidly in the direction of highest temperature gradient and hence show an anisotropic morphology. Those grains with $<100>$ directions parallel to the heat flow direction dominate the final microstructure. On further cooling, austenite nucleates and grows along prior δ–ferrite grain boundaries, thus adopting the columnar shape of the δ–ferrite grains.

Fine austenite grains provide more grain boundary nucleating sites; on the other hand coarse grains increase the hardenability of the weld metal. The columnar shape of the austenite results in few grain boundary junctions when compared with an equi–axed structure. This also contributes to an increase in hardenability.

The cooling rates in the weld metal depend on the distance from the heat source, heat input, interpass temperature and the geometry of the joint. Because the cooling rates are in practice quite high, weld solidification is a non-equilibrium phenomenon and thus solidification–induced segregation promotes an inhomogeneous microstructure in the weld metal. The amplitude of these concentration and microstructure variations become larger as the alloy concentration increases.

Another important feature, in flux based welding processes, is non–metallic inclusions. During welding, the flux reacts with atmospheric oxygen and cleans and protects the weld metal by forming oxides and rejecting them into slag. However, the process is not ideal due to convection and rapid solidification, so oxide particles are entrapped in the fusion zone during solidification. These are called slag inclusions, which can serve as nucleation sites within the weld pool. A small volume fraction of inclusions is desirable in welding, as they serve as heterogeneous nucleation sites for acicular ferrite. Large fractions are detrimental to the mechanical properties of weld metal.

1.3.2 As–deposited Weld Microstructure

The as–deposited microstructure is that which forms when the liquid weld pool cools to room temperature. This structure contains allotrimorphic ferrite, Widmanstätten ferrite and acicular ferrite, Fig. 1.6. In a few cases, microstructures containing martensite, bainite and traces of pearlite can be found. High–carbon martensite is a hard microstructure with low toughness and

ductility.

Allotriomorphic Ferrite

Allotriomorphic ferrite (α) usually forms between 1000 and 650 °C during cooling of steel weld deposits. Nucleation occurs heterogeneously at the columnar austenite grain boundaries. As the austenite grain boundaries are easy diffusion paths, austenite grain boundaries are decorated with thin layers of allotriomorphic ferrite and the thickness of which is controlled by the diffusion rate of carbon in austenite. In weld deposits, allotriomorphic ferrite appears to grow without the redistribution of substitutional alloying elements during transformation [8]. This mechanism of growth is termed "paraequilibrium", and occurs as a consequence of the fast cooling rates experienced by welds. In welds, allotriomorphic ferrite is detrimental to the toughness because the continuous network along grain boundaries offers less resistance to crack propagation than acicular ferrite [9].

Widmanstätten Ferrite

This microstructure results from further cooling below the temperature at which allotriomorphic ferrite forms. Primary Widmanstätten ferrite nucleates directly from the regions of austenite grain boundaries not covered by allotriomorphic ferrite. Secondary Widmanstätten ferrite nucleates at austenite/ferrite boundaries and grows as sets of parallel plates separated by thin regions of austenite. The austenite remains as retained austenite, or transforms to martensite or pearlite. These latter transformation products are collectively known as microphases in weld metal terminology, because they are generally present in small fractions. Widmanstätten ferrite is not desirable in weld metals.

Acicular Ferrite

Oxides and non-metallic inclusions serve as nucleation sites for acicular ferrite. Acicular ferrite forms within the columnar austenite grains in competition with Widmanstätten ferrite. It appears as a fine grained interlocking array of non–parallel laths. The microstructure is highly desirable in welds. The large number of non–parallel grains improve the weld metal toughness by increasing the resistance to crack propagation [10].

Microphases

These are last constituents to form in weld metal. Microphases correspond to the small carbon–rich regions in the weld metal where the last remaining volumes of austenite transform, and consist of mixtures of martensite, carbides, degenerated pearlite, bainite and retained austenite.

1.3.3 Secondary Microstructure

In many circumstances it is difficult to fill the gap at the joint by a single weld pass. Therefore thick sections are welded using many layers of deposited metal, Fig. 1.7. The deposition of each successive layer heat treats the underlying microstructure formed during cooling of the previous run. Some regions of the underlying layers are reheated above the austenitisation temperature, whereas others become tempered. All of the reheated regions contribute to the secondary microstructure.

The Heat Affected Zone

The heat affected zone is the portion of the metal which has not experienced melting, but whose microstructure is altered due to welding heat. There are well–defined microstructures in the heat affected zone as illustrated in Fig. 1.8. The region immediately adjacent to the fusion boundary is heated to very high temperatures (just below melting temperature) and forms coarse austenite. The austenite grain size decreases sharply with distance from the fusion line and the fine grained zone will have superior mechanical properties than the coarse grained zone. Moving further away, the peak temperature decreases and will result in partial austenite formation and tempered ferrite in that region; this is called the "partially austenitised zone". The region adjacent to this zone, which is not transformed to austenite will be tempered.

1.4 Ferritic Steels

Pure iron at room temperature has a body–centered cubic crystal structure, with the common designation α–ferrite, Fig 1.9. Between 910 and 1410 °C, face–centered cubic austenite (γ) becomes the stable phase, to be replaced again by δ–ferrite at higher temperatures, Fig. 1.10. The δ and α forms of ferrite have identical crystal structures. Steels usually contain alloying elements such as carbon, manganese, silicon, etc. Some are added deliberately, whereas others are present as impurities. Carbon is the main alloying element in steels, frequently present in the form of cementite. Cementite has the chemical formula Fe_3C. Some alloying elements such as carbon, manganese and nickel stabilise austenite, whereas tungsten, chromium, vanadium and niobium stabilise ferrite [11]. The latter also tend to form alloy carbides. The alloying of steels is a very large subject which has been reviewed [12].

1.4.1 Heat Resistant Steels

A power station converts fuel into electrical energy; in the case of fossil fuels, this is via steam. A power generation loop is shown schematically in Fig 1.11. Water is converted into steam in an evaporater before entering into the steam drum, where it is collected in headers. It is then

superheated before passing into the high pressure (HP) turbine, after which it is reheated before enters into the intermediate pressure (IP) turbine. After leaving the IP turbine it enters the low pressure (LP) turbine. The exhaust steam is finally condensed and returned to boiler.

Steels are used widely in the construction of power plant. They have to resist creep deformation, oxidation and corrosion. The superheater pipes carrying steam from boilers to high pressure (HP) turbines typically experience steam at 565 °C under 15.8 MPa pressure and are made of low–alloy steels. In HP turbines the rotor is fabricated as a single forging of 1Cr-MoV steel. Tempering at 700 °C leads to the formation of stable carbides which are distributed uniformly in the ferrite matrix. These carbides improve the creep resistance at the service temperature [13]. Turbine blades experience both erosion and high tensile forces. High strength and corrosion resistant 12CrMoV steel is used in fabrication of turbine blades [14]. The $3\frac{1}{2}$Ni–Cr–Mo–V alloy has good hardenability combined with high strength of about 1100 MPa and good toughness. These steels are air cooled from 870 °C and tempered at 650 °C. Due to their high strength and toughness these materials are used to fabricate the low pressure turbine rotor, which is nearer to the generator. The generator rotor is also fabricated with this material [15].

Steel	C	Si	Mn	Mo	Cr	V
$2\frac{1}{4}$Cr–1Mo	0.15	0.50	0.45	1.0	2.25	-
12Cr–1Mo	0.15	0.40	0.6	1.0	12	-
$3\frac{1}{2}$Ni–Cr–Mo–V	0.15	0.30	0.70	0.19	1.5	0.11

Table 1.1: Chemical composition of some steels have been used in power plant [16], all units are in wt%.

Cr-Mo Steels

These materials are resistant to corrosion by sulphur products and hence were used first in the petroleum industry. Once their oxidation resistance and high temperature strength were appreciated, they began to be applied in the steam power generating industry. More recently, these steels have been used in fabricating thick pressure vessels. The oxidation resistance and high temperature strength depends on the amount of chromium and molybdenum present in that alloy. Excellent high–temperature (565 °C) strength is obtained in $2\frac{1}{4}$Cr–1Mo steels (Table 1.1), which are generally used in the bainitic condition. A tempering heat–treatment gives the required alloy carbides; the most important are M_2C, M_7C_3 and $M_{23}C_6$, where M represents a metallic element.

1.4.2 Structural Steels

Steels for structural applications are used at ambient temperatures and the main property requirements are strength, ductility and toughness. The vast majority of these steels have a yield strength in the range 350–550 MPa with a mixed microstructure of ferrite and pearlite. These are used in critical applications, such as bridges, buildings or ship construction and may undergo sophisticated thermomechanical processing to refine the microstructure and greatly improve the toughness. Such alloys may contain quantities of fine bainite or even martensite when the overall carbon concentration is small.

All structural steels have to be welded. For this reason and to minimise the cost, the total alloy concentration is generally less than 5 wt%. The weld metals used for joining structural steels also range in yield strength between 350 and 550 MPa, but can be much stronger (900 MPa) for special steels used in the construction of submarines. The preferred weld microstructures contain large quantities of acicular ferrite which, because of its scale and chaotic arrangement, gives good toughness. However, quantities of allotriomorphic ferrite, Widmanstätten ferrite, martensite and retained austenite may also be present.

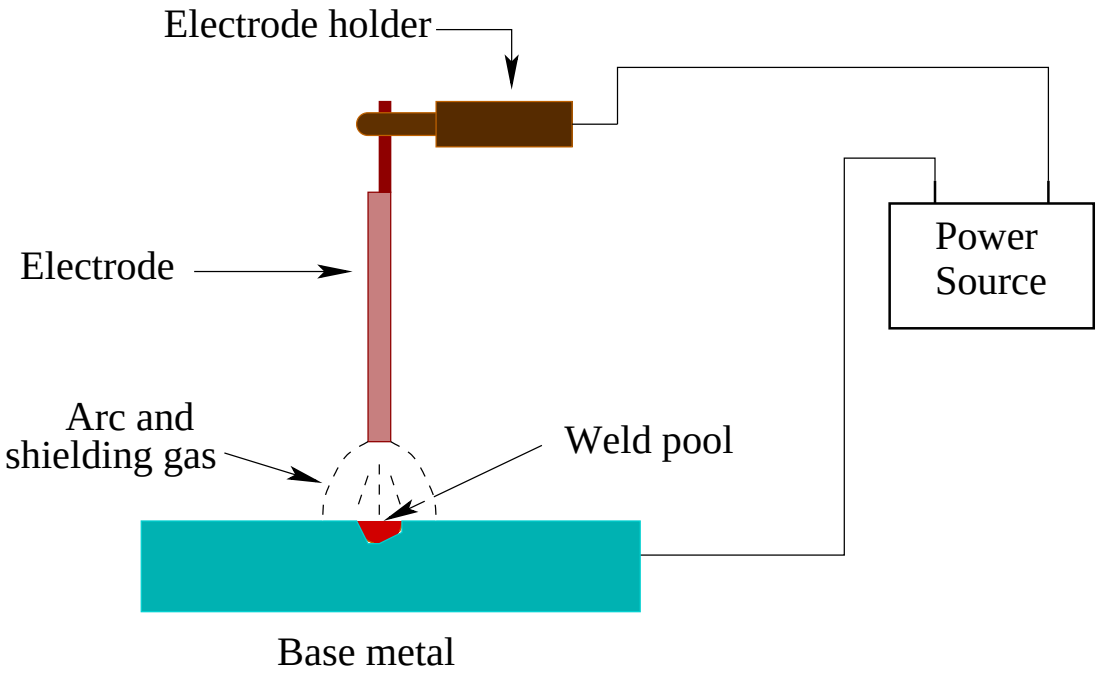

Figure 1.2: Schematic view of arc welding process.

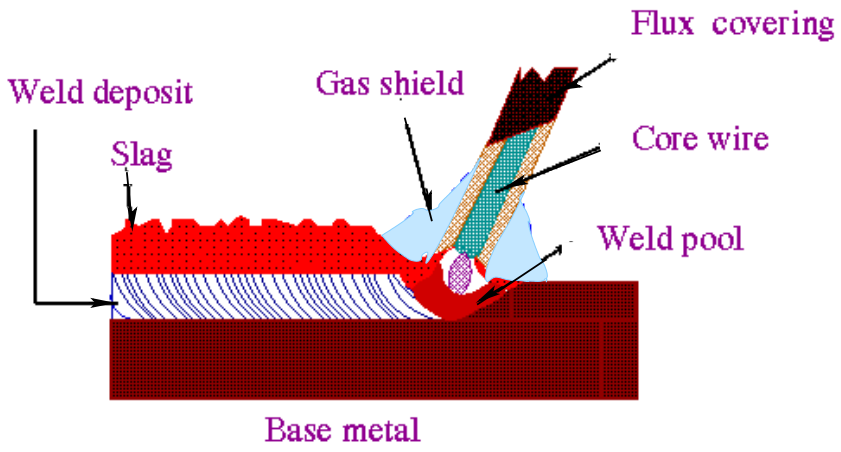

Figure 1.3: Schematic view of manual metal arc welding (MMAW).

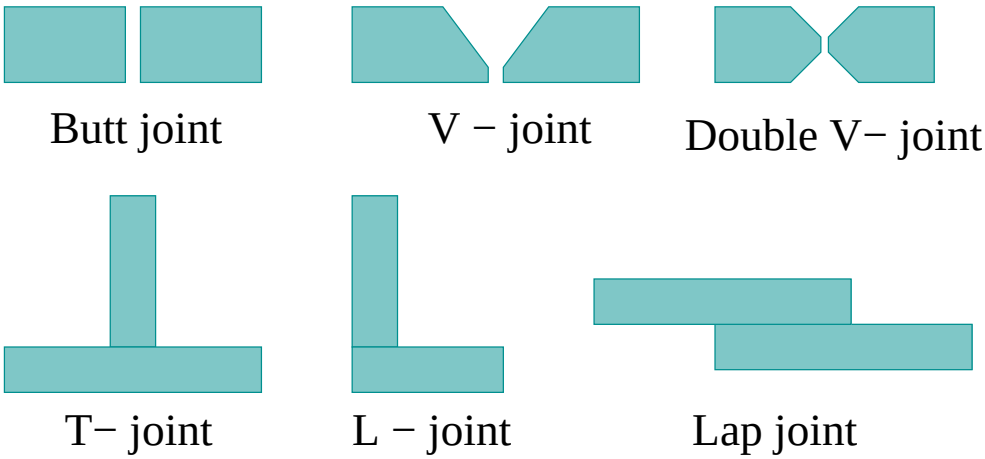

Figure 1.4: Different types of joint preparations.

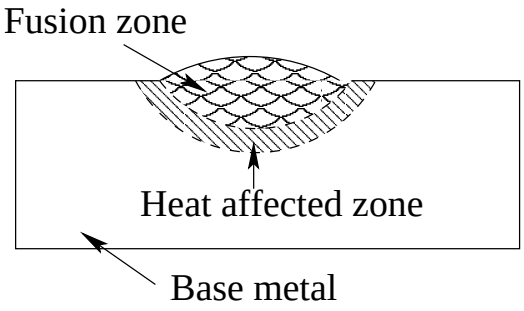

Figure 1.5: Schematic view of the various zones in a single pass weld metal.

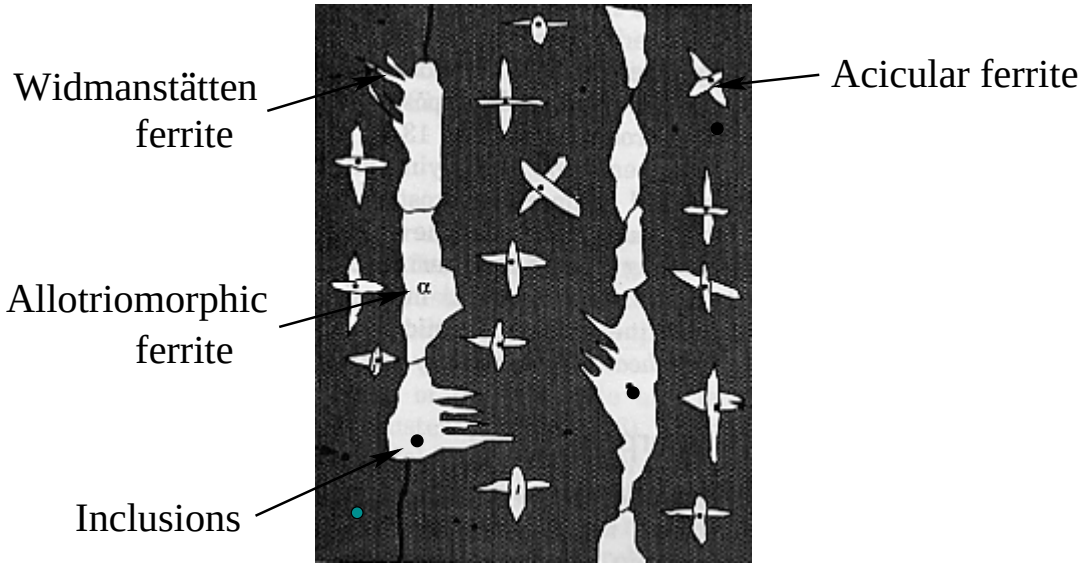

(a)

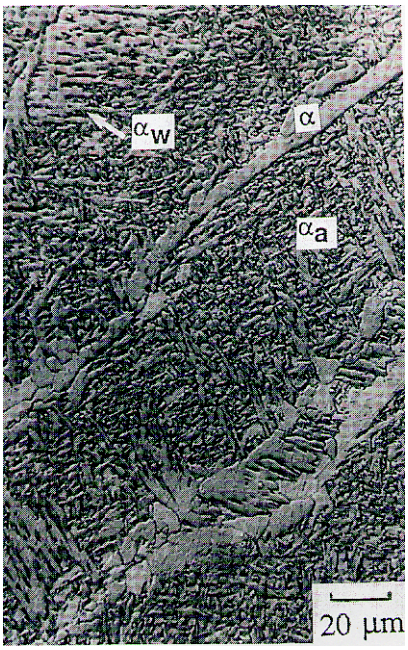

(b)

Figure 1.6: a) Schematic diagram showing different constituents of the primary microstructure in the columnar austenite grains of a steel weld [3], b) scanning electron micrograph of the primary microstructure of a steel weld [7]. α–allotrimorphic ferrite, α_w–Widmanstätten ferrite and α_a–acicular ferrite.

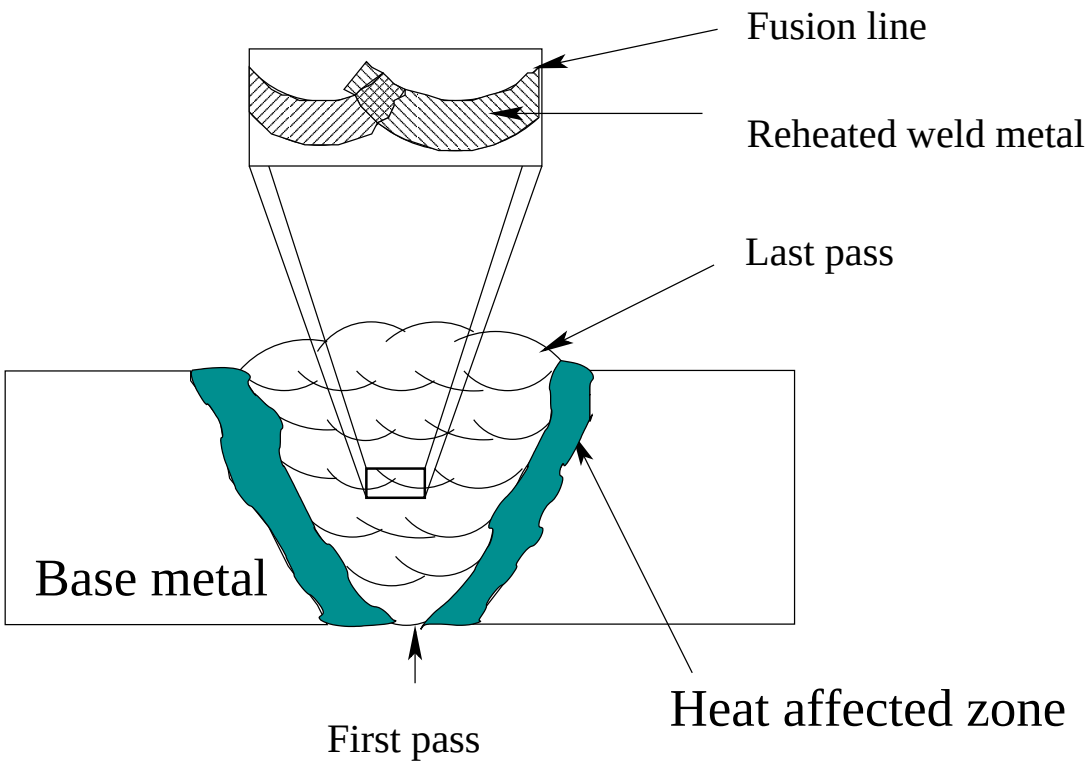

Figure 1.7: Various regions in a multilayer welding.

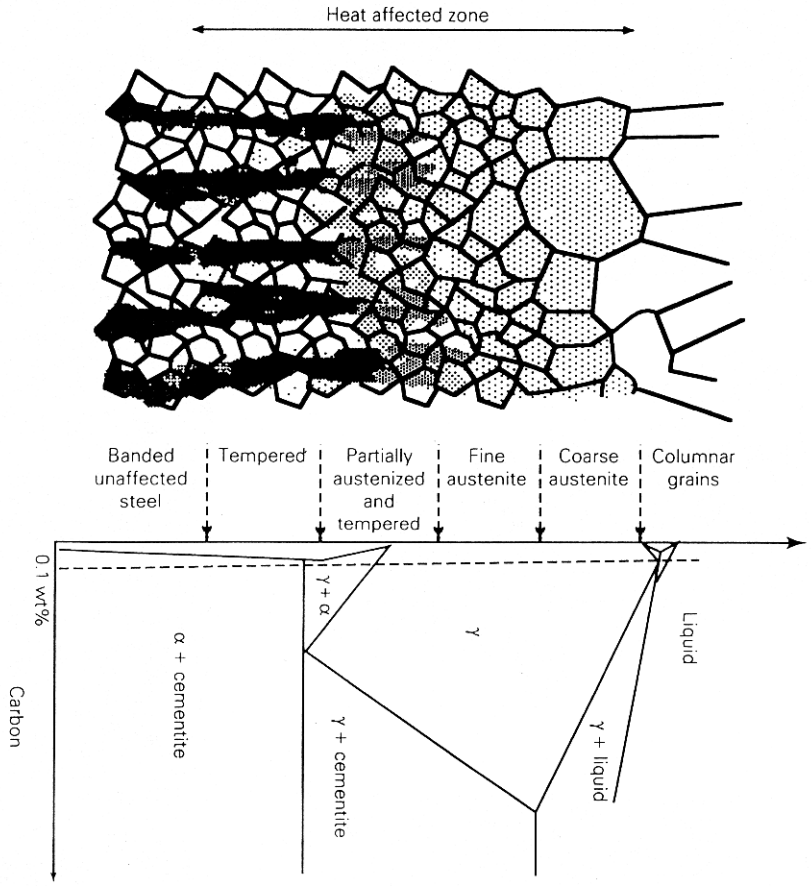

Figure 1.8: Microstructural variations in heat affected zone [7]. The banded structure is a characterisitic feature of segregated steels which have been rolled.

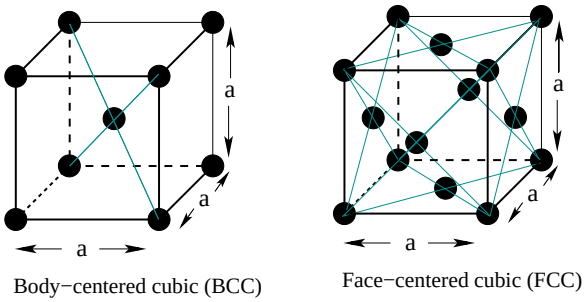

Figure 1.9: Schematic view of frequently observed crystal structures in steels.

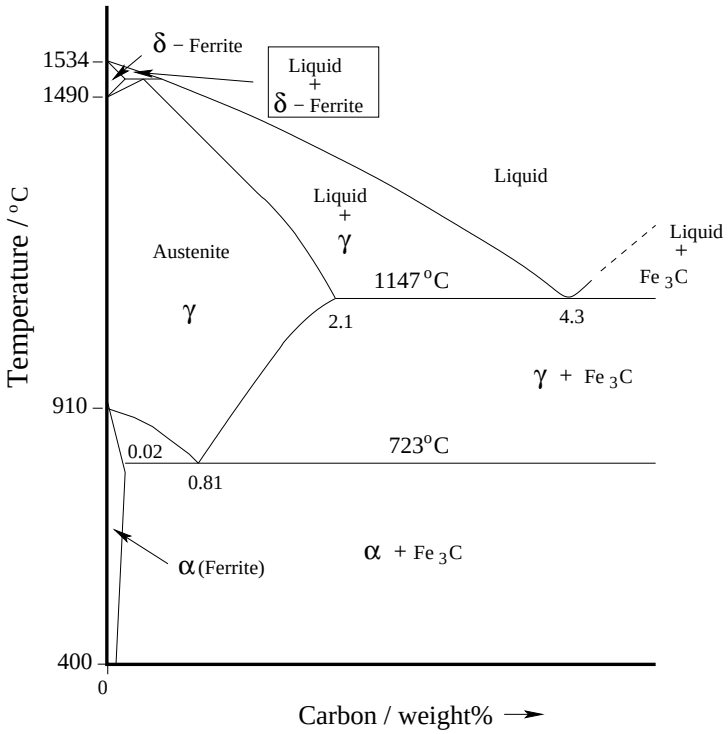

Figure 1.10: Schematic iron–cementite equilibrium phase diagram.

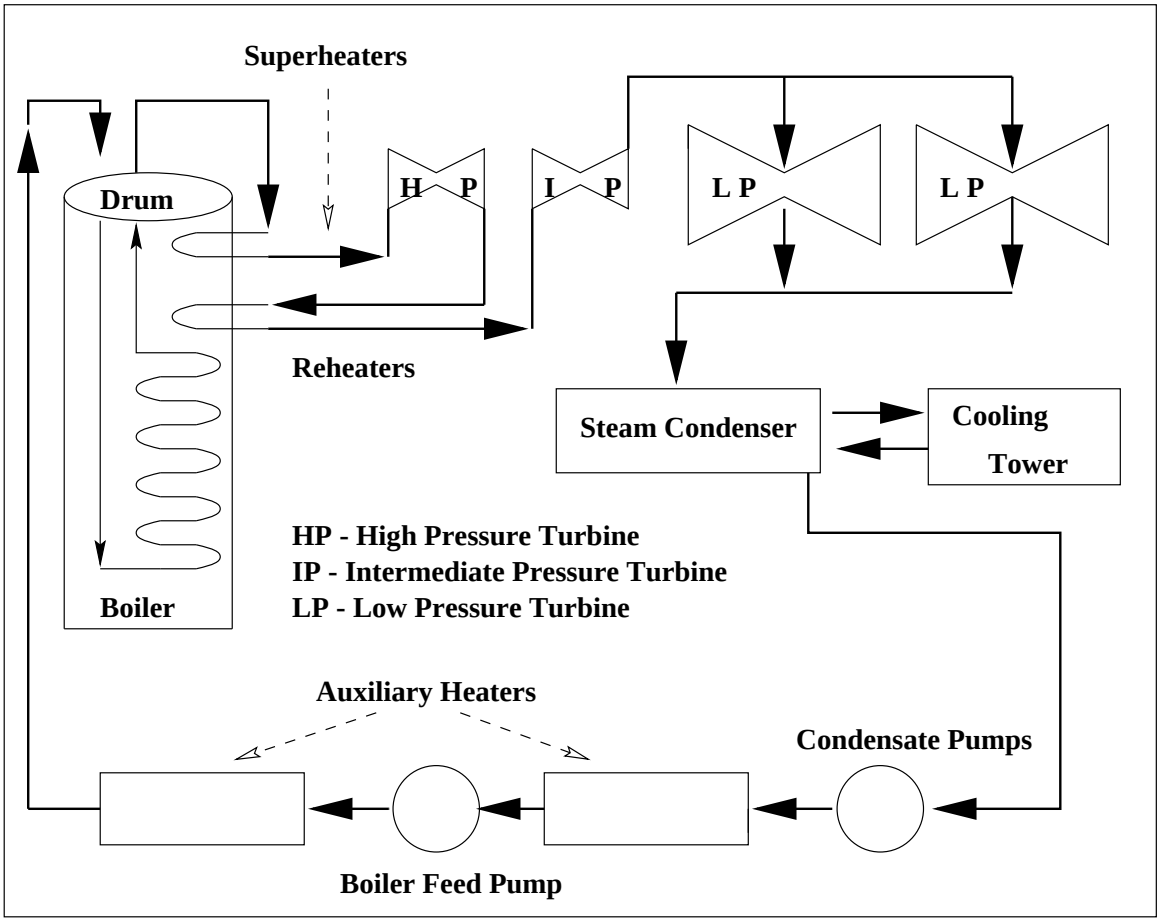

Figure 1.11: Schematic view of the components of a steam power plant.

Chapter 2

Mechanical Properties of Weld Deposits

Many engineering components are fabricated using welding. The integrity of the fabrication is usually asserted on the basis of mechanical properties. Strength, ductility and toughness are considered as the essential mechanical properties. Previous work on the modelling of weld metal mechanical properties is reviewed in this Chapter.

2.1 Strength

The capacity of a material to withstand static load can be determined using a tensile test, in which a standard specimen is subjected to a continually increasing uniaxial load until it fractures, Fig. 2.1. The load–elongation curve is plotted and the results are usually restated in terms of stress and strain, which within reasonable limits are independent of the geometry of specimen, Fig. 2.2a:

$$\text{Engineering stress, } \sigma_E = \frac{P}{A_0} \tag{2.1}$$

$$\text{Engineering strain, } \epsilon_E = \frac{L_f - L_0}{L_0} \tag{2.2}$$

where P is the load, A_0 is initial cross–sectional area and L_0 and L_f are initial and final lengths of the sample respectively.

The material at first extends elastically; if the load is released the sample returns to its original length. After exceeding the elastic limit the deformation is said to be plastic, so the sample does not regain its original length if the load is released. With continued loading the engineering stress reaches a maximum beyond which the sample develops a neck. This local decrease in cross-sectional area focuses deformation until the sample fractures.

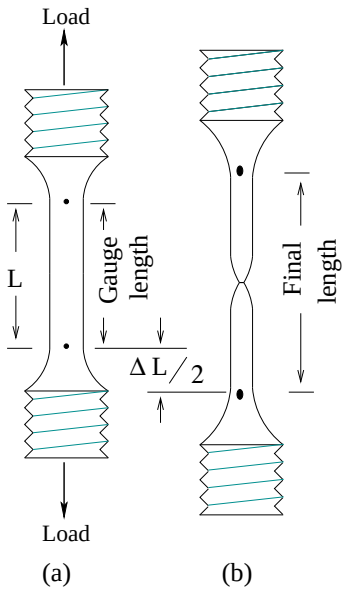

Figure 2.1: Schematic diagram of tensile test specimen, a) before testing b) after testing. $\triangle$ L is the total extension of the specimen during the tensile test.

The yield stress is defined as the stress at which plastic deformation just starts as the stress–strain curve deviates from linearity. Because of the difficulty in precisely measuring this deviation, a '0.2% proof stress' is used which is the stress at 0.002 plastic strain, Fig. 2.2b. The proof stress is sometimes referred as the 'yield stress'. The maximum engineering stress is called the 'ultimate tensile stress', whereas the stress at which the sample fractures is called the 'fracture stress'.

Engineering stresses and strains do not account for the change in the load bearing cross–sectional area of the sample during deformation. The true stress and strain do so and are defined as follows:

$$\sigma = \sigma_E(\epsilon_E + 1) \tag{2.3}$$

$$\epsilon = \ln(\epsilon_E + 1) \tag{2.4}$$

This leads to a change in the form of the stress–strain plot as illustrated in Fig. 2.3.

The engineering strain and true strain are comparable at small strains. The flow curve of many metals as expressed in terms of the true stress σ and true strain ϵ can be represented as:

$$\sigma = K\epsilon^n \tag{2.5}$$

where 'K' is value of flow stress at ϵ=1.0 and 'n' is the strain hardening exponent. Both these

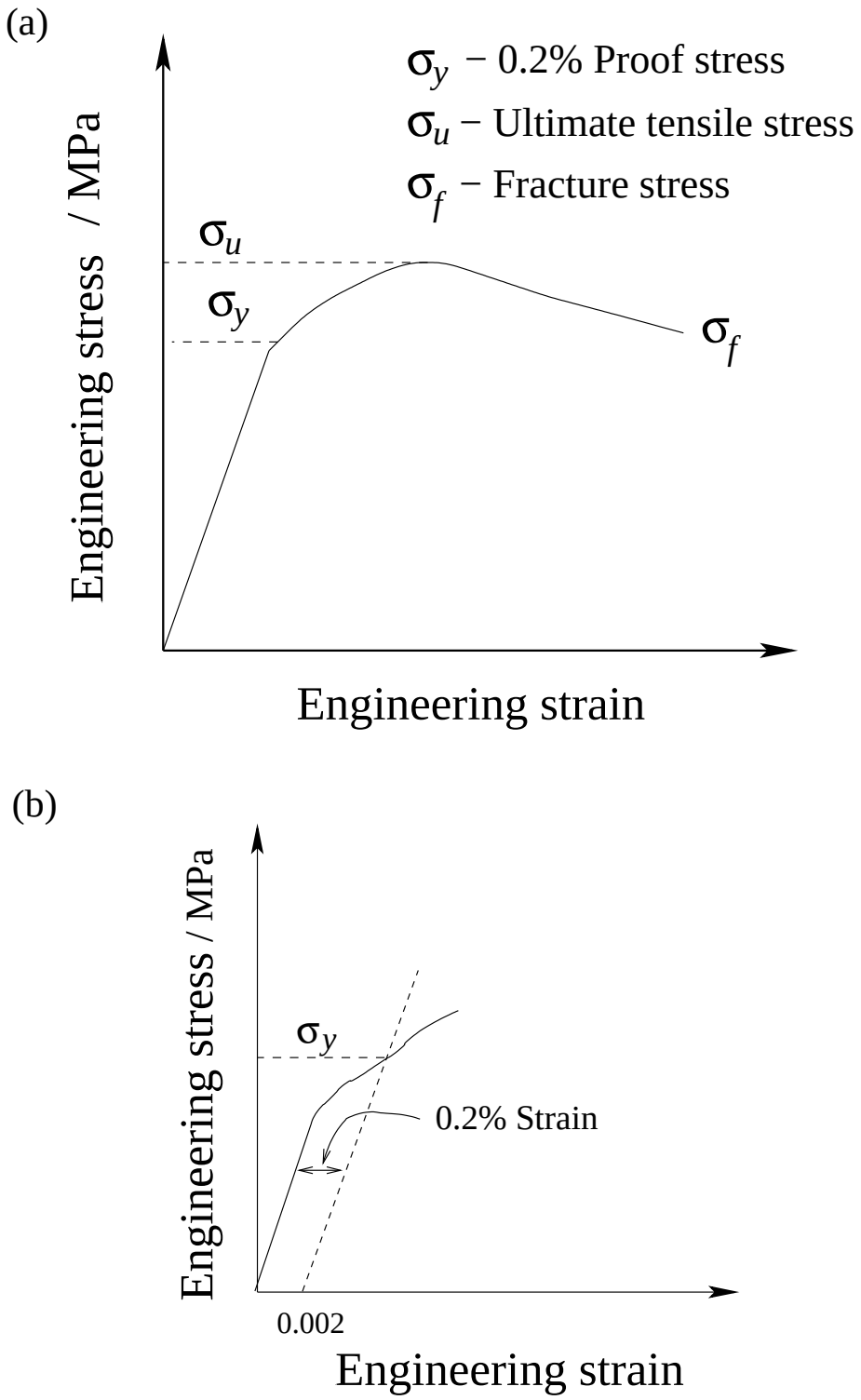

Figure 2.2: Engineering stress-strain curve showing a) different stresses, b) 0.2% proof stress.

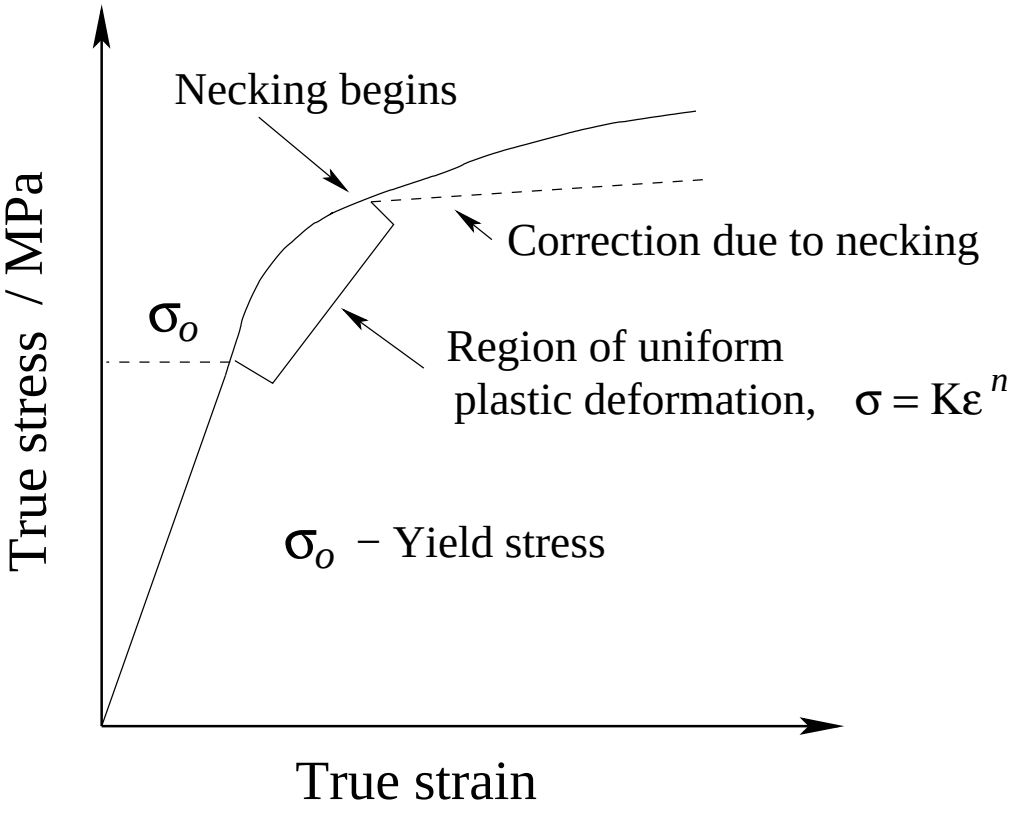

Figure 2.3: True stress - true strain curve (flow curve).

parameters can be estimated from a logarithmic plot of true stress and true strain. In practice, the strain hardening exponent may vary with strain but equation 2.5 is nevertheless a useful representation of plastic deformation.

2.2 Ductility

Ductility is important because an engineering component should show considerable plasticity before fracture. Ductility, as measured in a tensile test, is usually expressed as elongation or reduction in area:

$$\text{Elongation} = \frac{L_f - L}{L} \tag{2.6}$$

$$\text{Reduction in area} = \frac{A_f - A_0}{A_0} \tag{2.7}$$

where, L_f is the length of sample at fracture, L is initial length, A_0 is the initial area of cross-section and A_f is the area of cross–section at fracture. Both elongation and reduction in area

are frequently expressed as percentages.

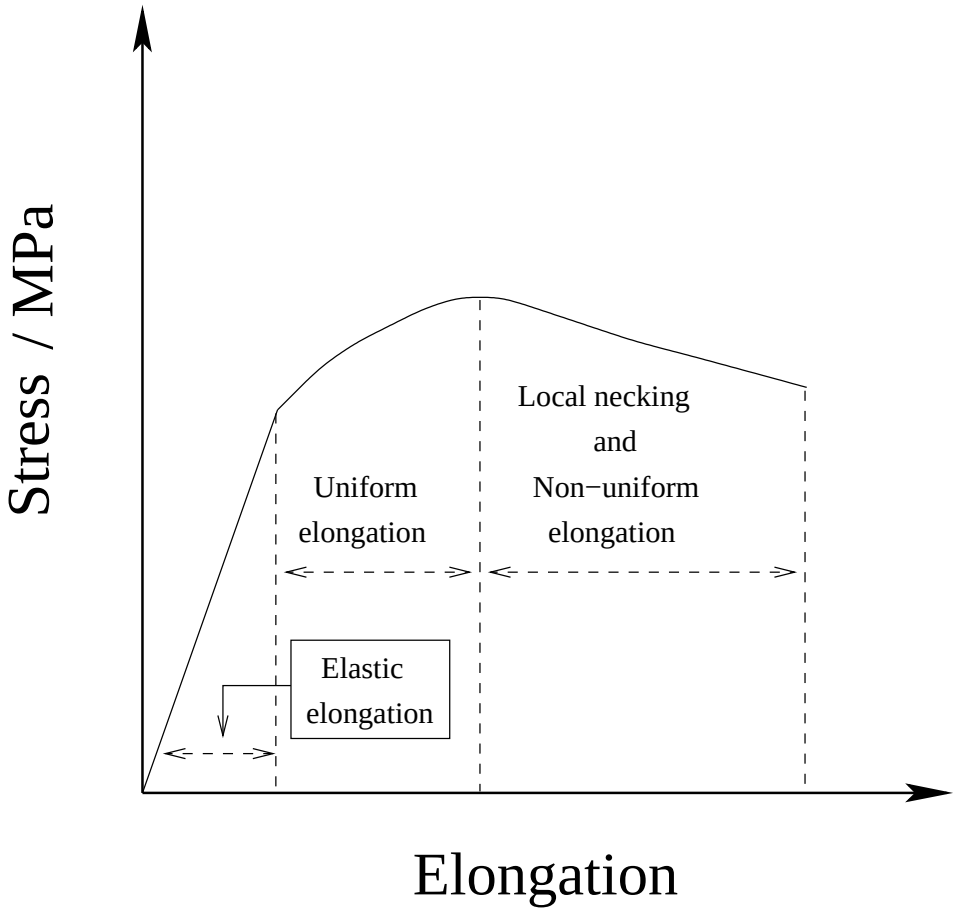

Figure 2.4: The stress-elongation curve. The elastic elongation is exaggerated for clarity.

Plastic strain can be subdivided into two components, an initial uniform strain where the cross–section of the sample is identical along the entire gauge length, and a non–uniform component beginning with the onset of necking. Assuming that equation 2.5 is a true representation of deformation, the stress at the point where necking begins is given by $\sigma = Kn^n$ [17].

2.3 Charpy Impact Toughness

Toughness is the ability of the material to absorb energy during the process of fracture. The ability to withstand occasional stresses above yield stress without fracturing is particularly desirable in engineering components. The welded joints should resist brittle fracture; therefore, the weld metal should be tough, with a great deal of energy being absorbed during the process of fracture. One of the popular test methods to characterise toughness is the Charpy impact

toughness test in which a square sectioned, notched sample (Fig. 2.5a) is fractured under specified conditions [18]. The absorbed energy during fracture is taken as a measure of toughness. However, Charpy impact test values are empirical since these results cannot be used directly in engineering design and can be used only to rank samples in research and development experiments. The test is usually conducted on a material over a range of temperatures to reveal any ductile–brittle transition, Fig. 2.5b.

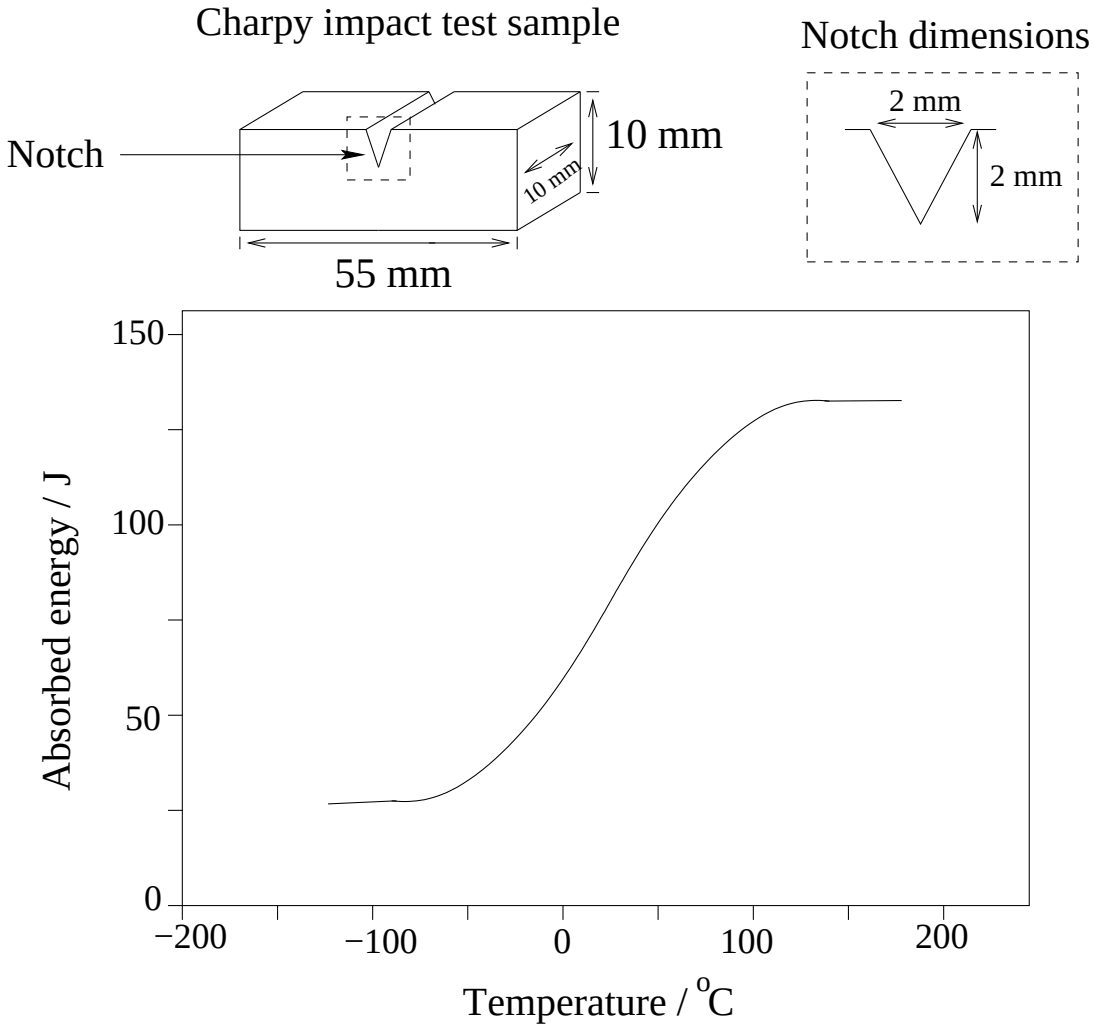

Figure 2.5: The Charpy impact test sample and impact toughness versus test temperature curve.

2.4 Strengthening Mechanisms

Iron in its pure form is weak and can have a yield strength as low as 50 MPa [19]. The strength of pure body–centered cubic iron in a fully annealed condition decreases rapidly as the temperature

is increased, Fig. 2.6. The strength is particularly sensitive to temperatures below -25 °C. In fact, it is this sensitivity to temperature which gives rise to the ductile–brittle transition. The cleavage strength of iron, is insensitive to temperature; at sufficiently low temperature it becomes less than the flow stress, making iron brittle.

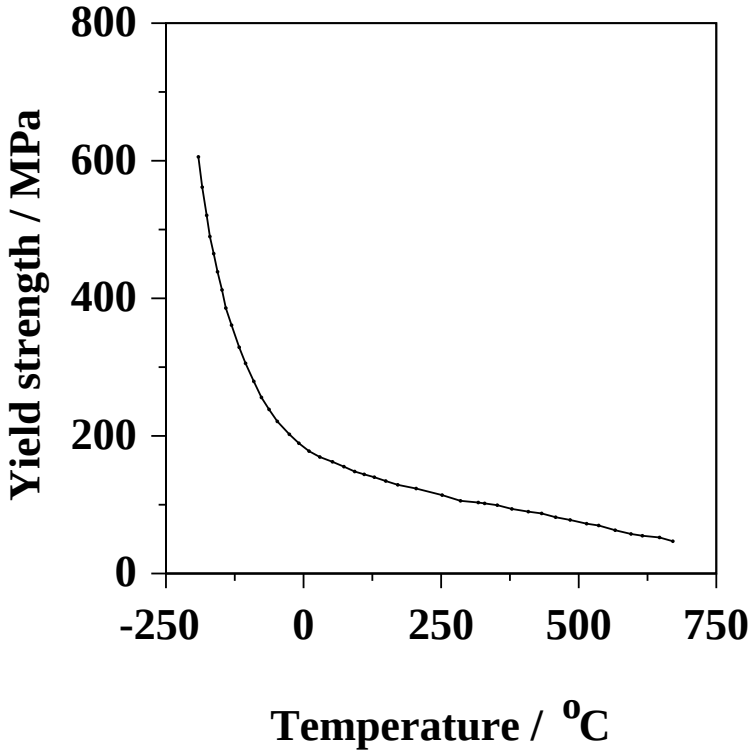

Figure 2.6: Temperature dependence of the yield strength of iron (gettered with titanium) at a plastic strain of 0.002 [12]. The strain rate is $2.5 \times 10^{-4}\ s^{-1}$.

2.4.1 Grain Refinement

The refinement of grain size leads not only to an increase in the strength but also toughness [20]. Grain boundaries are formidable obstacles to the movement of dislocations. The dependence of the yield strength on grain size is given by the Hall–Petch relationship [21]:

$$\sigma_y = \sigma_i + k_y d^{-1/2} \tag{2.8}$$

where 'd' grain diameter, σ_y is the yield stress, σ_i is the friction stress opposing the movement of dislocation in the grains and k_y is a constant.

The derivation of the Hall–Petch equation relies on the formation of a dislocation pile–up at a grain boundary, one which is large enough to trigger dislocation activity in an adjacent grain. Yield in a polycrystalline material is in this context defined as the transfer of slip across grains.

A larger grain is able to accommodate more dislocations in a pile–up, enabling a larger stress concentration at the boundary, thereby making it easier to promote slip in the nearby grain [22].

It is harder to propose a general mechanism by which grain refinement improves toughness. The argument for steels is that grain boundary cementite particles are finer when the grain size is small [22]. Fine particles are more difficult to crack and any resulting small cracks are difficult to propagate, thus leading to an improvement in toughness.

2.4.2 Solid Solution Hardening

The most common method of increasing the hardness and strength of steels is by solid solution strengthening. The degree of hardening or softening due to dissolved elements depends crudely on the relative difference in atomic size relative to an iron atom [12]. Large atoms induce compressive stress fields whereas smaller atoms are associated with tensile fields in the matrix. These distortion interact with dislocation motion. Solid solution strengthening also depends on disturbances to the electronic structure, expressed in terms of the difference of the solute and host atom [20].

In steels the smaller atoms carbon and nitrogen occupy interstitial sites whereas elements like silicon, manganese are substitutional. The interstitial solute atoms cause an asymmetrical distortion of the ferrite lattice whereas the substitutional solute produce symmetrical distortions. Therefore the increase in strength of α–iron by interstitial carbon or nitrogen is much greater than that of any substitutional alloying element Fig. 2.7. Isotropic distortion can only interact with the hydrostatic stress fields of dislocations. Much greater interactions are possible with the tetragonal strains associated with the interstitial atoms in ferrite.

Fig. 2.8 shows that the strengthening due to substitutional solutes often goes through maximum as a function of temperature. In a few cases there is some softening in body centered cubic α–iron at low temperatures because the presence of foreign solute atom locally assists dislocations to overcome the large Peierls barrier to dislocation motion [1].

2.4.3 Precipitation Hardening

Small and uniformly distributed precipitates can be effective barriers to dislocation movement. Precipitation hardened steels strengthening are usually first heat treated in the austenite phase field in order to dissolve solutes and then cooled rapidly to ambient temperatures to produce a supersaturated ferrite or martensitic transformation. Tempering then allows the excess solute to precipitate as carbides or nitrides, thereby strengthening the microstructure. In steels the strong carbide–forming elements titanium, vanadium, niobium, molybdenum, *etc.* are commonly used as the main precipitation strengthening elements. This mechanism is applied widely to increase the creep strength of power plant steels.

2.5 Tempering

During welding, there are regions created which are austenitised and then cooled rapidly, producing brittle microstructures such as martensite. Tempering is frequently used to restore the toughness, by heat treating in a temperature regime where austenite cannot form.

Thus, any excess carbon in solution is rejected to form carbides. In some cases the purpose of tempering is to induce the precipitation of alloy carbides. Power plant steels containing carbide forming elements such Cr, Mo, V, Nb, Ti, and W form stable carbides such as MX, M_3X, M_2X, M_7X_3, $M_{23}X_6$ and M_6X (where M represents metal atoms, X represents interstitial atoms) on tempering at temperatures where there is sufficient mobility for the diffusion of substitutional atoms. This generally means temperatures above 500 °C. The precipitation of alloy carbides and the associated strengthening is often referred to as 'secondary hardening' [23]. Fig. 2.9 shows the variety of carbides formed during tempering of water quenched $2\frac{1}{4}$Cr–1Mo steel from its austenitisation temperature.

2.6 Previous Weld Mechanical Property Models

Weld metal models can in general be categorised into two classes, those which are empirical and others founded on physical metallurgy. The latter are more meaningful, but as will be seen later, they are generally over–simplified and deal only with simple properties rather than the range of properties important in engineering design.

2.6.1 Regression Models

There have been numerous attempts to model weld metal mechanical properties by using linear regression analysis (e.g. Table 2.1). The strength of weld metal is frequently modelled as a function of chemical composition of weld metal, for cases where all the remaining variables associated with welding approximately constant. Equations like these are useful within the context of the experiments they represent. Naturally, the form of the relationships used may not necessarily be justified in detail.

2.6.2 The Sugden–Bhadeshia Model

Sugden and Bhadeshia tried to predict the strength of the as–deposited weld as a function of the chemical composition and microstructure [25]. The model is based on the assumption that the strength can be factorised into components; strength of pure iron, solid solution strengthening and strength due to microstructure, equation 2.9. The chosen microstructural constituents are allotriomorphic ferrite (α), Widmanstätten ferrite (α_w) and acicular ferrite (α_a) with the following assumptions:

Carbon–Manganese	YS = 335 + 439 C + 60 Mn + 361 (C.Mn) UTS = 379 + 754 C + 63 Mn + 337 (C.Mn)
Silicon–Manganese	YS = 293 + 91 Mn + 228 Si - 122 Si^2 UTS = 365 + 89 Mn + 169 Si - 44 Si^2
Chromium–Manganese	YS = 320 + 113 Mn + 64 Cr + 42 (Mn.Cr) UTS = 395 + 107 Mn + 63 Cr + 36 (Mn.Cr)
Nickel–Manganese	YS = 332 + 99 Mn + 9 Ni + 21 (Mn.Ni) UTS = 401 + 102 Mn + 16 Cr + 15 (Mn.Ni)

Table 2.1: Yield and ultimate tensile strength (MPa) models developed using regression analysis for as–welded carbon–manganese weld metals [2]. The alloying element concentrations are expressed in wt%.

1) The total strength of as–welded deposit is assumed to be a linear combination of individual components:

$$\sigma_y = \sigma_{\text{Fe}} + \sum_{i=1}^{n} \sigma_{SS,i} + \sigma_{\text{Micro}} \tag{2.9}$$

where σ_{Fe} is the strength of fully annealed pure iron as a function of temperature and strain rate, $\sigma_{SS,i}$ is the solid solution strengthening due to alloying element i and σ_{Micro} is strengthening due to weld metal microstructure.

2) The weld microstructure consists of allotriomorphic ferrite (α), Widmanstätten ferrite (α_w) and acicular ferrite (α_a). The variation in the grain sizes of α, α_w and α_a are not taken into account:

$$\sigma_{\text{Micro}} = \sigma_\alpha \, V_\alpha + \sigma_a \, V_a + \sigma_w \, V_w \tag{2.10}$$

where σ_α, σ_w and σ_a denote the contributions from 100% allotriomorphic ferrite, Widmanstätten ferrite and acicular ferrite respectively, and V_α, V_w and V_a are their corresponding volume fractions.

3) Nitrogen is assumed to be in solid solution and any strain ageing effects in the as-welded microstructure are assumed to be negligible.

4) The solid solution strengthening (σ_{SS}) is expressed as the sum of the contributions from each solute:

$$\sigma_{SS} = a \text{ Mn wt\%} + b \text{ Si wt\%} + ... \tag{2.11}$$

where the coefficients *a, b, ..* are functions of temperature, defining the role of the respective alloying elements. The values for these coefficients are taken from the published experimental data which are based on studies in which solid solution strengthening is studied in isolation.

An alloying element naturally influences more than just solid solution effects. However, the other consequences are included in the analysis via incorporation of microstructure. The authors were able to estimate the strength of individual microstructures (σ_α, σ_a and σ_w) by studying three welds which are made with identical welding conditions [25]. The chemical compositions were adjusted to give different fractions of microstructure in order to deduce the strengthening due to each microstructure (α, α_a and α_w). The final form of developed equation is;

$$\sigma_y = \sigma_{\mathrm{Fe}} + \sigma_{SS} + 27V_\alpha + 402V_a + 486V_w \quad \text{(MPa)} \tag{2.12}$$

where σ_{Fe} and σ_{SS} can be obtained from referred published literature [25].

Although the Sugden–Bhadeshia model has more physical meaning when compared with the empirical equations presented in Table 2.1, the model still has linear approximations which are not justified in detail. It is restricted to structural steel welds which have simple, untempered microstructures; bainite and martensite are excluded from the analysis, as is precipitation hardening. Young and Bhadeshia have developed the work for microstructures which are mixtures of bainite and martensite but this model has yet to be applied to weld metal microstructures. The model is nevertheless discussed below because it is interesting.

2.6.3 The Young–Bhadeshia Model

The Young–Bhadeshia strength model for high–strength steels [4] considered microstructures which are mixtures of martensite and bainite;

$$\sigma = \sigma_{\mathrm{Fe}} + \sum_i \sigma_{SS,i} + \sigma_C + K_L(\overline{L})^{-1} + K_D\rho_D^{0.5} + K_p\triangle^{-1} \tag{2.13}$$

where K_L, K_D and K_p are constants, σ_C is the solid solution strengthening due to carbon, $\overline{L}$ is a measure of the ferrite plate width, ρ_D is the dislocation density and $\triangle$ is the distance between any carbide particles. The other terms have their usual meanings.

Carbon

The carbon concentration in bainitic ferrite is assumed as 0.03 wt%, unlike the martensite which is supersaturated. Thus, the strengthening effect of carbon at the low concentrations typical in

bainite takes the form;

$$\sigma_{SS_C} = 1722.5 \times x^{1/2} \qquad \text{(MPa)} \tag{2.14}$$

where x is the concentration of carbon in wt%. For martensite when the carbon concentration can be large, there is evidence [26] to show that;

$$\sigma_{SS_C} = 1171.3 \times x^{1/3} \qquad \text{(MPa)} \tag{2.15}$$

Dislocations

The bainite and martensite transformations are associated with a shape deformation which may be accommodated by plastic relaxation. This leads to accumulation of dislocations. The amount of plastic deformation and dynamic recovery depends on the transformation temperature, therefore the dislocation density ρ_D is taken as a function of temperature, equation 2.16.

$$\log_{10}\{\rho_D\} = 9.2840 + \frac{6880.73}{T} - \frac{1780360}{T^2} \tag{2.16}$$

where T is the temperature in Kelvin and ρ_D is in m^{-2}. Equation 2.16 is taken from data over 570–920 K and should not be extrapolated. For transformation temperatures below 570 K the dislocation density is considered to be that at 570 K. The strengthening due to dislocations is estimated as;

$$\begin{aligned} \sigma_\rho &= 0.38\ \mu b(\rho_D)^{0.5} \\ &\cong 7.34 \times 10^{-6}(\rho_D)^{0.5} \qquad \text{(MPa)} \end{aligned} \tag{2.17}$$

where μ is the shear modulus and b is the magnitude of the Burgers vector.

Lath Size

Bainite and martensite in low alloy steels occur in the form of fine plates or laths. Here the dislocation sources are found at grain boundaries which is different from the classical Hall–Petch effect which considers the dislocations sources within individual grains. The increase in strength due to plate size is given by;

$$\sigma_G \cong 115(\overline{L})^{-1} \tag{2.18}$$

where σ_G is in MPa and $\overline{L}$ is the mean linear intercept taken on random sections and at random angles to the length of any plate section.

Carbide Particles

The strengthening σ_θ due to a uniform dispersion of spherical carbides particles is considered to be;

$$\sigma_\theta \cong 0.52 V_\theta \triangle^{-1} \qquad \text{(MPa)} \tag{2.19}$$

where $\triangle$ is the particle spacing and V_θ is the volume fraction of cementite. Bainite that occurs in high–strength low–alloy steels has most of its carbon partitioned into the residual austenite where it remains in solid solution. Young and Bhadeshia considered that cementite precipitation does not make significant contribution to the strength, but the carbon rejected into the austenite is important via its effects on the solid solution strengthening of martensite which forms during the cooling of austenite to ambient temperature.

The Young and Bhadeshia model can be applied to estimate the strength of bainitic and martensitic welds by using rule of mixtures. Even though the model had considered the microstructural influence the model still built on the some of the assumptions made in Sugden and Bhadeshia model like linear summation effect of solid solution strengthening.

2.6.4 Neural Network Models

Neural networks are parameterised non–linear regression models which are discussed in detail in Chapter 3. Cool *et al.* had developed neural network models to predict the yield strength, ultimate tensile strength of weld metals as a function of chemical composition, welding parameters and heat treatment [27]. Around 1652 individual experimental data were used in the analysis.

2.7 Conclusions

The basic strengthening mechanisms in steels related to weld metal mechanical properties have been reviewed and discussed. There has been substantial progress in understanding the origins of the yield strength of sample weld metal microstructure of allotriomorphic ferrite, Widmanstätten ferrite and acicular ferrite. Similar progress seems unlikely for those mechanical properties such as the ultimate tensile strength, ductility and toughness, all of which involve gross plasticity. Another difficulty is that the effects of heat treatments are not included explicitly in any mechanical property models.

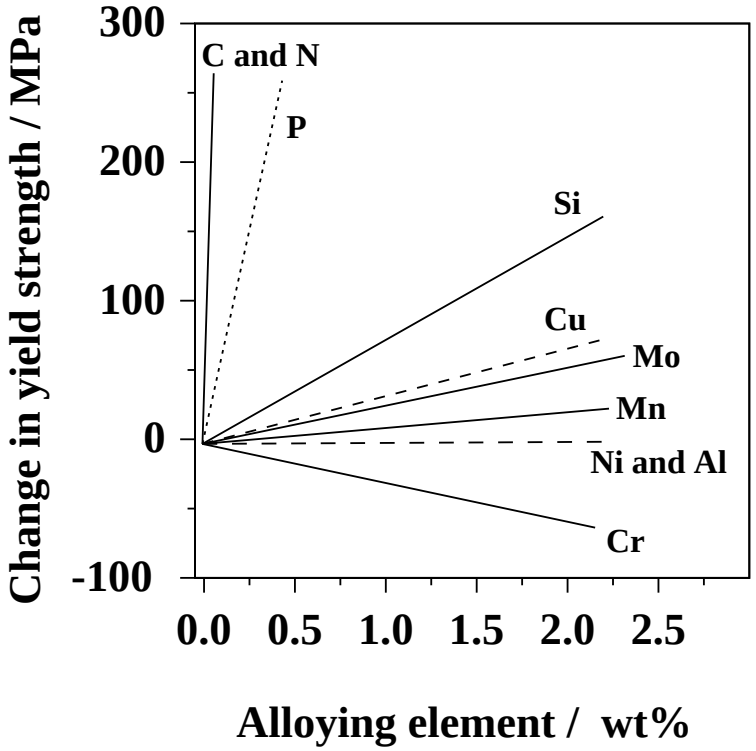

Figure 2.7: Contributions to the solid solution strengthening of ferrite [20].

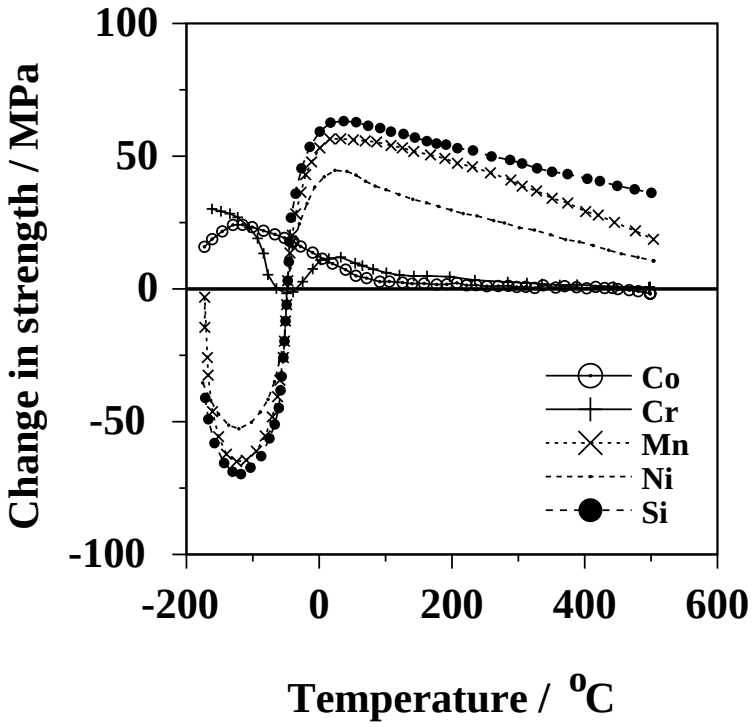

Figure 2.8: The effect of some substitutional solutes (3 at.%) on the yield strength of iron [12]. The strain rate is $2.5\times10^{-4}\ s^{-1}$.

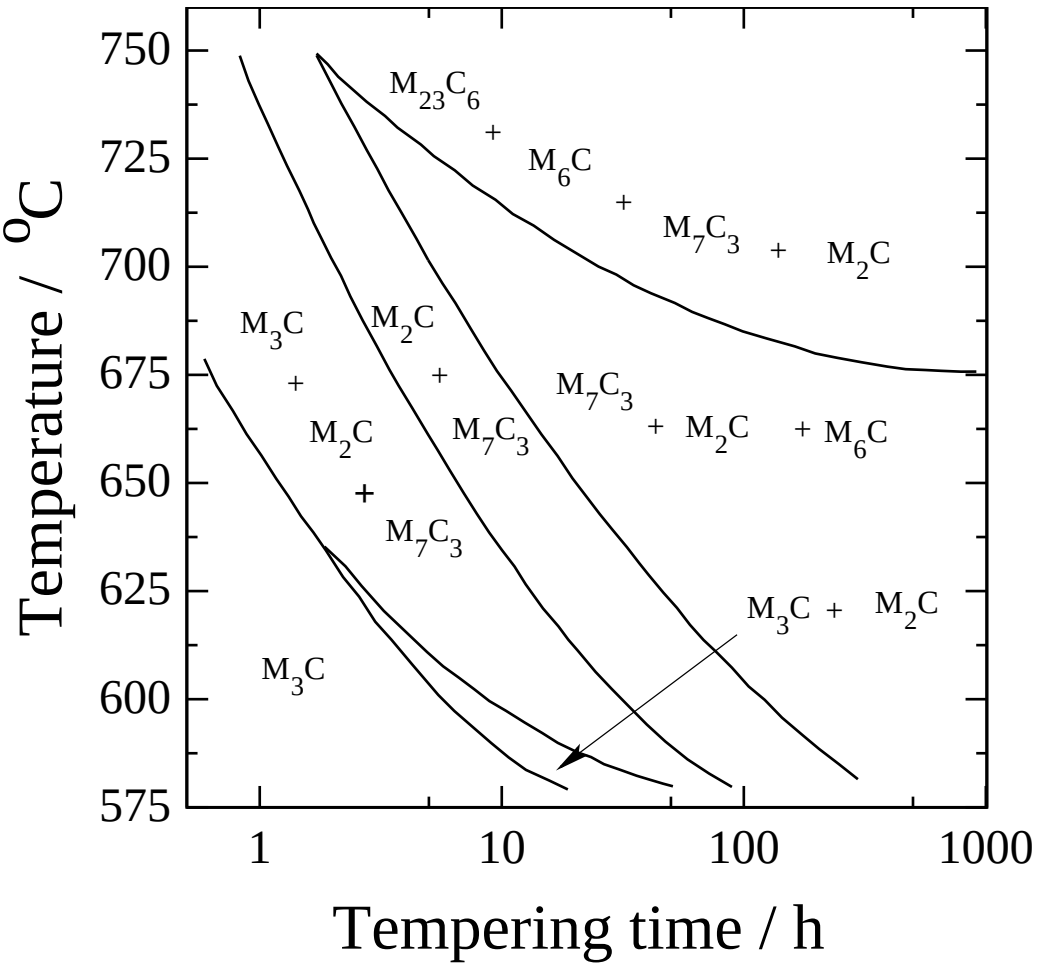

Figure 2.9: Carbide sequence in water quenched $2\frac{1}{4}$Cr–1Mo steel [24], where 'M' represents metallic elements.

Chapter 3

Neural Network Modelling

Regression analysis is familiar to scientists as a tool to fit experimental data empirically . The linear relationship is chosen before the best–fit coefficients are derived. The general form of the equation developed using linear regression is a sum of the inputs x_i multiplied by a corresponding coefficient or weight w_i and added with a constant (θ). The developed linear equation may contain non–linear terms, forming a pseudo–linear equation. In linear regression models the relationship between a input and output tends to be linear and applies across the entire span of the input space, which may not be reasonable. Neural networks is a general method of non–linear regression which avoids the difficulties occurs in linear regression technique. In this Chapter the fundamentals of neural networks and procedure followed to develop models are discussed.

3.1 Neural Networks

A neural network is a general method of regression analysis in which a very flexible non–linear function is fitted to experimental data. When compared with linear regression analysis, neural networks is a non–linear regression by introducing an another node which is hidden in between input and output as shown Fig 3.1. Similar to linear regression method the input variable x_i is multiplied by weight w_i^1, but the sum of all these products forms the argument of a another transfer function, in this present work it is hyperbolic tangent as in equation 3.2. The final output is defined as linear function of hidden nodes and a constant, equation 3.1. Thus, the dependent variable y is defined as;

$$y = \sum_i w_i^{(2)} h_i + \theta^{(2)}, \tag{3.1}$$

where h_i defined as;

$$h_i = \tanh\left(\sum_j w_{ij}^{(1)} x_j + \theta_i^{(1)}\right) \tag{3.2}$$

where x_j are the j variables on which the output y depends, w_i are the weights (coefficients) and θ_i are the biases (equivalent to the constants in linear regression analysis). The combination of equation 3.2 with a set of weights, biases, value of i and the minimum and maximum values of the input variables defines the network completely, Fig. 3.1. The availability of a sufficiently complex and flexible function means that the analysis is not as restricted as in linear regression where the form of the equation has to be specified before the analysis. The strength of the hyperbolic tangent transfer function is determined by the weight w_j, the exact shape can be varied by altering the weights. The shape of the hyperbolic transfer function will be varied according to the availability of data in the input space. A model with one hidden unit (Fig. 3.2a) may not sufficiently flexible to capture the information from the database, however non–linearity can be increased by combining several of the hyperbolic tangents as shown in Fig. 3.2b.

The neural network can capture interactions between the inputs because the hidden units are nonlinear. The nature of these interactions is implicit in the values of the weights, but the weights may not always be easy to interpret. For example, there may exist more than just pairwise interactions, in which case the problem becomes difficult to visualise from an examination of the weights. A better method is to actually use the network to make predictions and to see how these depend on various combinations of inputs.

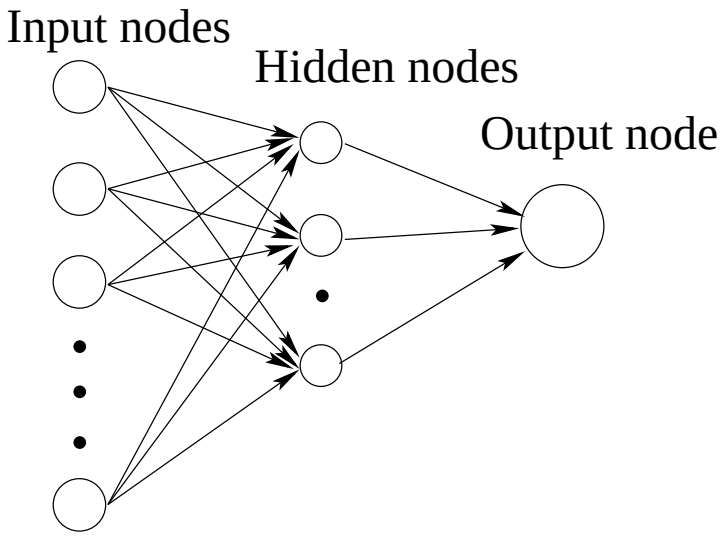

Figure 3.1: Schematic illustration of input, hidden and output layers of neural network model used in the present work.

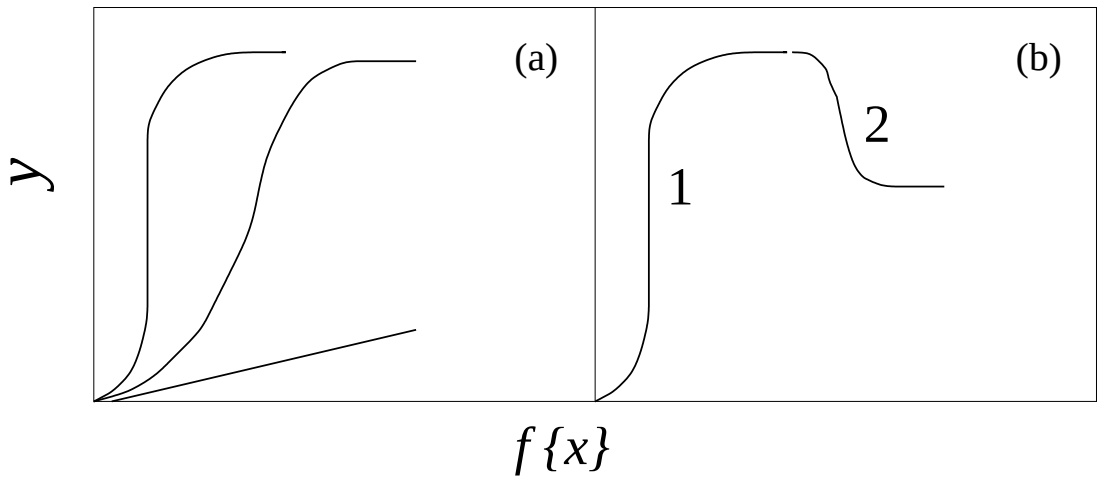

Figure 3.2: Hyperbolic tangent relation between inputs x and output y, a) single flexible hyperbolic tangent with varying weights b) combination of two tangents.

3.2 Error Estimation

The input parameters are generally assumed in the analysis to be precise and it is normal to calculate an overall error by comparing the predicted values (y_j) of the output against those measured (t_j), for example,

$$E_D \propto \sum_j (t_j - y_j)^2 \tag{3.3}$$

E_D is expected to increase if important input variables have been excluded from the analysis. Whereas E_D gives an overall perceived level of noise in the output parameter, it is, on its own, an unsatisfying description of the uncertainties of prediction.

MacKay has developed a particularly useful treatment of neural networks in a Bayesian framework [6], which allows the calculation of error bars representing the uncertainty in the fitting parameters. The method recognises that there are many functions which can be fitted or extrapolated into uncertain regions of the input space, without unduly compromising the fit in adjacent regions which are rich in accurate data. Instead of calculating a unique set of weights, a probability distribution of sets of weights is used to define the fitting uncertainty. The error bars therefore become large when data are sparse or locally noisy.

In this context, a very useful measure is the log predictive error because the penalty for making a wild prediction is reduced if that wild prediction is accompanied by appropriately large error bars [6]:

$$\text{LPE} = \sum_m \left[\frac{1}{2} \frac{(t^{(\text{m})} - y^{(\text{m})})^2}{\sigma_y^{(\text{m})^2}} + \log\left(\sqrt{(2\pi\sigma_y^{(\text{m})})}\right) \right] \tag{3.4}$$

where $\sigma^{(\text{m})}$ is the error bar calculated using Bayesian statistics [6]. A larger value of the log predictive error implies a better model, Fig 3.4b.

3.3 Overfitting

A potential difficulty with the use of powerful non–linear regression methods is the possibility of overfitting data. To avoid this, the experimental data can be divided into two sets, a *training* dataset and a *test* dataset. The Fig. 3.3 illustrates different degrees of complexity in fitting the training dataset and the test data. A linear model is simple and does not capture the real information form the data. An overcomplex model fits all the data in the training dataset, but badly generalised. The optimum model which is a generalised model captures real complexity in the database, Fig. 3.3.

The model is produced using only the training data. The test data are then used to check that the model behaves itself when presented with previously unseen data. The training error tends to decrease continuously as the model complexity increases, Fig 3.4a. It is the highest log predictive error (Fig 3.4b) which enables that model to be chosen which generalises best on unseen data [6].

The analysis uses normalised values of the variables in the range ± 0.5 as follows:

$$x_N = \frac{x - x_{min}}{x_{max} - x_{min}} - 0.5 \tag{3.5}$$

where x is the original value from the database, x_{max} and x_{min} are the respective maximum and minimum of each variable in the original data and x_N is the normalised value. This step is not essential to the running of the neural network but is a convenient way of comparing the effect of different variables on the output. Fig. 3.1 shows the general structure of the simple three layer neural network.

3.4 Model Development Procedure

The experimental data collected are stored in a particular format. These data are normalised using equation 3.5. The normalisation of experimental data is not necessary for the development of models, but it helps in comparing the relative influence of different input variables. Around 80 different neural network models are selected for training over chosen functions (Equ 3.1 and 3.2). These models will differ in number of hidden units and seed to generate random starting weights. Before 'training' of the model, the experimental database is randomised in order to divide the

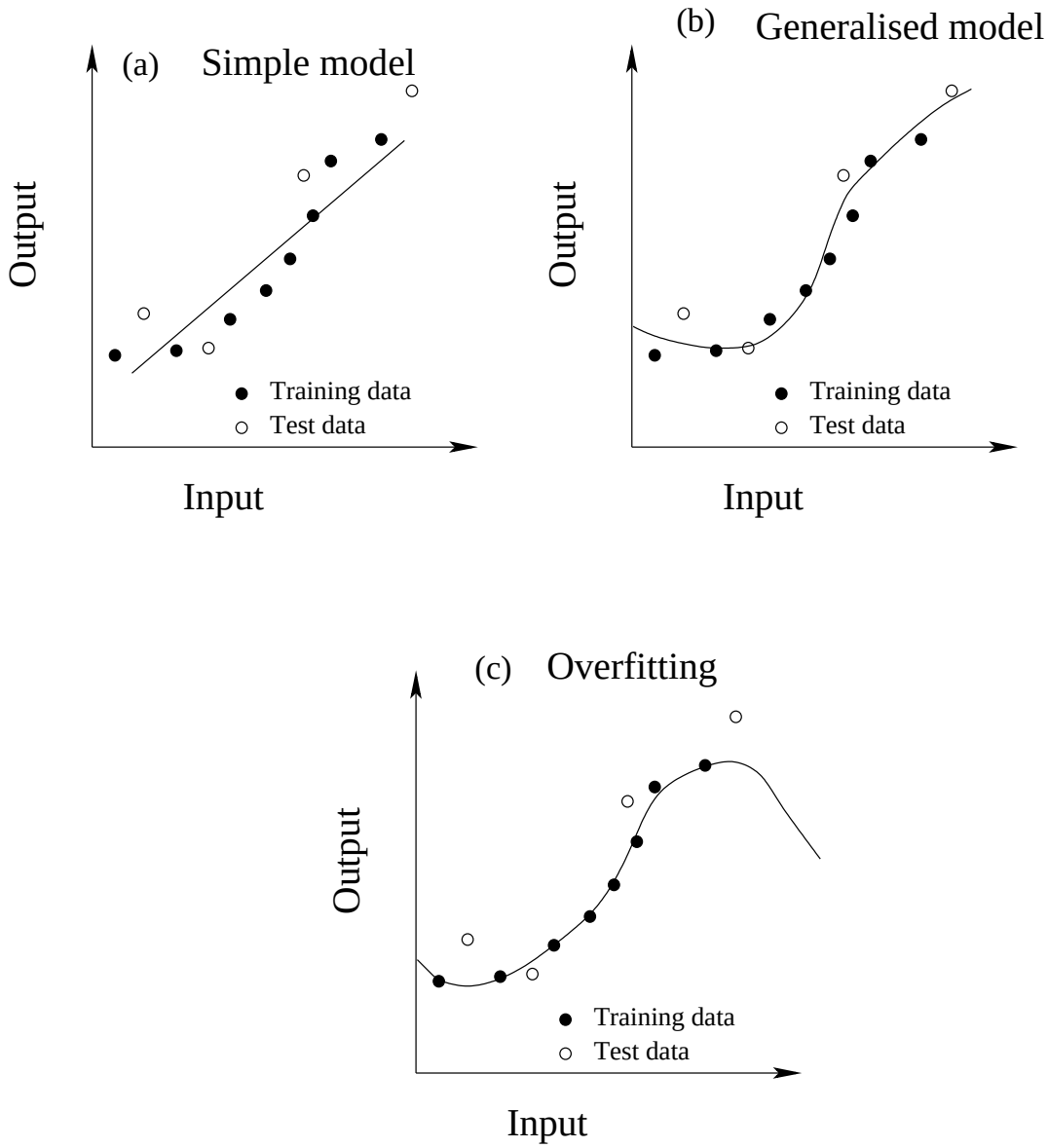

Figure 3.3: Different degrees of complexity of fitting a input and output in a model.

information into test and training datasets in a fair manner. The first half of the randomised dataset is used for training and the remaining is for testing how the trained models behave with unseen data.

For a trained model with database 'D', the overall error 'E_{D}' is the sum of squared error between the desired output (target) 't' and calculated output 'y, equation 3.6.

$$E_{\mathrm{D}} = \frac{1}{2}\sum_{m} \left(t^{(\mathrm{m})} - y^{(\mathrm{m})}\right)^2 \tag{3.6}$$

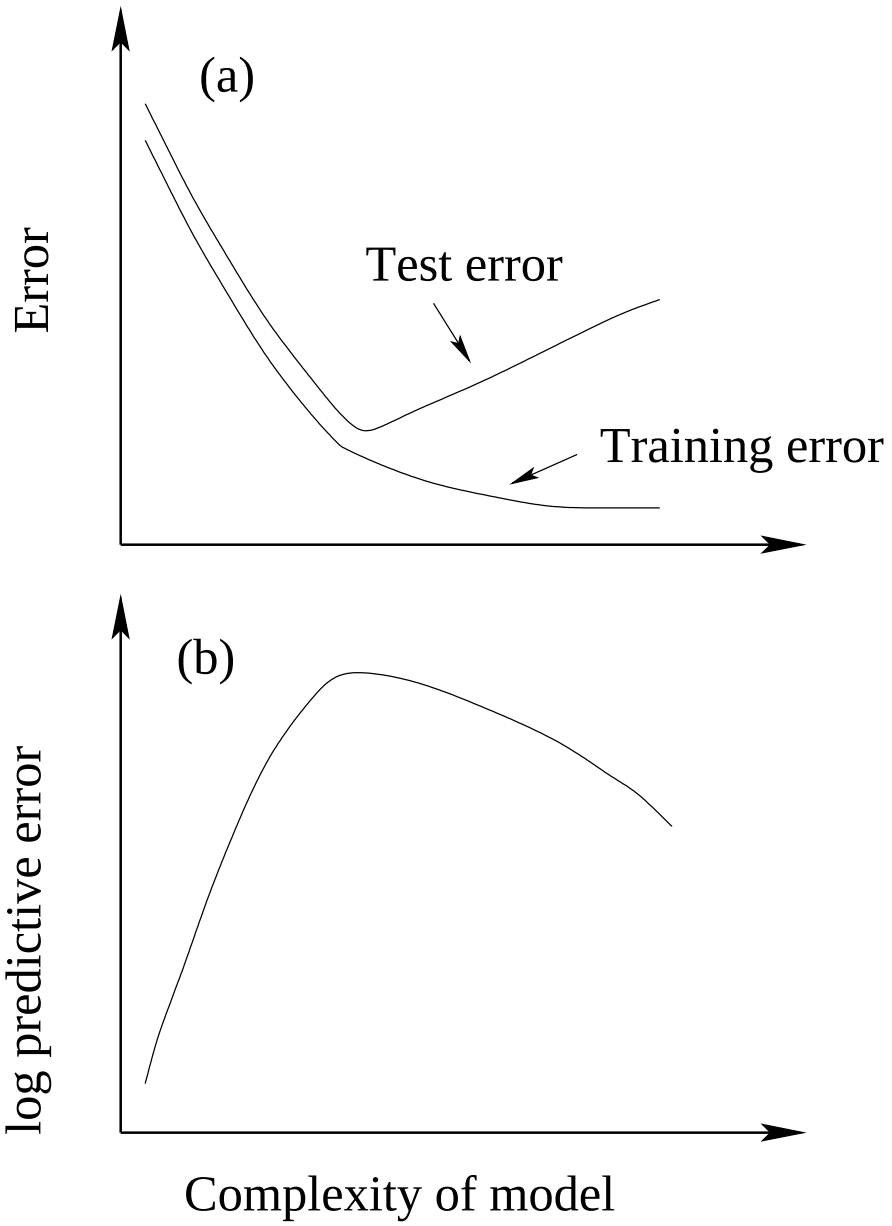

Figure 3.4: Ranking procedure of trained models with varying model complexity a) considering the variation in the test and training error b) log predictive error [6].

Then to have predictions with error bars, the trained models are ranked with decreasing magnitude of log predictive error. It is possible that a committee of models can make a more reliable predictions than an individual model [6]. Starting from the best model, the committee models are selected until the minimum validation or test error is obtained. The committee prediction is the average value of individual model predictions. During predictions using the committee model containing 'L' individual models, average output ($\bar{y}$) and the committee error

bar (σ) are calculated using following equations;

$$\bar{y} = \frac{1}{\mathrm{L}} \sum_{l} y^{(l)} \tag{3.7}$$

$$\sigma^2 = \frac{1}{L} \sum_{l} \sigma_y^{(l)^2} + \frac{1}{L} \sum_{l} (y^{(l)} - \bar{y})^2 \tag{3.8}$$

Without changing the complexity of individual models, the committee is retrained on whole database. During the retraining the weights are adjusted to better fit whole database.

The committee model predictions are the average of calculated values of each individual model in the committee. The architecture (hidden units, seed, etc.) of committee model is complex. This complexity is considered by the neural networks during the training and testing of each individual model. The committee model does not contain any information about any perceived significance of each individual input variable over the output variable like individual model, but the only way to know the effect of each input variable on output is by doing predictions for a given set of input variables and varying the single input variable over a range. Note that error bars have to be taken into consideration during the predictions.

3.5 Interpretation

The neural network can capture interactions between the inputs because the hidden units are non–linear. The nature of these interactions is implicit in values of weights, which difficult to interpret. Interpretation is best done by making predictions and examining the trends taking error bars into consideration.

These error bars, which are calculated using Bayesian inference [6] have special meaning when compared with regression analysis error calculations. As shown in Fig. 3.5, the error bar is a measure of uncertainty in fitting parameters in the noisy data region (A) or the warning message generated when it is making calculations in the region of input space where the data (with which it was trained) are sparse (B). Thus error bars calculated using Bayesian neural network represents both experimental noise and the uncertainty in prediction due lack of information in that data range. The models developed using neural networks are discussed in next chapter.

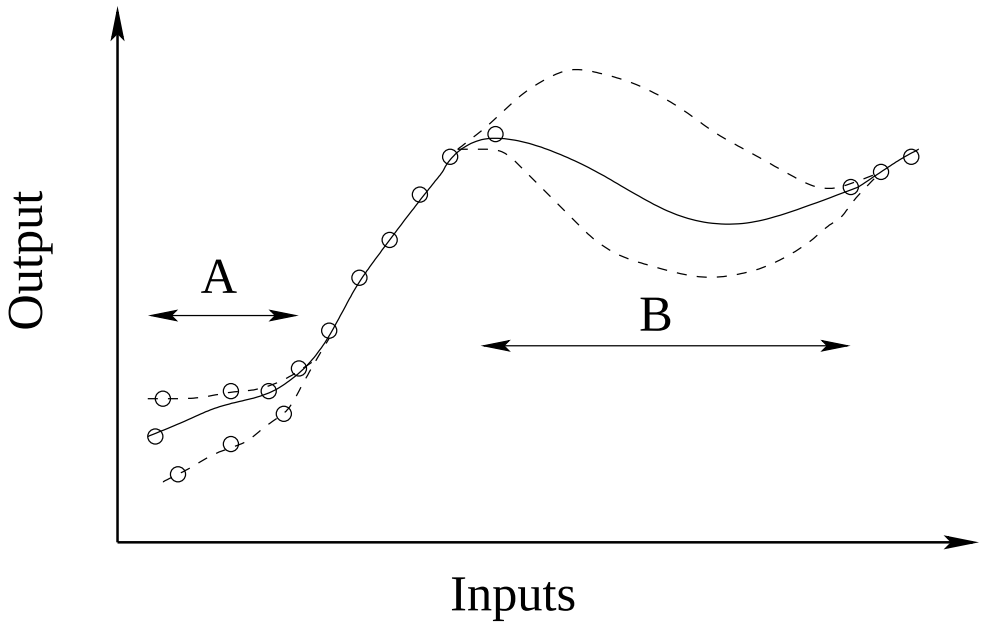

Figure 3.5: Schematic illustration of the uncertainty in defining a fitting function in regions where data are sparse (B) or where there is scatter (A). The dashed lines represent error bounds due to uncertainties in determining the weights.

Chapter 4

Yield and Ultimate Tensile Strength Models

The conventional method for developing a new weld metal with desired mechanical properties involves the design of a series of weld metals, varying chemical compositions and welding parameters. These welds are then manufactured and tested. A choice is then made of a particular combination of variables which best meets the requirements. Cost and time savings might be achieved with the help of appropriate models which reduce the number of steps needed.

The physical models discussed in Chapter 2, based on strengthening mechanisms, are not sufficiently sophisticated to enable a proper treatment of the problem. At the same time linear regression methods are not capable of representing the real behaviour which is far from linear when all the factors are taken into account.

On the other hand, the neural network method described in Chapter 3 is ideally suited to complex phenomena with many variables. In the present work, neural networks are used to model the yield strength and ultimate tensile strength of weld metal as a function of weld metal chemical composition, welding parameters and heat treatment conditions. Previous research along these lines by Cool *et al.* [27] was based on a rather limited database. The models are then used to design new alloys of use in the fabrication of power plant components.

4.1 Database

All of the data collected are from multirun weld deposits in which the joint is designed to minimise dilution from the base metal, to enable specifically the measurement of all–weld metal properties. Furthermore, they all represent electric arc welds made using one of the following processes: manual metal arc (MMAW), submerged arc welding (SAW) and tungsten inert gas (TIG). The welding process itself was represented only by the level of heat input. This is because a large number of published papers did not specify welding parameters in sufficient detail to enable the creation of a dataset without missing values. Missing values cannot be tolerated

in the method used here. If the effect of a welding process is not properly represented by the heat input and chemical composition, then neglect of any important parameters will make the predictions more 'noisy'. As discussed below, the noise in the output was found to be acceptable; a greater uncertainty arises from the lack of a uniform coverage of the input space. The data were collected from a large number of sources [28] to [88].

The aim of the neural network analysis was to predict the yield and tensile strength as a function of a large number of variables, including the chemical composition, the welding heat input and any heat treatment. The databases for the yield and ultimate tensile strength (UTS) are different because the UTS database also included the oxygen concentration since tensile failure should depend on inclusions which nucleate voids. As a consequence, the yield strength database consists of 2002 separate experiments whereas the UTS database is slightly smaller at 1972 experiments since the oxygen concentration was not always reported. Neural network method used in this work cannot cope with missing values of any of the variables. In 14 cases the sulphur and phosphorus concentrations were not available. Since these impurities might be important, it would not be satisfactory to set them to zero. Missing values of sulphur and phosphorus were therefore set at the average of the database.

4.1.1 Yield Strength Database

Table 4.1 shows the range, mean and standard deviation of each variable including the output (yield strength). The purpose here is simply to list the variables and provide an idea of the range covered. It is emphasised however, that unlike linear regression analysis, the information in Table 4.1 cannot be used to define the range of applicability of the neural network model. This is because the inputs are in general expected to interact. We shall see later that it is the Bayesian framework of our neural network analysis which allows the calculation of error bars which define the range of useful applicability of the trained network. A visual impression of the spread of data is shown in Fig. 4.1. It can be concluded from Fig. 4.1 that the effect on yield strength of carbon, manganese, silicon, nickel, molybdenum and heat input have been systematically studied. Hence, future experiments could focus on examining the effect of chromium in the range 3–8 wt%, vanadium (0.1–0.2 wt%), cobalt at all concentrations but in greater variety of alloy systems, tungsten at low and high concentrations, titanium and boron in high strength weld. The effect of tempering temperature in the range 250–500 °C also needs to be studied.

4.1.2 Ultimate Tensile Strength Database

Table 4.2 shows the range, mean and standard deviation of each variable including the output (ultimate tensile strength). The corresponding visual impression of the UTS database is similar

Input element	Minimum	Maximum	Mean	Standard deviation
Carbon (wt%)	0.01	0.22	0.072	0.025
Silicon (wt%)	0.01	1.63	0.344	0.138
Manganese (wt%)	0.27	2.31	1.192	0.41
Sulphur (wt%)	0.001	0.14	0.009	0.006
Phosphorus (wt%)	0.001	0.25	0.012	0.009
Nickel (wt%)	0.0	4.79	0.43	0.888
Chromium (wt%)	0.0	12.1	0.808	1.952
Molybdenum (wt%)	0.0	2.4	0.221	0.368
Vanadium (wt%)	0.0	0.32	0.026	0.06
Copper (wt%)	0.0	2.18	0.063	0.185
Cobalt (wt%)	0.0	2.8	0.007	0.115
Tungsten (wt%)	0.0	3.86	0.091	0.427
Titanium (p.p.m.)	0.0	900	64.9	112.14
Boron (p.p.m.)	0.0	195	5.8	19.08
Niobium (p.p.m.)	0.0	1770	69.6	168.13
Heat input (kJ mm^{-1})	0.55	7.9	1.6	1.234
Interpass temperature (°C)	20	375	207.8	52.67
Tempering temperature (°C)	20	780	358.3	249.29
Tempering time (h)	0.0	50	6.5	6.45
Yield strength (MPa)	288	1003	533.9	113.64

Table 4.1: The input variables for yield strength model. 'p.p.m.' corresponds to parts per million by weight.

to that of the yield strength. The UTS contains an extra input variable oxygen Fig. 4.2, the effect of which at higher concentrations (above 900 p.p.m.) needs to be studied.

4.2 Yield Strength Model

Some eighty yield strength neural network models were trained on a training dataset which consisted of a random selection of half the data (1001) from the yield strength dataset. The remaining 1001 data formed the test dataset which was used to see how the model generalises on unseen data. Each model contained the 19 inputs listed in Table 1 but with different numbers of hidden units or the random seeds used to initiate the values of the weights. Fig. 4.3 shows the results. As expected, the perceived level of noise (σ_ν) in the normalised yield strength decreases as the number of hidden units increases, Fig. 4.3a. This is not the case for the test error, which goes through a minimum at three hidden units, Fig. 4.3b, and for the log predictive error which reaches a maximum at six hidden units, Fig. 4.3c.

The error bars presented throughout this work represent a combination of the perceived level of noise σ_ν in the output and the fitting uncertainty estimated from the Bayesian framework. It

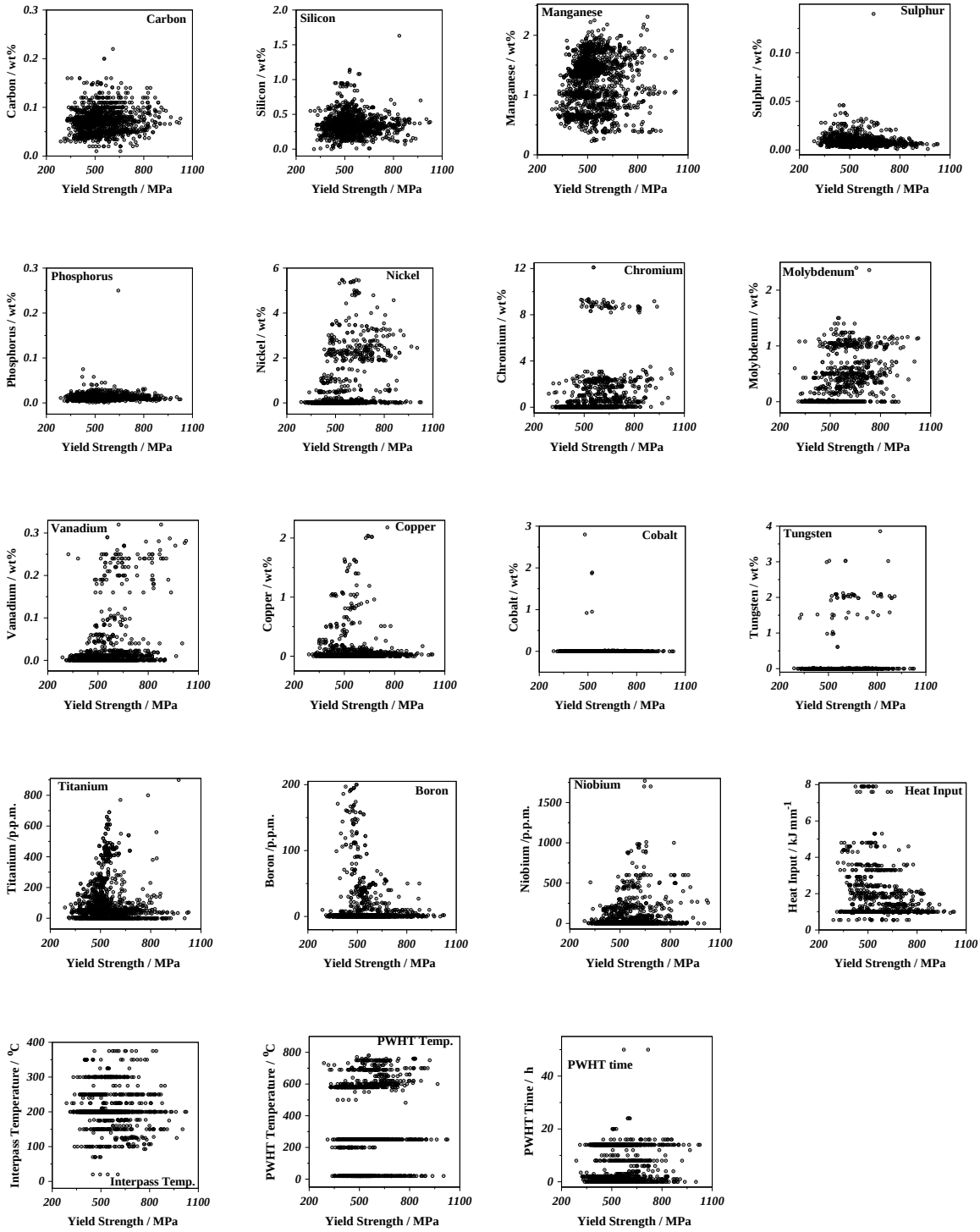

Figure 4.1: Database distribution used for yield strength model. 'p.p.m.' corresponds to parts per million by weight.

is evident that there are a few outliers in the plot of the predicted versus measured yield strength for the test dataset, Fig. 4.3f. Each of these outliers has been investigated and found to represent

Input element	Minimum	Maximum	Mean	Standard deviation
Carbon (wt%)	0.01	0.22	0.072	0.024
Silicon (wt%)	0.01	1.63	0.345	0.142
Manganese (wt%)	0.27	2.31	1.191	0.410
Sulphur (wt%)	0.001	0.14	0.009	0.006
Phosphorus (wt%)	0.001	0.25	0.012	0.009
Nickel (wt%)	0.0	4.79	0.426	0.900
Chromium (wt%)	0.0	12.1	0.748	1.810
Molybdenum (wt%)	0.0	2.4	0.219	0.370
Vanadium (wt%)	0.0	0.32	0.0252	0.060
Copper (wt%)	0.0	2.18	0.053	0.160
Cobalt (wt%)	0.0	2.8	0.008	0.110
Tungsten (wt%)	0.0	3.86	0.093	0.500
Oxygen (p.p.m.)	0.0	1650	362	200.8
Titanium (p.p.m.)	0.0	900	67	116.5
Boron (p.p.m.)	0.0	195	6	19.3
Niobium (p.p.m.)	0.0	1770	66	163.6
Heat input (kJ mm^{-1})	0.55	7.9	1.56	1.17
Interpass temperature (°C)	20	375	209	51.8
Tempering temperature (°C)	20	770	368	241.8
Tempering time (h)	0.0	50	6.9	6.5
Ultimate tensile strength (MPa)	440	1151	624	117.5

Table 4.2: The input variables for ultimate tensile strength model. 'p.p.m.' corresponds to parts per million by weight.

unique data which are not represented in the training dataset, Fig. 4.3e. For example, there is a weld with a sulphur concentration of 0.15 wt.% and another with a phosphorus concentration of 0.25 wt.%, both extremely high and unusual level of impurities in weld metals.

It is possible that a committee of models can make a more reliable prediction than an individual model (Chapter 3). The best models are ranked using the values of the log predictive errors Fig. 4.3c. Committees are then formed by combining the predictions of the best L models, where $L = 1, 2, \ldots$; the size of the committee is therefore given by the value of L. A plot of the test error of the committee versus its size gives a minimum which defines the optimum size of the committee, as shown in Fig. 4.3d.

The test error associated with the best single model is clearly greater than that of any of the committees Fig. 4.3d. The committee with twenty eight models was found to have an optimum membership with the smallest test error. The committee was therefore retrained on the entire data set without changing the complexity of any of its member models. The final comparison between the predicted and measured values of the yield strength for the committee of twenty eight is shown in Fig. 4.4.

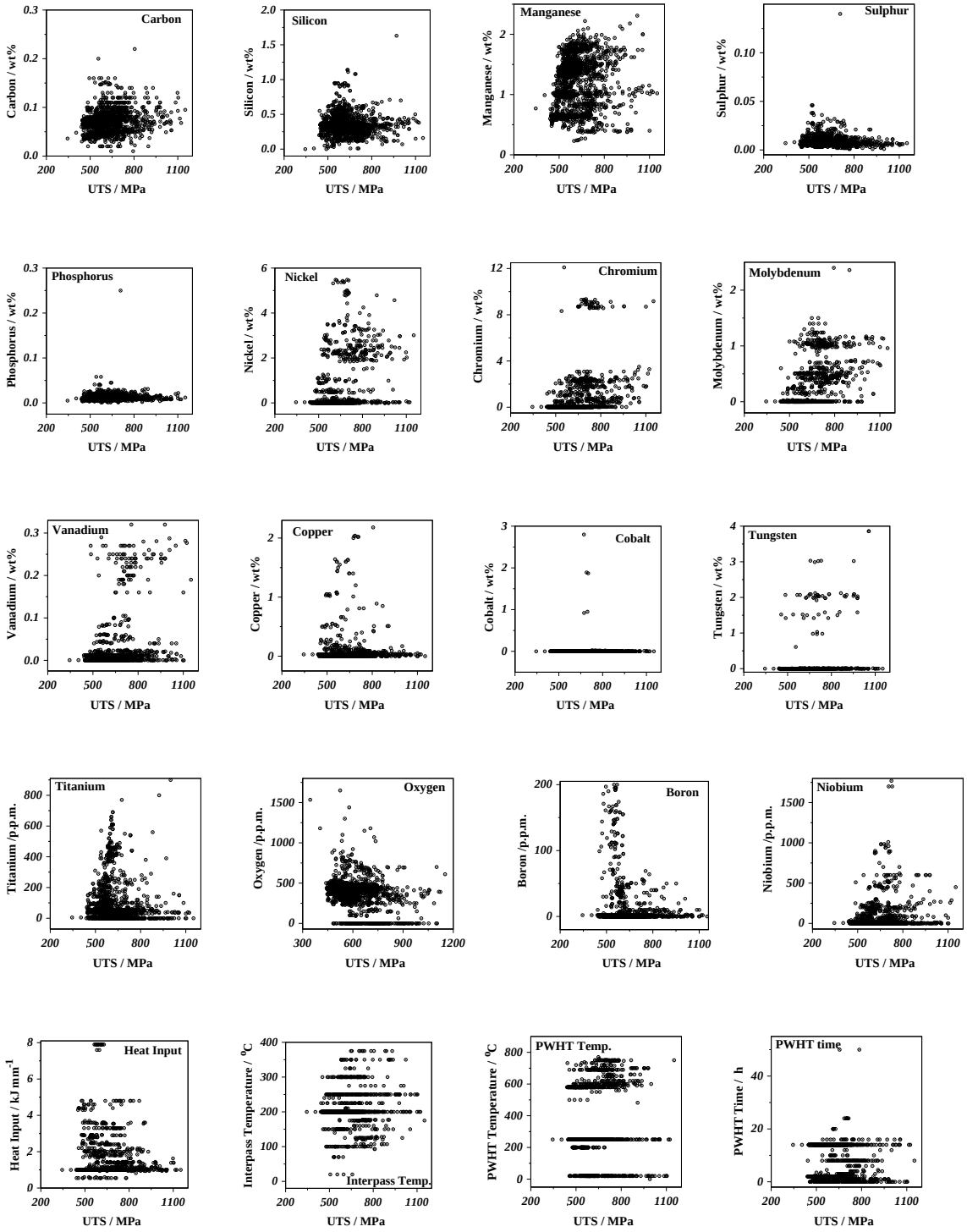

Figure 4.2: Database distribution used for ultimate tensile strength model. 'p.p.m.' corresponds to parts per million by weight.

Fig. 4.5 indicates the significance (σ_w) of each of the input variables, as perceived by first five neural network models in the committee. The σ_w value represents the extent to which a

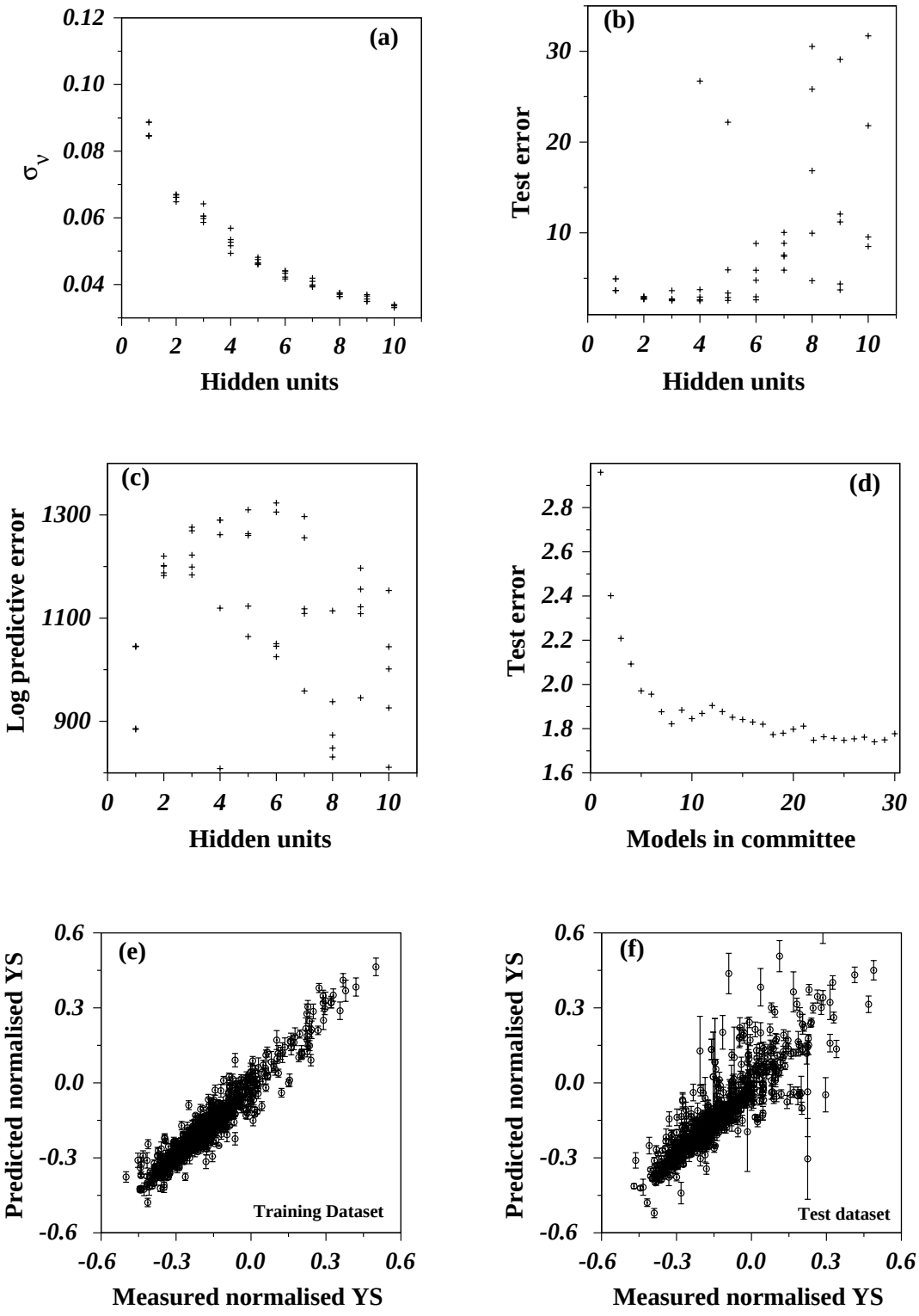

Figure 4.3: Yield strength (YS) model features.

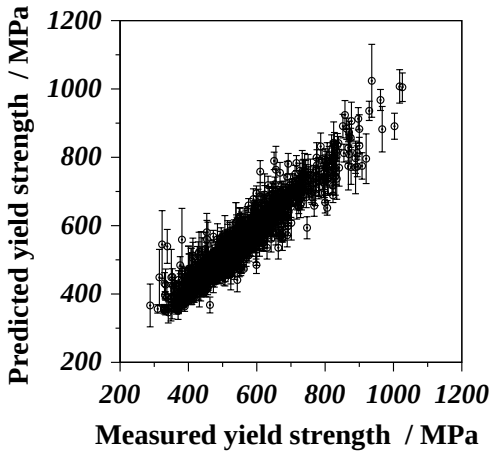

Figure 4.4: Yield strength model optimum committee model results.

particular input explains the variation in the output, rather like a partial correlation coefficient in linear regression analysis. The post-weld heat treatment temperature on the whole explains a large proportion of the variation in the yield strength Fig. 4.5. All of the variables considered are found to have a significant effect on the output indicating a good choice of inputs.

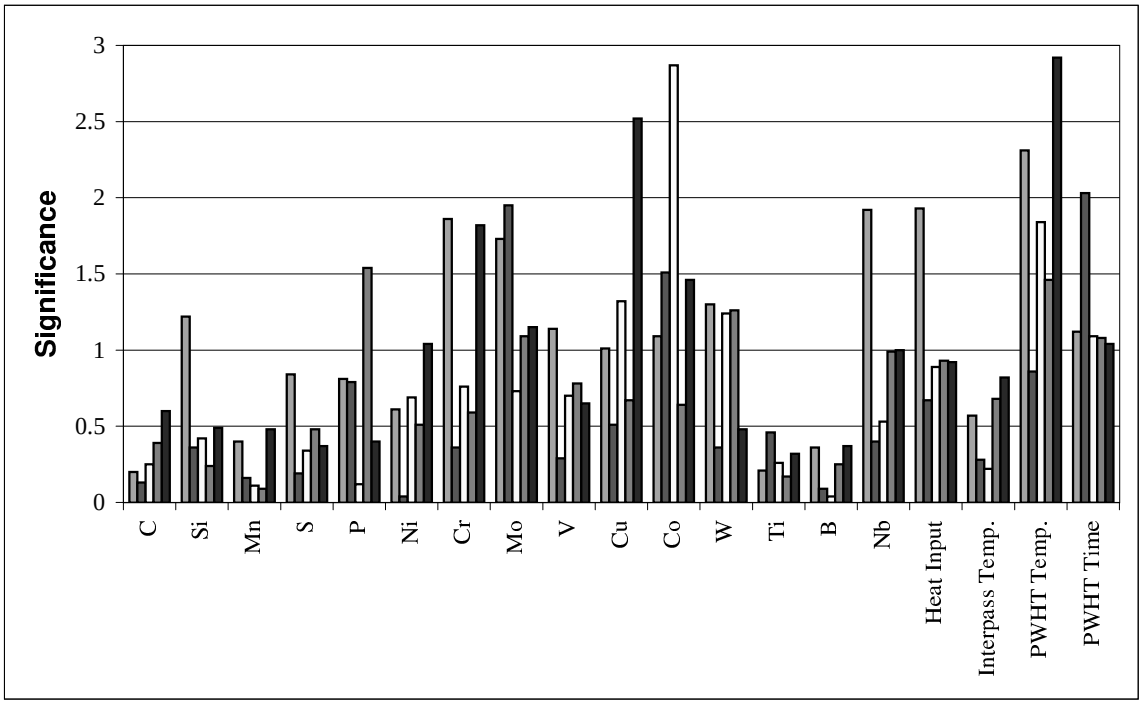

Figure 4.5: The perceived significance σ_w values of best five yield strength models for each of the inputs.

4.3 Ultimate Tensile Strength Model

The models were trained on 1972 individual experimental measurements, of which a random half of the data formed the training dataset and the other half the test dataset. The procedures are otherwise identical to those described for the yield strength model, resulting in the characteristics illustrated in Fig. 4.6 and the performance of the optimum committee of best models is illustrated in Fig. 4.7. The perceived significance values of the first five models are shown in Fig. 4.8. Here the additional input variable oxygen shows more significance along with post-weld heat treatment variables.

4.4 Application to C–Mn Weld Metals

Carbon–manganese weld metals refer to a popular class of ferritic steels in which the substitutional solutes other than silicon and manganese are generally kept to low concentration levels. They are interesting because there is a great deal already known about them, making it easy to interpret the physical significance of the neural network model. Furthermore, there exists an alternative semi–empirical model for the estimation of the yield and tensile strengths of such multirun welds [89] enabling a further comparison. The semi–empirical model is henceforth referred to as the "physical model" or PM for short. The basic values of the variables used in applying the model to carbon–manganese welds are listed in Table 4.3. The specified low–temperature heat treatment is simply a standard hydrogen removal treatment (250 °C for 14 h) applied to most welds before mechanical testing.

The results as a function of the carbon and manganese concentrations are illustrated in Fig. 4.9 for a variety of interesting cases. The calculated yield strength is in all cases found to be consistent with that expected from the physical model, although there are systematic differences at high yield strength values for all cases other than at the highest manganese concentration. However, the deviations are all within the error bounds of the neural network model for yield strength. The major discrepancies arise with the UTS especially at high UTS values. It is believed that the physical model is poorly constructed since the UTS is essentially taken arbitrarily to be linearly related to a single variable, the yield strength, Fig. 4.10 shows the comparison between the measured and strength estimation by the physical model. The physical model at higher strength values behaved very poorly; it estimated the strength higher than the measured.

An interesting feature of strengthening due to substitutional solutes is the synergistic effect with carbon. Fig. 4.11a and b shows that the dependence of the strengthening effect of molybdenum on the carbon concentration is particularly large; the effect of molybdenum in strengthening the weld is greater than that of Cr or Mn. This is consistent with published literature [90]. El-

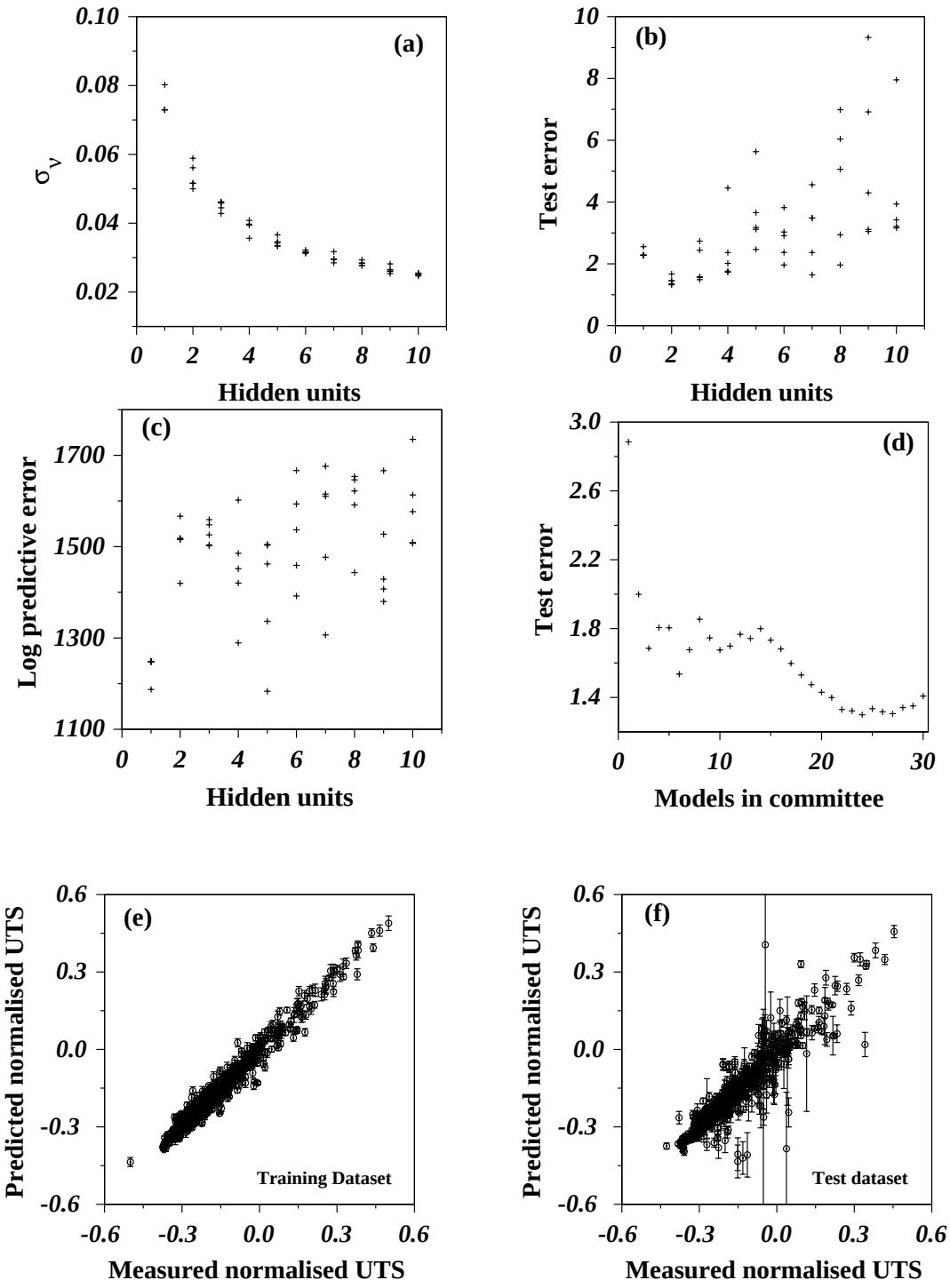

Figure 4.6: Ultimate tensile strength (UTS) model features.

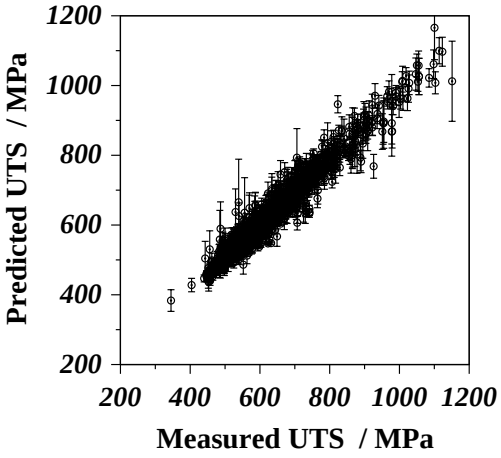

Figure 4.7: Ultimate tensile strength model optimum committee model results.

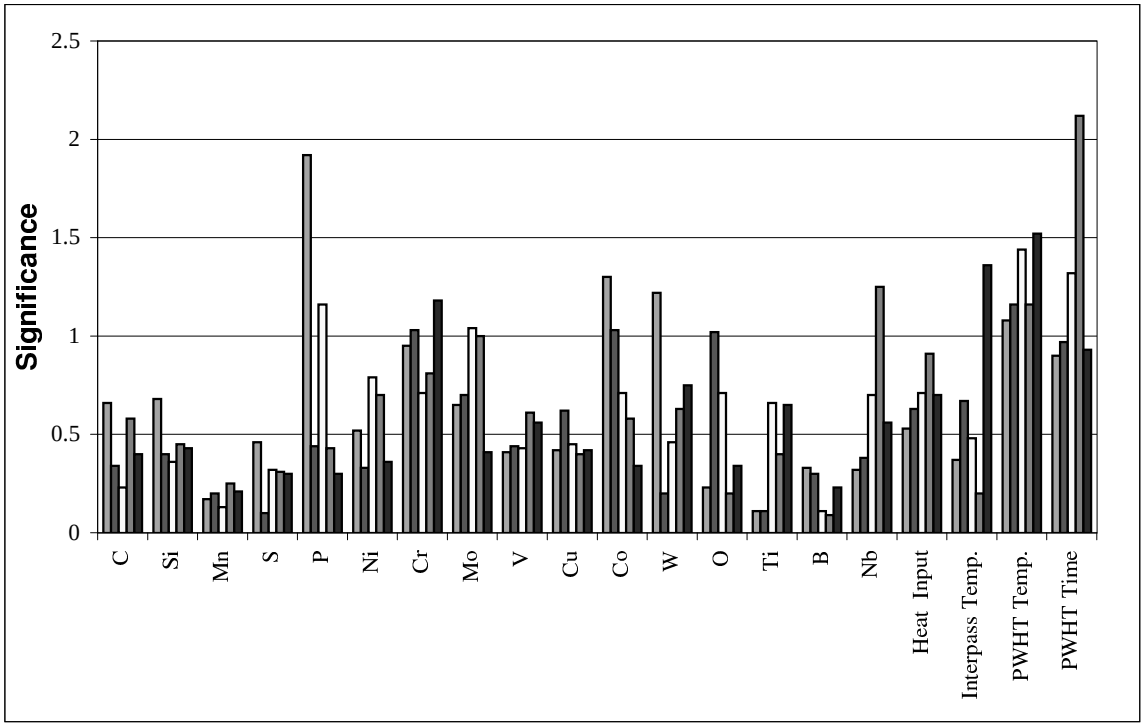

Figure 4.8: The perceived significance σ_w values of best five ultimate tensile strength models for each of the inputs.

ements such as molybdenum and vanadium are associated with strong secondary hardening effects which frequently trigger a reduction in toughness. In ordinary carbon–manganese multirun welds, the secondary microstructure, *i.e.* regions of weld metal which are tempered by subsequent weld runs, lose most of their microstructural strength. This is not necessarily the case in weld metal containing strong carbide formers. For example, it is well–established that

Input variable	
C (wt%)	0.06
Si (wt%)	0.5
Mn (wt%)	1.5
S (wt%)	0.006
P (wt%)	0.008
Ni (wt%)	0.0
Cr (wt%)	0.0
Mo (wt%)	0.0
V (wt%)	0.0
Cu (wt%)	0.0
Co (wt%)	0.0
W (wt%)	0.0
Ti (wt%)	0.0
O (p.p.m.)	300
B (p.p.m.)	0.0
Nb (p.p.m.)	0.0
Heat input (kJ mm^{-1})	1.14
Interpass temperature ($^{\circ}$C)	175
Tempering temperature ($^{\circ}$C)	250
Tempering time (h)	14

Table 4.3: The input variables of carbon–manganese steel weld metal used in the analysis.

the yield strength calculated using the Young–Bhadeshia model (Chapter 2) is always underestimated with molybdenum–containing welds, the degree of underestimation increasing with the molybdenum concentration [1]. The behaviour observed in Fig. 4.11a is not therefore surprising.

The sensitivity of strength to carbon concentration and the net magnitude of the strengthening effect decreases for the ultimate tensile strength, Fig. 4.11. This is expected since the UTS is measured at large plastic strains whereas the yield strength is much more sensitive to the initial microstructure.

The predicted dependence of the strengthening effect of niobium on the carbon concentration is shown in Fig. 4.11 . The strength increment plotted on the vertical axis is based on the average effect of niobium in the concentration range 0-1500 parts per million by weight for any given carbon concentrations. The strength increment per weight percent of niobium is obviously very large and this may be reason why niobium is generally not suggested [89].

Fig. 4.12 shows other predictions; although there are no surprises, it is worth noting the error bars. These error bars can be used to identify regions of the input space where further

experiments would be useful. For example, the prediction uncertainties associated with niobium, or with large heat inputs, are much larger than, for instance with changes in the manganese concentration. This is where future experiments could be focussed.

4.5 Application to $2\frac{1}{4}$Cr–1Mo Weld Metals

The $2\frac{1}{4}$Cr1Mo weld metal system is designed primarily for applications where the components will serve at elevated temperatures (450–565 °C) for long periods of time ($\simeq$30 years). This is in contrast to carbon–manganese weld metals which are used in structural applications such as buildings and bridges which are essentially at ambient temperature. Consequently, the post–weld heat treatment is of vital importance to $2\frac{1}{4}$Cr1Mo weld metals, not only to relieve residual stresses but also to generate a stable microstructure in which the carbides hinder creep deformation. The basic values of the variables used in applying the models to $2\frac{1}{4}$Cr1Mo welds are listed in Table 4.4. The specified high–temperature heat treatment is a typical post–weld heat treatment (PWHT).

Input variable	
C (wt%)	0.11
Si (wt%)	0.20
Mn (wt%)	0.80
S (wt%)	0.002
P (wt%)	0.005
Ni (wt%)	0.20
Cr (wt%)	2.25
Mo (wt%)	1.0
V (wt%)	0.0
Cu (wt%)	0.0
Co (wt%)	0.0
W (wt%)	0.0
Ti (wt%)	0.0
O (p.p.m.)	300
B (p.p.m.)	0.0
Nb (p.p.m.)	0.0
Heat input (kJ mm^{-1})	1.5
Interpass temperature (°C)	200
Tempering temperature (°C)	690
Tempering time (h)	8

Table 4.4: The input variables of 2.25Cr–1Mo wt% steel weld metal used in the analysis.

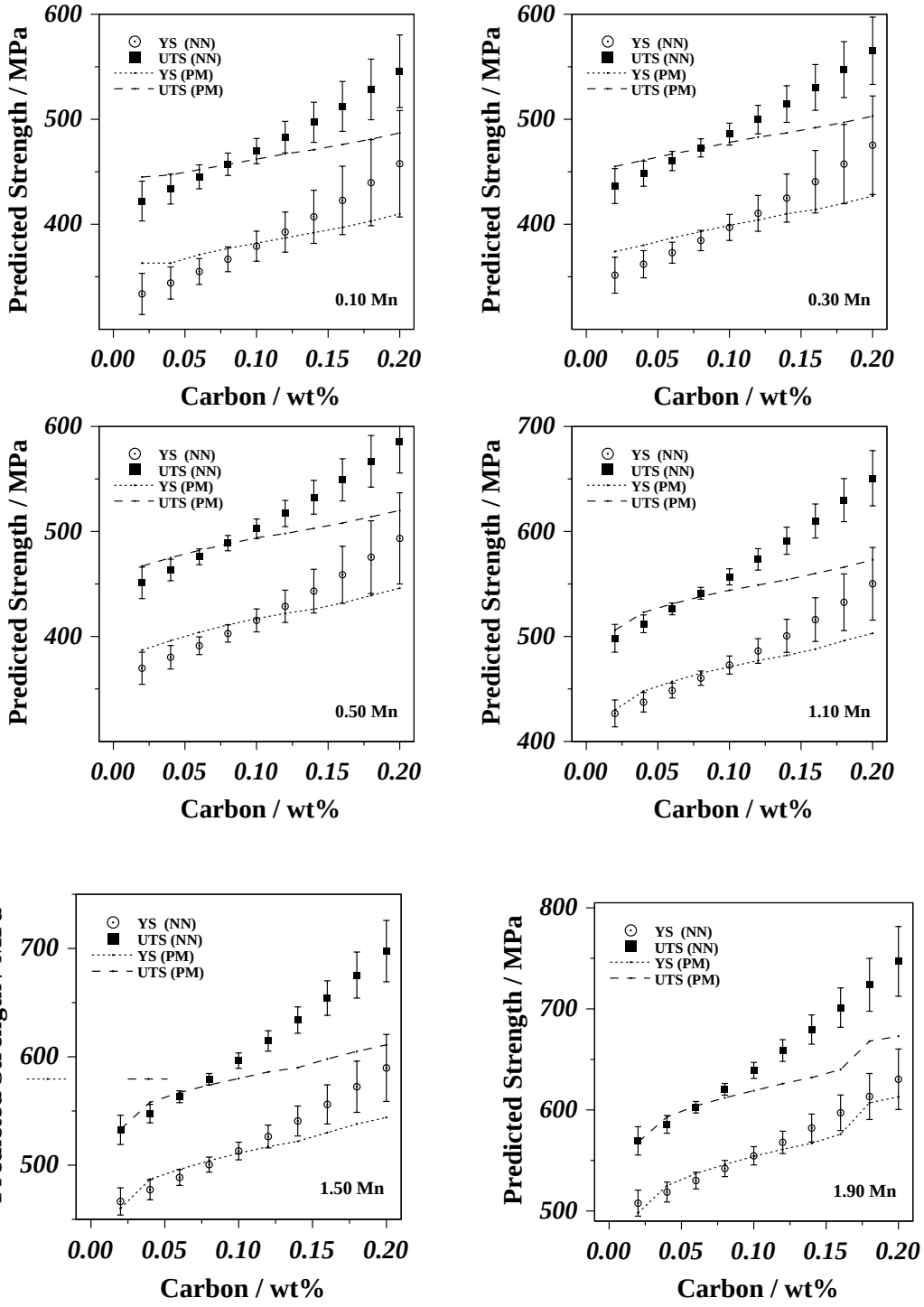

Figure 4.9: A series of calculations for carbon–manganese welds, using both the neural network committee models and an alternative published model [90]

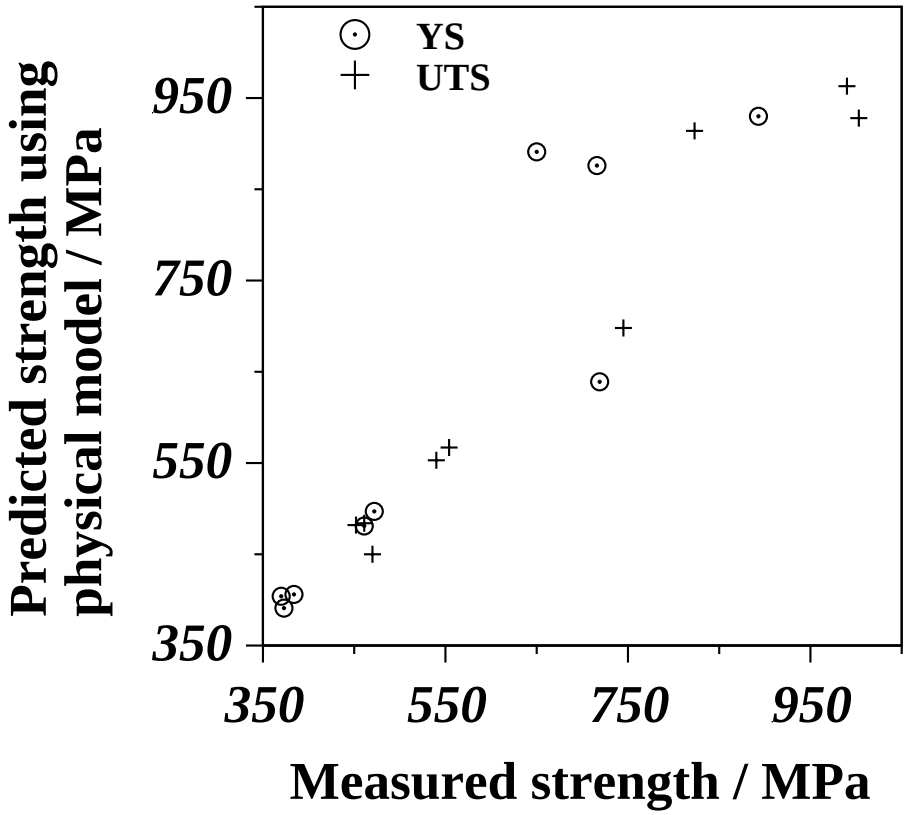

Figure 4.10: Comparison between measured and published physical model calculations [90].

It is notable from the predictions illustrated in Fig. 4.13 that there are greater uncertainties (larger error bars) associated with the estimation of mechanical properties for the $2\frac{1}{4}$Cr1Mo system when compared with the carbon–manganese welds. This is largely because there are fewer data available for $2\frac{1}{4}$Cr1Mo welds.

Another striking feature is that the sensitivity of the strength to alloying elements, in the PWHT condition, is far smaller than in the as–welded condition. This is not surprising given the severe nature of the post–weld heat treatment at 690 °C for 8 hours. It is emphasised that although the yield and tensile strengths are not particularly sensitive to composition in the PWHT condition, this will not be the case for creep properties where the tempering heat treatment is essential for the generation of alloy carbides and to provide a microstructure which has long term stability.

4.6 Conclusions

The yield strength and ultimate tensile strength of ferritic steel weld metal have been analysed using a neural network method within a Bayesian framework. The data used were mostly

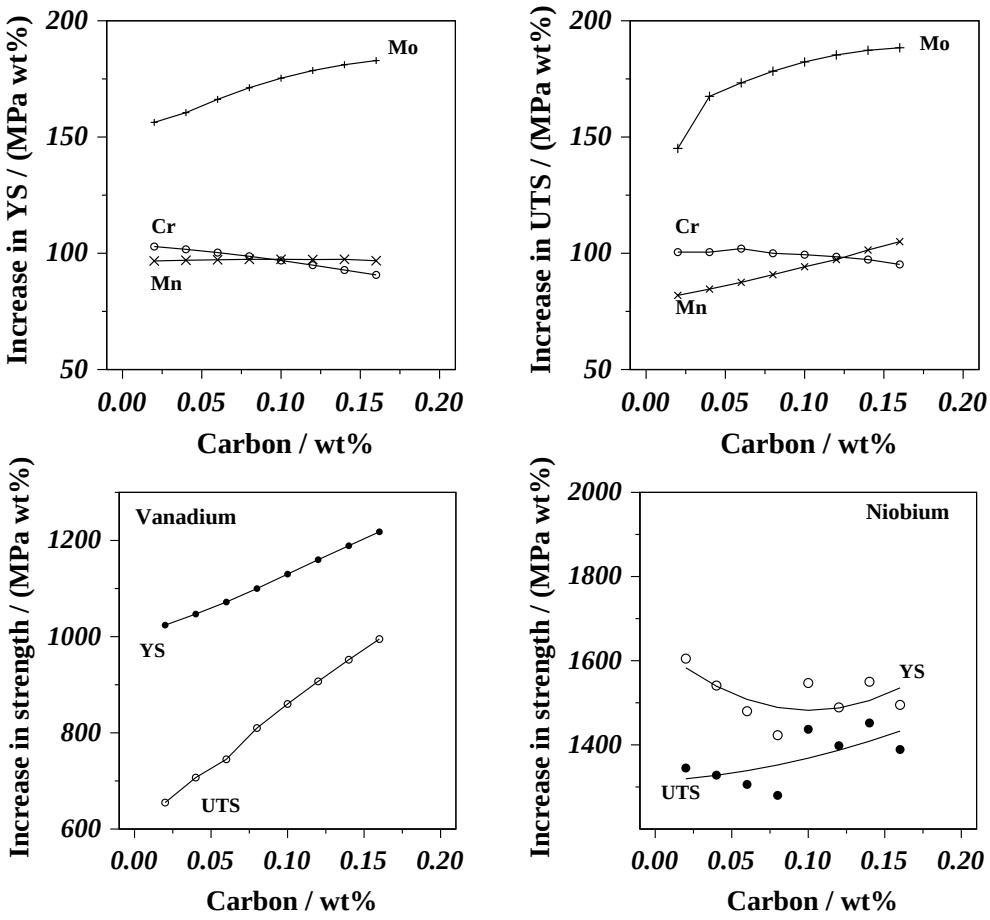

Figure 4.11: Change in strength and the YS/UTS ratio as a function of a wt% of substitutional solute content in carbon–manganese steel welds. The error bars are not included for clarity, but the maximum values are 60.

obtained from the published literature and represent a wide cross–section of alloy compositions and arc–welding processes.

Trends predicted by the models appear to be consistent with those expected metallurgically, although it must be emphasised that only the simplest of trends have been examined since the number of variables involved is very large. The models can be applied widely because the calculation of error bars whose magnitude depends on the local position in the input space is an inherent feature of the neural network used. The error bar is not simply an estimate of the perceived level of noise in the output but also includes an uncertainty associated with fitting the function in the local region of input space. This means that the method is less dangerous in extrapolation or interpolation since it effectively warns when experimental data are lacking or are exceptionally noisy. The work has clearly identified regions of the input space where

further experiments should be encouraged. These models are applied to design new structural, heat resistant and high strength steel welds without any experimental trials are discussed in Chapter 6.

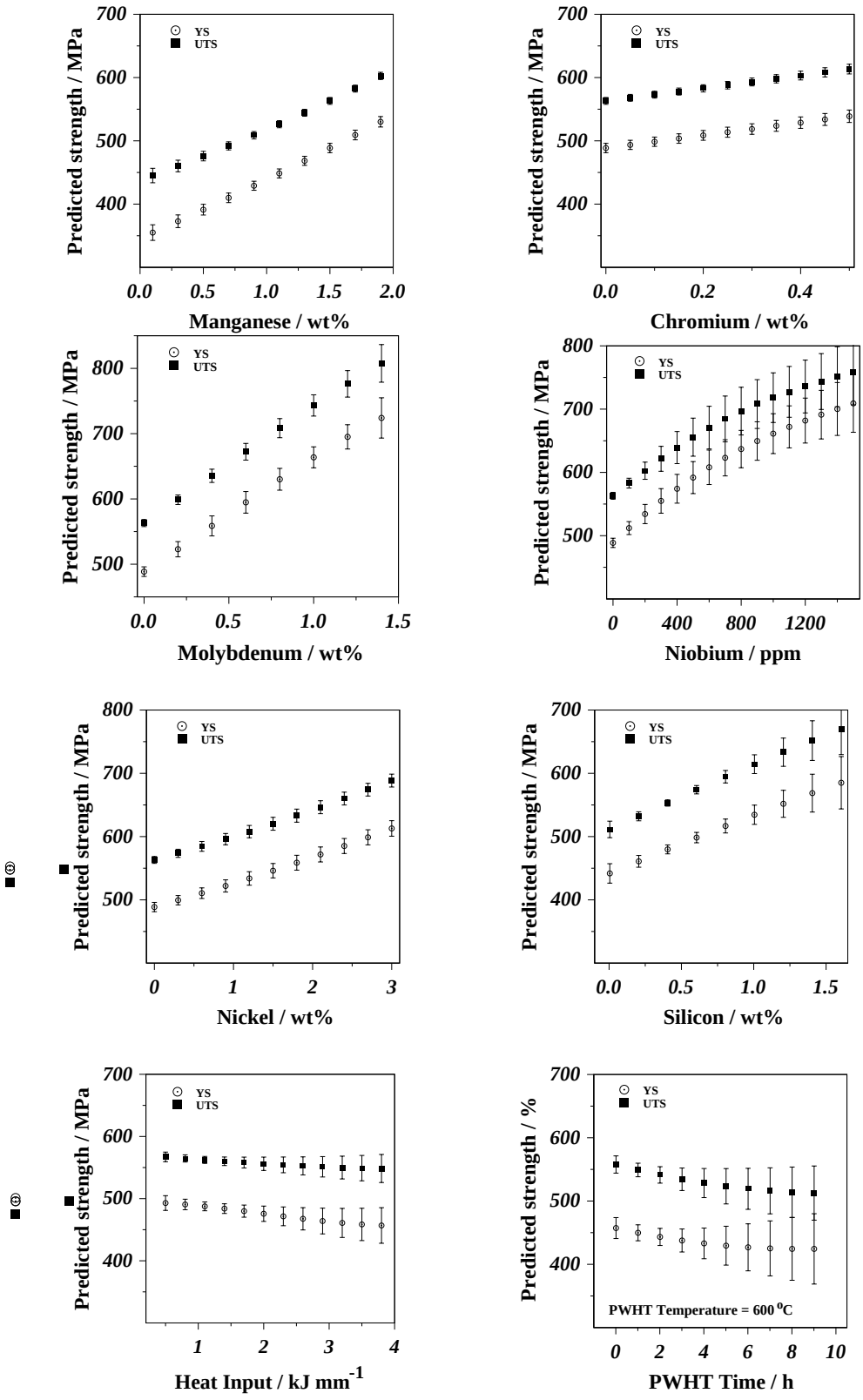

Figure 4.12: Variations in the yield and ultimate tensile strengths of carbon–manganese weld metal as a function of alloying elements and heat treatment.

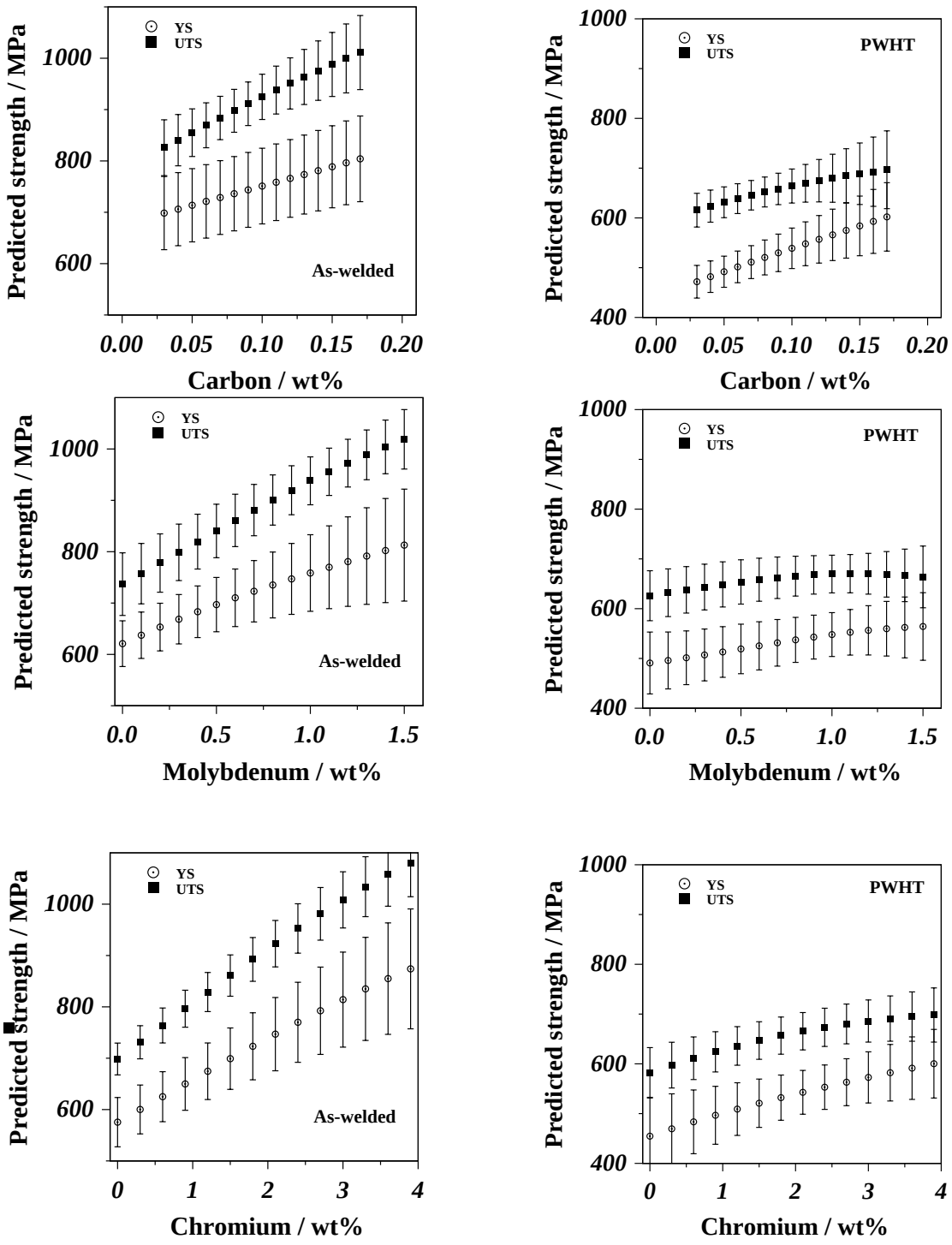

Figure 4.13: The effect of carbon, molybdenum and chromium concentrations on the strength of $2\frac{1}{4}$Cr–1Mo wt% welds in the as–welded and PWHT (690 °C, 8 h) conditions.

Chapter 5

Elongation and Toughness Models

The most common experiments done on weld metals include the testing of a sample in tension to measure the strength and ductility, and the measurement of the Charpy impact toughness. Although these tests are quite simple to conduct, the principles governing the properties that are measured are understood only on a qualitative basis. In the previous chapter, neural network models which allow the estimation of the yield and ultimate tensile strengths of ferritic steel weld metals using a vast quantity of data collected from the published literature and from commercial sources were developed. The predictions that can be made using these models are associated with error bars which consist of the perceived level of noise in the output and a component representing the uncertainty of fitting. The predictions are reliable when the error bars are small, but have to be used with caution when they are not; large error bars can indicate a need for further experiments to fill gaps in knowledge. In this sense, all predictions are useful irrespective of the magnitudes of the error bars.

The purpose of the work presented here was to develop similar models for the elongation and Charpy properties. There has been little practical progress in modelling the tensile ductility of weld metals [91]. The ductility can to a good approximation be divided into two components whose magnitudes are assumed to be controlled by different physical processes. These components are the uniform plastic strain, as recorded prior to the onset of necking in the tensile specimen, and the non–uniform component which is the remainder of the plastic strain.

By factorising the ductility in this way, it is possible to express the nonuniform component in terms of the inclusion content of the weld deposit, after taking into account variations in specimen cross–sectional area A_O and gauge length L_O [92]:

$$\text{nonuniform elongation}, \% = 100 \times \beta \frac{A_0^{0.5}}{L_0} \tag{5.1}$$

where β is Barba's constant, but now expressed as a function of the inclusion content [93]:

$$\beta \simeq 1.239 - 9.372 \times (\text{wt.\%O}) + (\text{wt.\%S}) \tag{5.2}$$

There is as yet no reliable model for estimating the uniform component of strain, but such a model would require a detailed knowledge of the strain hardening behaviour of the individual phases of the microstructure, together with some theory for multiphase deformation. As far as the nonuniform component is concerned, equation 5.1 emphasises the role of particles in reducing ductility. There are only two inputs to equation 5.2, whereas a vast number of other variables are known to influence the elongation that is measured in a tensile test. Hence the need for a different approach which encompasses a wider set of variables.

The concept of toughness as a measure of the energy absorbed during fracture is well–developed [18, 94]. It is often measured using notched–bar impact tests of which the most common is the Charpy test. A square section notched bar is fractured under specified conditions and the energy absorbed during fracture is taken as a measure of toughness. The Charpy test is empirical in that the data cannot be used directly in engineering design. It does not provide the most searching mechanical conditions. The sample has a notch, but this is less sharp than an atomically sharp brittle crack. Although the test involves impact loading, there is a requirement to start a brittle crack from rest at the tip of the notch, suggesting that the test is optimistic in its comparison against a propagating brittle crack [94]. Most materials can be assumed to contain sub–critical defects so that the initiation of a crack seems seldom to be an issue.

The Charpy test is nevertheless a vital quality control measure which is specified widely in international standards, and in the ranking of samples in research and development exercises. It is the most common first assessment of toughness and in this sense has a proven record of reliability. The test is usually carried out at a variety of temperatures in order to characterise the ductile–brittle transition intrinsic to body–centered cubic metals with their large Peierls barriers to dislocation motion.

It would therefore be useful to be able to quantitatively model the Charpy toughness as a function of metallurgical variables that are believed to influence the cleavage and ductile fracture modes of commercial steels. Some of these variables have in the past been studied quantitatively (for example, the flow stress as a function of temperature [25]) whereas others (such as the degree of organization in the microstructure [5]) have been expressed using language alone.

Complex problems such as those described above, can usefully be modelled empirically using an artificial neural network. The method has been discussed thoroughly in Chapter 3.

5.1 Elongation Model

This model consists of the 20 input variables listed in Table 5.1, which are considered to influence ductility. The detailed chemical composition, the heat treatment and the welding heat input and interpass temperature essentially determine the microstructure and properties. It is easy to imagine other variables which might be important, such as the size distribution of

oxide particles. However, the compilation of a dataset for neural network analysis is always a compromise between two factors. Firstly, a larger dataset is of value in creating a model based on a greater span of knowledge. However, the probability of finding appropriate data diminishes as the number of variables is increased, because incomplete sets of inputs can not be used in the analysis. The database reflects multipass welds made using the submerged arc, gas tungsten arc and manual metal arc welding processes. The welding parameters are represented by the heat input and the interpass temperature; the post–weld heat treatment conditions are represented by temperature and time. The sources of the data are listed in references [29] to [105]. The elongation values are those measured on standard, cylindrical tensile test specimens, where the gauge length is generally specified to be $5.65\times\sqrt{A}$, where A is the cross–sectional area.

Input element	**Minimum**	**Maximum**	**Mean**	**Standard deviation**
Carbon (wt%)	0.01	0.16	0.07	0.0184
Silicon (wt%)	0.01	1.14	0.35	0.124
Manganese (wt%)	0.24	2.31	1.23	0.386
Sulphur (wt%)	0.002	0.14	0.008	0.005
Phosphorus (wt%)	0.001	0.25	0.01	0.007
Nickel (wt%)	0.0	5.48	0.322	0.88
Chromium (wt%)	0.0	9.4	0.45	1.19
Molybdenum (wt%)	0.0	2.4	0.17	0.358
Vanadium (wt%)	0.0	0.32	0.015	0.044
Copper (wt%)	0.0	2.04	0.063	0.204
Cobalt (wt%)	0.0	2.8	0.005	0.097
Tungsten (wt%)	0.0	3.86	0.024	0.207
Oxygen (p.p.m.)	63.0	1650	414	118
Titanium (p.p.m.)	0.0	1000	86	127
Boron (p.p.m.)	0.0	200	11	30
Niobium (p.p.m.)	0.0	1770	48	141
Heat input (kJ mm^{-1})	0.55	4.8	1.23	0.71
Interpass temperature (°C)	20	350	204	35
Tempering temperature (°C)	20	750	321	191
Tempering time (h)	0.0	32	10	6.2
Elongation (%)	7.4	41.1	26	5

Table 5.1: The variables used in developing the elongation model. 'p.p.m.' corresponds to parts per million by weight.

A total of 1972 individual experimental data were gathered. In 19 cases, the sulphur and phosphorus concentrations were not reported, in which case they were set to the average values of the other data in the database. This is a better procedure than setting the concentrations to zero because all welds inevitably contain impurities. On the other hand, alloying additions such as molybdenum can be set to zero when they are not added deliberately, without affecting

the overall microstructure or mechanical property outcomes. A visual impression of the whole elongation database is shown in Fig. 5.1. The mean and standard deviation of the percentage elongation are 26 and 5 respectively, showing that most of the data lie in the range 21-31%, Fig. 5.2.

The training, test and log predictive errors [6] associated with each of the eighty models created are shown in Fig. 5.3. The behaviour of the single best model is illustrated in Fig. 5.3d,e. From the set of 80 models, a committee of 58 of the best models was found to give the lowest test error, Fig. 5.3c; each member of the committee was then retrained on the entire dataset to create the final committee model Fig. 5.3f). The details of all these procedures are described in Chapter 3. Fig. 5.4 shows the significance σ_w of each of the input variables. The behaviour of the committee model in making predictions for specific cases is now illustrated for C–Mn weld metals.

5.1.1 Application to C–Mn Weld Metals

The set of variables used for analysis is listed in Table 5.2; any variations illustrated in subsequent diagrams are about these values. An increase in the strength is expected to lead to a decrease in elongation [106]. It is not surprising, therefore, that the elongation decreases when the manganese and carbon concentrations are increased, Fig. 5.5. Notice also that the effect is more pronounced at higher manganese concentrations, consistent with the corresponding effect on strength (Chapter 4).

Ductile fracture can be described in terms of the nucleation, growth and coalescence of voids. Macroscopic fracture occurs when the voids link on a large enough scale. If the number density of voids is large, then their mean separation is reduced and coalescence occurs rapidly, giving a minimal amount of plastic deformation before fracture, and reducing the overall ductility (Fig. 5.6).

It has generally been assumed that in weld metals both sulphur and oxygen contribute to the inclusion content and hence must be detrimental to the toughness. Whereas it is found that an increase in the oxygen concentration definitely reduces the elongation (Fig. 5.7a), the picture for sulphur is not clear. The data in fact show a slight increase in elongation with the sulphur concentration but the trend is not meaningful when the error bars are taken into account (Fig. 5.7b). Oxides are the main inclusions in weld metals [90] whereas sulphur tends to be deposited in the form of very thin layers on top of the oxide particles [107]. The observed trends may not therefore be unreasonable in weld metals as opposed to wrought steels which tend to have a very low oxygen concentration with a predominance of sulphide inclusions.

Another interesting feature of the difference between weld metals and C–Mn type hot–rolled steels is revealed by comparing the dataset used in a previous analysis for wrought alloys [108]

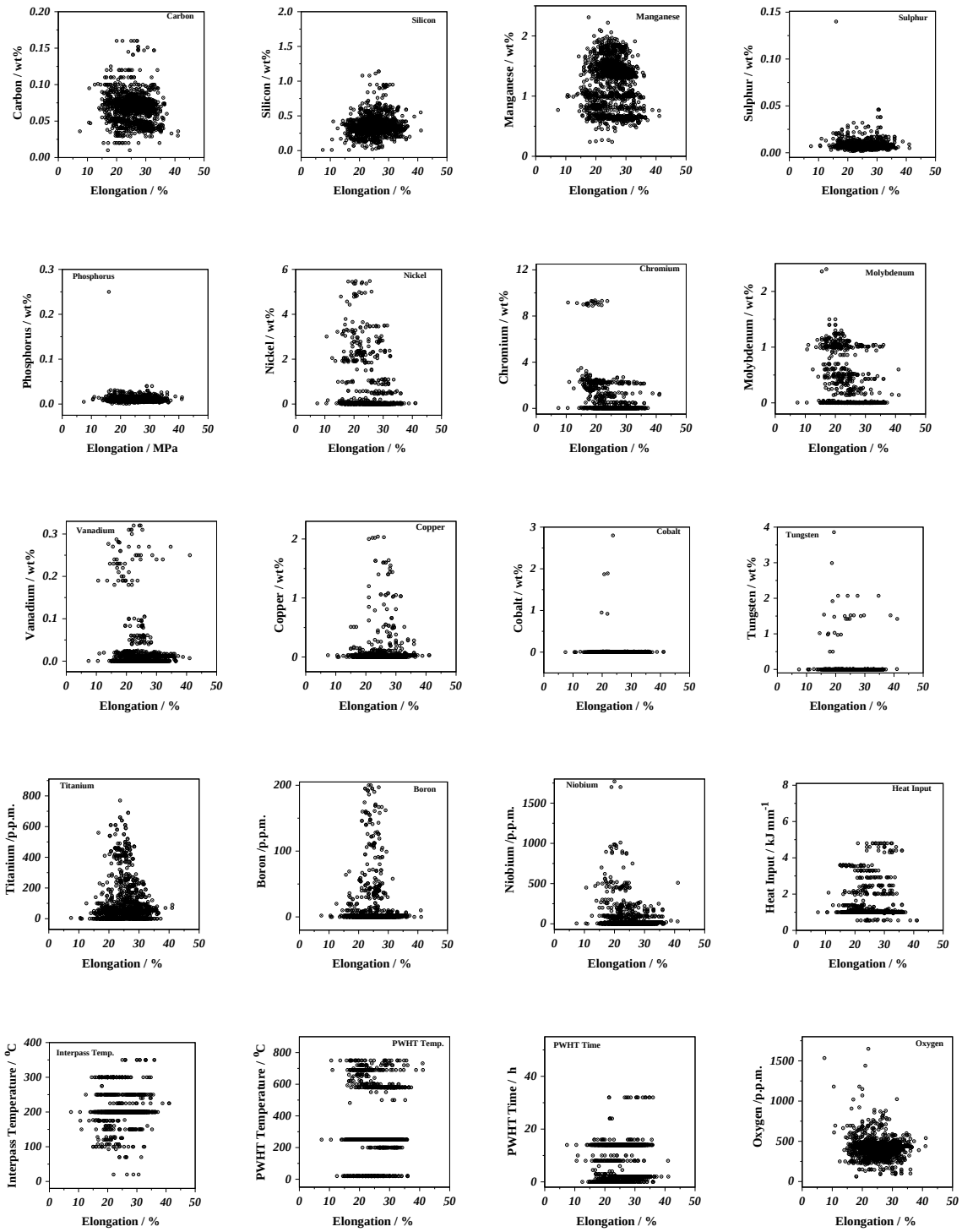

Figure 5.1: The database values of each variable versus the elongation. 'p.p.m.' refers to parts per million by weight.

with the present work which is on weld metals (Fig. 5.8). The difference between the yield strength (σ_{YS}) and ultimate tensile strength (σ_{UTS}) for welds is approximately constant at

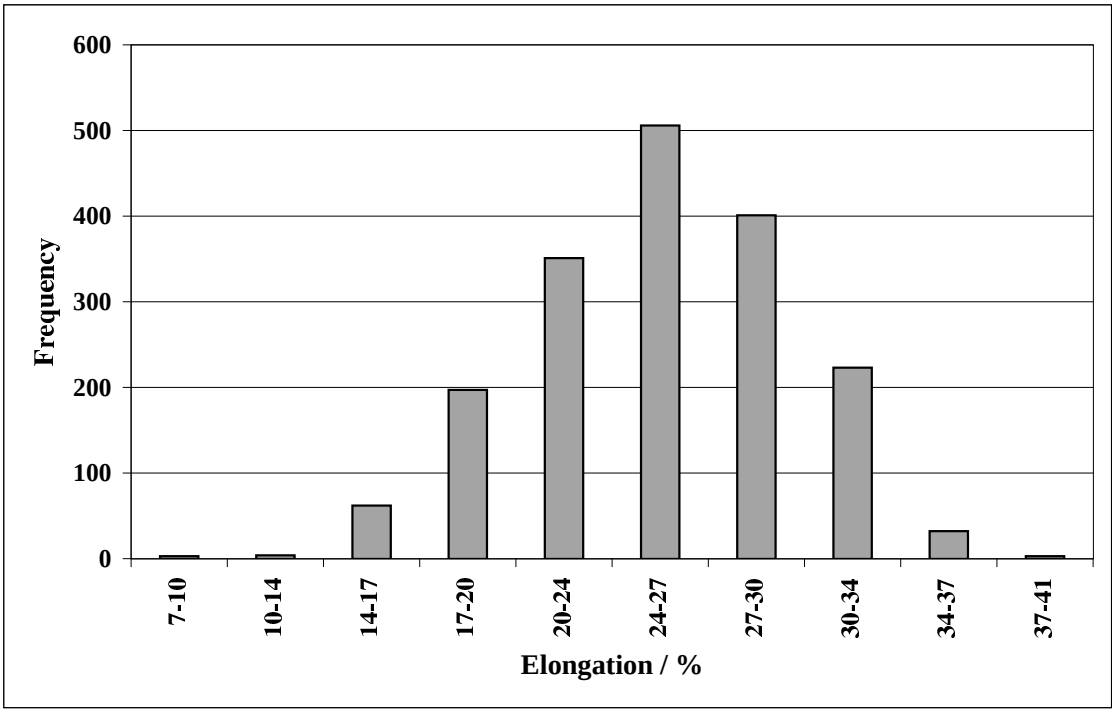

Figure 5.2: The elongation data frequency distribution.

100 MPa whereas for plates, the difference becomes smaller as the strength increases. The stress can be described as a function of plastic strain ε using a power law of the form

$$\sigma = K\varepsilon^n \tag{5.3}$$

where K and n are constants, the latter being the strain hardening coefficient. Since the yield strength is measured at a plastic strain of 0.02, and the UTS is given by Kn^n, it follows that

$$\sigma_{UTS} - \sigma_{YS} = K[n^n - 0.02^n] \tag{5.4}$$

Since for the welds, $\sigma_{UTS} - \sigma_{YS} \simeq 100\,\text{MPa}$, it follows that the strain hardening coefficient must be approximately constant for all the welds considered. This in turn means that the uniform strain component of the measured elongation of most ferritic steel welds must be about constant, the total elongation being a function mostly of the non–uniform component which occurs beyond necking during a tension test. Of course, the non–uniform component of the elongation depends largely on void nucleation, growth and coalescence so it is not surprising that the total elongation depends strongly on inclusions.

We note that this interpretation does not explain why the strain hardening coefficient for

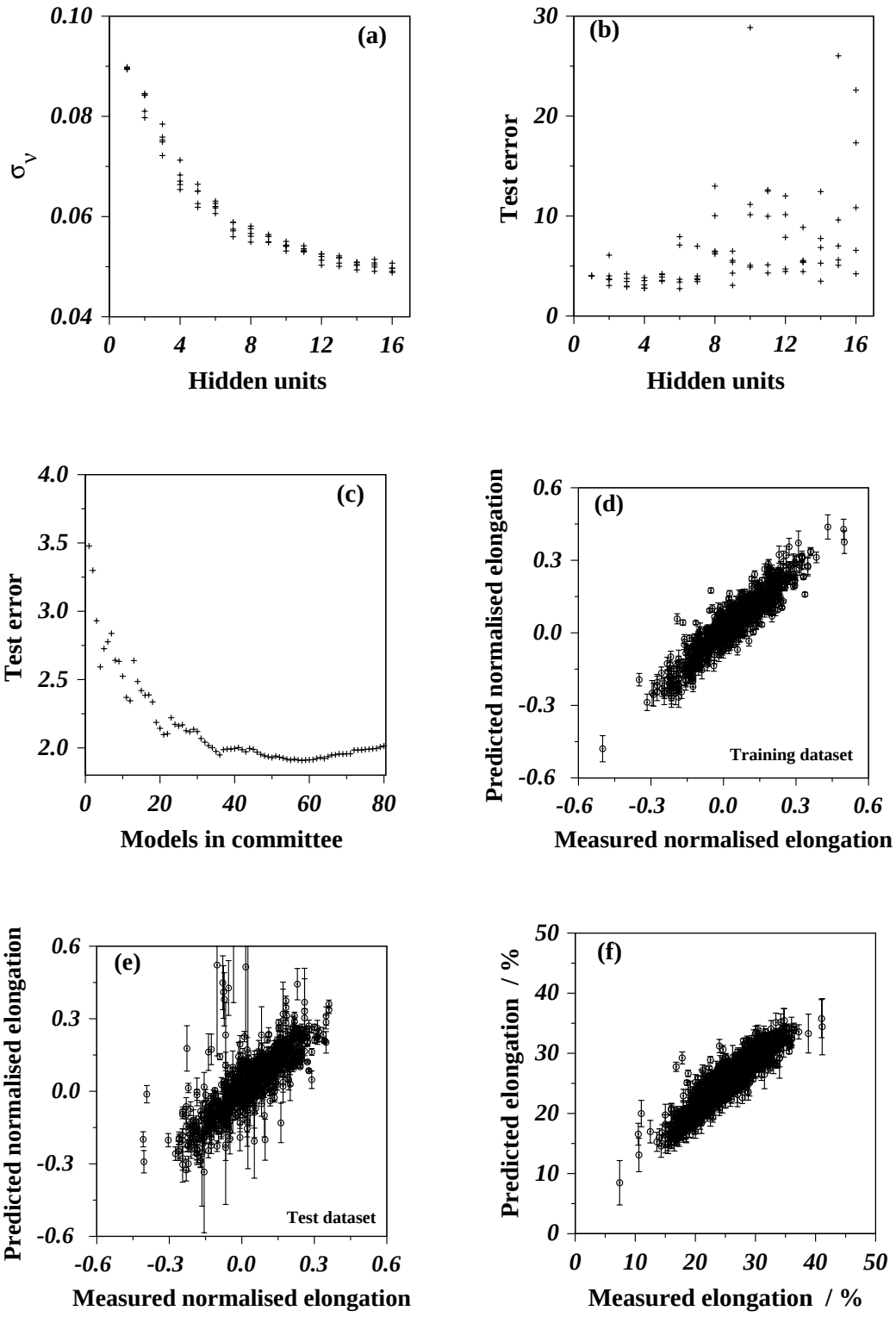

Figure 5.3: Characteristics of the elongation model. σ_ν is the model perceived level of noise in the elongation. (d) and (e) represent the behaviour of the best single model, whereas (f) shows the performance of the optimum committee model on the entire dataset.

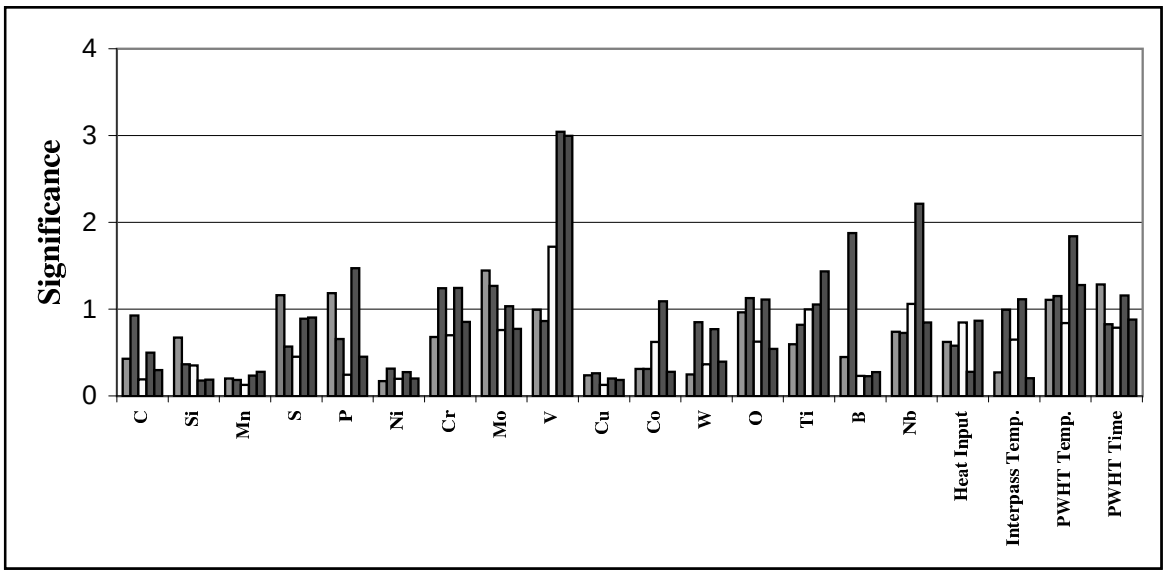

Figure 5.4: The perceived significance σ_w of each of the input variables, as perceived by first best five neural network models in committee, in influencing the elongation.

welds is approximately constant whereas that of plates is not. This remains an issue for further work.

A further consequence of these observations is that the ratio of the yield to ultimate tensile strength will increase more rapidly for welds than for plates, which may in turn have consequences on the fatigue properties. The fatigue resistance is generally higher for materials where there is a large difference between the yield and ultimate tensile strength. Indeed, Fig. 5.9 shows that unlike plate steels, there is not much that can be done to control the ratio σ_{YS}/σ_{UTS} by alloying.

5.2 Charpy Toughness Model

This model was developed with 22 input variables, Table 5.3, the nitrogen concentration and the test temperature being the additional variables when compared with the elongation model (Fig. 5.10). The test temperature is expected to be an important variable because of the ductile–brittle transition in ferritic iron, and the nitrogen concentration is known to have an influence via strain hardening effects. Unfortunately, the Charpy data that are available are not uniformly distributed (Fig. 5.11) because the tests are frequently reported in literature at specified Charpy toughness values.

Input variable	
Carbon (wt%)	0.06
Silicon (wt%)	0.50
Manganese (wt%)	1.50
Sulphur (wt%)	0.006
Phosphorus (wt%)	0.008
Nickel (wt%)	0.0
Chromium (wt%)	0.0
Molybdenum (wt%)	0.0
Vanadium (wt%)	0.0
Copper (wt%)	0.0
Cobalt (wt%)	0.0
Tungsten (wt%)	0.0
Oxygen (p.p.m.)	300
Titanium (p.p.m.)	0.0
Boron (p.p.m.)	0.0
Niobium (p.p.m.)	0.0
Heat input (kJ mm^{-1})	1.00
Interpass temperature (°C)	175
Tempering temperature (°C)	250
Tempering time (h)	14.0

Table 5.2: The input variables of carbon–manganese steel weld metal used in the analysis.

The models were created from a dataset containing 3142 individual experiments and the results are shown in Fig. 5.12. An optimum committee consisting of around 62 of the best models was used in all subsequent analyses.

5.2.1 Application to C–Mn Welds

The reference values of the variables used in making predictions are listed in Table 5.4. Fig. 5.13 shows the calculated variation in Charpy values for 0 °C as a function of the manganese and carbon concentrations. There are two competing effects:

(i) At first an increase in hardenability leads to a replacement of deleterious phases such as allotriomorphic and Widmanstätten ferrite with the desirable acicular ferrite [90], leading to an increase in toughness. It is for this reason that the peak in toughness occurs at a higher carbon concentration when the manganese concentration is low. For equivalent hardenability, the carbon concentration must be larger when that of manganese is small.

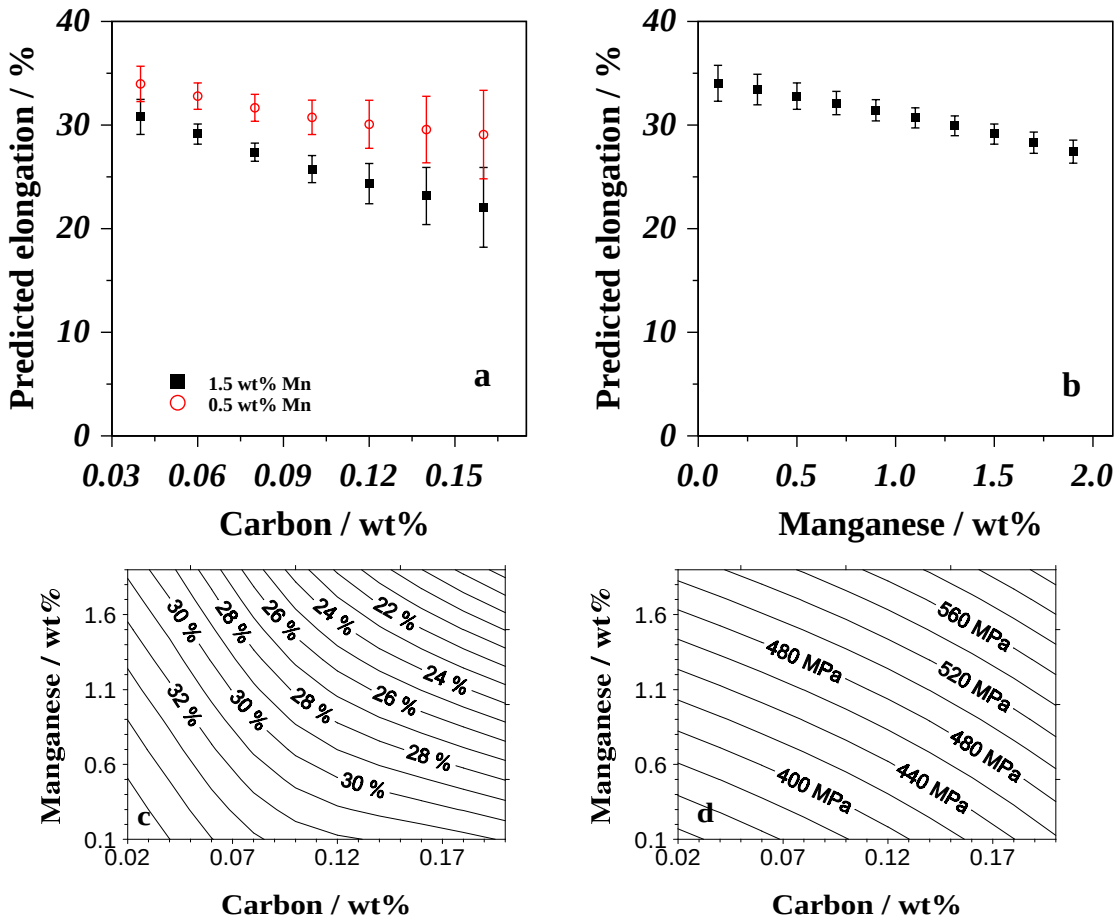

Figure 5.5: (a, b) Predicted elongation as a function of carbon and manganese in carbon–manganese weld metal. (c, d) Contour plots showing the variation in elongation and yield strength as a function of the carbon and manganese concentrations. The error bars have been omitted for clarity but range from ±2–6% in elongation and ±10–30 MPa in the strength plots.

(ii) The strength increases with the Mn and C concentration. In general, an increase in strength leads to a deterioration in toughness because plastic flow becomes more difficult, making cleavage cracking more probable. This increase in strength may also be accompanied by the formation of undesirable phases such as martensite. It follows that the toughness should eventually begin to decrease as the carbon or manganese concentrations are increased.

Both of these effects are well illustrated by the computed data shown in Fig. 5.13. The microstructures for the welds described in Fig. 5.13 were calculated using a published physical model [90]. Fig. 5.14 shows that the above interpretations are correct in that the initial increase in toughness corresponds to an improvement in the microstructure, with the subsequent

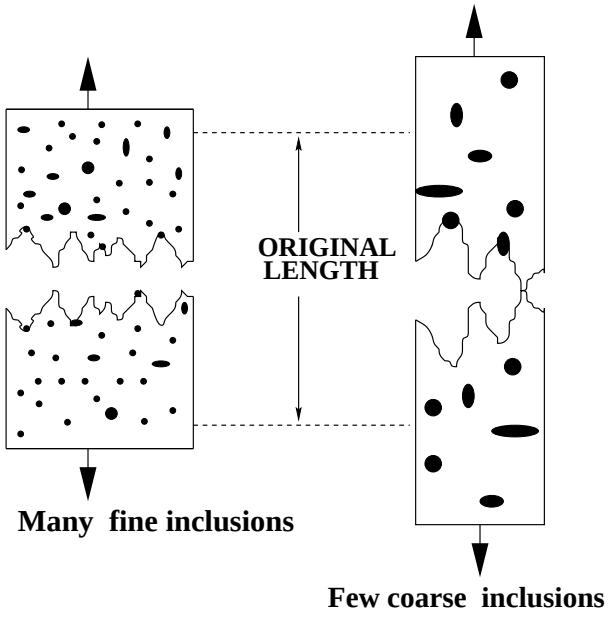

Figure 5.6: An illustration of how a large density of void nucleating particles can result in fracture with a low overall ductility, even though the material fails by gross plastic deformation on a microscopic scale.

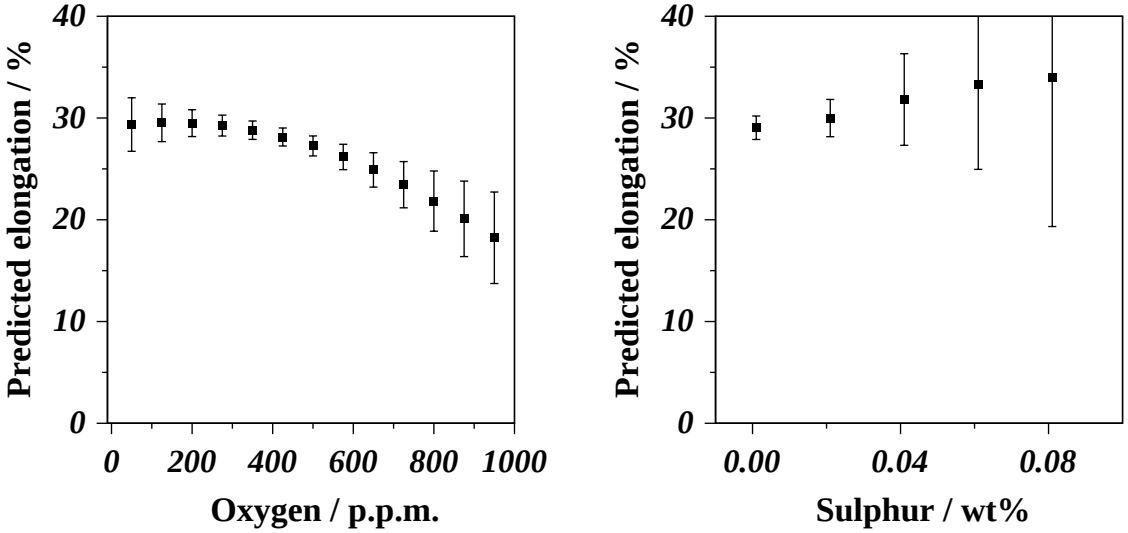

Figure 5.7: Change in elongation in carbon–manganese weld metal as a function of (a) the oxygen concentration and (b) the sulphur concentration. It is evident that sulphur does not have a significant effect on the ductility of welds of the type considered in the present work.

decrease in toughness explained by the increase in strength. The Fig. 5.15 shows clearly that in the context of Charpy impact toughness tests, there is always an optimum combination of manganese and carbon.

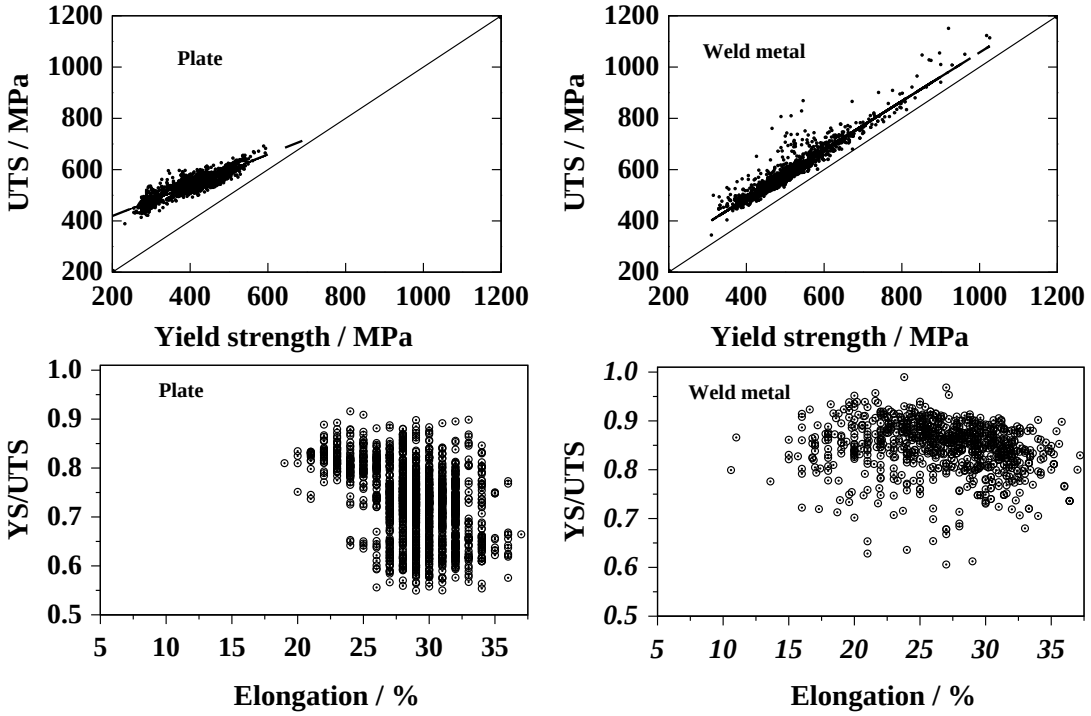

Figure 5.8: Plots of the ultimate tensile strength versus yield strength for (a) hot–rolled C–Mn steel plates; (b) weld metals. Plots of the elongation versus yield strength for (c) hot–rolled C–Mn steel plates; (d) weld metals. All of the data plotted are experiments, those for plates coming from previous work [108], those for the weld deposits from the present analysis.

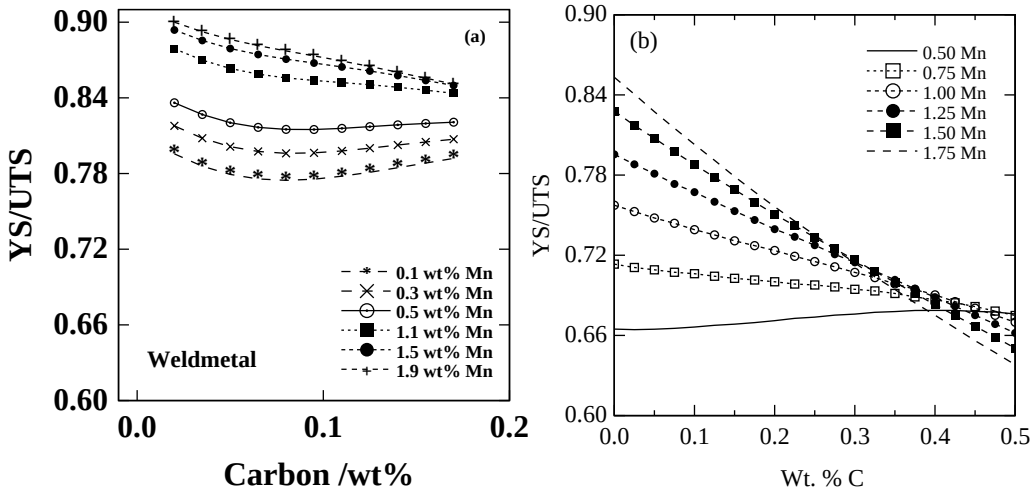

Figure 5.9: The effect of carbon, manganese on YS/UTS ratio on a) weld metal and b) steel plate [108].

Input element	Minimum	Maximum	Mean	Standard deviation
Carbon (wt%)	0.022	0.19	0.07	0.0192
Silicon (wt%)	0.01	1.63	0.36	0.126
Manganese (wt%)	0.23	2.31	1.25	0.403
Sulphur (wt%)	0.002	0.14	0.008	0.008
Phosphorus (wt%)	0.003	0.25	0.01	0.0134
Nickel (wt%)	0.0	5.58	0.366	1.012
Chromium (wt%)	0.0	11.8	0.453	1.387
Molybdenum (wt%)	0.0	1.54	0.153	0.336
Vanadium (wt%)	0.0	0.53	0.0136	0.0424
Copper (wt%)	0.0	2.18	0.0658	0.222
Cobalt (wt%)	0.0	0.016	0.0005	0.0023
Tungsten (wt%)	0.0	3.86	0.0076	0.1555
Oxygen (p.p.m.)	63.0	1535	409	112
Titanium (p.p.m.)	0.0	770	102	138
Nitrogen (p.p.m.)	21.0	1000	96.5	63
Boron (p.p.m.)	0.0	200	14.3	35
Niobium (p.p.m.)	0.0	1770	40.55	139.6
Heat input (kJ mm^{-1})	0.6	6.6	1.194	0.69
Interpass temperature (°C)	20	350	199.7	30
Tempering temperature (°C)	20	760	182.5	261
Tempering time (h)	0.0	100	2.2	5.66
Testing temperature (°C)	-151	136	-43.9	34.4
Charpy toughness (J)	2.6	300	74	43

Table 5.3: The input variables for the Charpy impact toughness model. 'p.p.m'. corresponds to parts per million by weight.

Nickel is known to have an intrinsic beneficial effect on toughness by increasing the work necessary to create cleavage cracks [110]. Thus, the toughness at low temperatures is found to increase with the nickel concentration (Fig. 5.16a); however, the optimum concentration of nickel is found to depend significantly on that of manganese. Higher concentrations of nickel are beneficial only at low concentrations of manganese (Fig. 5.16b) because both elements enhance the hardenability and strength of the weld deposit.

As might be expected, Fig. 5.17a shows that the toughness at 0 °C decreases with an increase in the oxygen concentration; oxides are sites for the nucleation of cracks and voids. The toughness can nevertheless be optimised by selecting the right manganese concentration, 0.7 wt% in the case illustrated. This is because low manganese concentrations lead to bad microstructures whereas too high a concentration raises the weld strength. Fig. 5.17b shows that the toughness is maximised when the manganese to silicon ratio is about 2:1. This may have something to do with deoxidation practice but the details are not understood.

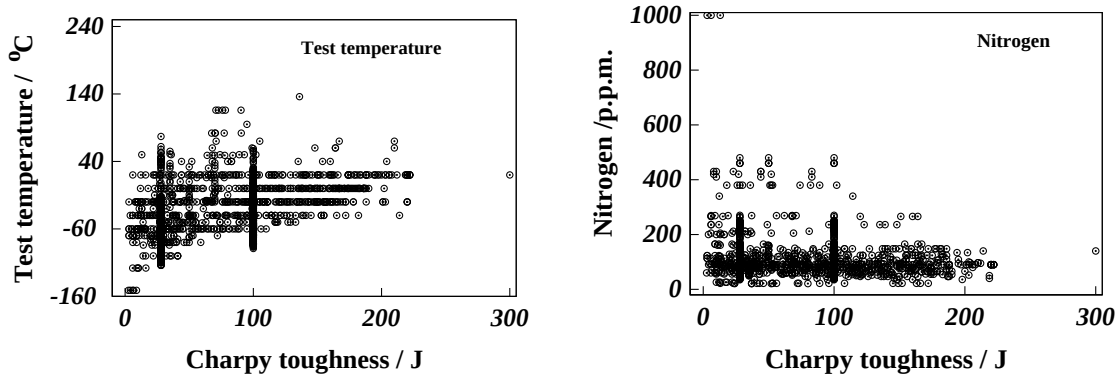

Figure 5.10: The additional variables used in the Charpy toughness model.

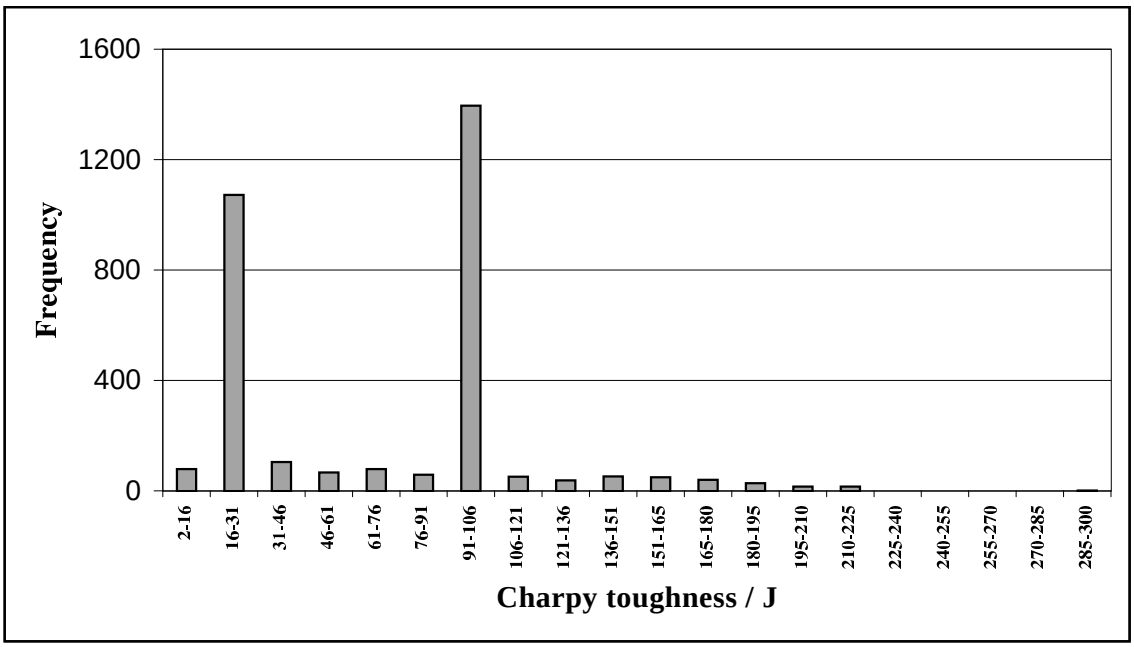

Figure 5.11: Frequency distribution for the Charpy toughness data.

5.2.2 Further Improvements

The analysis presented here is very useful and is the first quantitative model covering a vast range of variables. At the same time the model captures many non–linear dependencies. However, as Fig 5.16 shows the analysis is far from ideal in term of the spread of impact toughness.

To rectify this a more comprehensive set of Charpy results was complied from Evans [54], but these were restricted to carbon–manganese and low–alloy weld metals. The detailed analysis

Input variable	
Carbon (wt%)	0.07
Silicon (wt%)	0.50
Manganese (wt%)	1.50
Sulphur (wt%)	0.006
Phosphorus (wt%)	0.008
Nickel (wt%)	0.0
Chromium (wt%)	0.0
Molybdenum (wt%)	0.0
Vanadium (wt%)	0.0
Copper (wt%)	0.0
Cobalt (wt%)	0.0
Tungsten (wt%)	0.0
Oxygen (p.p.m.)	300
Titanium (p.p.m.)	0.0
Nitrogen (p.p.m.)	80
Boron (p.p.m.)	0.0
Niobium (p.p.m.)	0.0
Heat input (kJ mm^{-1})	1.00
Interpass temperature (°C)	175
Tempering temperature (°C)	20
Tempering time (h)	0.0
Testing temperature (°C)	0.0

Table 5.4: The input variables of carbon–manganese steel weld metal used in the analysis.

of these data is presented in Appendix A. One of the major aims in doing this additional work was to confirm the exciting trend noted in Fig. 5.16. It seems that the widespread belief in industry that nickel additions unconditionally improve low temperature toughness is not entirely justified. Fig. 5.16 confirms that nickel does indeed improve the toughness, but only at low manganese concentrations. Bearing in mind that the importance of this result and the fact that the model from which Fig. 5.16 was generated has a highly non–uniform distribution of data, it is heartening to see that the more comprehensive analysis (Appendix A) confirms the trend, as illustrated in Fig. A.19.

5.3 Impact Energy Transition Temperature Model

As emphasied earlier, the Charpy toughness of a steel weld is one of the important quality control parameters, widely specified in industry and used as a ranking parameter in consumable research

and development programmes. Body–centered cubic iron undergoes a ductile–brittle transition as the test temperature is reduced. Consistent with international norms, the toughness is therefore frequently characterised by a transition temperature corresponding to a particular value of the absorbed impact energy. In a recent paper, French [111] conducted a careful series of experiments in which the temperature T_{27J} corresponding to a measured Charpy impact energy of 27 J was characterised as a function of the yield strength, oxygen content and the microstructure. The latter included the fraction of acicular ferrite in the as–deposited microstructure, but since the work was done on multipass welds, an overall percentage of reheated microstructure was also measured. Three different welding processes were used: flux–cored arc welding (FCAW), gas metal arc welding (GMAW) and manual metal arc welding (MMAW).

The resulting data were analysed using linear regression as follows:

$$T_{27J} = 0.007(YS) + 550(O) + 0.034(R) - 0.31(AF) - 74 \qquad ^{\circ}\mathrm{C} \tag{5.5}$$

where YS is the yield strength in MPa, O is the concentration of oxygen in wt%, and the reheated microstructure R and acicular ferrite AF are area percentages. The range of applicability of the equation can be gauged from Table 5.5, which contains information from 59 separate measurements.

Input element	**Minimum**	**Maximum**	**Mean**	**Standard Deviation**
Yield Strength (MPa)	360	630	516	55
Oxygen (wt%)	0.03	0.12	0.06	0.02
Reheated Material (%)	20	79	41	13
Acicular Ferrite (%)	5	86	54	15
Temperature at 27J (°C)	-88.0	-13	-54	18

Table 5.5: Characteristics of the measured parameters in the experiments conducted by French [111].

The analysis indicated a standard error of $\pm 12\,^{\circ}\mathrm{C}$, with a correlation coefficient of 0.78. It is possible that a better interpretation of the data and associated uncertainties can be obtained using a non–linear regression method, which does not have an *a priori* assumption of the relationship between the variables, which accounts for the interactions between the variables, and which comments not only in the perceived level of noise in the output, but also on how the uncertainty of fitting depends on the particular region of input space where the prediction is being made. The introduction to the method of neural network analysis is presented in Chapter 3.

5.3.1 The Analysis

The aim was to be able to estimate T_{27J} as a function of the variables shown in Table 5.5. All the input variables and the output were normalised within the range ± 0.5 (Chapter 3). This step is not essential to the running of the neural network but later allows a convenient way to compare the results of the output.

For several runs of the neural network, Fig. 5.18 shows the model perceived noise σ_ν in T_{27J}. It is very interesting that the level of noise in the normalised output parameter T_{27J}, as perceived by the network, is $\sim 0.15 - 0.18$. This amounts to $\pm 11 - 14\,^{\circ}$C, which compares favorably with the $\pm 12^{\circ}$C deduced by French using linear regression analysis. It is also worth noting that the error, irrespective of the model, is quite large when considering the physical meaning of T_{27J}. Furthermore, one standard error corresponds to a 68% confidence limit whereas two standard errors give the more acceptable 95% error bound. The important conclusion is that the noise level is not reduced by using a non–linear analysis, giving evidence that the problem is not well specified; there are missing variables which clearly affect the toughness. It cannot be speculated what these missing variables could be, but factors such as the hydrogen and nitrogen concentrations, the scale of the microstructure *etc.* come to mind. Note also that the nature of the welding process is not explicitly taken into account.

A second outcome is that this particular problem illustrates the soundness of the neural network technique used here, where the proper use of the training and test dataset prevents the accidental modelling of true noise in the output.

Fig. 5.19 shows the predictions for the training and test data for the best model, identified as the one with the highest log predictive error [6]. It is clear that the model is reasonably well behaved in the sense that the test data are predicted to a similar level of accuracy as the training data. It is important to note that the error bars plotted in Fig. 5.19a,b do not include σ_ν, but only the fitting error, which depends on the position in the input space. Fig. 5.19c shows the corresponding plot for the test data where the error bars contain both the σ_ν and the fitting error. All subsequent plots also include both components since it is logical to consider both the perceived level of noise in the output and the fitting error. As will be seen subsequently, the latter is particularly important when extrapolating or interpolating, since large fitting errors are calculated in regions where the experimental knowledge is sparse or noisy.

A plot of the test error of the committee versus its size gives a minimum which defines the optimum size of the committee, as shown in Fig. 5.20. The test error associated with the best single model is clearly greater than that of any of the other committees. It was determined in this case that a committee of thirteen models would be the best choice, being the committee of the lowest test error. The committee was then retrained on the entire data set without changing the complexity of any of its members.

The predictions of the committee trained on the entire data set can be compared with the original dataset as shown in Fig. 5.21.

Another parameter, σ_w, indicates the importance of an input in terms of its variation having an effect on the output of the model. Fig. 5.22 compares the values of σ_w for each of the inputs for the thirteen models in committee. A high value of σ_w for a specific input can be caused by the corresponding variable inducing a large variation in the output, but it can be seen from Fig. 5.22 that different models can assign varying significance to the same input. This is one of the reasons why a committee of models can be more reliable than the single model judged to be best on the basis of a parameter such as σ_ν.

5.3.2 Use of the Model

It is worth illustrating a few predictions, to emphasis the point that the error bars will not be constant as in [111]. It is important to note that as in equation 5.5, the predictions are for the case where just one input variable is altered, keeping all other fixed. This may not be possible when conducting experiments. The variables used for analysis are shown in Table 5.6. Fig. 5.23a shows that T_{27J} increases with the oxygen concentration; this is expected since the oxygen is inevitably present in the form of oxide inclusions which, for a constant microstructure, are detrimental to toughness.

Input variable	
Yield Strength (MPa)	515
Oxygen (wt%)	0.05
Reheated Material (%)	41
Acicular Ferrite (%)	54

Table 5.6: The input variables of carbon–manganese steel weld metal used in the analysis.

It is not surprising that Fig. 5.23b shows that acicular ferrite improves the toughness. However, the neural network model shows that the results are not certain at large fractions of acicular ferrite when all the other variables are kept constant.

Fig. 5.24 shows contour plots of T_{27J} as a function of the acicular ferrite and oxygen concentrations. A simple interpretation of the linear regression model (Fig. 5.24b) indicates that for optimum toughness, the acicular ferrite must be maximised at a zero oxygen concentration. However, there are no welds in the dataset with zero oxygen concentration and such a suggestion is probably not justified since oxides are needed to nucleate acicular ferrite. The neural network analysis, on the other hand, correctly indicates an optimum combination of acicular ferrite and oxygen concentration.

5.4 Embrittlement Model

Welding alloys designed for creep–resistant steels frequently have to be tempered in a temperature range where they are susceptible to embrittlement by impurity elements such as antimony or phosphorus. The segregation of these deleterious elements to the prior austenite grain boundaries leads to intergranular failure and consequently, a reduction in toughness. Whereas this mechanism of embrittlement is well–understood from a vast amount of research published over the last five decades, there are no quantitative methods capable of estimating the degree of embrittlement as a function of the chemical composition and heat treatment.

It was in this context that Bruscato [112] reported a large number of experiments, based on the classical $2\frac{1}{4}$Cr1Mo composition, but with variations in the phosphorus, antimony, tin and arsenic concentrations. There were also some variations in the concentrations of the major alloying additions including C, Mn, Si, Cr and Mo. The tendency to embrittlement was monitored by comparing the impact toughness of both post–weld heat treated (PWHT) and step–aged samples. The latter heat treatment exaggerates the extent of embrittlement. Bruscato used an embrittlement factor $\overline{X}$ to interpret his data:

$$\overline{X} = \frac{10\mathrm{P} + 5\mathrm{Sb} + 4\mathrm{Sn} + \mathrm{As}}{100} \tag{5.6}$$

where the concentrations of the elements are in parts per million by weight. A large value of $\overline{X}$ implies a greater tendency to temper embrittlement. This led him to conclude that the embrittlement of $2\frac{1}{4}$Cr1Mo welds is directly related to the manganese, silicon, phosphorus, tin, arsenic and antimony concentrations, with the first four being of greatest significance. The derivation of the equation for $\overline{X}$ was not presented in the original paper, although it is stated that it is based on data from chromium–steels. In the present work Bruscato's original data was analysed using neural network analysis, and his conclusions were examined in more detail.

5.4.1 The Data

Bruscato published results on thirty separate weld deposits; the range of parameters is listed in Table 5.7. The Charpy toughness of the step–aged samples represents the output to be modelled as a function of all the other variables listed in Table 5.7. All of the thirty welds had been given an identical heat treatment. For the purposes of the analysis, the data were all normalised in the range ± 0.5 in order to compare the significance of each of the input variables.

The data were divided at random into two parts, a training and a test dataset. The neural network models were then created using just the training data (Chapter 3). The resulting models were assessed on their ability to generalise on the unseen test data. From the models created, a committee of three models was found to give the best generalisation on unseen data.

Input element	Minimum	Maximum	Mean	Standard Deviation
Silicon (wt%)	0.32	1.19	0.636	0.195
Manganese (wt%)	0.54	0.79	0.691	0.0609
Phosphorus (wt%)	0.004	0.018	0.009	0.003
Molybdenum (wt%)	0.9	1.27	1.102	0.095
Tin (p.p.m.)	70	300	108.7	38.8
Antimony (p.p.m.)	0.9	22	5.2	3.73
Arsenic (p.p.m.)	0.0	130	59.8	27.7
Charpy toughness after step aging (J)	6.78	136.96	60.4	29.2

Table 5.7: The range of values reported by Bruscato, and used in the present work. 'p.p.m.' corresponds to parts per million by weight.

These three models had 13, 11 and 11 hidden units with σ_ν values of 0.083293, 0.083149 and 0.083118 respectively; σ_ν is the perceived level of noise in the normalised output. An increase in the number of hidden units enables the network to recognise more complex relationships. The committee members were finally optimised on the entire dataset. The performance of the committee is illustrated in Fig. 5.25.

Fig. 5.26 shows the significance σ_w of each of the input variables. The value of σ_w for a particular input variable indicates the ability of that input to explain variations in the output (Charpy toughness). Three σ_w values are presented for each input, corresponding to each of the three members of the committee of models. A consistent value of σ_w, for a given input, indicates that there exists a well–defined relationship between that input and the output. Fig. 5.26 shows that tin, antimony and arsenic have very little effect on the embrittlement of the $2\frac{1}{4}$Cr1Mo welds studied, whereas phosphorus has a very large effect.

These observations can be illustrated further by making predictions. Calculations were done using the base set of input values listed in Table 5.8, while varying each input individually.

Input variable	
Silicon (wt%)	0.58
Manganese (wt%)	0.78
Phosphorus (wt%)	0.008
Molybdenum (wt%)	1.05
Tin (p.p.m.)	120
Antimony (p.p.m.)	1.6
Arsenic (p.p.m.)	36

Table 5.8: Base input values used in the application of the embrittlement model. The values correspond to weld Q in [112]. 'p.p.m.' corresponds to parts per million.

Fig. 5.27 shows the effects of molybdenum, silicon, manganese and phosphorus concentrations. As expected, phosphorus has a strong and very significant tendency to embrittle the weld metal; as stated earlier, the mechanism of phosphorus embrittlement is well–understood, involving its segregation to prior austenite grain boundaries. On the other hand, molybdenum actually improves the resistance to embrittlement. This is also expected, because molybdenum and phosphorus atoms tend to associate so that the latter are prevented from segregating to the prior austenite grain surfaces [113].

It is exciting that significant trends are recognised also for manganese and silicon. The manganese effect is consistent with work which suggests that it reduces the intergranular fracture strength [114]. Silicon is known to promote the segregation of phosphorus to the austenite grain boundaries [115].

By contrast, there are no significant trends notable for arsenic, tin or antimony (Fig. 5.28). Based on these observations, we do not find that As, Sn and Sb are important contributors to embrittlement in the particular alloy system studied here. It is possible that this result is a consequence of the fact that the welds all contain phosphorus in concentrations large enough to swamp the much smaller effects of As, Sn and Sb. Thus, the mean phosphorus concentration is 90 p.p.m, with a standard deviation of 30 p.p.m.

5.5 Summary

Tensile elongation and Charpy toughness models have been developed taking into account chemical composition, heat treatment and welding parameters. These models were successfully applied to analyse carbon–manganese weld metals and exciting results were obtained. Theoretically unexplained results were found in few cases of carbon–manganese welds.

It was shown that neural networks does not reduce the large perceived level of noise in the Charpy impact toughness transition temperature (T_{27J}) model. As there are many more variables which control the impact toughness when compared with the restricted set studied in the transition temperature model. The standard error quoted for the linear regression models must be regarded as an underestimate of the real uncertainty, since there will be regions of the input space where the fitting function itself has great uncertainty. This is relevant in both extrapolation and interpolation, which is taken into account by using Bayesian neural networks over other standard regression methods. The transition temperature model, unlike the regression model correctly predicts that there is a combination of acicular ferrite and oxygen which optimises toughness.

With the embrittlement model (Section 5.4) it was found that phosphorus, silicon and manganese all make $2\frac{1}{4}$Cr1Mo welds susceptible to temper embrittlement, with the embrittling potency decreasing in that order. Molybdenum decreases the tendency to impurity induced

embrittlement. These observations are all expected from published work. By contrast, As, Sb and Sn have no perceptible effect on the welding alloys studied, probably because of the overwhelming influence of phosphorus. It follows that any attempt to reduce the effects of temper embrittlement should focus primarily on reduction in the phosphorus.

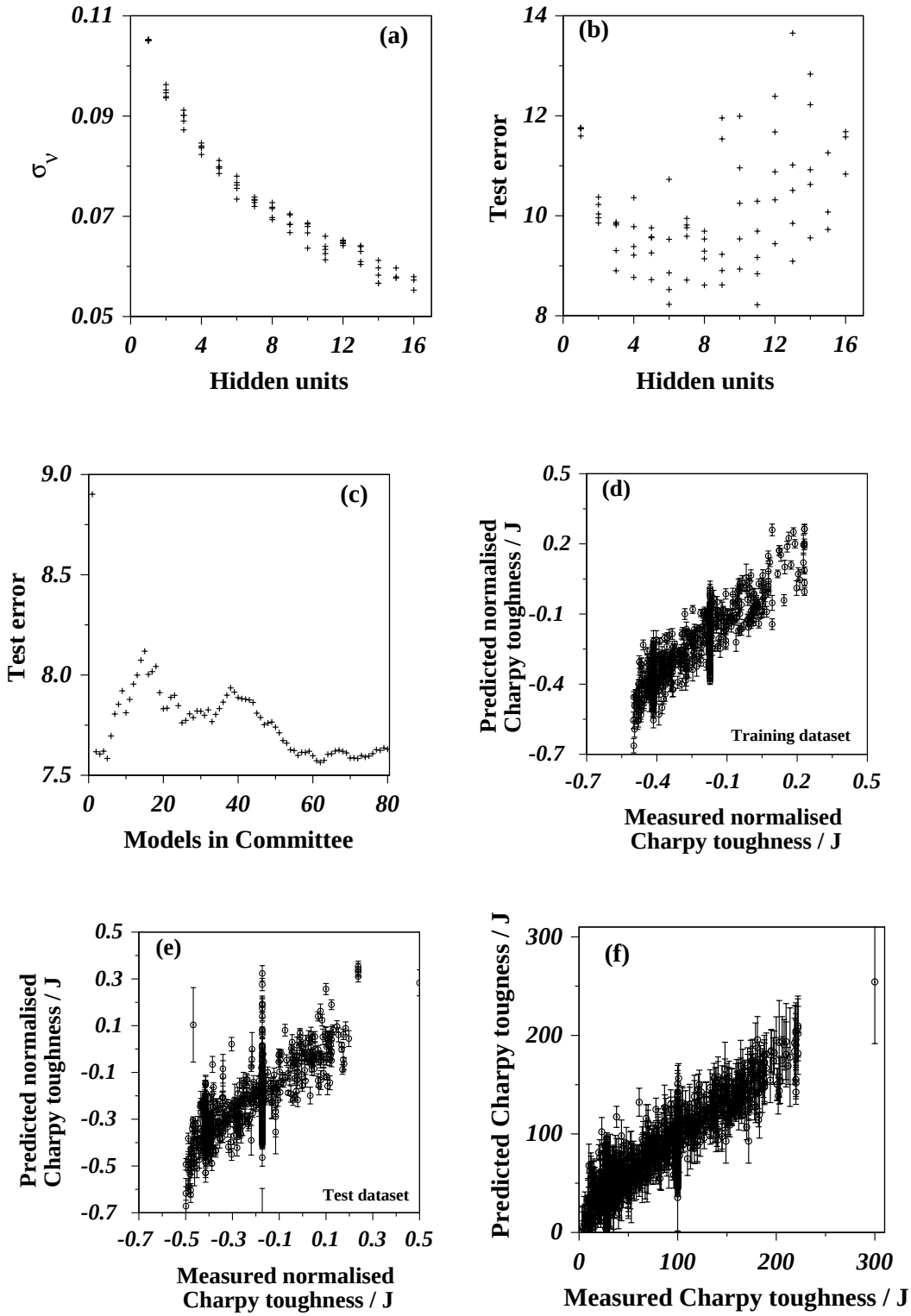

Figure 5.12: Characteristics of the Charpy impact toughness model. σ_ν is the model perceived level of noise in the toughness. (d) and (e) represent the behaviour of the best single model, whereas (f) shows the performance of the optimum committee model on the entire dataset.

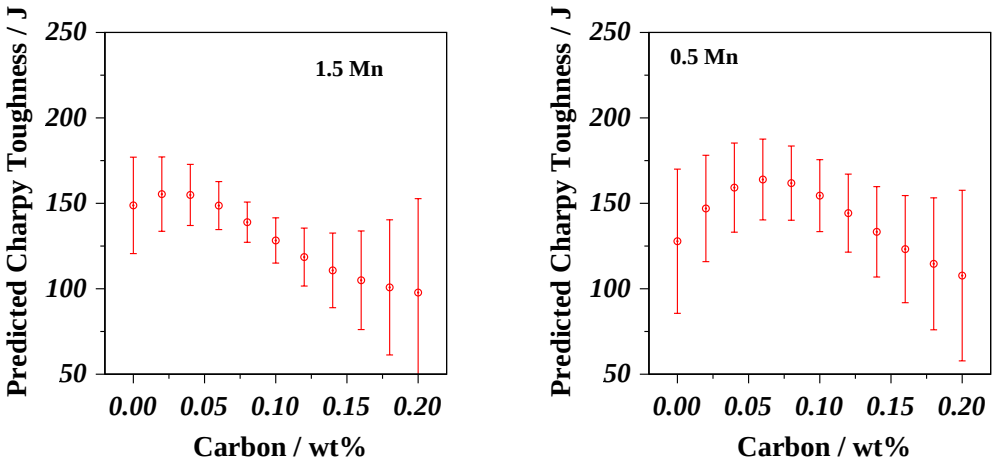

Figure 5.13: Effect of carbon at 1.5 and 0.5 wt% manganese, 0°C, on the Charpy impact energy.

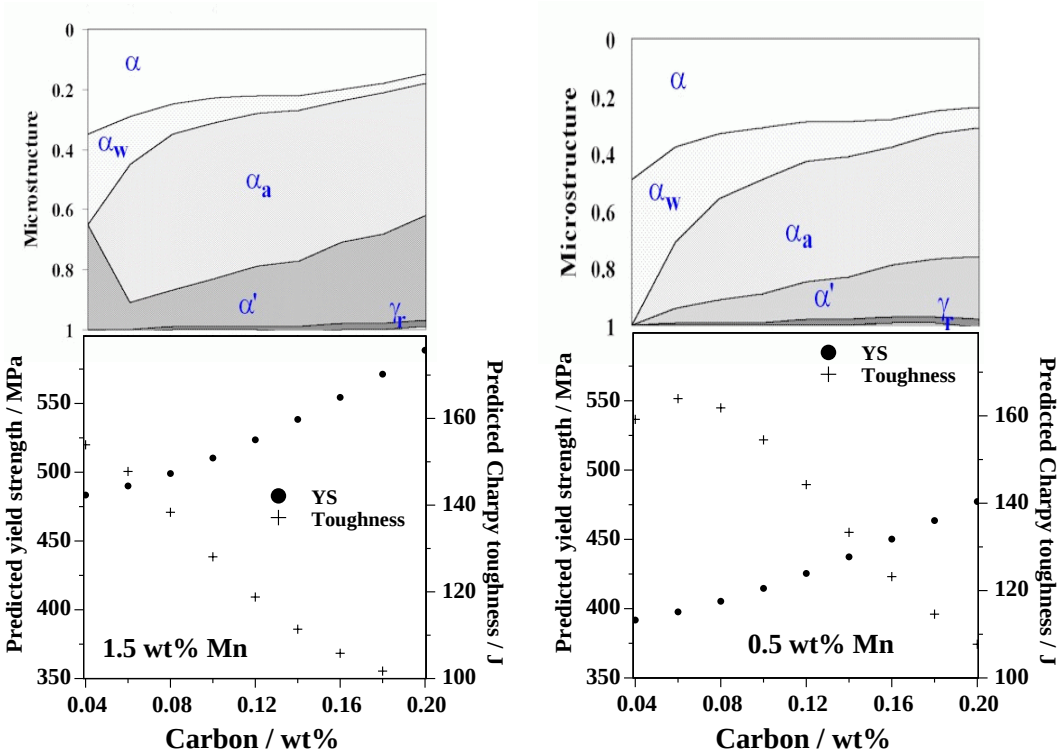

Figure 5.14: Effect of carbon at 1.5 and 0.5 wt% manganese at on yield strength and the calculated microstructural fraction using published physical model [109]. (allotriomorphic ferrite – α, Widmanstätten ferrite – α_w, acicular ferrite + bainite – α_a, martensite – α' and retained austenite – γ_r)

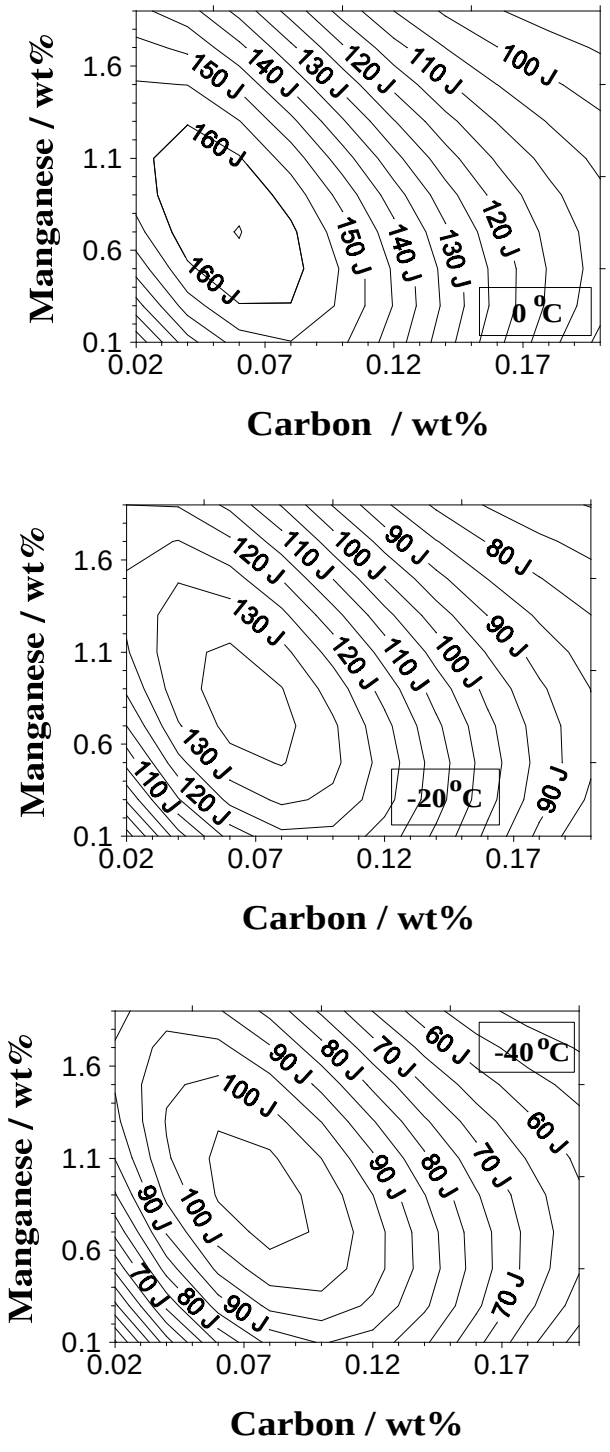

Figure 5.15: Predicted variations in Charpy impact toughness as a function of the carbon and manganese concentrations and the test temperature. The error bars have been omitted for clarity but range from ±10–45 J.

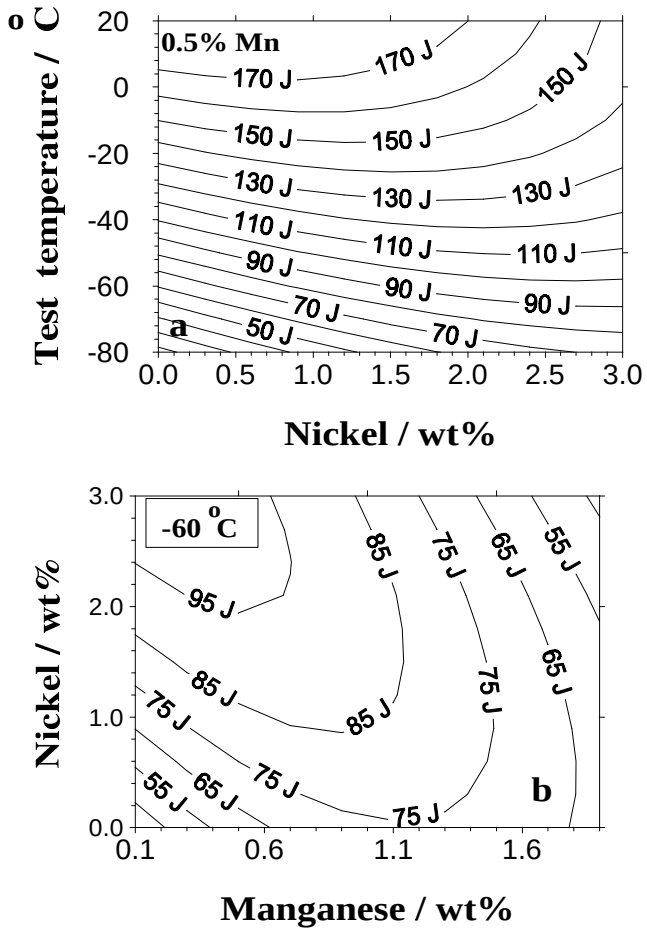

Figure 5.16: The effect of nickel and manganese on the Charpy toughness. (a) Nickel improves the toughness at low temperatures. (b) The optimum concentration of nickel depends on the manganese concentration. The error bars have been omitted for clarity but range from ±10–25 J.

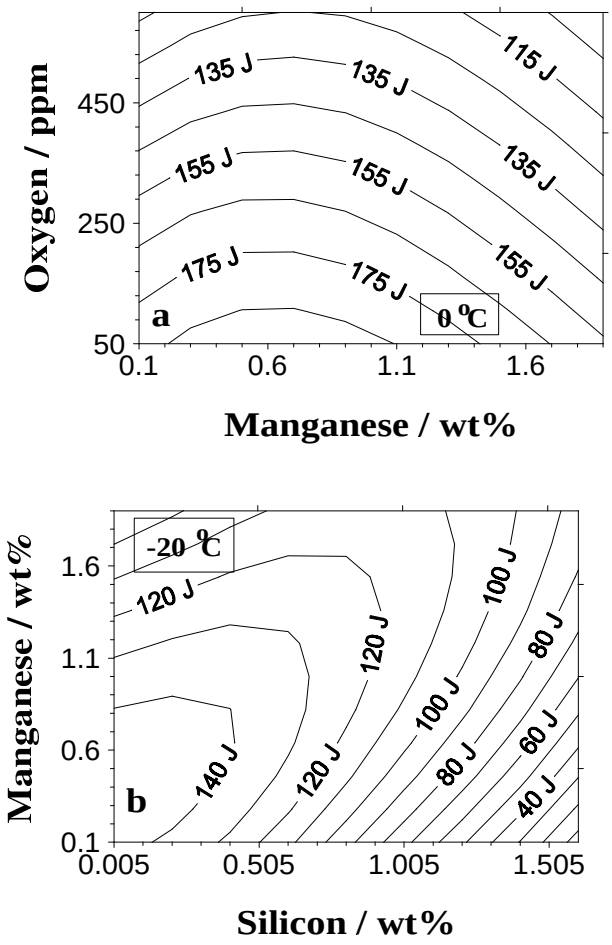

Figure 5.17: (a) The combined effect of manganese and oxygen on the toughness at 0 °C. (b) The combined effect of manganese and silicon on the toughness at -20 °C. The error bars have been omitted for clarity but range from ±10–60 J.

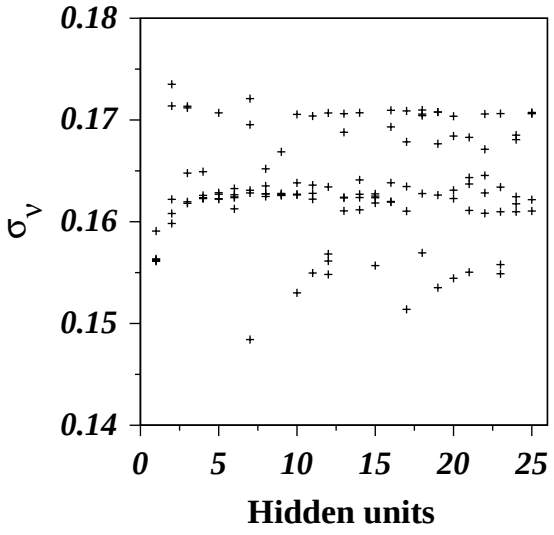

Figure 5.18: Variation in σ_ν as a function of the number of hidden units. Several values are presented for each set of hidden units because the training for each network started with a variety of random seeds.

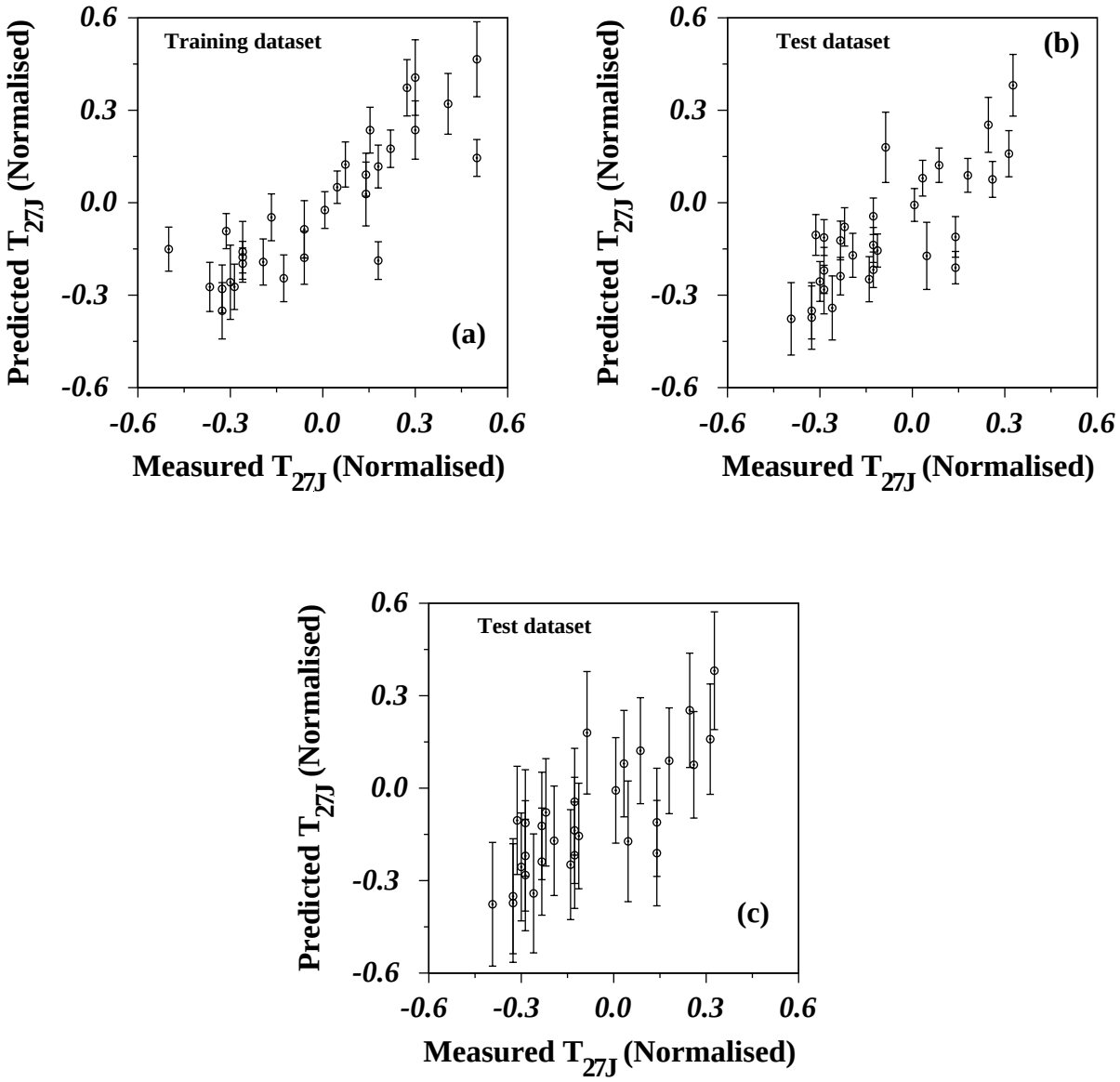

Figure 5.19: Comparison of the predictions made using the best model and measured values of T_{27J}, (a) training data plotted with the fitting error, (b) test data plotted with the fitting error, (c) test data with the error bars representing both the fitting error and σ_ν.

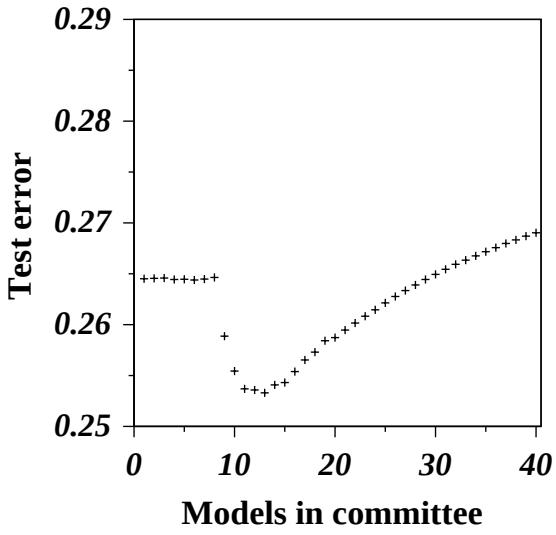

Figure 5.20: Comparison of test error of increasing size of committees.

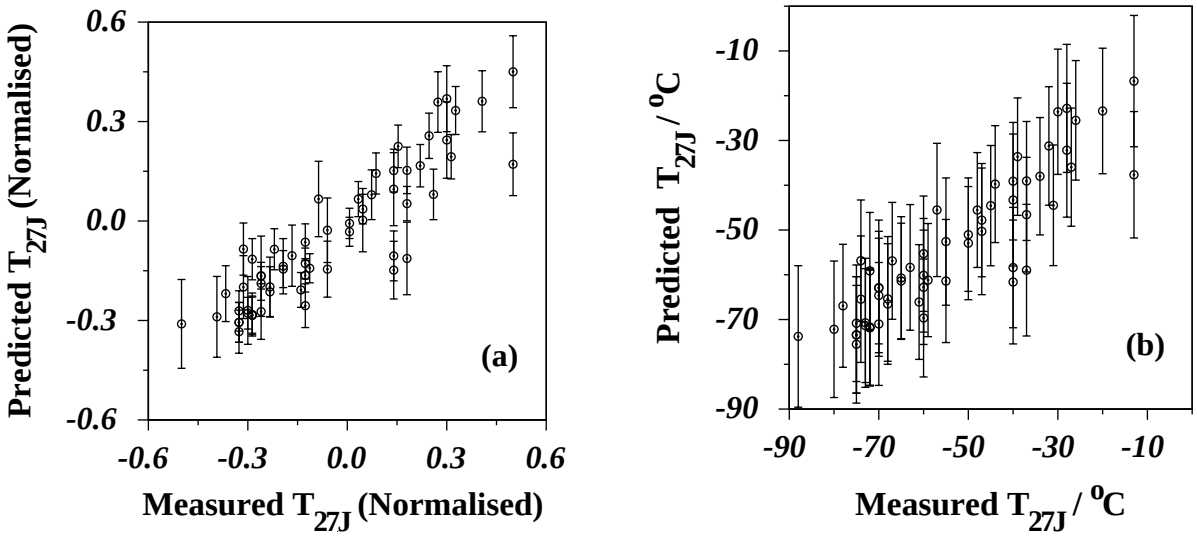

Figure 5.21: Comparison of predicted values and experimental values for the optimum committee using entire dataset a) before unnormalisation, here the error bars contains only the fitting error. b) after unnormalisation, with fitting error and σ_ν.

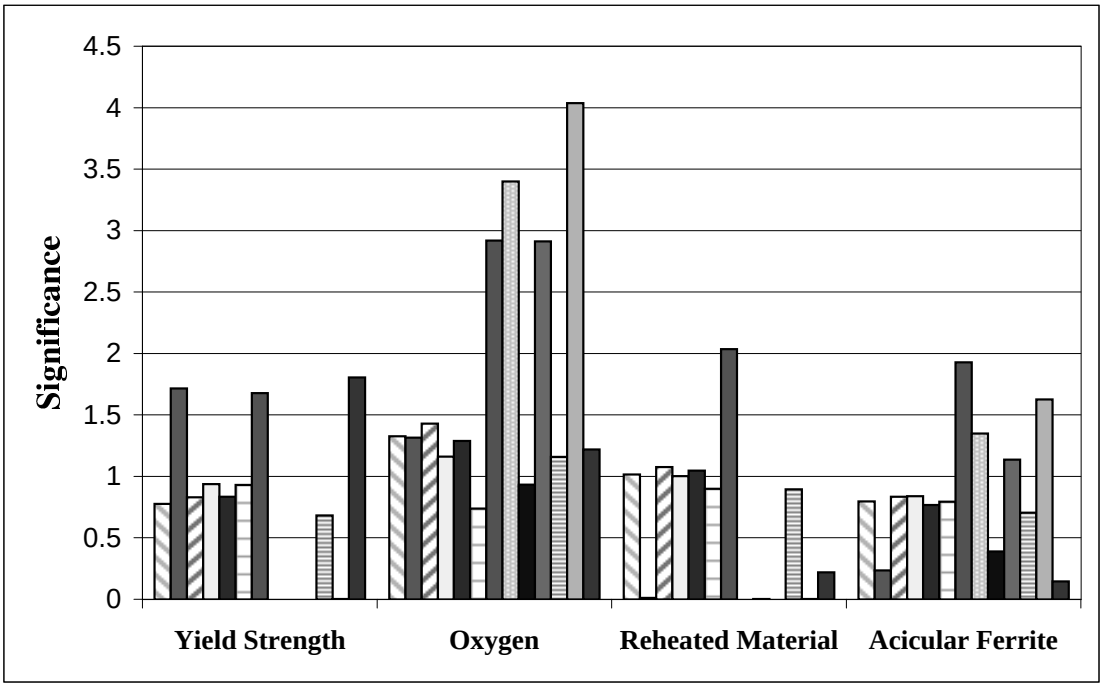

Figure 5.22: Bar chart showing the perceived significance (σ_w) for each input variable. There are thirteen bars plotted per input, corresponding to each of the thirteen members of the optimum committee.

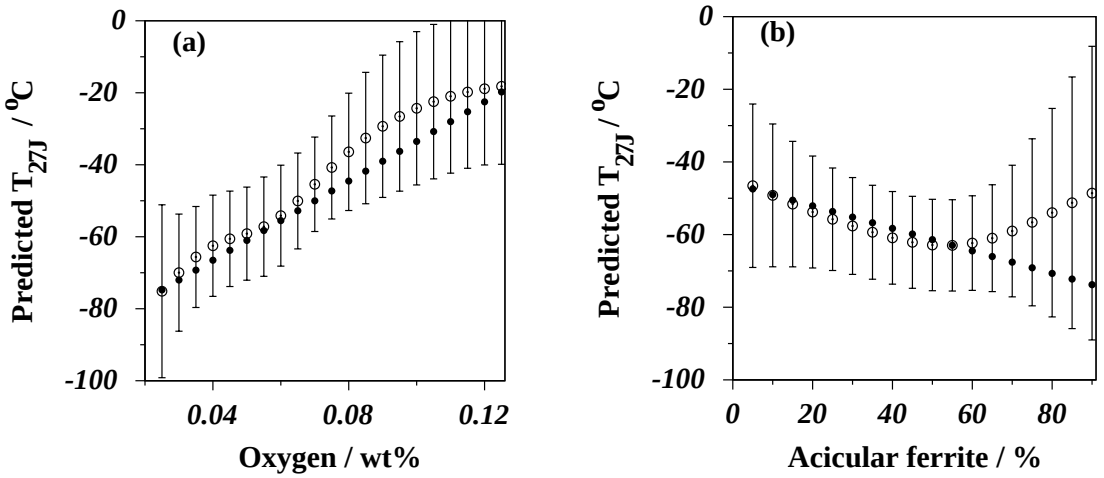

Figure 5.23: Calculations as a function of the oxygen and acicular ferrite contents. In each case, the values of the remaining input variables are as listed in Table 5.6. The open circles with error bars are represent neural network model predictions whereas the filled circles are from equation 5.5.

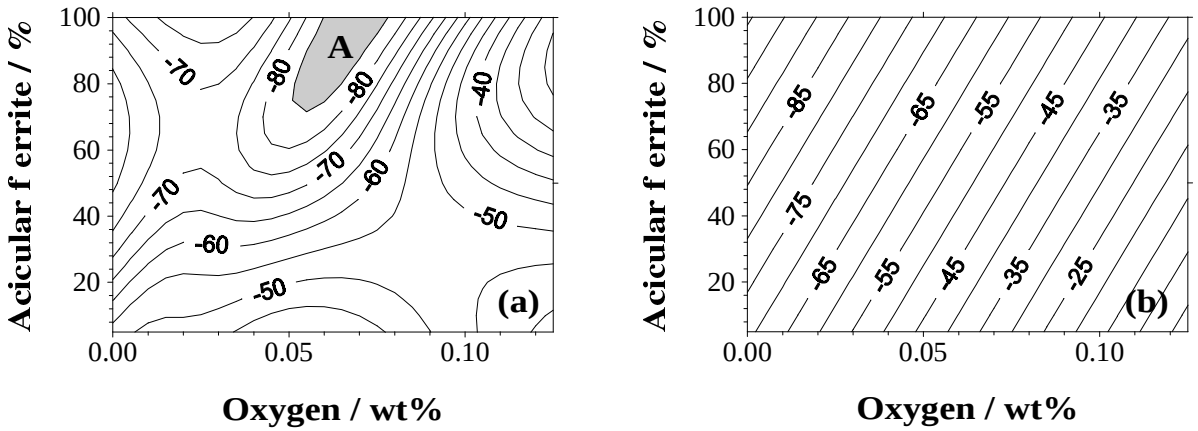

Figure 5.24: Contour plots for calculations made using the following inputs: 510 MPa yield strength and 20% reheated material. The contour lines are expressed in °C, a) neural network predictions, here the error bars have been omitted for clarity but range from ±15–75 °C. The region marked 'A' shows that an optimum value of T_{27J} occurs at finite oxygen concentrations, b) using equation 5.5.

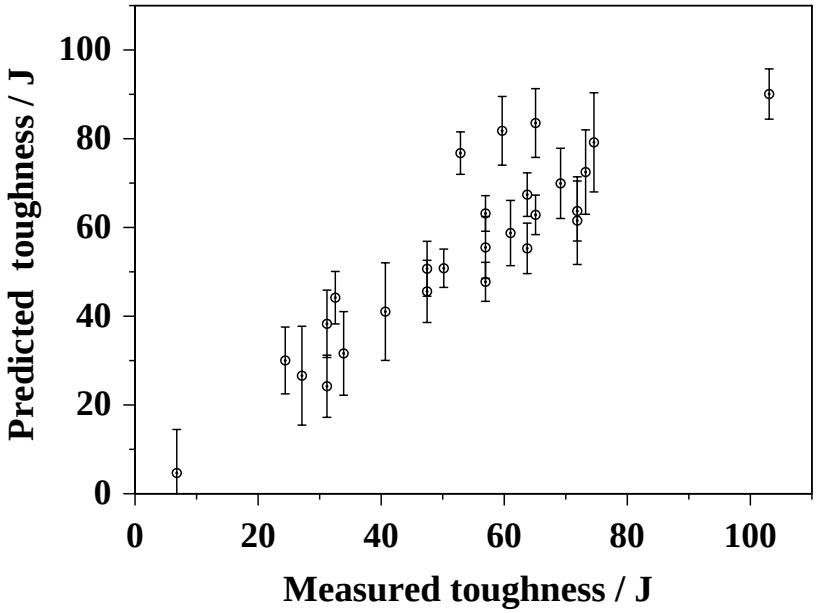

Figure 5.25: Comparison of the predicted and measured values of the Charpy toughness. The predictions are made using the committee of three models.

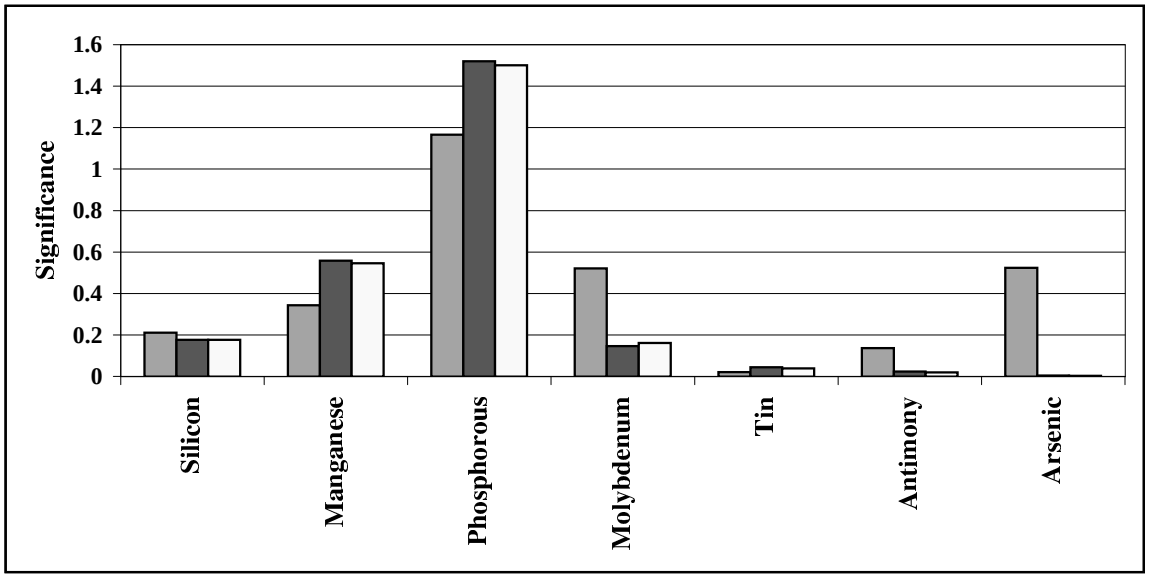

Figure 5.26: The perceived significance σ_w values of three committee models for each of the inputs.

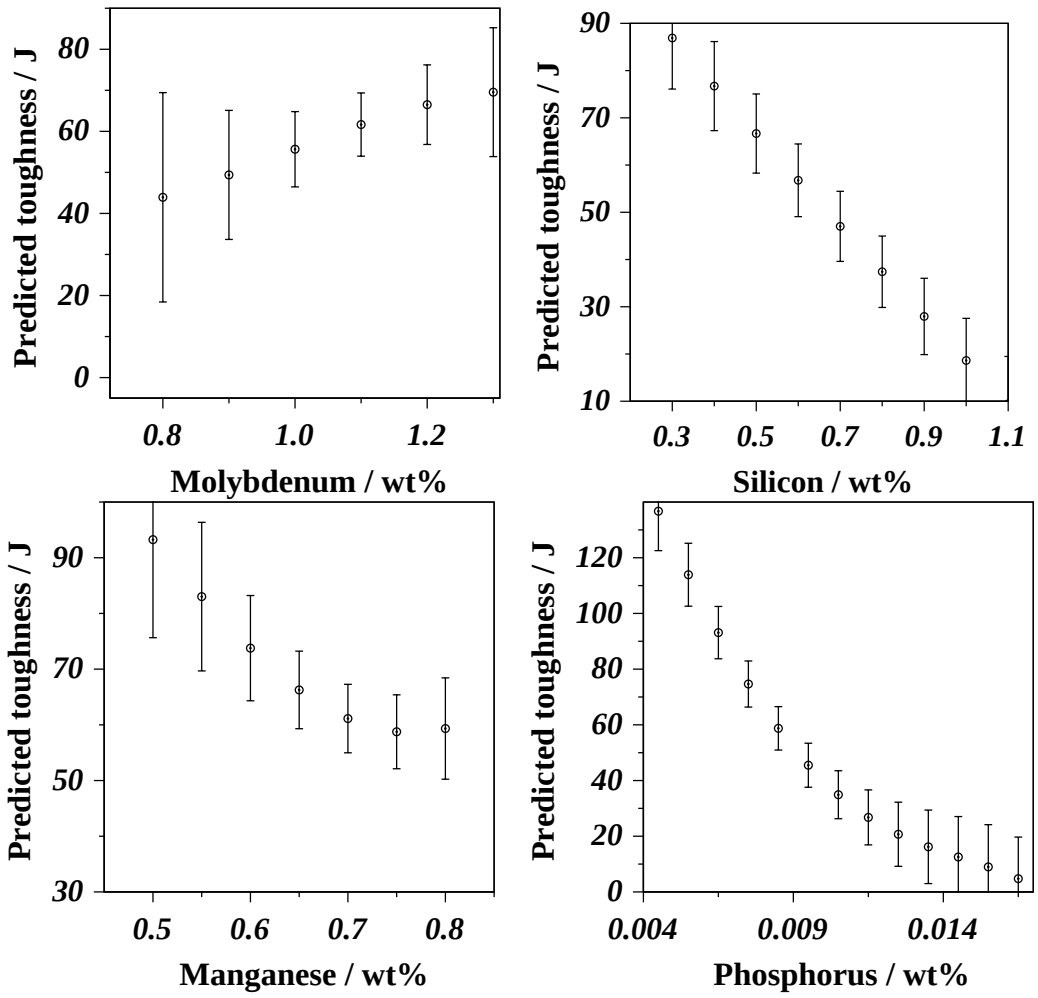

Figure 5.27: Analysing the effects of molybdenum, silicon, manganese and phosphorus on toughness after step aging.

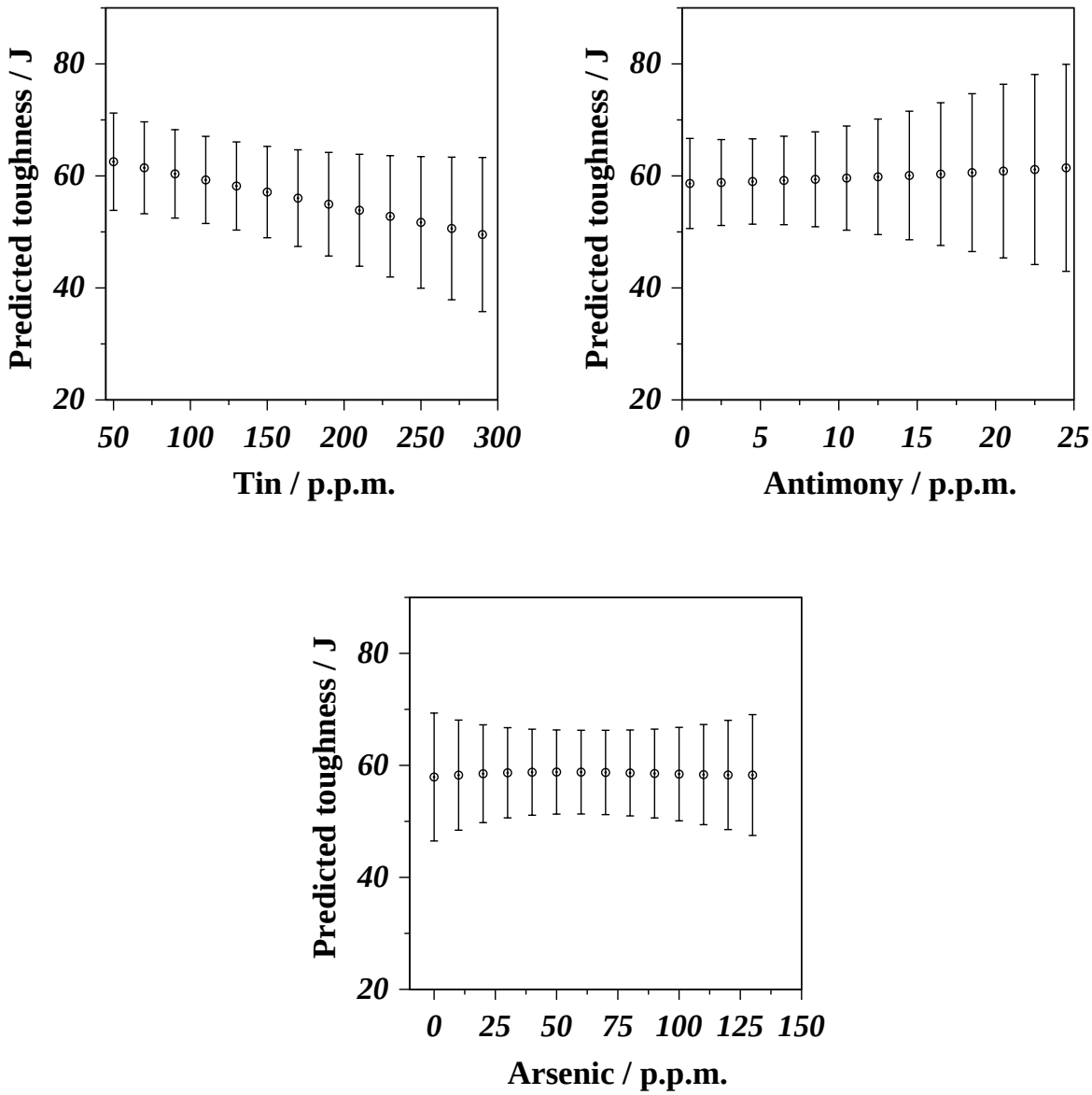

Figure 5.28: The effects of tin, antimony and arsenic on toughness after step aging. 'p.p.m.' corresponds to parts per million.

Chapter 6

Design of Weld Metal Avoiding Post–Weld Heat Treatment

Low–carbon creep–resisting steels used in the construction of power plant or in the petrochemical industry generally contain chromium, molybdenum, niobium or vanadium as the significant alloying additions. These elements either provide oxidation and corrosion protection (for example, chromium) or on tempering they form stable carbides which impede creep deformation. The steels have major applications in the fabrication of pressure vessels, boiler steam pipes, steam generating and handling equipment, high pressure tubes with thick walls, turbine rotors, superheater tubes, coal to methane conversion plants and petrochemical reactors for the treatment of heavy oils and tar sands bitumen [116]. The steels might typically be used within the temperature range 480–600 °C, the service stresses being of the order of 15–40 MPa. The required microstructure is produced by austenitisation followed by tempering at a temperature which is above that encountered during service. A typical tempering heat treatment may therefore involve temperatures in the range 650–750 °C, for some 4–20 h, depending on the detailed chemical composition and also the section size.

Further heat treatments are required following welding operations. The heat introduced during welding has a significant influence on the solid metal in the close proximity of the weld. Microstructures may be created in this heat–affected zone, which are hard (martensitic) and untempered. Furthermore, residual stresses arise from the shrinkage of the weld as it cools from the liquid state. One purpose of a post–weld heat treatment is to ameliorate both of these changes due to welding.

There are many components of a power plant where it is incredibly difficult to introduce post–weld heat treatments, primarily because of the large scale of the plant involved, but also due to the tight packing of components. One such case is the boiler which contains a myriad of pipes, as illustrated in Fig. 6.1. To reduce the costs of implementing post–weld heat treatments in such circumstances, Mitsubishi Heavy Industries in Japan has developed a new steel, designated

HCM2S, which replaces the classical $2\frac{1}{4}$Cr–1Mo alloy [117]. The latter requires post–weld heat treatment whereas the former, due to its lower hardness in all microstructural conditions, does not. The development of the new steel does not entirely resolve the difficulties since the weld metal used to fill the gaps between plates to be joined also requires heat–treatment. The purpose of the work presented in this Chapter was therefore to design, using the methodologies described in earlier Chapters, a welding alloy which itself does not require post–weld heat treatment.

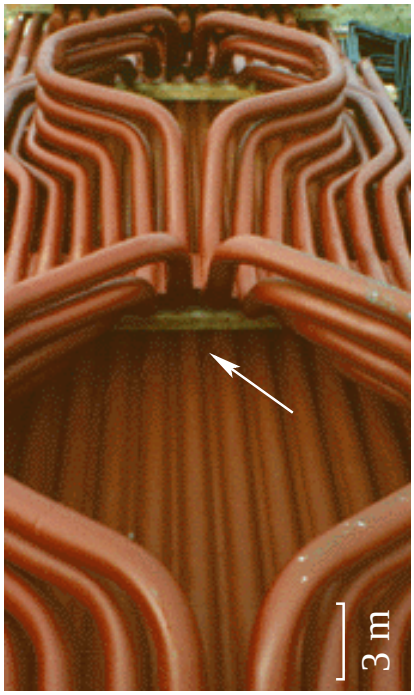

Figure 6.1: Complex shapes of boiler tubes used in power plant. The arrow shows two boiler tubes joined together with a supporting plate.

6.1 Novel Cr–W–V–Nb Steel (HCM2S)

This material was developed in 1993 [118] for the construction of boilers, with the aim of avoiding post–weld heat treatments. This essentially requires a relatively low hardness following an austenitisation treatment of the kind which might occur in the heat–affected zone of a weld, without compromising the creep properties. Conventional $2\frac{1}{4}$Cr–1Mo wt% steel contains a carbon concentration of 0.1 wt% or more; it needs post–weld heat treatment to restore the ductility and decrease the hardness in the heat–affected zone. The hardness of $2\frac{1}{4}$Cr–1Mo steel is attributed mainly to its carbon and molybdenum concentrations, whereas the chromium serves primarily to provide limited oxidation and corrosion resistance. Molybdenum serves to form a carbide which enhances creep strength.

Therefore, the idea behind the new steel HCM2S was to reduce the carbon concentration, to replace molybdenum with tungsten (which remains in solid solution) and to enhance creep strength using small concentrations of niobium and vanadium, both of which are strong carbide formers [119], Table 6.1. The gross microstructure following heat treatment is essentially the same as that of $2\frac{1}{4}$Cr–1Mo, consisting of tempered bainite Fig. 6.2.

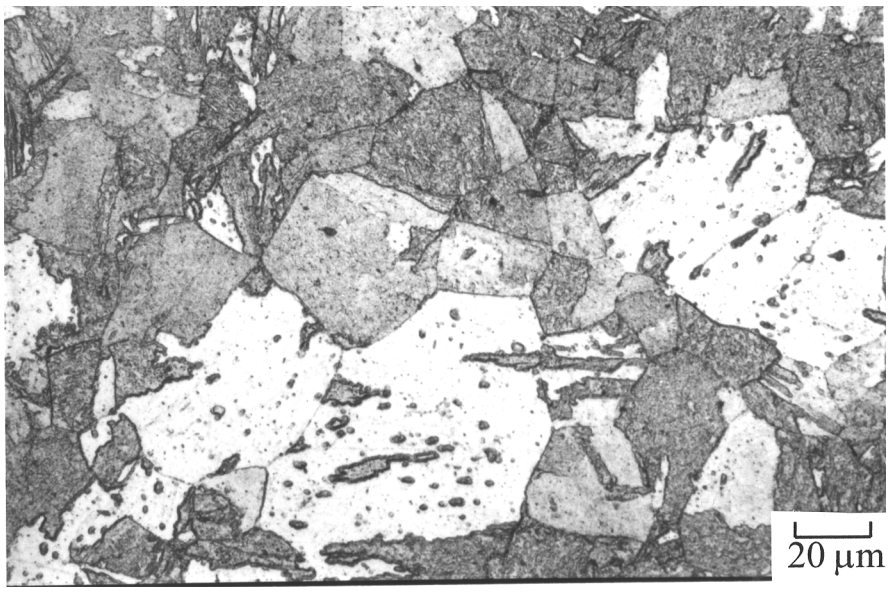

Figure 6.2: Tempered microstructure of as–received HCM2S steel tube. The tube is tempered at 770 °C for 1 hour after air cooling from 1050 °C (1 h). The sample is etched using 2% nital.

The flow chart illustrating the development of HCM2S steel is shown in Fig. 6.3. Due to the lower carbon concentration in HCM2S, the maximum hardness obtained for typical cooling rates is reduced to about 300 HV which is some 50 HV lower than $2\frac{1}{4}$Cr–1Mo steel, Fig. 6.4. Insensitivity to cooling rate at higher cooling rates is desirable in welding. The excellent creep strength of HCM2S is due to the substitution of tungsten for molybdenum, with slight additions of boron together with the precipitation of vanadium and niobium carbide. Here the solid solution strengthening is due to tungsten and the precipitation strengthening due to vanadium and niobium. The addition of boron has the effect of stabilising $M_{23}C_6$ and $M_{23}(C,B)_6$ on grain boundaries, thereby retarding the recrystallisation of grains during service [120]. A comparison of the creep resistance of HCM2S against conventional $2\frac{1}{4}$Cr–1Mo steels is shown in Fig. 6.5. HCM2S has the composition 1.6W-0.1Mo-0.25V-0.05Nb wt% with 0.06 wt% average carbon content.

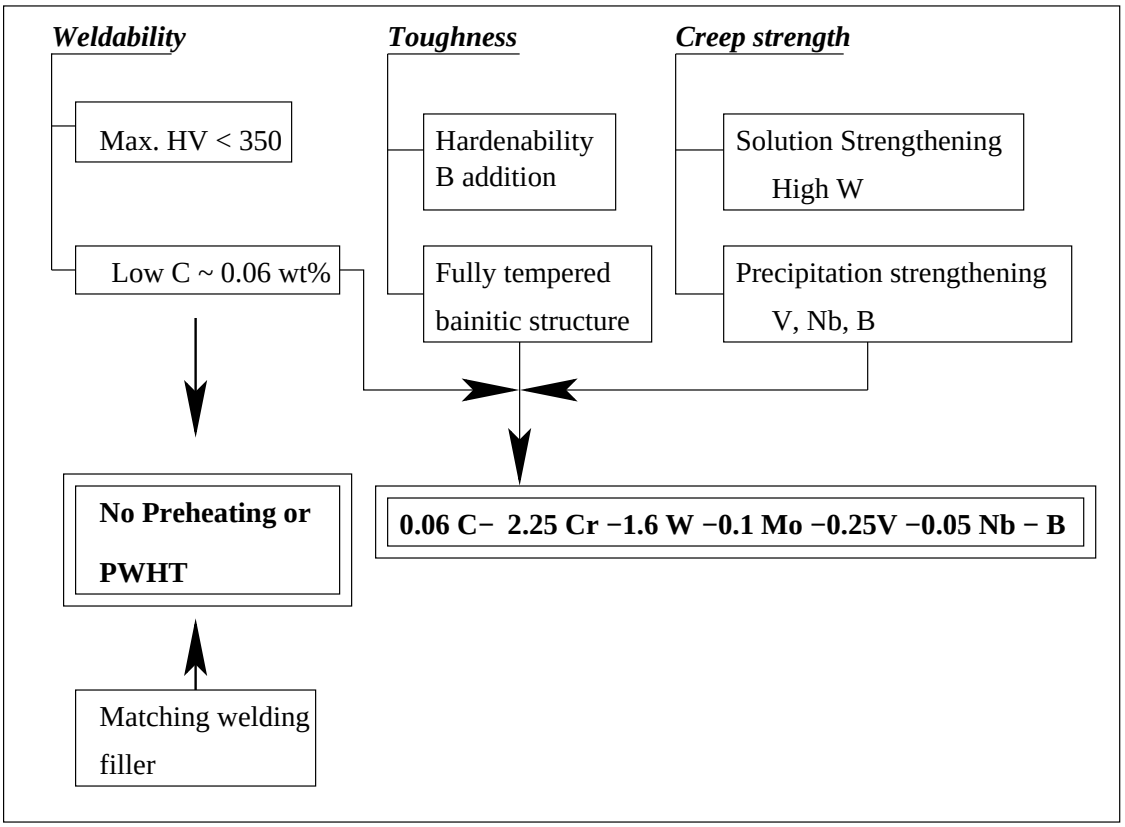

Figure 6.3: Development philosophy of HCM2S steel [117]. PWHT corresponds to post–weld heat treatment.

C	Si	Mn	P	S	Ni	Cr	Mo	W	V	Nb	B	Al	N
0.06	0.20	0.47	0.006	0.002	0.10	2.27	0.09	1.50	0.23	0.05	0.004	0.009	0.008

Table 6.1: Chemical composition (in wt%) of HCM2S base metal [119, 117].

6.1.1 Welding of HCM2S Steel

Some research has already been done at Sumitomo Metal Industries in Japan to attempt the welding of HCM2S steel. Their weld metal chemical compositions are shown in Table 6.2. The heat input used in the gas tungsten arc welding (GTAW) process is 1.85 kJ mm^{-1} and in shielded metal arc welding (SMAW) 1.5 kJ mm^{-1}, with an interpass temperature of 225 °C in each case. The maximum as–welded yield strength (YS) of the weld metal is reported to be 877 MPa (Table 6.3) and the Vickers hardness is stated to be in the range 300 to 350. The weld metals clearly have good mechanical properties and the creep rupture strength of the weld joint falls within the scatter band of the base metal at 500 °C, 600 °C and 650 °C [119].

One weld joint made using the Sumitomo welding electrode and the manual metal arc weld-

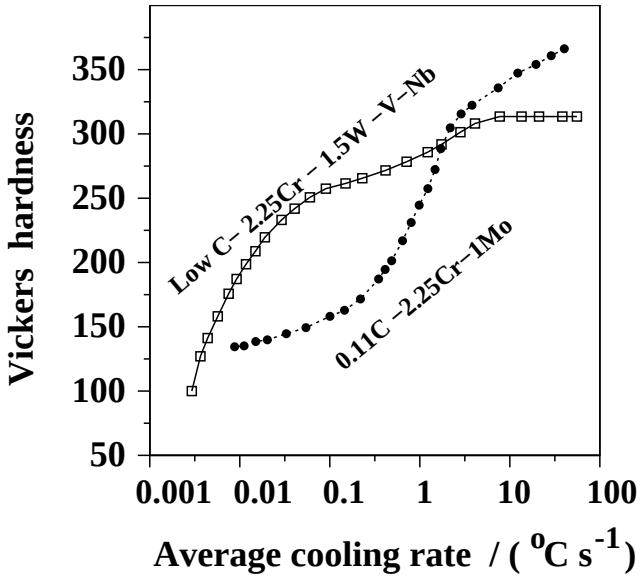

Figure 6.4: Hardness variation in $2\frac{1}{4}$Cr–1Mo and low C–$2\frac{1}{4}$Cr-1.56W-V-Nb steel cooled from the austenitisation temperature. The average cooling rate is that measured in the temperature range 800 °C and 300 °C. The $2\frac{1}{4}$Cr–1Mo steel is austenitised at 950 °C for 0.5 h and low C–$2\frac{1}{4}$Cr-1.56W-V-Nb is at 1050 °C for 0.5 h [121].

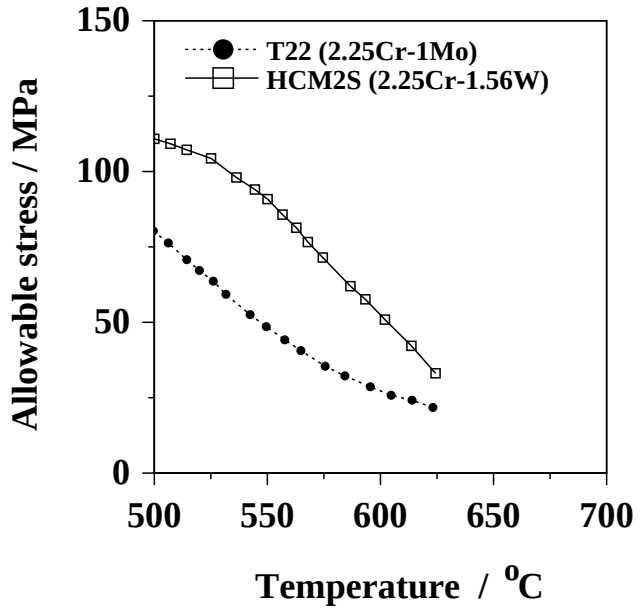

Figure 6.5: The allowable stresses in $2\frac{1}{4}$Cr–1Mo and HCM2S steels at different service temperatures [122].

ing process was provided by National Power, UK. The base plates joined in the process are both $2\frac{1}{4}$Cr–1Mo plates, as shown in Fig. 6.6. The microstructures are as expected, a banded

Process	C	Si	Mn	P	S	Ni	Cr	Mo	W	V	Nb	B	Al
GTAW	0.04	0.50	0.49	0.002	0.005	0.49	2.19	0.10	1.59	0.24	0.033	0.001	0.008
SMAW	0.06	0.41	0.80	0.004	0.002	0.99	2.25	0.10	1.58	0.32	0.040	0.001	—

Table 6.2: Chemical composition (in wt%) of as–deposited weld metal [119].

Process	PWHT	0.2% YS (MPa)	UTS(MPa)	Elongation (%)	Reduction in area (%)
GTAW	As–welded	775	856	20.8	82.2
SMAW	As–welded	877	978	19.8	50.2
SMAW	715 °C × 1h	623	755	21.0	72.0

Table 6.3: Mechanical properties of as–deposited metal [119].

structure in the base plates and a columnar prior austenite grain structure in the weld metal. There is also a clear heat–affected zone. The much more important point is that tests revealed a mean weld metal hardness of 338 HV, with values in the range 306–368 HV. This was considered unacceptable in the context of welding without post–weld heat treatment. Note that the hardness is less than that obtained in the as–welded condition for a $2\frac{1}{4}$Cr–1Mo weld metal (410 HV) but is not low enough to avoid post–weld heat treatment. The task therefore was to design a heat–resistant weld metal having an as–welded hardness less than 300 HV (preferably less than 250 HV).

6.2 Adaptation of Neural Network Weld–Database

A significant difficulty arose during the first attempts at designing the new tungsten–containing weld metal to meet the engineering requirements described above. The problem is illustrated in Fig. 6.7a which was calculated using the input variables described in Table 6.5, and an early version of the neural network model due to Cool *et al.* [27]. The figure shows that the addition of tungsten causes a decrease in the yield strength of the as–deposited weld. This is surprising, since the only role of tungsten in the as–deposited condition is to contribute to solid solution strengthening.

The difficulty arises because the original work [27] was based on a limited weld metal database which included alloys with tungsten, but only for the 9Cr–1Mo type metal. In that system, tungsten promotes the formation of δ–ferrite which weakens the microstructure [123]. The network has learnt this trend and in the absence of knowledge about the influence of tungsten on low–alloy steels, the network simply extrapolates the tungsten influence from the 9Cr–1Mo type alloys to the low–alloy weld metals.

There is, of course, no possibility of δ–ferrite in the final microstructure for the lean alloys considered here. This was verified here using phase diagram calculations [124]. The calculations

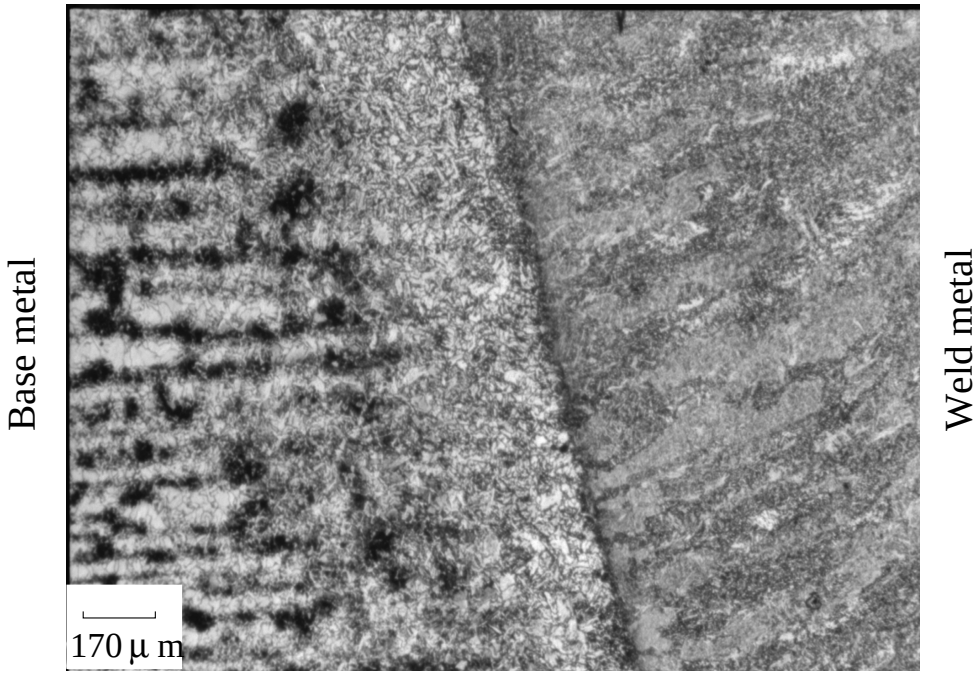

Figure 6.6: $2\frac{1}{4}$Cr-1Mo wt% steel welded using matching HCM2S electrode with manual metal arc welding process. The sample is etched using 2% nital.

show that δ–ferrite does not form in any of the compositions studied. It clearly is necessary to provide the network with knowledge about the role of tungsten in low–alloy steel weld metals. Unfortunately, there are no such data apart from the two welds made by Sumitomo Metal Industries. A procedure was therefore implemented to increase the necessary information in the database, as follows.

In research on fusion reactors, there is an intense effort to develop steels which are resistant to large fluxes of neutrons, particularly in the context of transmutations which lead to radioactive isotopes with large half–lives. There is a search for specific alloys whose radioactivity decays most rapidly once they are removed from the radioactive environment. These are the so–called *reduced activation* alloys which have minimal concentrations of Mo, Ni, Nb, Cu and nitrogen, all of which have long–lived radioactive isotopes [65, 125]. Some of these elements are key constituents of creep–resistant steels, but can be eliminated by using tungsten instead of molybdenum and by substituting vanadium and tantalum for niobium. Some examples of steels which have been studied specifically for their reduced activation are listed in Table 6.4.

There is, therefore, a considerable amount of data on low–alloy tungsten–containing steels in the literature. It was decided to adapt these data and integrate them into the weld metal

Steel	C	Si	Mn	Cr	V	W	Ta	B
$2\frac{1}{4}$Cr–V	0.1			2.25	0.25			
$2\frac{1}{4}$Cr–1WV	0.1			2.25	0.25	1		
$2\frac{1}{4}$Cr–2W	0.1			2.25		2		
$2\frac{1}{4}$Cr–2WV	0.1			2.25	0.25	2		
5Cr–2WV	0.1			5	0.25	2		
9Cr–2WV	0.1			9	0.25	2		
9Cr–2WVTa	0.1			9	0.25	2	0.07	
12Cr–2WV	0.1			12	0.25	2		
$2\frac{1}{4}$Cr–2WVTa	0.1	0.12	0.40	2.41	0.24	2.03	0.05	
$2\frac{1}{4}$Cr–2WVB	0.090	0.12	0.38	2.37	0.24	2.04		0.005
$2\frac{1}{4}$Cr–2WVTaB	0.093	0.12	0.38	2.36	0.24	2.04	0.05	0.005
2.6Cr–2WVTa	0.11	0.11	0.39	2.59	0.25	2.02	0.05	
2.6Cr–2WVTaB	0.11	0.11	0.39	2.60	0.25	2.07	0.05	0.004
$2\frac{1}{4}$Cr–2W	0.11	0.15	0.39	2.48		1.99		
$2\frac{1}{4}$Cr–2WV	0.11	0.20	0.42	2.41	0.24	1.98		
9Cr–2WVTa	0.10	0.23	0.43	8.72	0.23	2.09	0.07	

Table 6.4: Chemical compositions (wt%) of reduced–activation steels, Klueh *et al.* [65]. All of these steels are bainitic with the exception of the 9Cr and 12Cr steels which are martensitic. The chemical compositions of the first group of steels are nominal.

database, by artificially adding a concentration of 300 p.p.m. of oxygen, assuming an interpass temperature of 150 °C, and a heat input of 1.0 kJ mm^{-1}. These modifications all approximately represent average values for the manual metal arc welds. In this way, it was possible to supplement the weld metal database with 34 sets of data on $2\frac{1}{4}$Cr-W-V wrought steels [126, 127, 64]. The new neural network model created using this supplemented database gave trends in the strength of HCM2S which are far more realistic in terms of the trend as a function of the tungsten concentration, Fig. 6.7b.

6.3 Experimental Welds

The wrought $2\frac{1}{4}$Cr–W–V steel data collected from the literature are a minor contribution to the total data set (34 out of 2000). The data add value in the regime of low chromium steels containing tungsten. Nevertheless, the use of plate data to represent welds in the supplemented database left a sense of uncertainty. For this reason, it was decided that it would be useful to measure the mechanical properties of six experimental welds, designed using the neural network based on the supplemented database. The purpose was to see whether the modified network made useful predictions in the regime of interest. In any case, the new experimental data thus generated could be used to create the next generation of neural network models. Using the modified model, six welds were designed with systematic variations in the carbon and tungsten

Input variable	
C (wt%)	0.06
Si (wt%)	0.41
Mn (wt%)	0.87
S (wt%)	0.002
P (wt%)	0.004
Ni (wt%)	0.99
Cr (wt%)	2.01
Mo (wt%)	0.1
V (wt%)	0.27
Cu (wt%)	0.0
Co (wt%)	0.0
W (wt%)	1.52
Ti (wt%)	0.0
B (p.p.m.)	10
Nb (p.p.m.)	400
Heat input (kJ mm^{-1})	1.14
Interpass temperature(°C)	225
Tempering temperature (°C)	715
Tempering time(h)	1

Table 6.5: The input variables of 2.25Cr–1.56W–0.1Mo wt% (HCM2S) steel weld metal used in the analysis of previously developed model.

concentrations, in order to cover a wide range in the $2\frac{1}{4}$Cr–W class of compositions. The variations were around the HCM2S weld metal (Table 6.6).

The set of six experimental manual metal arc welds were made on our behalf and tested by Babcock Welding Products Ltd., UK using a heat input of 1.38 kJ mm^{-1}; the actual chemical compositions are listed in Table 6.7. The results are presented in Table 6.8 and in Fig. 6.8; the experimental data have been predicted to a remarkable degree of accuracy in all three aspects of the tensile test, justifying the use of the plate data within the large weld–database. Given this validation, the new experimental data were themselves incorporated into the plate–supplemented database and a final neural network model was created; this is the one described in detail in Chapter 4, and used in the design of a novel weld deposit for use in industry, as described in the next section.

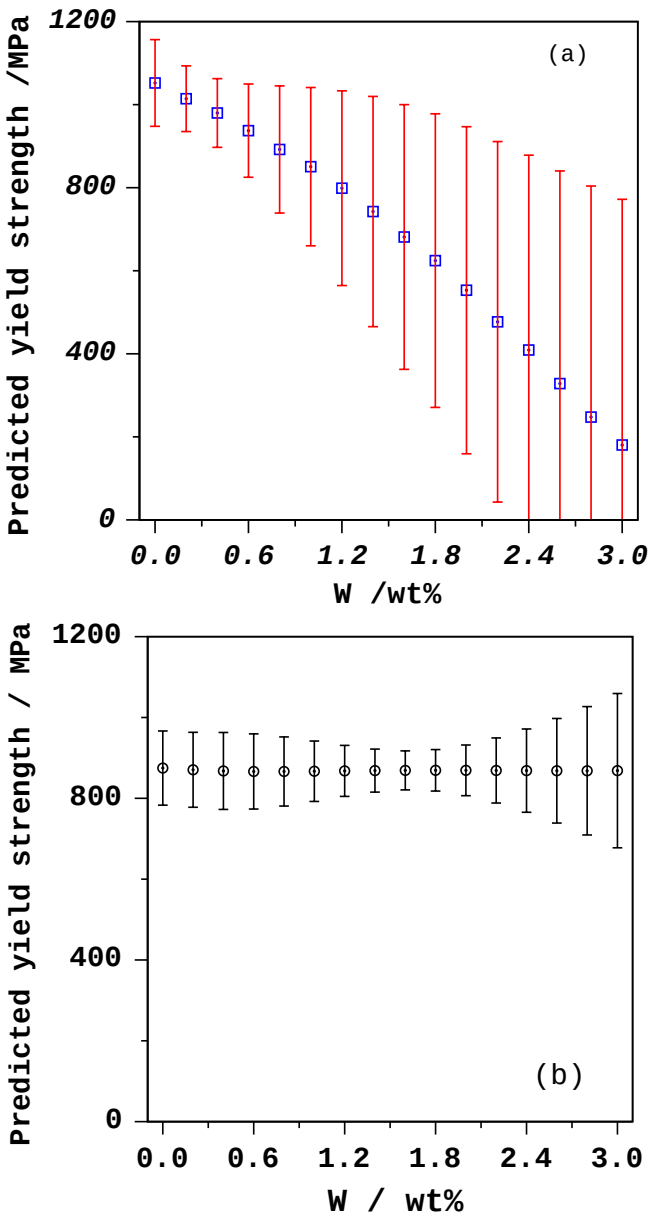

Figure 6.7: The variation in strength in $2\frac{1}{4}$Cr–1.56W–0.1Mo wt% (HCM2S) weld metal in the as–deposited condition, a) using published model [27] b) using the model developed including wrought plate data.

6.4 Theoretical Design of New Weld Metal

The main task was to design a heat–resistant weld metal with hardness consistently lower than 300 HV. Since the neural network model predicts strength rather than hardness, it is necessary to convert between these two variables. The hardness can be estimated as a function of the yield

Variable	Weld 1	Weld 2	Weld 3	Weld 4	Weld 5	Weld 6
C (wt%)	0.06	0.06	0.06	0.10	0.10	0.10
Si (wt%)	0.3–0.4	0.3–0.4	0.3–0.4	0.3–0.4	0.3–0.4	0.3–0.4
Mn (wt%)	0.6	0.6	0.6	0.6	0.6	0.6
S (wt%)	0.005–0.01	0.005–0.01	0.005–0.01	0.005–0.01	0.005–0.01	0.005–0.01
P (wt%)	0.005–0.01	0.005–0.01	0.005–0.01	0.005–0.01	0.005–0.01	0.005–0.01
Cr (wt%)	2.1–2.4	2.1–2.4	2.1–2.4	2.1–2.4	2.1–2.4	2.1–2.4
Mo(wt%)	≤ 0.1	≤ 0.1	≤ 0.1	≤ 0.1	≤ 0.1	≤ 0.1
Ni (wt%)	1.0	1.0	1.0	1.0	1.0	1.0
B (p.p.m.)	10	10	10	10	10	10
O (p.p.m.)	300	300	300	300	300	300
N (p.p.m.)	80	80	80	80	80	80
Nb (p.p.m.)	400	400	400	400	400	400
V (wt%)	0.25	0.25	0.25	0.25	0.25	0.25
W(wt%)	0.5	1.0	1.5	0.5	1.0	1.5

Table 6.6: The designed weld metals with variations in carbon and tungsten.

Variable	Weld 1	Weld 2	Weld 3	Weld 4	Weld 5	Weld 6
C (wt%)	0.053	0.059	0.059	0.11	0.10	0.10
Si (wt%)	0.27	0.32	0.34	0.40	0.39	0.4
Mn (wt%)	0.6	0.68	0.7	0.72	0.72	0.76
S (wt%)	0.007	0.007	0.006	0.006	0.006	0.007
P (wt%)	0.010	0.012	0.012	0.012	0.012	0.012
Cr (wt%)	2.22	2.22	2.29	2.26	2.31	2.35
Mo (wt%)	0.04	0.04	0.04	0.04	0.04	0.04
Ni (wt%)	0.99	0.97	1.03	0.98	0.99	0.99
B (p.p.m.)	≤ 10	≤ 10	≤ 10	≤ 10	≤ 10	≤ 10
O (p.p.m.)	550	550	550	550	550	550
N (p.p.m.)	180	160	130	130	130	140
Nb (p.p.m.)	300	400	400	500	500	500
V(wt%)	0.20	0.22	0.23	0.23	0.23	0.24
W (wt%)	0.5	1.01	1.48	0.5	1.02	1.54

Table 6.7: Experimental weld metals made with heat input 1.38 kJ mm^{-1} and interpass temperature of 300–350 °C.

strength as follows [128]:

$$\text{Yield strength} \cong \frac{\text{Vickers Hardness}}{3} \times 9.81 \qquad \text{(MPa)} \tag{6.1}$$

The base composition for the new weld metal is similar to that of HCM2S steel but with certain key modifications, Table 6.2. To avoid excessive hardness in the as–welded condition, the carbon concentration has been restricted to a maximum of 0.05 wt%. HCM2S steel contains

Property	Predicted Weld 1	Measured Weld 1	Predicted Weld 2	Measured Weld 2
YS (MPa)	796 ± 88	705	838± 77	842
UTS (MPa)	851 ± 79	844	905 ± 76	899
Elongation (%)	20 ± 8	19	21 ± 8	21
	Weld 3	**Weld 3**	**Weld 4**	**Weld 4**
YS(MPa)	853 ± 57	804	891 ± 105	893
UTS (MPa)	930 ±64	924	1001 ± 148	1048
Elongation (%)	30 ± 11	30	22± 9	22
	Weld 5	**Weld 5**	**Weld 6**	**Weld 6**
YS (MPa)	895 ± 95	828	913 ± 72	922
UTS (MPa)	1006 ± 136	1085	1031 ± 135	1155
Elongation(%)	21 ± 9	21	21 ± 11	21

Table 6.8: The predicted and measured values for the experimental as-welded metals.

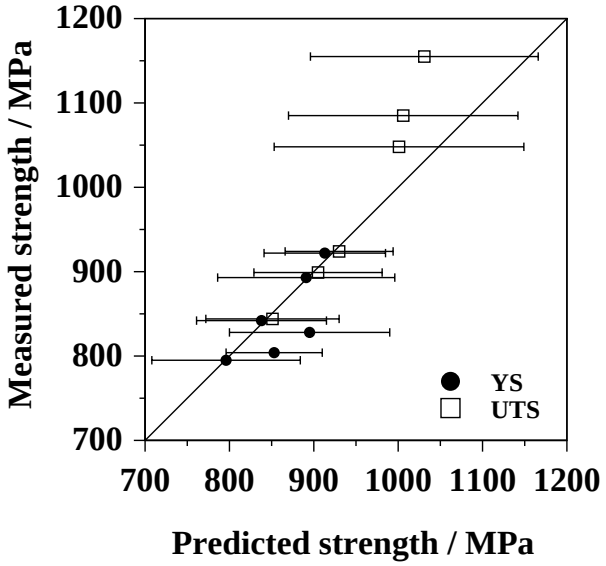

Figure 6.8: Comparison between predicted and measured strengths of designed experimental welds. The error bars represent the predicted range.

400 p.p.m. of niobium, but the literature [129, 29] suggests that niobium is harmful in the context of low–alloy steel welds because it leads to a deterioration in the toughness. A number of mechanisms have been proposed for the effect of niobium; for example, it may cause precipitation hardening, increase the yield strength and hence reduce the toughness. However, there are quite contradictory reports on its influence on microstructure, particularly in altering the balance between acicular ferrite and bainite. None of these effects are well–established, but the experimental evidence regarding toughness is clear. Therefore, it was decided to avoid niobium altogether. It will be seen later that MX type precipitates probably contribute to the creep

strength of HCM2S, but the steel also contains a larger fraction of vanadium carbonitrides. The omission of niobium was therefore judged not to be of critical importance in the design of the weld metal. It turned out in practice that it was not possible to completely avoid niobium because of the commercial purity raw materials used for the welding consumable manufactured as a consequence of the work presented in this Chapter.

Vanadium in steels forms stable V_4C_3 carbides which are beneficial in the context of creep; vanadium is therefore a key element in the proposed weld metal.

Recent work has suggested that a reduction in the manganese concentration can lead to an improvement in creep strength [120]. A reduction in the manganese concentration in HCM2S slows down M_6C precipitation, which contains tungsten as the major metallic element. Thus, a lower manganese concentration allows tungsten to remain dissolved in ferrite and strengthen the solid solution. However, in shielded metal arc welding, around 0.6 wt% manganese is essential as a deoxidising element and to ensure good weldability. In manual metal arc welding, manganese and silicon assist the formation of a fluid slag at low melting temperature, thus preventing slag inclusions in the weld metal. Boron is beneficial in increasing the creep life [120]. It stabilises $M_{23}(C,B)_6$ precipitates along grain boundaries, thereby preventing the recrystallisation of grains during service at high temperatures. However, it is also a difficult element to control during its transfer across the welding arc; the weld metal design therefore does not rely on boron which is set at a trace concentration of 10 p.p.m. The ideal composition that emerged after careful analysis of the role of each of the chemical constituents using the final neural network models described in detail in Chapter 3, and in the light of experience from physical metallurgy, is given in Table 6.9. The table also includes a set of tolerances which were arrived at by discussion with manufacturing industry.

The error bars presented in Table 6.9, however, refer to the mean composition only. It must be emphasised that the error bars consist of two components (Chapter 3), one describing the perceived level of experimental noise ($\sigma_\nu \simeq \pm 0.048$), and the other reflecting the uncertainty in fitting a function within a local region of the input space. This latter error will necessarily be large when dealing with novel alloys not available at the time of the creation of the neural network model. The magnitude of this fitting error gives a warning that the model is being used in extrapolation or in a region where there is a lack of knowledge, but the mean prediction may nevertheless be reliable if the proper functional form has been recognised in the region covered by data. The hardness values were calculated using equation 6.1.

6.4.1 Creep Rupture Strength

Cole *et al.* [130] have developed a comprehensive neural network model which permits the estimation of the creep rupture strength of ferritic steels as a function of the detailed chemical

Input variable	
C (wt%)	0.05 ± 0.02
Si (wt%)	0.30 ± 0.15
Mn (wt%)	0.70 ± 0.15
S (wt%)	0.007
P (wt%)	0.010
Ni (wt%)	≤ 0.05
Cr (wt%)	2.22 ± 0.2
Mo (wt%)	0.20 ± 0.1
V (wt%)	0.20 ± 0.005
Cu (wt%)	0.03
Co (wt%)	0.0
W (wt%)	0.6 ± 0.1
O (p.p.m.)	300
Ti (wt%)	250 ± 50
B (p.p.m.)	10 ± 5
Nb (p.p.m.)	50 ± 10
Heat input (kJ mm^{-1})	1.38
Interpass temperature (°C)	300
Tempering temperature (°C)	20
Tempering time (h)	0
Estimated YS (MPa)	714 ± 216
Estimated UTS (MPa)	851 ± 112
Estimated elongation (%)	19 ± 15
Estimated Vickers hardness	225

Table 6.9: The designed input variables of 2.25Cr–0.56W–0.2Mo wt% (HCM2S) as–welded metal.

composition and a set of up to three separate heat treatments. Furthermore, it has been demonstrated that by assuming a selected austenitisation heat treatment, the model can be used to estimate the creep rupture life of weld deposits even though the neural network has no prior knowledge of welds.

It would obviously be useful to be able to estimate the creep rupture life of the new weld described in Table 6.9. However, Cole's model suffers from the same problem as encountered here, that there are virtually no data on the creep of low chromium, tungsten–containing steels. There are plenty of data on 9Cr–1Mo type alloys with tungsten, but the metallurgy of tungsten in those alloys is different for the reasons described previously. In view of the lack of low–Cr data, it would be useful to study the behaviour of the Cole model with respect to four experimental

data that exist for the Sumitomo Metal Industries welding alloys described in [119]. Fig. 6.9a shows that the actual creep rupture stress is greatly overestimated; that this is due to the lack of appropriate knowledge in the Cole model can be proved by repeating the calculation whilst setting the tungsten concentration to zero, as illustrated in Fig. 6.9b, which shows that the experimental data are well–predicted. The importance of the latter result is that it should be possible to estimate the creep rupture life of the proposed new weld (Table 6.9), simply by ignoring the fact that it contains a small concentration of tungsten. The results are illustrated in Fig. 6.10, which shows that the long–term creep rupture strength of the new welding alloy should be comparable to that of HCM2S tube.

6.5 New Welding Alloy: Experimental Results

The new welding alloy was manufactured by Mitsui Babcock Welding Products Ltd., UK and Table 6.10 shows a comparison between what was proposed and what was achieved in practice. The table also shows that the theoretical design procedure has been very successful in predicting the mechanical properties; the electrode is now marketed with the commercial designation BWPL (Babcock Welding Products Ltd.) J–type electrode. It is intended to market this both for power plant boiler components and for other applications where welding can be conducted without the need for post–weld heat treatment. Microstructural studies of the new alloy will be described in Chapter 7.

6.6 Conclusions

The series of neural network models created in this work have been used, along with metallurgical experience, to create a new welding alloy which is now available on a commercial scale. The entire design process, including the creation of the models, took less than two years and was successful at the first attempt. The models can now be used to develop new electrodes over much shorter time scales. There are also some lessons learnt about the neural network method, in particular how the database can be "manipulated" for specific purposes. The models themselves can be manipulated to reduce uncertainties, as illustrated with the estimation of creep rupture life for the new alloy. The design example presented here is but one of the success stories of the present work – some other examples are listed in Appendix B.

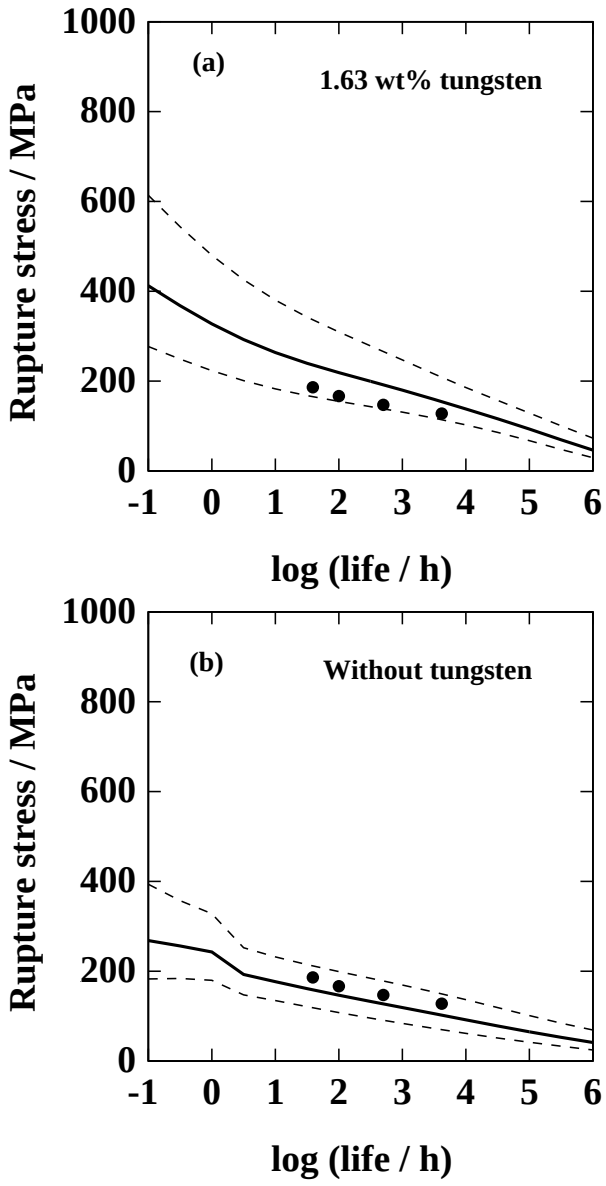

Figure 6.9: Effect of tungsten on the calculated creep strength of 0.062C–0.1Mn–2.27Cr–0.026V–0.05Nb wt% weld metal, using a published model [130]. The measured points are for 1.63 wt% tungsten from literature [120].

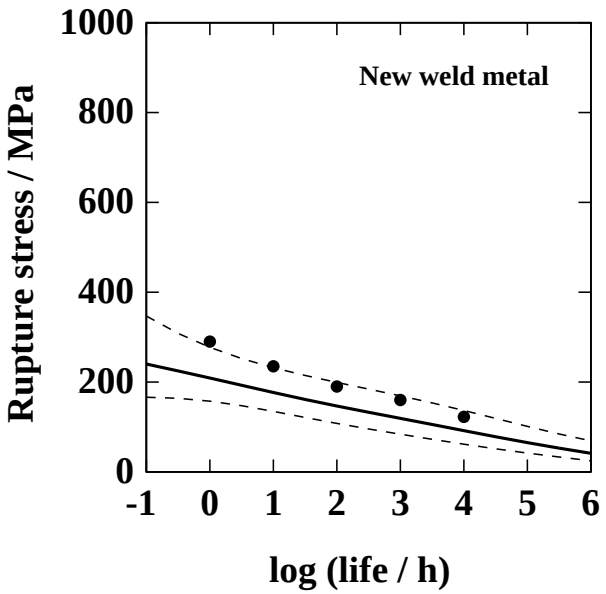

Figure 6.10: Calculated creep strength of designed weld metal (with 0.1 wt% manganese) using a published neural network model [130]. The points are for HCM2S steel tube creep data are extracted from published literature [131].

Input variable	**Proposed**	**Actual**
C (wt%)	0.05 ± 0.02	0.057
Si (wt%)	0.30 ± 0.15	0.32
Mn (wt%)	0.70 ± 0.15	0.67
S (wt%)	0.007	0.005
P (wt%)	0.010	0.009
Ni (wt%)	≤ 0.05	0.07
Cr (wt%)	2.22 ± 0.2	2.10
Mo (wt%)	0.20 ± 0.1	0.20
V (wt%)	0.20 ± 0.005	0.20
Cu (wt%)	0.03	≤ 0.02
Co (wt%)	0.0	0.0
W (wt%)	0.6 ± 0.1	0.63
O (p.p.m.)	300	≤ 0.02
Ti (wt%)	250 ± 50	≤ 200
B (p.p.m.)	10 ± 5	≤ 20
Nb (p.p.m.)	50 ± 10	≤ 200
Heat input(kJ mm^{-1})	1.38	1.35
Interpass temperature ($^{\circ}$C)	300	350 (max.)
Tempering temperature ($^{\circ}$C)	20	**as–welded**
Tempering time (h)	0	-
YS (MPa)	714 ± 216	678
UTS(MPa)	851 ± 112	774
Elongation(%)	19 ± 15	19.5
Vickers hardness	225	228

Table 6.10: Comparison between the proposed and experimental results of new weld metal.

Chapter 7

Tempering Resistance

7.1 Introduction

It was demonstrated in the last chapter that the weld metal designed using the neural network models and the general principles of physical metallurgy achieved the properties demanded by industry. The material is intended primarily for use in the welding of boiler components in large power plant. As such, the service temperature is likely to be in the range 500–600 °C. The weld metal is therefore likely to temper during service. It would be interesting therefore to examine experimentally the tempering resistance of the new weld metal and to compare it with HCM2S tube steel.

At the same time, two further experimental welds were made for this work, using the manual metal arc welding process at ESAB AB (Sweden). Neither both of these contained vanadium or niobium as deliberate additions, but were conceived to reveal the effect of substituting tungsten for molybdenum in a classical $2\frac{1}{4}$Cr–1Mo weld metal. They also contained a low carbon concentration consistent with the HCM2S philosophy.

The compositions of the three alloys and the new weld metal discussed in Chapter 6 are listed in Table 7.1. It is worth noting that the atomic concentration of tungsten in the Cr–W alloy is almost identical to the atomic concentration of molybdenum in the Cr–Mo alloy, the atomic weight of tungsten is much higher than that of molybdenum.

Phase diagram calculations were carried out using MTDATA [124] with the SGTE Steels database to reveal the equilibrium precipitates to be expected at 500 and 600 °C. MTDATA works by accessing thermodynamic data from the SGTE database in order to use solution models and minimise the free energy of the system to find the equilibrium states. In all cases, the calculations allowed for the existence of Laves phase, chromium carbides, vanadium carbides, α-ferrite, M_3C, M_7C_3, M_6C, $M_{23}C_6$, MC phases and the following components: Fe, C, Mn, Si, Cr, Mn, Mo, Ni, N, Nb, V, W and Ti.

The results are listed in Table 7.2, but more details will be presented during the discussion of

the experimental data. It is evident at this stage that there are significant differences between the equilibrium states of the four alloys and when the two tempering temperatures are compared. These results will be compared against actual tempering experiments later in this Chapter. Because of the time taken in designing the new weld metal, it was not possible to study its tempering behaviour for 500 °C.

	C	Si	Mn	P	S	Ni	Cr	Mo	W	V	Nb	B	N
HCM2S	0.060	0.20	0.47	0.006	0.002	0.10	2.27	0.09	1.50	0.23	0.05	0.004	0.008
Cr–W	0.073	0.38	0.74	0.011	0.011	0.04	2.11	0.01	1.99	0.016	-	-	0.02
Cr–Mo	0.068	0.38	0.74	0.010	0.011	0.06	2.11	0.93	0.01	0.021	-	-	0.02
New WM	0.057	0.32	0.67	0.010	0.007	0.10	2.10	0.2	0.63	0.20	$\leq$ 0.02	$\leq$0.002	0.015

Table 7.1: Chemical composition (in wt%) of HCM2S steel [119, 117] and low–alloy Cr–Mo, Cr–W weld metals and designed new weld metal (New WM).

	500 °C	**600** °C
Cr–Mo Weld metal	$M_{23}C_6$, VN, Cr_2N	$M_{23}C_6$, Cr_2N
Cr–W Weld metal	$M_{23}C_6$, M_6C, Cr_2N	M_7C_3, M_6C, Cr_2N
HCM2S Steel	M_6C, VN, (Nb,V)C	M_6C, CrNbC, V_4C_3
New weld metal	$M_{23}C_6$, M_6C, V(C,N), CrNbC	M_7C_3, $M_{23}C_6$, M_6C, CrVTiN

Table 7.2: Calculated equilibrium precipitates, calculated using MTDATA [124].

7.2 Experimental Procedure

Various experimental techniques were employed to understand and evaluate the tempering resistance of these alloys.

7.2.1 Heat Treatment

The HCM2S was received in the form of tubes which had been heat treated at 1050 °C for 1 h followed by air cooling to generate a bainitic microstructure, which was in turn tempered at 770 °C for 1 h. This is the standard commercial heat–treatment prior to service. The weld metals were all produced using the manual metal arc welding process with 4 mm diameter electrodes, as "bead–on–plate" deposits on mild steel plate. Each deposit was 4 cm thick and consisted of seven layers so that dilution effects essentially disappeared after the first layer. All samples were machined avoiding the first layer. For heat–treatment purposes, the samples were machined as $8 \times 8 \times 10$ mm square–sectioned rods, which were then sealed in quartz tubes filled with a partial pressure of argon. To ensure a consistent starting microstructure, each sample,

irrespective of alloy type, was heated to 1100 °C for 10 min; the sealed sample was then quenched in water whilst breaking the quartz tubes. The samples were then sealed again in quartz tubes for prolonged tempering at either 500 or 600 °C. The heat–treatment procedure is illustrated in Fig. 7.1.

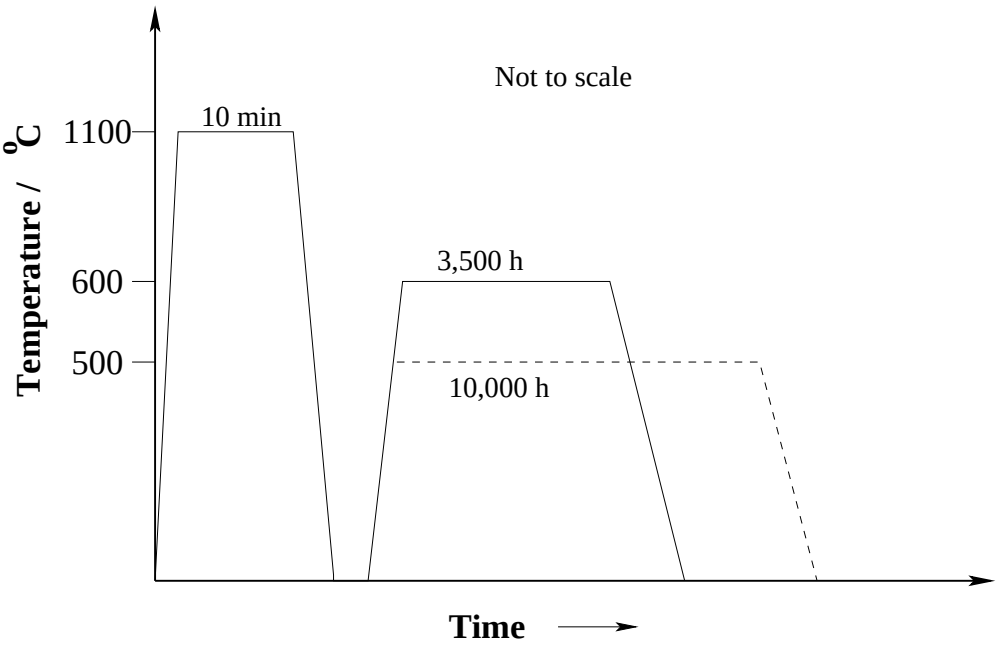

Figure 7.1: The heat treatment cycle followed in the present work.

7.2.2 Hardness Measurements

A Vickers hardness testing machine with 10 kg load and $\frac{2}{3}''$ objective was used to measure the macrohardness of the steel samples. The load was applied for 15 seconds during testing. Ten measurements were taken diagonally covering the whole sample surface. The samples were mounted on conductive Bakelite, then ground to 600 grit paper before testing.

7.2.3 Optical Microscopy

All samples were prepared for microstructural examination by hot mounting in conductive Bakelite powder, followed by grinding upto 1200 grit, then diamond polished to 1 μm. A 2% nital etchant(2% concentrated nitric acid in methanol solution) was used to etch the samples.

7.2.4 Scanning Electron Microscopy

A JEOL JSM 820 scanning electron microscope (SEM) was used to view the etched samples prepared as described in Section 7.2.3.

7.2.5 Transmission Electron Microscopy

For transmission electron microscopy (TEM) examination, thin foil and extraction carbon replicas were used.

Camera Constant

A TEM consists of electromagnetic lenses which amongst other things control the magnification of the diffraction patterns. The magnification of diffraction patterns in a TEM is expressed as a camera length, as shown in Fig. 7.2.
The camera constant is expressed as;

$$Rd_{hkl} = L\lambda = \text{Camera constant} \tag{7.1}$$

where R is the real distance between the transmitted spot and the diffracted spot, L is the camera length, d_{hkl} is the spacing of the $\{hkl\}$ crystallographic planes and λ is calculated using the following equation:

$$\lambda = \frac{h}{\sqrt{2meV(1 + \frac{eV}{2mc^2})}} \qquad (\text{Å}) \tag{7.2}$$

where h is Plank's constant, m and e are the electron mass and charge respectively, V is the accelerating voltage of the electrons and c is the speed of light in vacuum.

The camera constant was measured by examination of the diffraction pattern from sputtered gold on a copper grid at 200 kV on JEOL 200CX TEM. For a given electron beam direction a number of particles are oriented so as to satisfy the Bragg equation [132] hence each plane gives a number of reflections lying in a cone of angle 4θ. The final diffraction pattern contains a number of concentric rings corresponding to the $\{hkl\}$ planes which are diffracting, Fig 7.3.

To calculate the camera constant the diameters of the rings in the diffraction pattern were measured, then the ratio of the squares of the radii of the outer rings to those of the first or second low–index ring were calculated. This enables the N values corresponding to each of the rings to be found using equation 7.3.

$$N^2 = h^2 + k^2 + l^2 \tag{7.3}$$

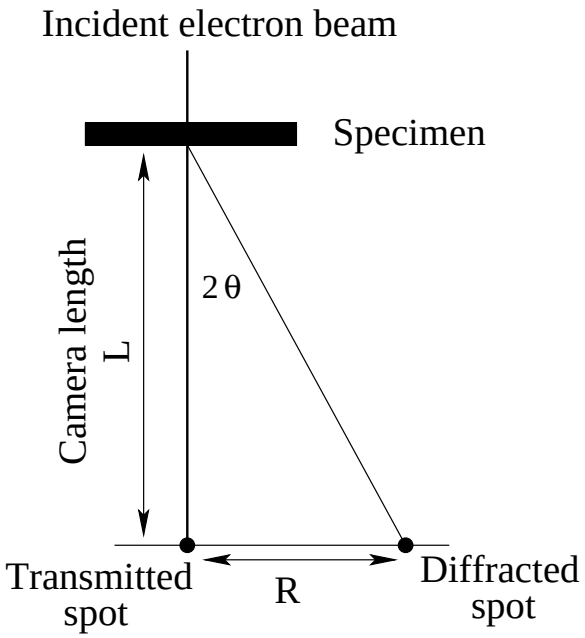

Figure 7.2: Schematic diagram showing the magnification of a diffraction pattern by electron microscopic lenses.

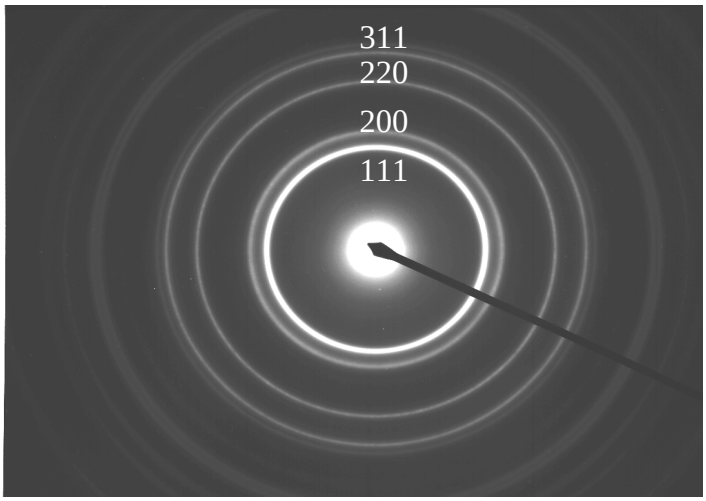

Figure 7.3: Diffraction pattern from the sputtered gold film used to determine the camera constant at 137 cm camera length (L) and 200 kV.

where *h, k and l* are the plane indices. Then *d*–spacings were calculated using equation 7.4 for cubic systems.

$$d = \frac{a}{\sqrt{N}} \tag{7.4}$$

The accurate lattice parameter (a) of gold is 4.0780 Å [133] and the calculated d–spacings are shown in Table 7.3. The calculated camera constants at different camera lengths at 200 kV are shown in Table 7.4.

Precipitates were identified using selected area electron diffraction. Convergent beam electron diffraction technique was used for very small particles.

Ring	Lattice spacing (d) in Å
1	2.355
2	2.039
3	1.442
4	1.230
5	1.177
6	1.096
7	0.935
8	0.912
9	0.832

Table 7.3: The calculated d–spacing in gold.

Camera length / cm	Calculated camera constant / 10^{-12} m^2
82	2.00
137	3.36
205	5.18

Table 7.4: Calculated camera constants for a number of different camera lengths at electron accelerating voltage of 200 kV.

Thin Foils

Thin samples were sliced using a high–speed SiC cutting wheel and 3 mm diameter discs were punched from these slices. The discs were ground to 50 μm by hand on 1000 grit paper. The thinned discs were then electropolished using a twin–jet electropolisher at 45 V. The electropolishing solution used was 5% perchloric acid, 20% glycerol in alcohol. A JEOL 200CX transmission electron microscope was used to examine thin foils.

Carbon Replicas

Carbon replicas can be more useful than thin foils in the identification of precipitates. Carbon replicas eliminate magnetic effects due to the ferrite matrix and enable a large area to be examined. The procedure followed to extract the replicas from surfaces prepared using optical microscopy is shown in Fig. 7.4. Carbon was deposited in a vacuum of 10^{-5} torr on to the etched sample. Then the deposited carbon layer on the sample surface was cut into 2 mm square pieces to enable the removal of several small sections covering the whole area of the sample. Then the film was detached from the sample by electrolytic etching in a solution 5% hydrochloric acid in methanol at 1.5 volts. Each replica was washed in methanol and then in distilled water. Finally the floating replicas in distilled water were collected on 400 square mesh copper grids for examination in the transmission electron microscope.

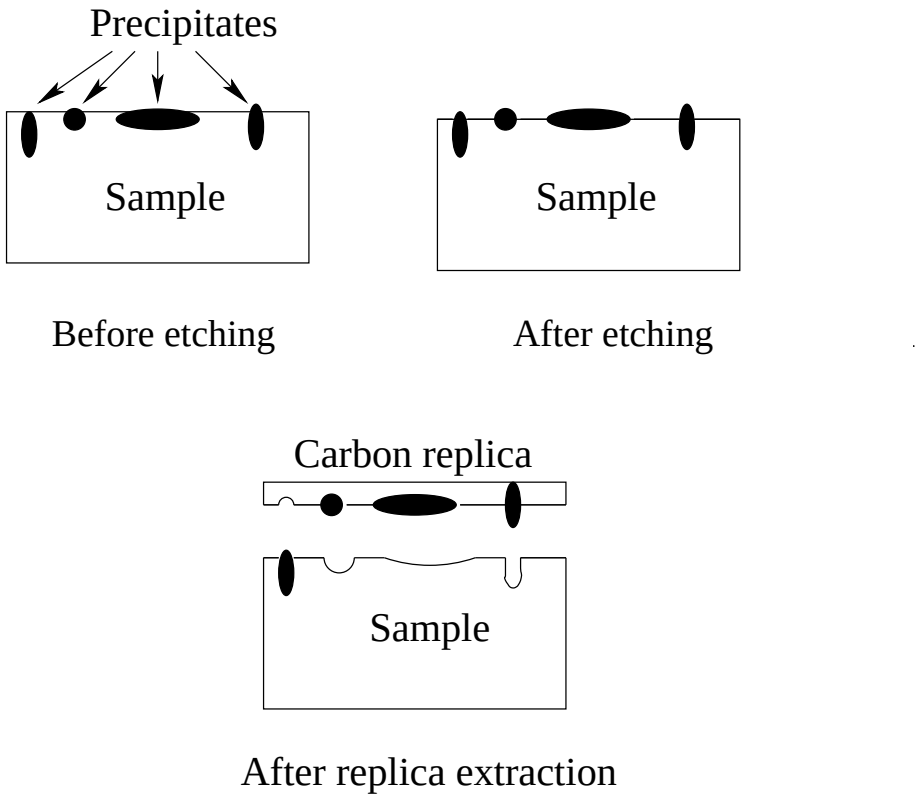

Figure 7.4: Schematic diagram illustrating the preparation of carbon replicas.

7.2.6 Analysis of Electron Diffraction Patterns

An electron diffraction pattern is essentially a planar section of the reciprocal lattice, each reciprocal lattice vector lying along the normal to a plane and of magnitude equal to the inverse

of the interplanar spacing. Thus, the distance of each diffracted spot from the central beam is inversely proportional to the spacing of the planes that it represents. The angle between a pair of reciprocal lattice vectors represents the angle between the normals to those planes. The geometry of the electron diffraction pattern in a transmission electron microscope is illustrated in Fig. 7.2.

As can be seen from the list of crystal structures presented in Table 7.5, many of the structures are not cubic and are complicated in detail. This makes it quite difficult to interpret the patterns, since plane normals and directions with the same indices are then not necessarily parallel. The problem can be ameliorated by using a computer program [134, 135] which deals with the analysis of the patterns for any crystal structure. Data from the diffraction pattern are fed into the program, together with an estimate of measurement accuracy and a trial crystal structure. The program then searches the reciprocal space to find zone axes which are consistent with the pattern. However, the number of trial crystal structures is very large in the present work. Therefore, a new modified program was created, so that it is no longer necessary to input a trial structure, but instead, a list of possible trial structures is read by the program. The program then searches through the entire set to find matches with the experimental data. This proved vital because many of the electron diffraction patterns were found to be ambiguous with respect to the precipitate phase. In those circumstances, it was found that the intensities of the diffraction spots could be compared with standard X–ray tables to reduce or eliminate ambiguities. Intensities, take into account the structure factor which the computer program described above does not (it only has systematic absences, such as those differentiating the primitive cubic and body–centered cubic lattices). Information about the computer programs is presented in Section B.3.

7.2.7 X–ray Diffraction

Bulk precipitates were extracted from bulk samples by electrolyticaly dissolving the matrix in 5% hydrochloric acid in methanol solution at 1.5 V. The specimen was made the anode and platinum the cathode. After 5–6 h the anodic sample dissolved in the electrolyte, leaving the precipitates which were filtered on filter paper containing 1 μ pores, washing throughly during filtration with methanol. X–ray diffraction of the extracted particles was used for the identification of various precipitates formed during tempering. A Siemens D500 diffractometer (CuK_α target) was used to scan between 20° and 140° θ at a step size of 0.04° for 10 seconds. The diffraction peak positions were located using Phillips Analytical software, which was also used to calculate the associated intensities of the peaks. X–ray diffraction was used as verification of the precipitates identified using electron diffraction analysis.

Precipitate	Crystallographic system	Lattice parameter(s) in Å	Reference
M_3C	Orthorhombic	a=4.525, b=5.087, c=6.743	[116]
M_7C_3	Orthorhombic	a=4.526, b=7.01, c=12.142	[116]
M_2C	Hexagonal	a=2.888, c=4.559	31–0403 [136]
M_6C	Cubic	a=11.082	[116]
$M_{23}C_6$	Cubic	a=10.621	[116]
NbC	Cubic	a=4.4702	10–181 [136]
Nb_4N_3	Tetragonal	a=4.382, c=8.632	20–0803 [136]
VN	Cubic	a=4.09	25–1252 [136]
VC	Cubic	a=4.3	74–1220 [136]
V_4C_3	Cubic	a=4.16	1–1159 [136]
WC	Hexagonal	a=2.9062, c=2.83	25–1047 [136]
W_2C	Hexagonal	a=2.99, c=4.72	2–1134 [136]
CrNbN	Tetragonal	a=3.037, c=7.391	25–0591 [136]

Table 7.5: The crystallographic data used to identify the selected precipitates in electron diffraction pattern. Numbers in reference column indicate X–ray data card number.

7.3 Comparison of Cr–W and Cr–Mo Weld Deposits

The hardness data from tempering experiments at 500 °C, for time periods up to 11,000 h, are presented in Fig. 7.5, along with hardness curves obtained using neural network models fitted with the experimental data in Fig. 7.6 and 7.7. Both alloys show a significant resistance to tempering when compared with a plain carbon steel of the same carbon concentration, Fig. 7.5. This must be due to secondary hardening. Secondary hardening is associated with the formation of carbides during tempering of water quenched material containing strong carbide forming elements such as Cr,V, Mo, Nb, etc.

The initial and final hardnesses are not very different in these materials, but the peak hardness attained is important. Transmission electron microscopy and electron diffraction revealed that a key difference between the alloys is the presence of M_2X in the Cr–Mo alloy, Fig. 7.13. Some electron diffraction patterns and TEM micrographs are provided in Figs 7.8 to 7.16. In molybdenum–containing steels, Mo_2C is an important precipitation strengthening carbide [23]. It commonly precipitates as fine needles (Fig. 7.13) parallel to the $< 110 >_\alpha$ direction in ferrite. The orientation relationship is that of Pitsch–Schrader [137]:

$$(011)_\alpha \parallel (0001)_{M_2C},\ [100]_\alpha \parallel [11\bar{2}0]_{M_2C}$$

This Mo_2C is a key strengthening phase in Cr–Mo weld metal, and indeed, is responsible for the secondary hardening peak as illustrated in Fig 7.5. In multirun welding secondary hardening

causes an increase in the hardness in the reheated regions, which is not desirable in keeping the as–welded hardness low. Tungsten is beneficial in this respect because it does not harden the microstructure during reheating in multirun welding [138, 139]. Figs 7.6 and 7.7 illustrate the hardness variation with tempering time as measured and smoothed using neural network representation. Here the neural networks helped to visualise the trends in hardness.

The hardness of the tungsten–containing alloy begins to drop abruptly beyond about 90 h at temperature whereas that of the Cr–Mo alloy is maintained to some 256 h. The precipitates identified are tabulated in Table 7.7. To summarise, the main consequences of the substitution of tungsten for molybdenum in this class of steels are as follows:

a. M_2X precipitation only occurs in the molybdenum–containing alloy; since this is a significant strengthening precipitate, the tempering resistance of molybdenum–containing steel is expected and found to be larger.

b. Tungsten has a high solubility in M_6C; therefore, $M_6C$is an equilibrium phase in the Cr–W alloy but not in the Cr–Mo alloy, Table 7.6. Furthermore, the precipitation of $M_{23}C_6$is accelerated in the Cr–W alloy. Robson and Bhadeshia [140] have demonstrated both theoretically and experimentally that the large volume fractions of metastable M_2X and M_7C_3, which form prior to $M_{23}C_6$, deplete the matrix and therefore suppress $M_{23}C_6$ precipitation [140]. This does not happen in the Cr–W system, where $M_{23}C_6$is obtained more rapidly. $M_{23}C_6$is not very effective as a hardening precipitate in low–alloy steels [23].

c. It is interesting to note that precipitation in the Cr–W alloy effectively removes almost all the tungsten from solid solution, Table 7.6 . The main role of tungsten, in the long term, is therefore to form M_6C.

7.4 Comparison of HCM2S and New Welding Alloy

The new weld metal and HCM2S steel were subjected to austenitisation at 1100 °C, followed by water quenching and then tempered at 600 °C. The results are shown in Fig. 7.17 and TEM micrographs of HCM2S steel and the new weld metal are provided in Figs 7.19 to 7.27. The new weld metal is softer than HCM2S steel by around 50 HV. The precipitates found in these materials are shown in Table 7.8 and corresponding constituents of each equilibrium precipitate are given in Table 7.9. The softness of the new weld metal can be explained that the HCM2S steel contains V_4C_3 as a thermodynamically stable precipitate, whereas it is a metastable precipitate in the new weld metal. In addition, HCM2S has the CrNb nitride. Furthermore, HCM2S has a higher tungsten content. Fine precipitates were found in HCM2S steel (Fig. 7.19a) after 4 h and 3,500 h (Fig. 7.21) of tempering, whereas in the new weld metal coarse precipitates were

	Cr-W weld metal			Cr-Mo weld metal		HCM2S steel		
Total number of moles	1784.0			1801.0		1783.0		
	Cr_2N	$M_{23}C_6$	M_6C	Cr_2N	$M_{23}C_6$	(Nb,V)C	VN	M_6C
Amount in moles	4.37	12.1	**24.72**	3.4	27.3	2.65	1.8	**20.28**
Element (mole fraction)								
Fe	0.001	0.15	0.45	0.001	0.169	0.0	0.0	0.38
C	0.11	0.21	0.14	0.003	0.21	0.27	0.015	0.14
Cr	0.58	0.56	0.006	0.60	0.52	0.001	0.085	0.006
Mn	0.007	0.082	0.0	0.011	0.0	0.0	0.001	0.0
N	0.32	0.0	0.0	0.33	0.0	0.0	0.32	0.0
W	0.015	0.0	**0.40**	0.0	0.0	0.01	0.001	**0.35**
Mo	0.0	0.0	0.0	0.04	0.10	0.0	0.0	0.05
V	-	-	-	-	-	0.36	0.58	0.075
Nb	-	-	-	-	-	0.15	0.0	0.0

Table 7.6: Equilibrium mole fraction of elements in equilibrium precipitates in Cr–W, Cr–Mo weld metals and HCM2S steel at 500 °C, calculated using MTDATA [124]. In Cr–W weld metal and HCM2S steel at equilibrium, the major phase M_6C contains tungsten as a main constituent.

	66 h	128 h	10,000 h
Cr–W weld metal	M_3C, M_7C_3	-	M_7C_3, $M_{23}C_6$, M_3C
Cr–Mo weld metal	-	M_3C, M_7C_3, M_2C	M_7C_3, M_3C, M_2C

Table 7.7: The precipitates identified in Cr–W and Cr–Mo weld metals during tempering at 500 °C upto 10,000 h.

found (Fig. 7.25) after 3,500 h of tempering. However, in practice the HCM2S steel is heavily tempered (780 °C for 1 h) prior to service, so that its as–received hardness is about 200 HV and its yield strength is 400 MPa. The designed weld metal self tempers during service and matches the hardness of HCM2S steel base plate. The new weld metal hardness is comparable with that of normalised and tempered HCM2S steel, Fig. 7.18. Moreover the service temperature of this designed new weld metal is much lower than 600 °C.

7.5 Comparison of HCM2S and Cr–W Weld

HCM2S is much more resistant to tempering than the straight Cr–W alloy purely because of vanadium and niobium carbonitrides. This was found during the comparative study of HCM2S steel and Cr–W weld metal. In HCM2S steel after 960 h of tempering, the precipitates CrNbN, M_3C, V_4C_3 and M_7C_3 were found. The presence of CrNbN (Fig. 7.32) was verified with X–ray

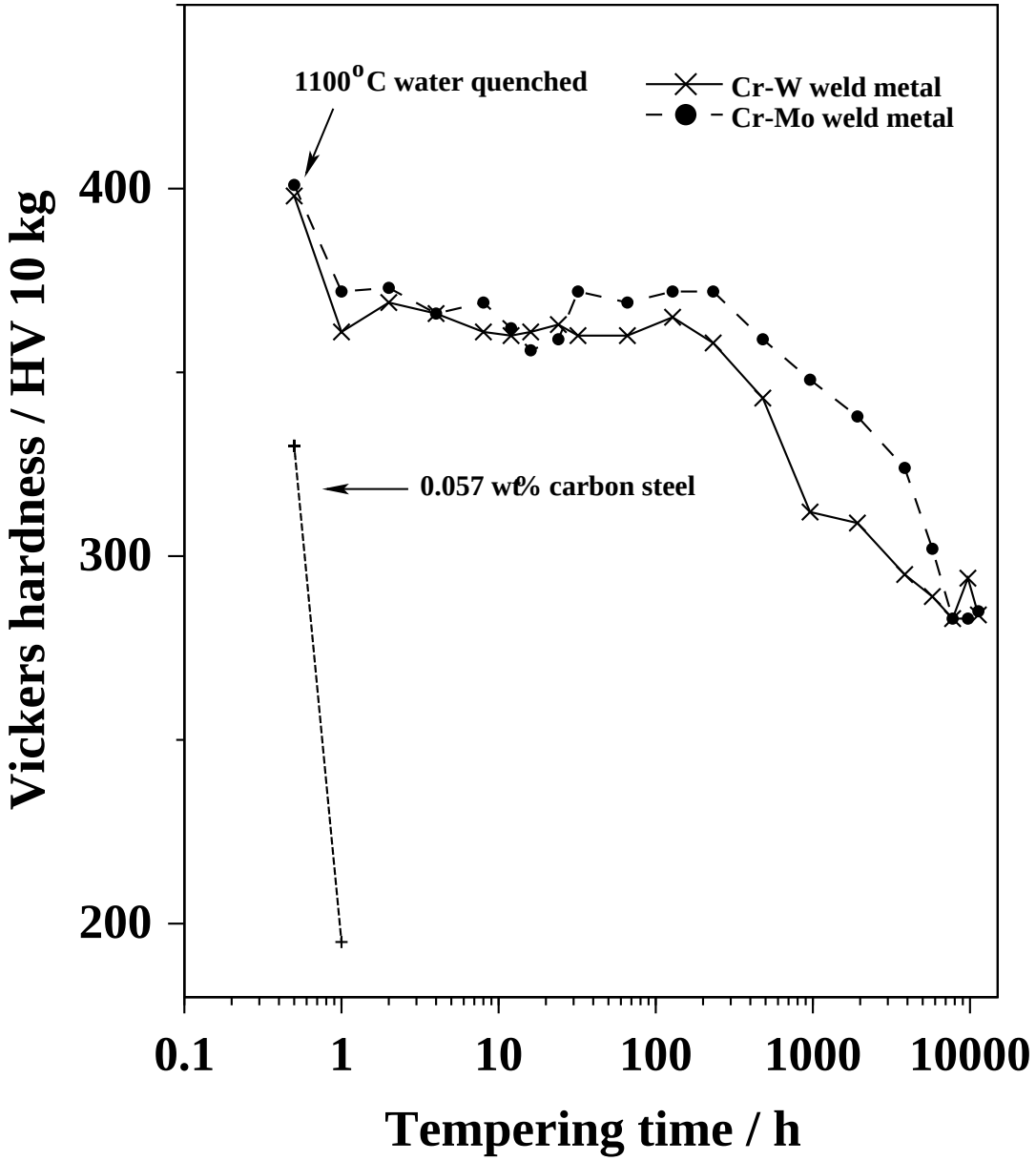

Figure 7.5: The change in hardness in Cr–Mo and Cr–W weld metals tempered at 500 °C. Data for a plain carbon steel [20] are shown for comparison.

diffraction on extracted bulk precipitates. The electron diffraction patterns and TEM micrographs are presented in Fig. 7.31 to 7.34. HCM2S steel is more stable than Cr–W weld metal (Fig. 7.28) the hardness remaining constant (Fig. 7.29). In Cr–W weld metal the major equilibrium phase is M_6C which is a coarse carbide which decreases the amount of tungsten in solid solution thus reducing the solid solution strengthening. The coarse precipitate M_6C is an ineffective precipitation strengthener. In the case of HCM2S steel coarse grain boundary precipitates

	2 h	4 h	3,500 h
HCM2S steel	-	M_3C, M_7C_3, CrNbN	M_7C_3, W_2C, V_4C_3, VC, M_3C
New weld metal	M_3C, M_7C_3	-	M_7C_3, W_2C, V_4C_3, VC, WC

Table 7.8: Precipitates identified in HCM2S steel and new weld metal during tempering at 600 °C upto 3,500 h.

	HCM2S steel			New weld metal			
Total number of moles	1783.0			1796.0			
	V_4C_3	CrNbC	M_6C	CrVTiN	M_7C_3	$M_{23}C_6$	M_6C
Amount in moles	3.95	1.552	16.61	4.286	2.75	15.6	4.73
Element (mole fraction)							
Fe	0.0012	0.001	0.41	0.005	0.096	0.26	0.42
C	0.321	0.33	0.143	0.0001	0.3	0.2	0.014
Cr	0.002	0.21	0.01	0.11	0.525	0.45	0.011
Mn	0.007	0.00	0.0	0.002	0.016	0.0	0.0
N	0.144	0.0	0.0	0.33	0.0	0.0	0.0
W	0.002	0.075	0.35	0.002	0.0025	0.02	0.34
Mo	0.0	0.036	0.037	0.0	0.0	0.064	0.038
V	0.53	0.085	0.055	0.45	0.06	0.00	0.05
Nb	0.0	0.26	0.0	-	-	-	-
Ti	-	-	-	0.1	0.0	0.0	0.0

Table 7.9: Equilibrium mole fraction of elements in equilibrium precipitates in HCM2S steel and new weld metal at 600 °C, calculated using MTDATA [124].

and fine precipitates with the grains were found (Fig. 7.30); the fine precipitates are vanadium and niobium carbonitrides which are major contributors to the strength of HCM2S steel.

7.6 Hardness of HCM2S in different conditions

Welding will induce a heat–affected zone in the HCM2S steel in the vicinity of the fusion boundary. The microstructures expected in the HAZ are essentially mixtures of bainite and martensite in different proportions. These will then temper during service. The purpose of the work presented here was to see if there are any significant differences in the tempering behaviour. Samples austenitised and water–quenched (*i.e.* martensitic) were therefore compared against an austenitised and air–cooled bainitic microstructure. Fig. 7.35 shows that, as expected, the samples start off with different hardness values, the martensitic sample being some 100 HV harder because the carbon is in solid solution. The difference in hardness decreases as the tempering

time is increased until it vanishes at about 3500 h of tempering at 600 °C. Therefore, the HAZ should become mechanically homogeneous during service. It is worth noting that the difference in hardness persists to long tempering times, much longer than expected simply from the removal of carbon from solid solution. Unfortunately, the reason for this could not be investigated due to time limitations, but it is likely that the precipitation of alloy carbides may have been altered as a function of starting microstructure. For example, it is expected that precipitation from supersaturated martensite must be finer with greater number densities of particles, whereas with a bainitic starting microstructure the cementite particles generated during the bainite transformation are known to be coarser [116].

7.7 Theoretical Analysis of Coarsening Resistance

Particle coarsening is the process of dissolution of small precipitates and the simultaneous growth of larger precipitates at a fixed volume fraction. Finally, the system should tend towards one large particle. The driving force for the process is a decrease in interfacial energy (σ) between the matrix (α) and precipitate (θ). The theory of precipitate coarsening includes the size and shape of the precipitates, the relationship between size and solubility and the mode of reaction, whether diffusion–controlled or interface–controlled [141]. A precipitate θ in a ferrite matrix α is in equilibrium when the interface is flat. When the interface becomes curved, as in spherical precipitates (Fig. 7.36) the equilibrium concentration becomes a function of the radius of curvature, given by $c_r^{\alpha\theta}$ and $c_r^{\theta\alpha}$ where $c_r^{\alpha\theta}$ is the solute concentration in the ferrite matrix and $c_r^{\theta\alpha}$ solute concentration in the precipitate θ, r is the radius of curvature of precipitate.

When the radius of curvature tends to zero, means when the curved interface becomes flat, then $c_r^{\alpha\theta} = c^{\alpha\theta}$. The solute concentration in ferrite near small particles will be greater than that near to larger particle, and it is this concentration gradient which helps the coarsening of larger precipitate at the expense of small precipitate, Fig. 7.36.

The concentration difference $c_r^{\alpha\theta} - c^{\alpha\theta}$, which drives the diffusion flux, is given by:

$$c_r^{\alpha\theta} - c^{\alpha\theta} = \frac{\sigma V^{\alpha}}{kT\, r} \times \frac{c^{\alpha\theta}(1 - c^{\alpha\theta})}{(c^{\theta\alpha} - c^{\alpha\theta})} \tag{7.5}$$

where k is the Boltzmann constant, T is the absolute temperature and V^{α} is the molar volume of ferrite matrix. Thus interfacial velocity v is proportional to the diffusion flux which in turn depends on the diffusion coefficient of solute atom in the matrix and is expressed as [142];

$$v \propto D\frac{\sigma V^{\alpha}}{kT\, r} \times \frac{c^{\alpha\theta}(1 - c^{\alpha\theta})}{(c^{\theta\alpha} - c^{\alpha\theta})^2} \tag{7.6}$$

Steels contain many solutes; each solute will influence the diffusion flux in matrix. Venugopalan *et al.* [143] suggested as effective diffusion coefficient D_{eff} by treating the fluxes as a combination of parallel electrical conductances. The interfacial velocity;

$$\frac{1}{v} \propto \frac{1}{D_i}, \qquad \text{where} \qquad \frac{1}{D_{eff}} = \sum_i \frac{1}{D_i} \times \frac{\left(c_i^{\theta\alpha} - c_i^{\alpha\theta}\right)^2}{c_i^{\alpha\theta}(1 - c_i^{\alpha\theta})} \tag{7.7}$$

where D_{eff} ($cm^2\ s^{-1}$) is the effective diffusion coefficient, D_i is the diffusion coefficient of individual solute 'i' in α–ferrite, $c_i^{\theta\alpha}$ is the solute concentration in α–ferrite and $c_i^{\alpha\theta}$ is the solute concentration of element 'i' in the precipitate (θ).

From equation 7.7; the lower the value of D_{eff} slower the growth of the precipitate. Using the above theory, D_{eff} of each precipitate for the tempered materials were calculated, Table 7.10. Here the mole faction of elements in a precipitate were calculated using MTDATA [124]. Table 7.10 shows that in the long term, well outside the scope of the experiments reported here but within the design life, it is the vanadium and niobium compounds that are the most stable and hence these will form the backbone of the creep resistance.

	D_{eff} at **500** °C	D_{eff} at **600** °C
Cr–Mo weld metal		
$M_{23}C_6$	3.15×10^{-18}	4.2×10^{-16}
Cr_2N	2.22×10^{-18}	2.74×10^{-17}
Cr–W weld metal		
M_7C_3	-	2.9×10^{-16}
$M_{23}C_6$	3.93×10^{-18}	-
M_6C	2.08×10^{-19}	2.92×10^{-17}
Cr_2N	3.01×10^{-19}	5.27×10^{-17}
HCM2S steel		
M_6C	3.4×10^{-19}	4.63×10^{-17}
V_4C_3	-	2.86×10^{-17}
VN	2.43×10^{-19}	-
(Nb, V)C	3.8×10^{-22}	-
CrNbC	-	3.0×10^{-19}
New weld metal		
M_7C_3	-	2.79×10^{-16}
$M_{23}C_6$	1.59×10^{-18}	2.38×10^{-16}
M_6C	2.85×10^{-19}	3.18×10^{-17}
V(C, N)	3.71×10^{-19}	-
CrVTiN	-	2.76×10^{-17}
CrNbC	1.0×10^{-21}	-

Table 7.10: Calculated effective diffusion coefficients ($cm^2\ s^{-1}$) for equilibrium precipitates.

7.8 Conclusions

The tempering resistance of the new welding alloy, and the changes in its hardness over a long period of time at 600 °C, have been found to be satisfactory with respect to the original design concepts. Thus, the hardness drops to about 200 HV, which is comparable to that of HCM2S when it enters service in a severely tempered state. Vanadium and niobium carbonitrides are probably vital in ensuring the long–term creep strength of both HCM2S and the new welding alloy. They form precipitates which should be more resistant to coarsening than any other precipitates found in the alloys considered. The HAZ of HCM2S should be well–behaved with respect to long periods in service in spite of the variations in major microstructural components as induced by welding. The substitution of tungsten for molybdenum keeps as-welded hardness low during multirun welding.

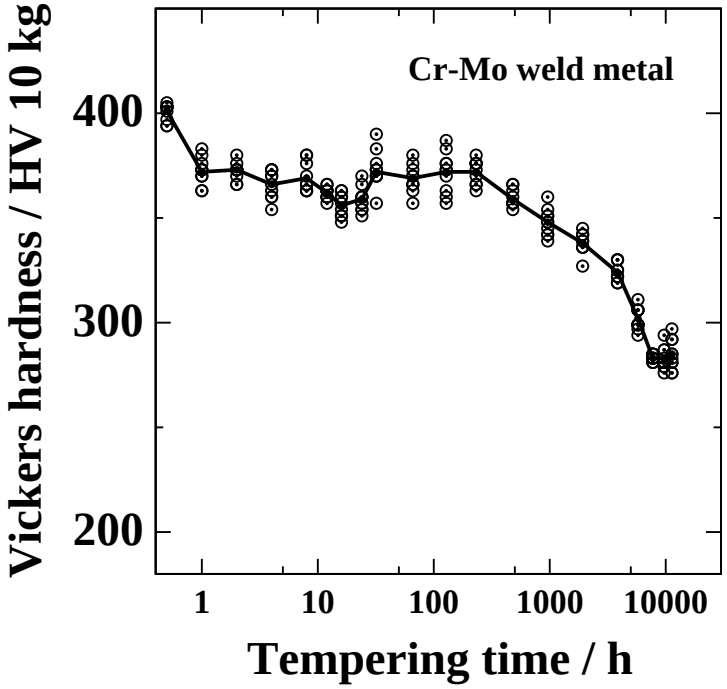

(a)

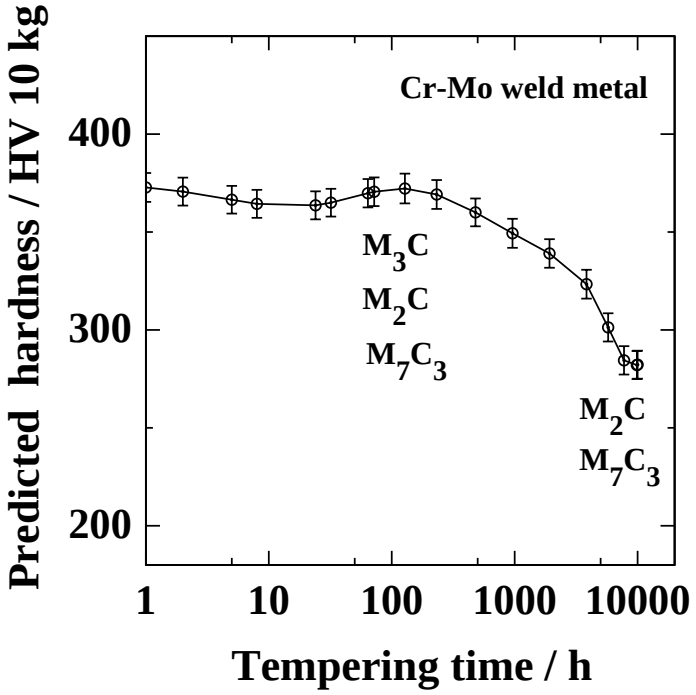

(b)

Figure 7.6: Hardness variation in Cr–Mo weld metal tempered at 500 °C, a) measured hardness, the line shows the variation in average hardness b) neural network representation of hardness data.

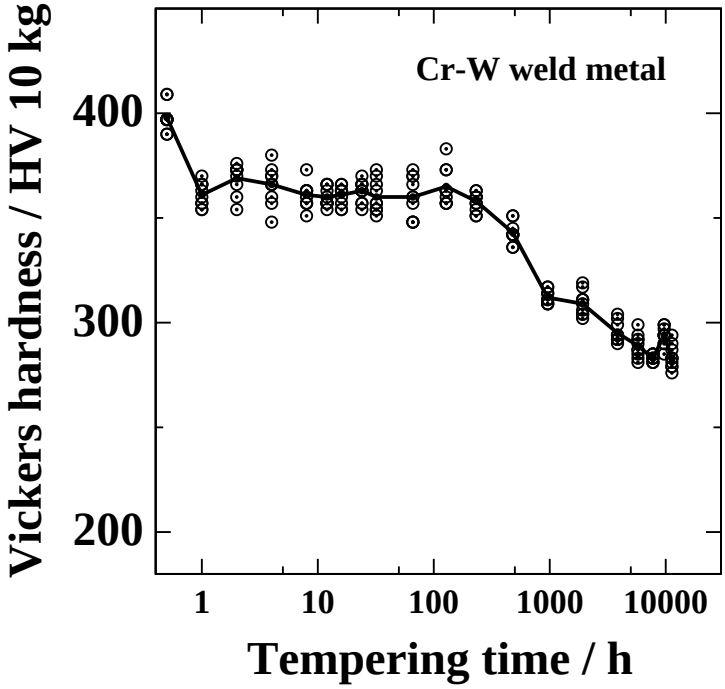

(a)

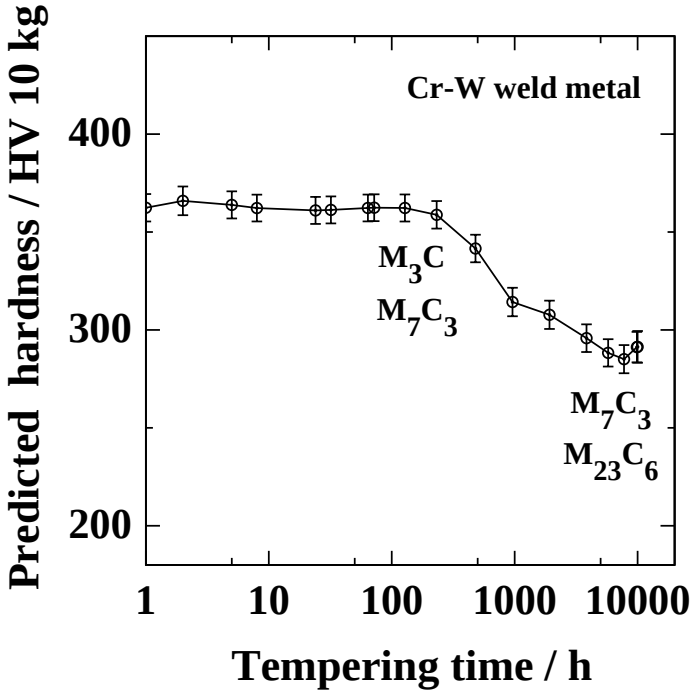

(b)

Figure 7.7: Hardness variation in Cr–W weld metal tempered at 500 °C, a) measured hardness, the line shows the variation in average hardness b) neural network representation of hardness data.

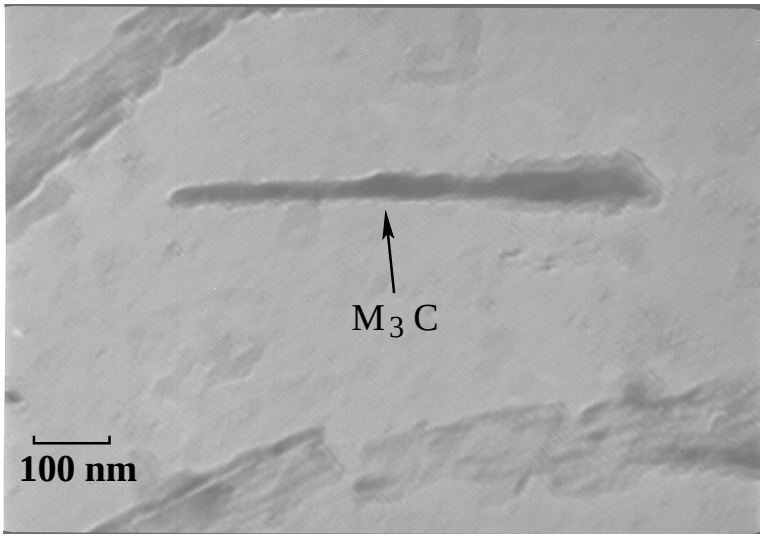

(a)

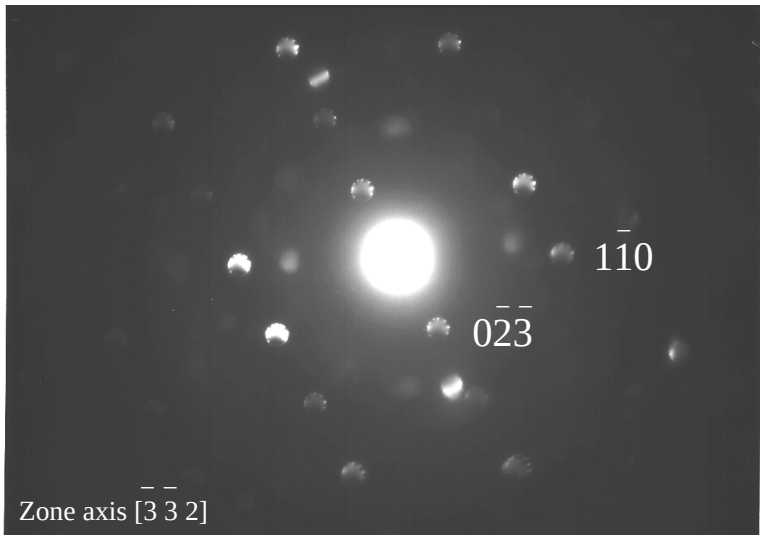

(b)

Figure 7.8: M_3C precipitate found in Cr–W weld metal tempered at 500 °C for 66 h, a) carbon replica b) electron diffraction from M_3C.

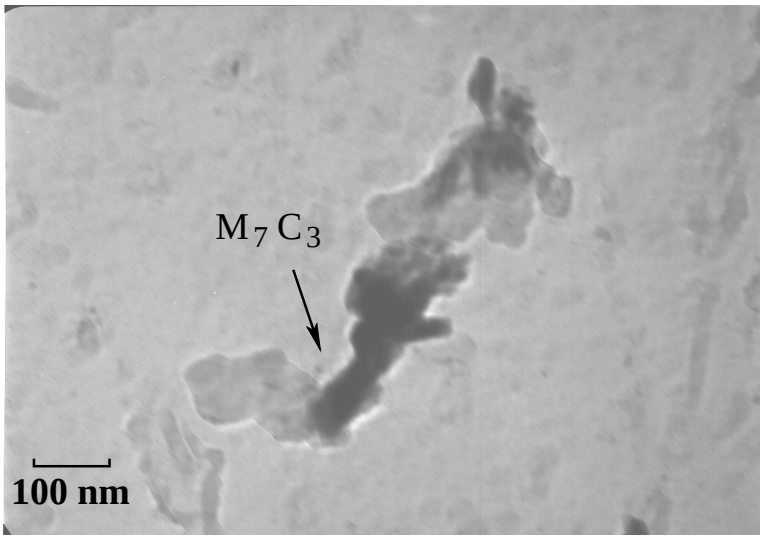

(a)

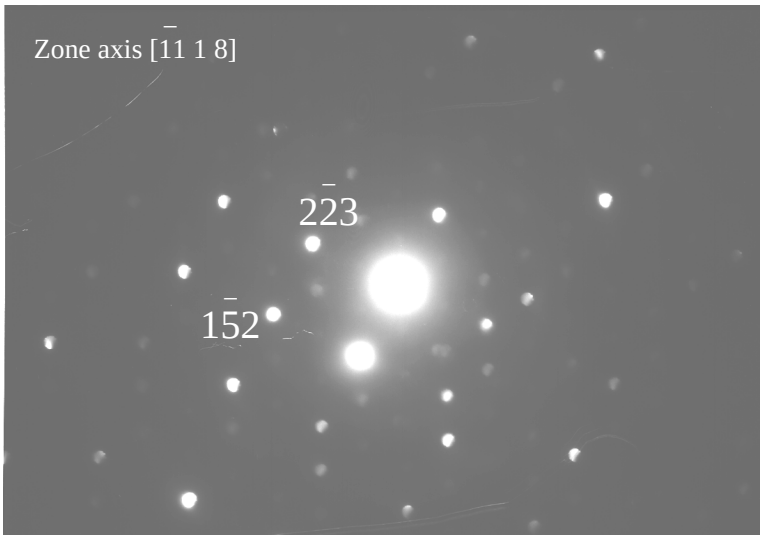

(b)

Figure 7.9: M_7C_3 precipitate found in Cr–W weld metal tempered at 500 °C for 66 h, a) carbon replica b) electron diffraction from M_7C_3.

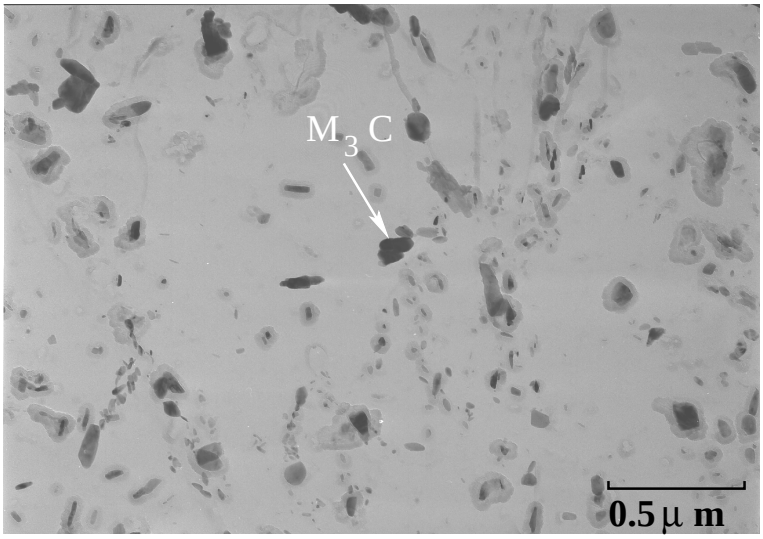

(a)

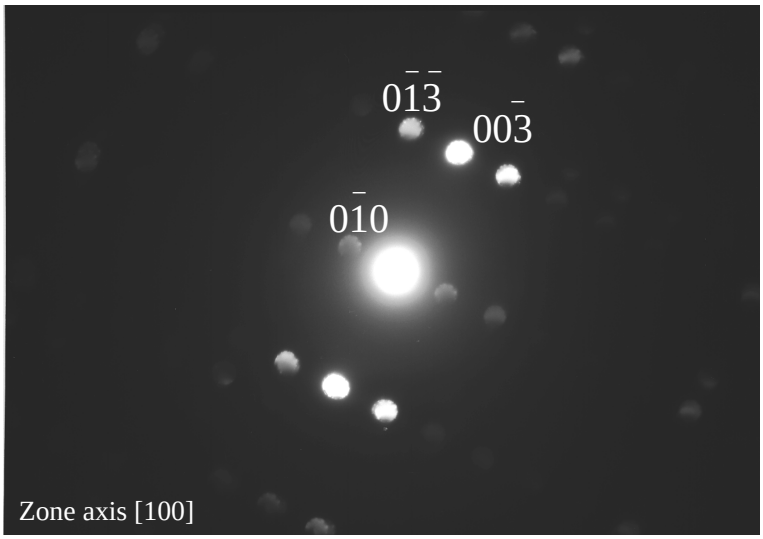

(b)

Figure 7.10: M_3C precipitate found in Cr–W weld metal tempered at 500 °C for 10,000 h, a) carbon replica b) electron diffraction from M_3C.

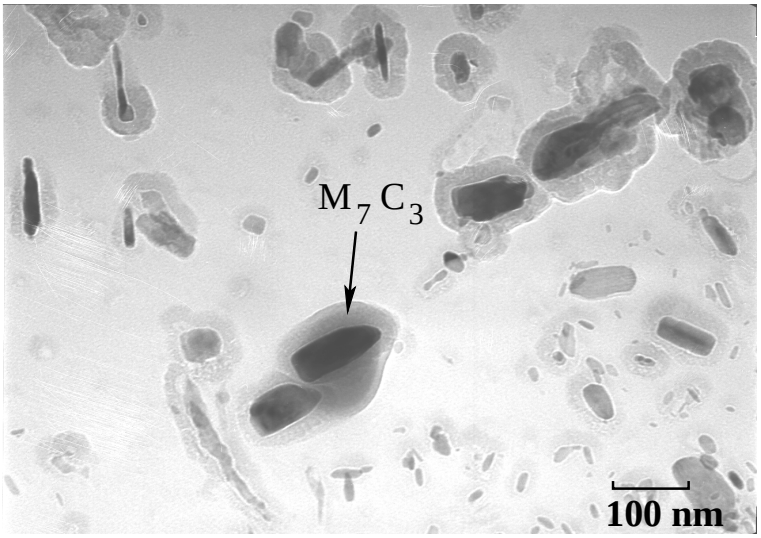

(a)

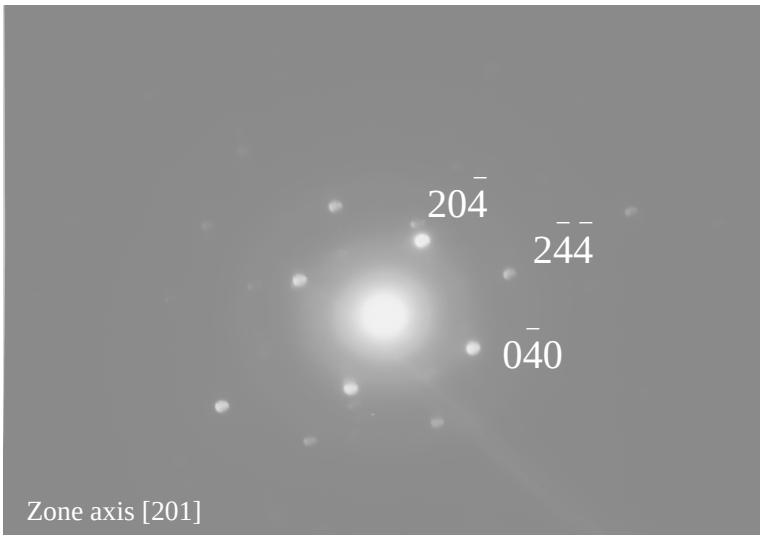

(b)

Figure 7.11: M_7C_3 precipitate found in Cr–W weld metal tempered at 500 °C for 10,000 h, a) carbon replica b) electron diffraction from M_7C_3.

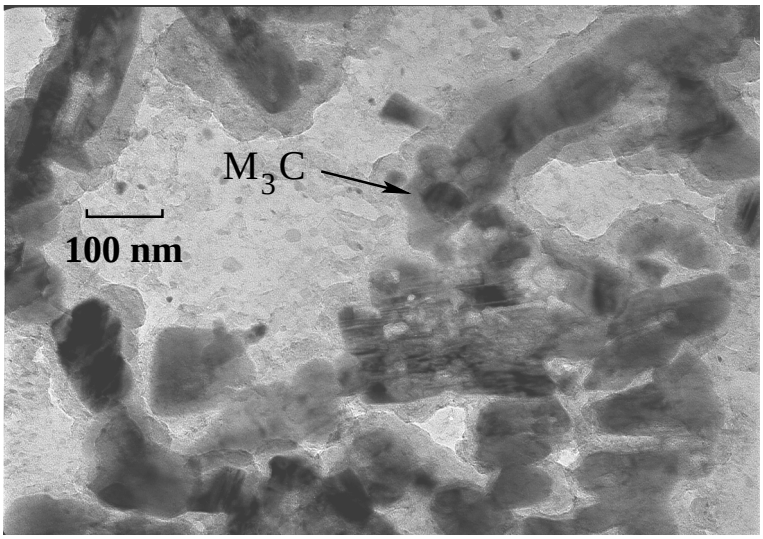

(a)

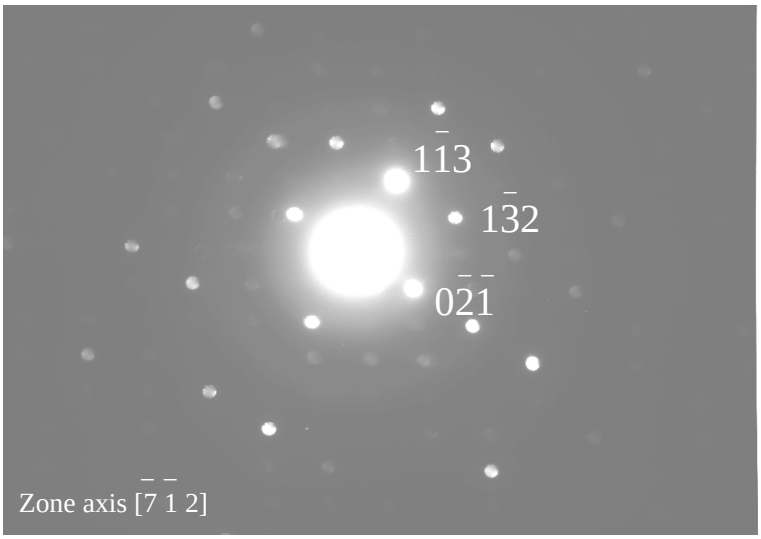

(b)

Figure 7.12: M_3C precipitate found in Cr–Mo weld metal tempered at 500 °C for 128 h, a) carbon replica b) electron diffraction from M_3C.

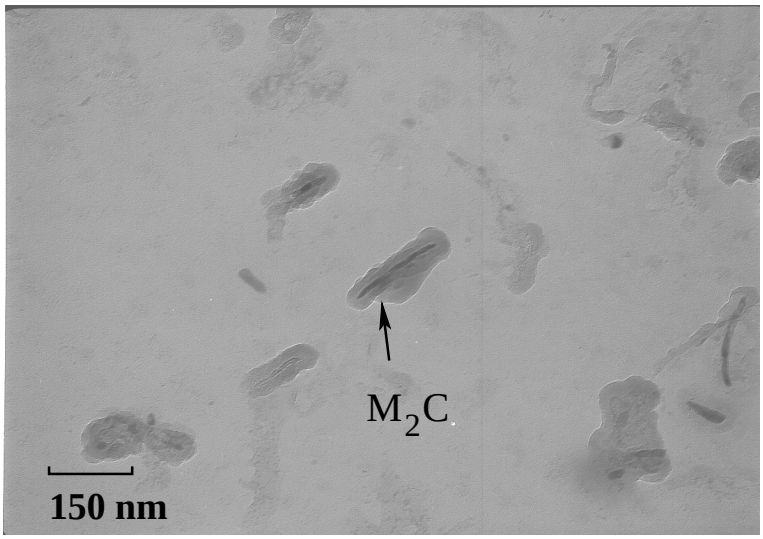

Figure 7.13: M_2C precipitate found in Cr–Mo weld metal tempered at 500 °C for 128 h, carbon replica.

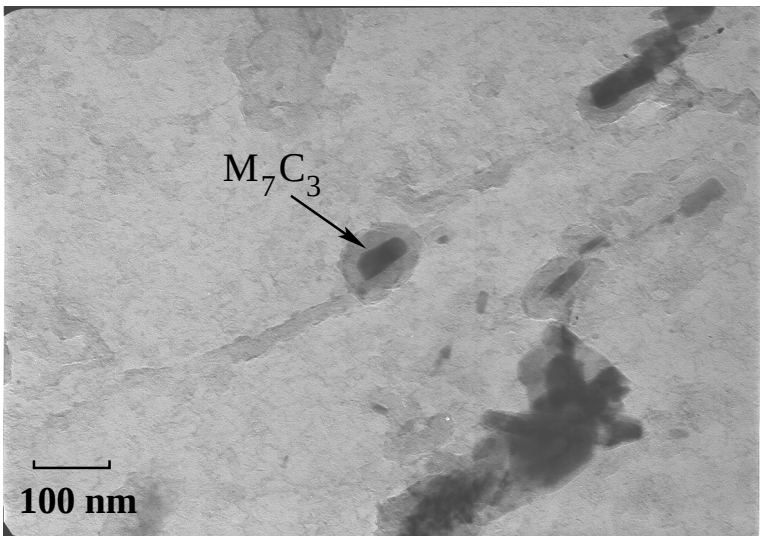

(a)

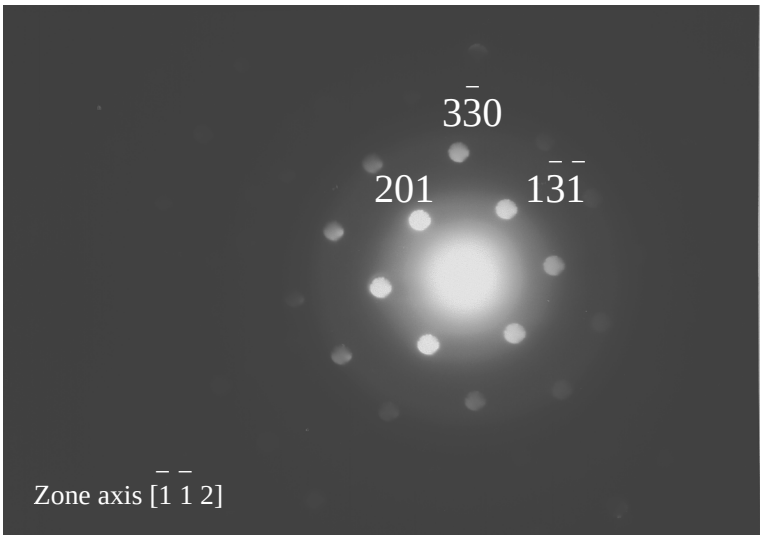

(b)

Figure 7.14: M_7C_3 precipitate found in Cr–Mo weld metal tempered at 500 °C for 10,000 h, a) carbon replica b) electron diffraction from M_7C_3.

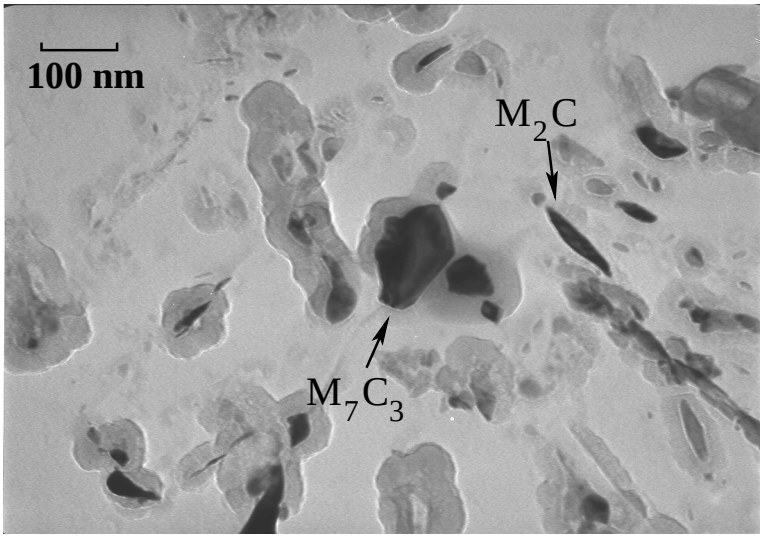

(a)

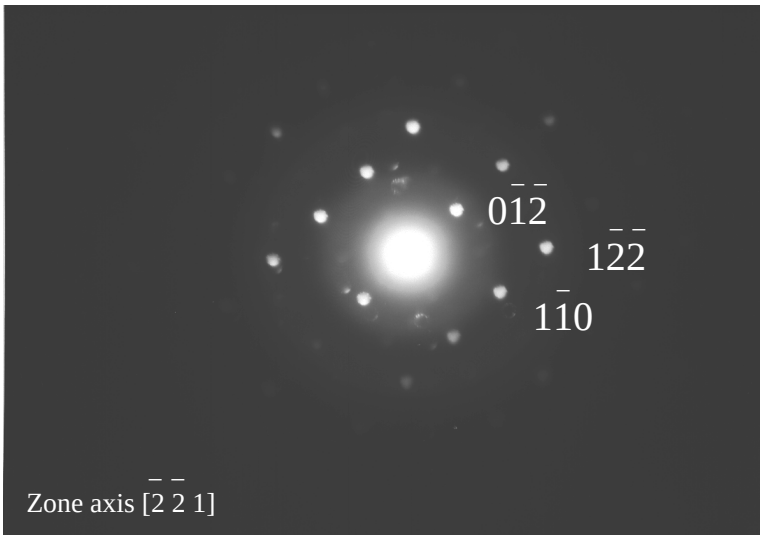

(b)

Figure 7.15: M_2C precipitate found in Cr–Mo weld metal tempered at 500 °C for 10,000 h, a) carbon replica b) electron diffraction from M_2C.

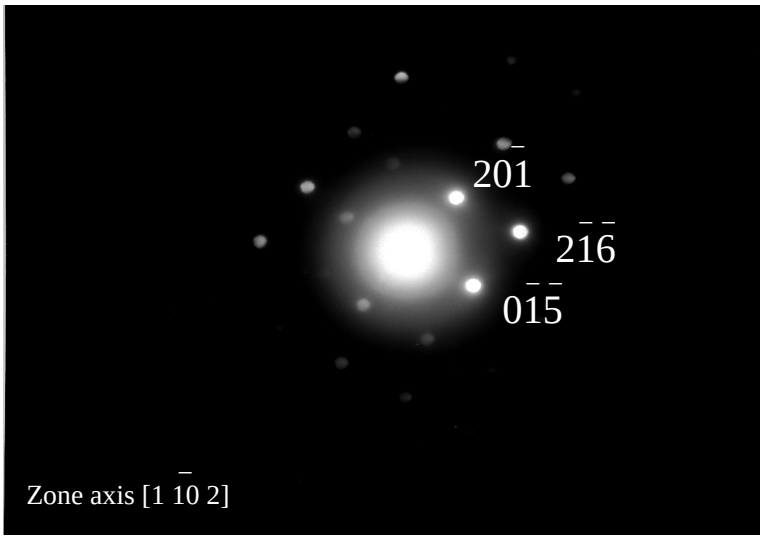

Figure 7.16: Electron diffraction pattern from the M_7C_3 precipitate found in the Cr–Mo sample, tempered at 500 °C for 10,000 h.

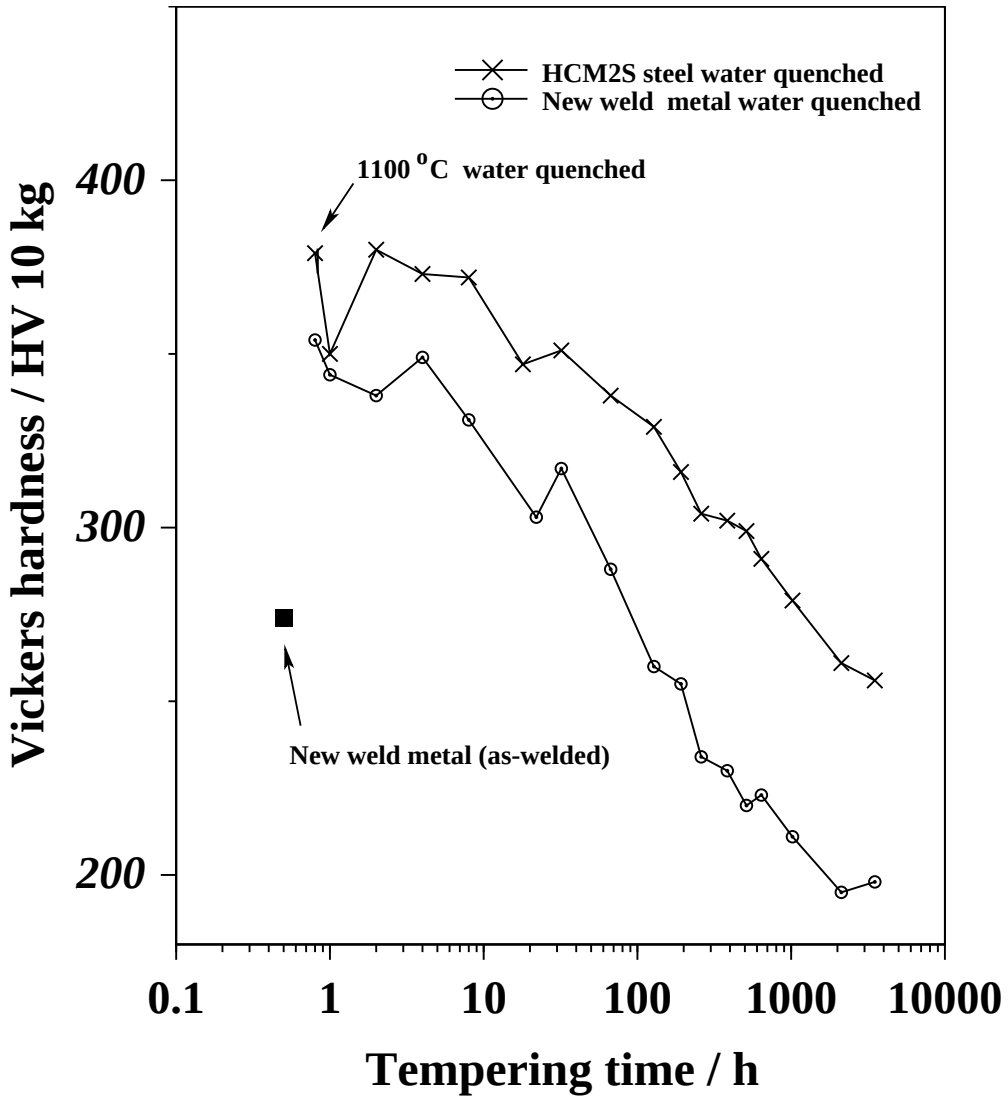

Figure 7.17: Comparison between HCM2S steel and new weld metal tempered at 600 °C.

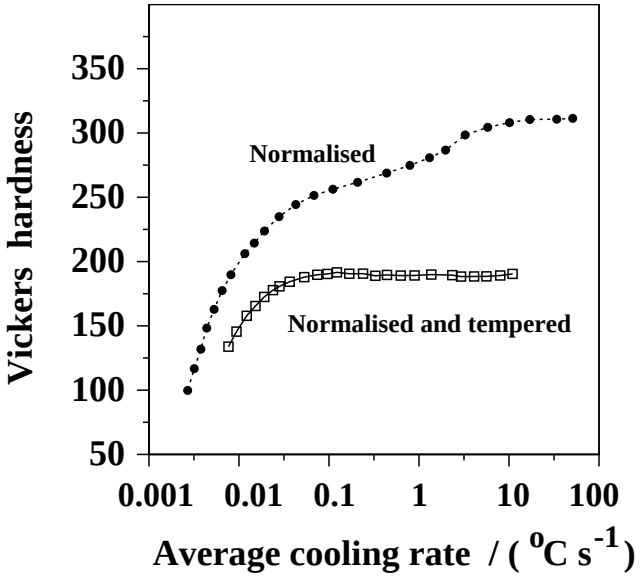

Figure 7.18: Variation in hardness of HCM2S at different cooling rates [121]. The tempering was carried at 770 °C for 1 h.

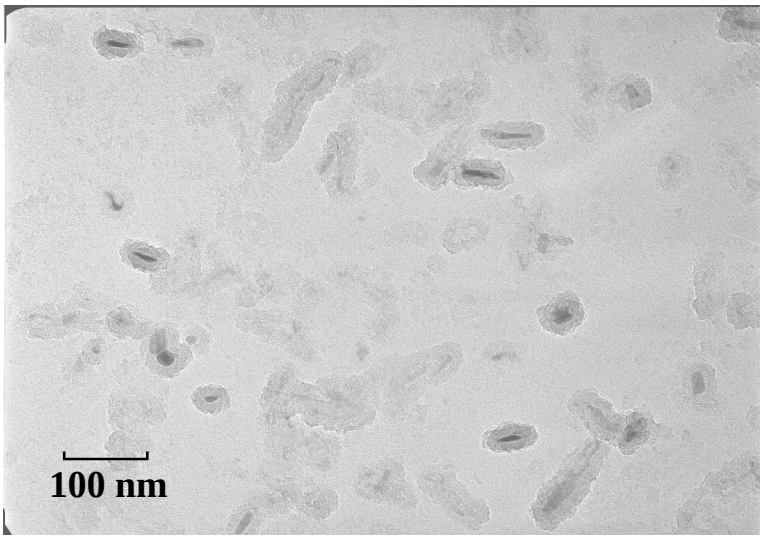

(a)

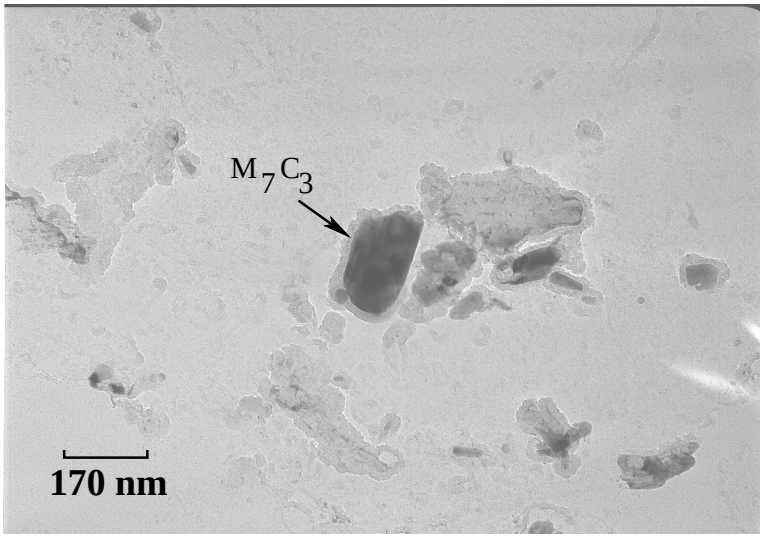

(b)

Figure 7.19: HCM2S steel tempered at 600 °C for 4 h, a) fine precipitates, carbon replica b) M_7C_3 precipitate.

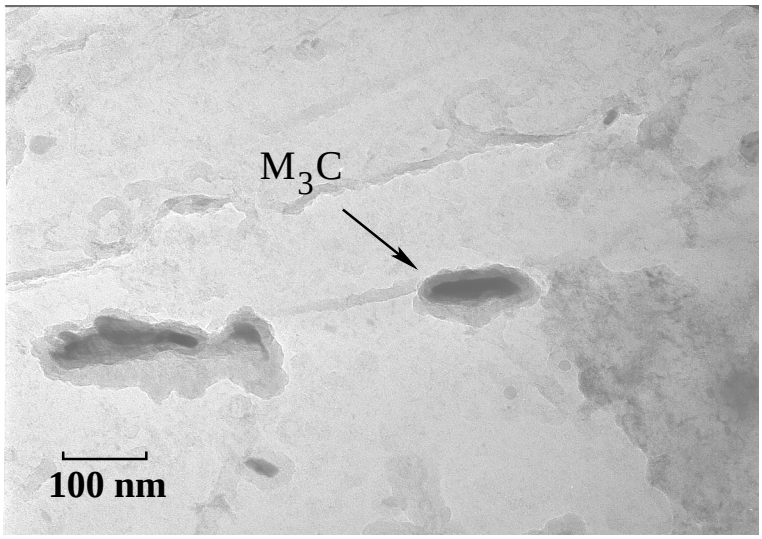

(a)

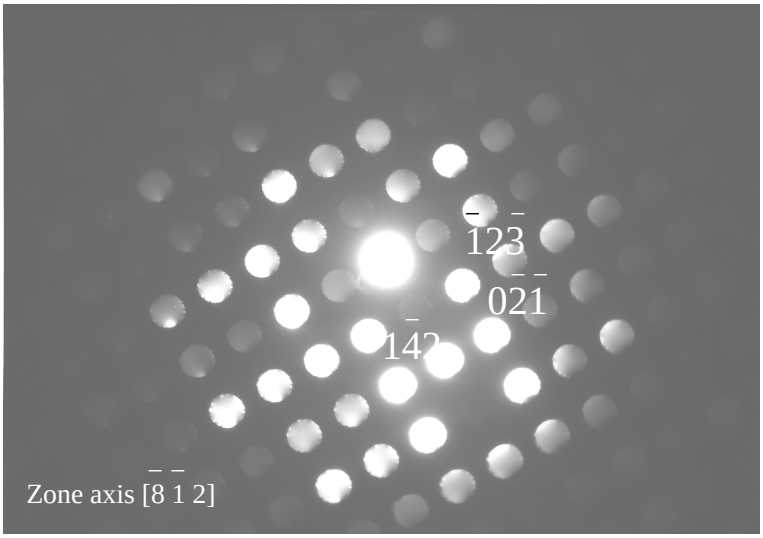

(b)

Figure 7.20: Cementite in HCM2S steel tempered at 600 °C for 4 h, a) carbon replica b) electron diffraction pattern from M_3C.

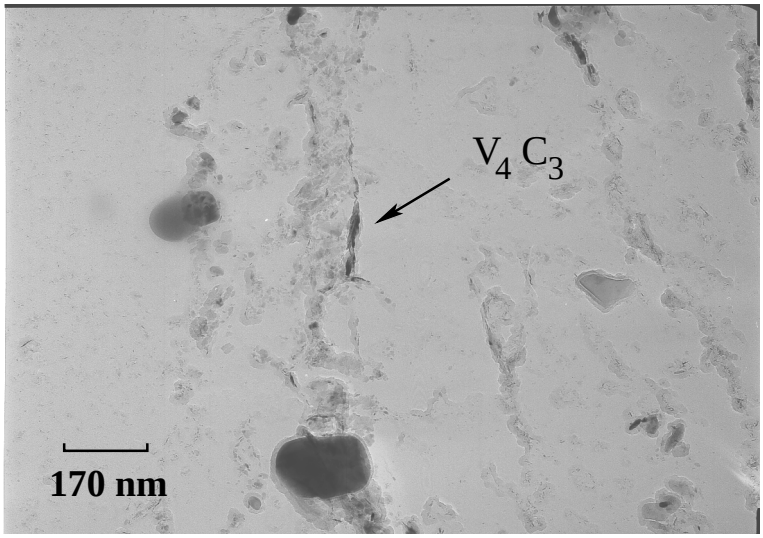

(a)

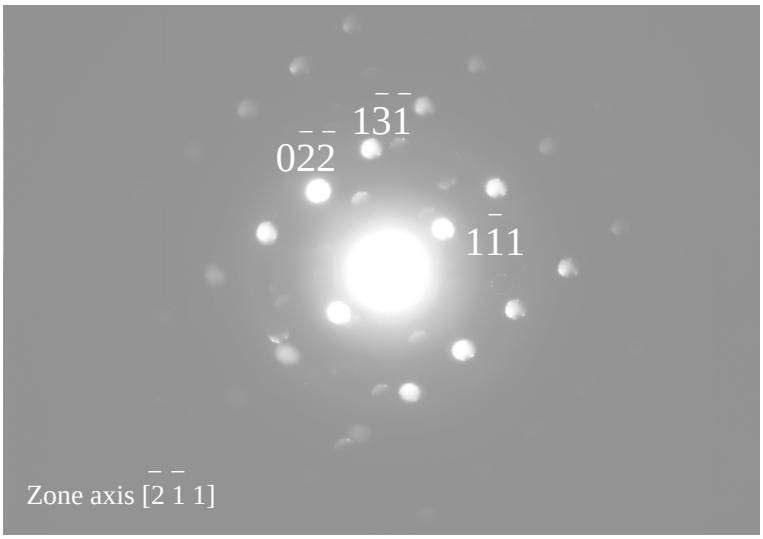

(b)

Figure 7.21: Precipitate V_4C_3 in HCM2S steel tempered at 600 °C for 3500 h, a) carbon replica b) electron diffraction from V_4C_3.

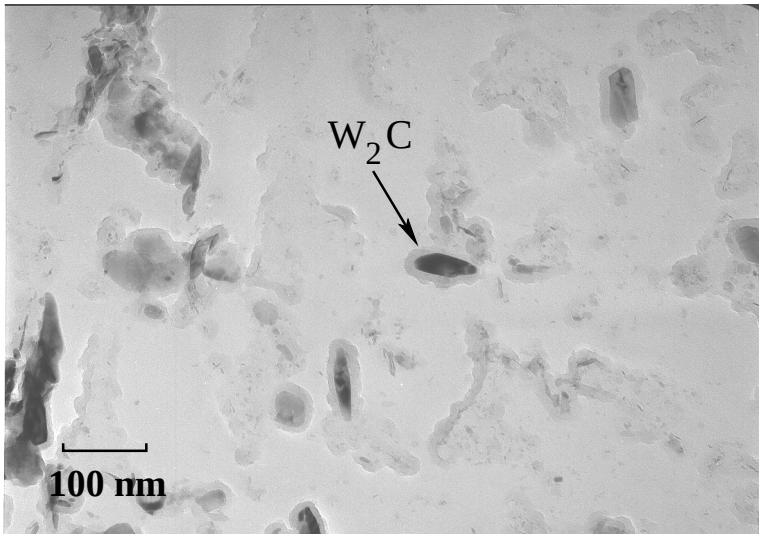

(a)

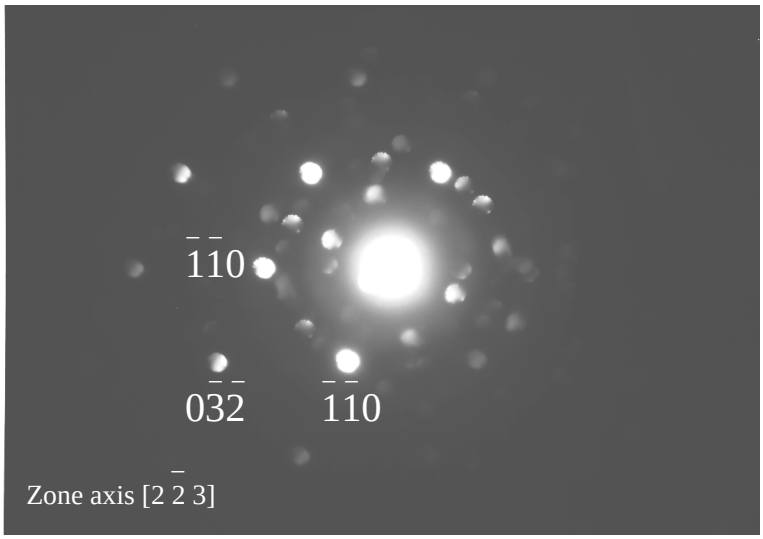

(b)

Figure 7.22: W_2C found in HCM2S steel tempered at 600 °C for 3500 h, a) electron carbon replica b) electron diffraction from W_2C.

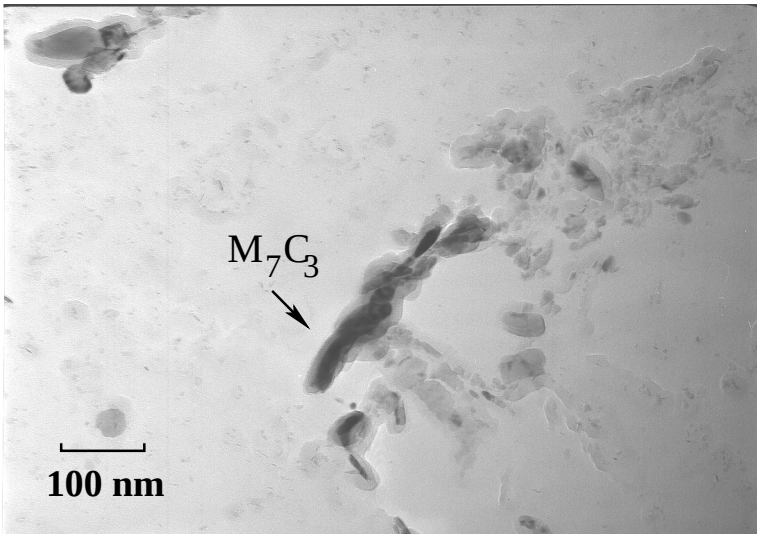

(a)

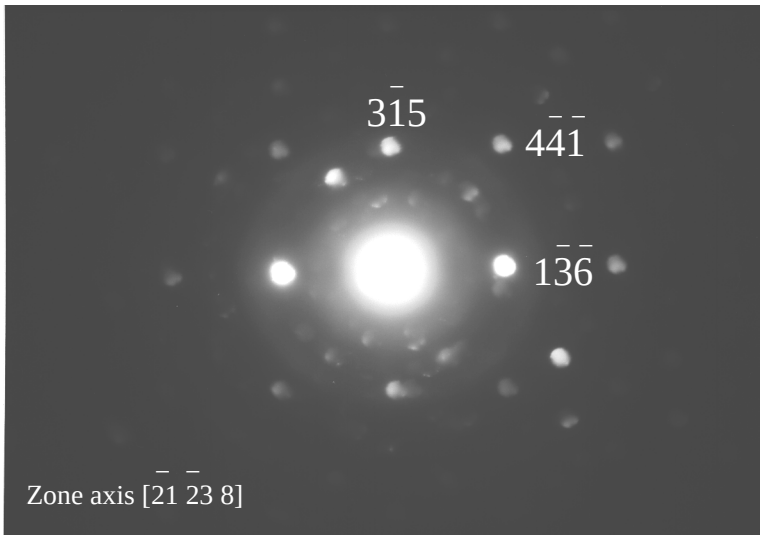

(b)

Figure 7.23: Precipitate M_7C_3 found in HCM2S steel tempered at 600 °C for 3500 h, a) carbon replica b) electron diffraction pattern from M_7C_3.

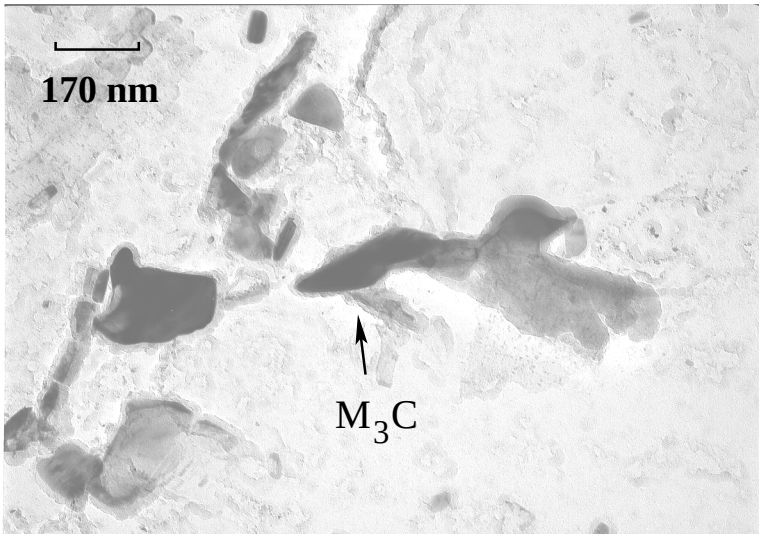

Figure 7.24: Cementite found in new weld metal tempered at 600 °C for 2 h.

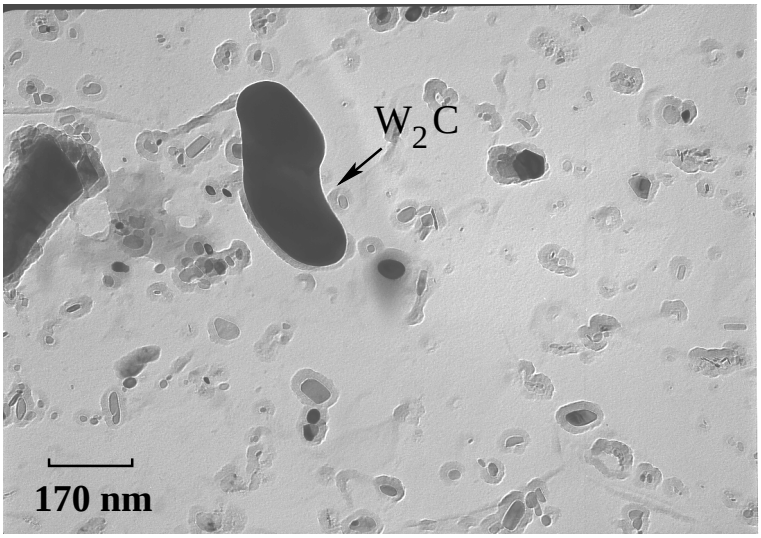

(a)

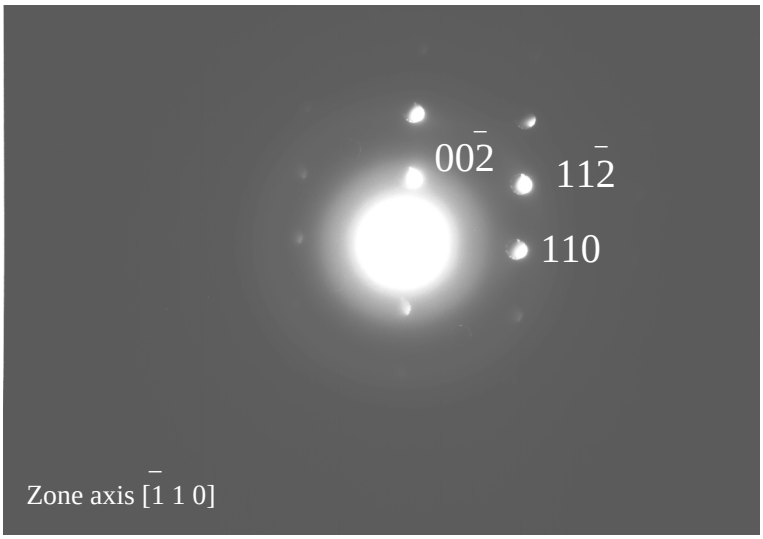

(b)

Figure 7.25: Tungsten carbide (W_2C) found in new weld metal tempered at 600 °C for 3500 h, a) carbon replica b) electron diffraction from W_2C

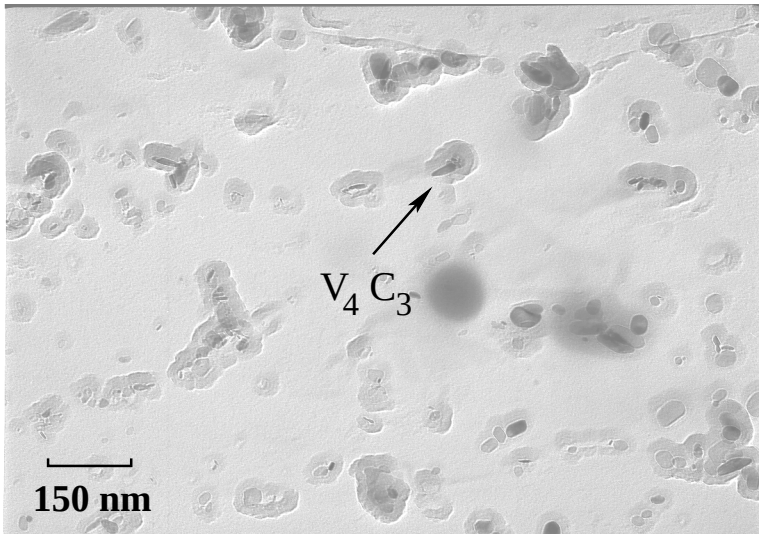

(a)

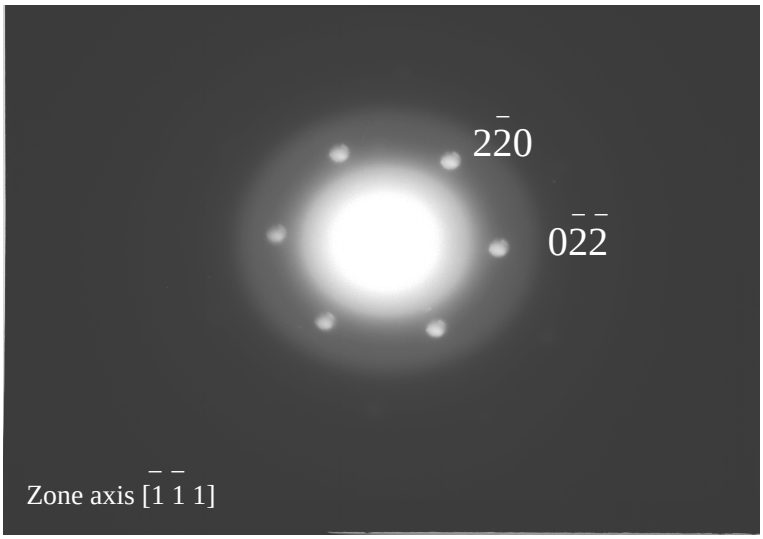

(b)

Figure 7.26: Precipitate V_4C_3 found in new weld metal tempered at 600 °C for 3500 h, a) carbon replica b) electron diffraction pattern from V_4C_3

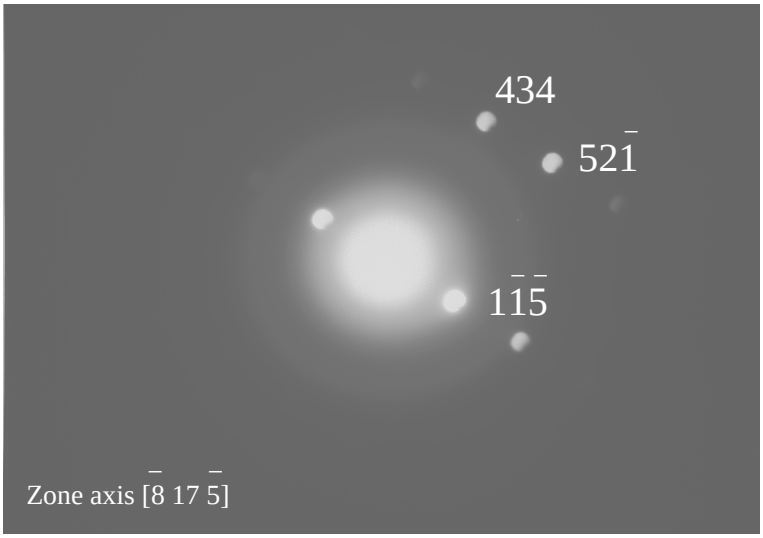

(a)

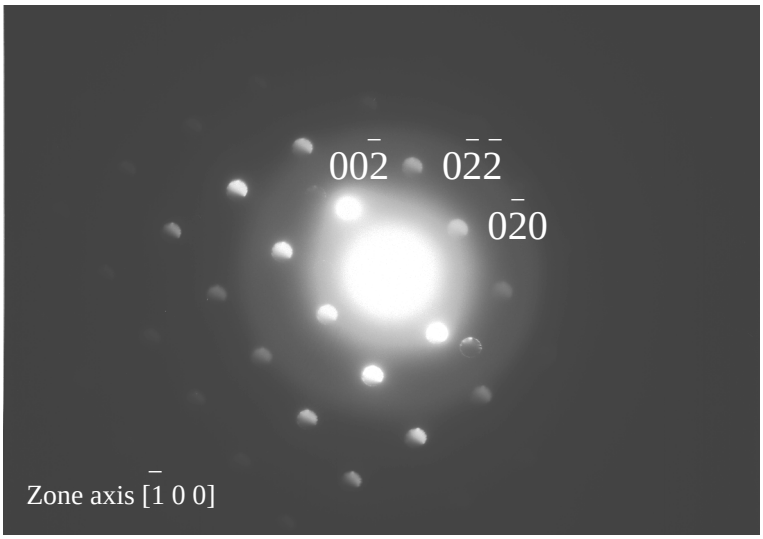

(b)

Figure 7.27: New weld metal tempered at 600 °C for 3500 h, a) electron diffraction pattern from M_7C_3 b) electron diffraction pattern from VC.

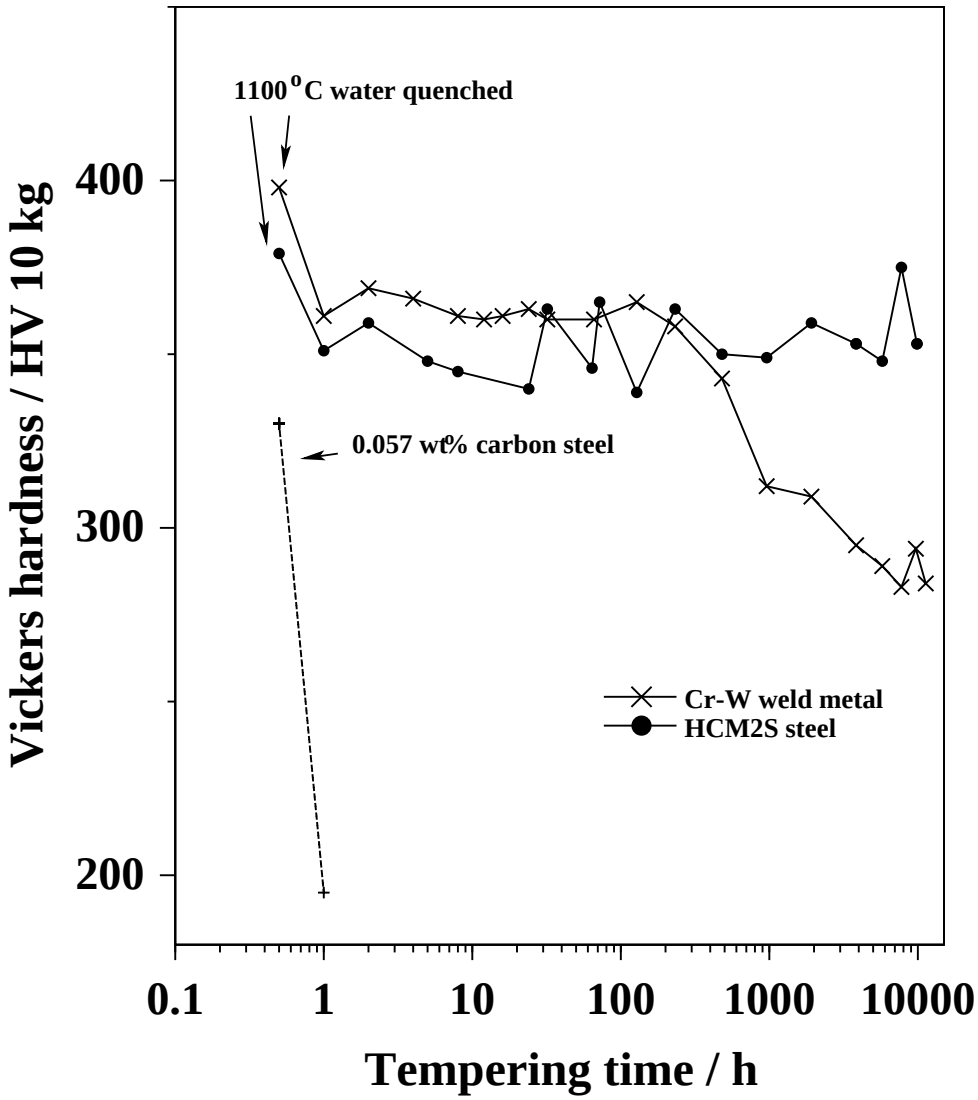

Figure 7.28: Hardness variation in HCM2S steel and Cr–W weld metal tempered at 500 °C.

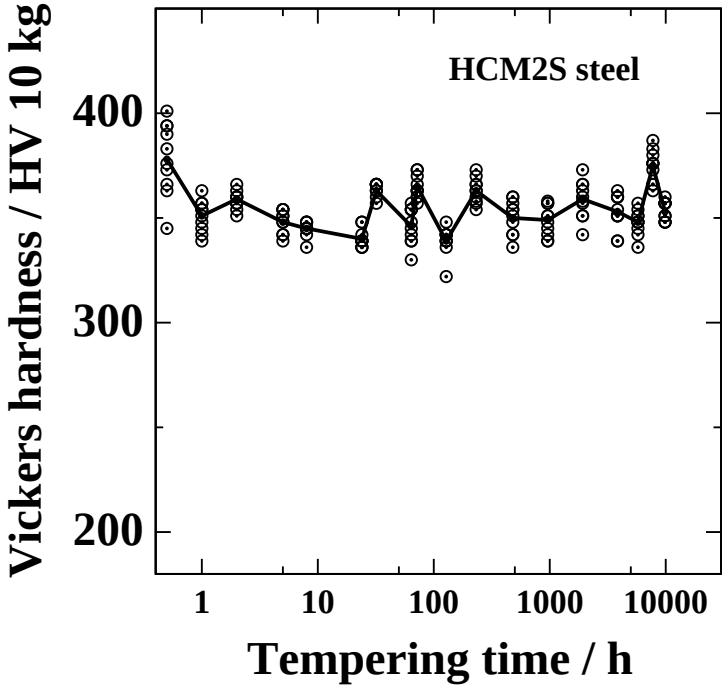

(a)

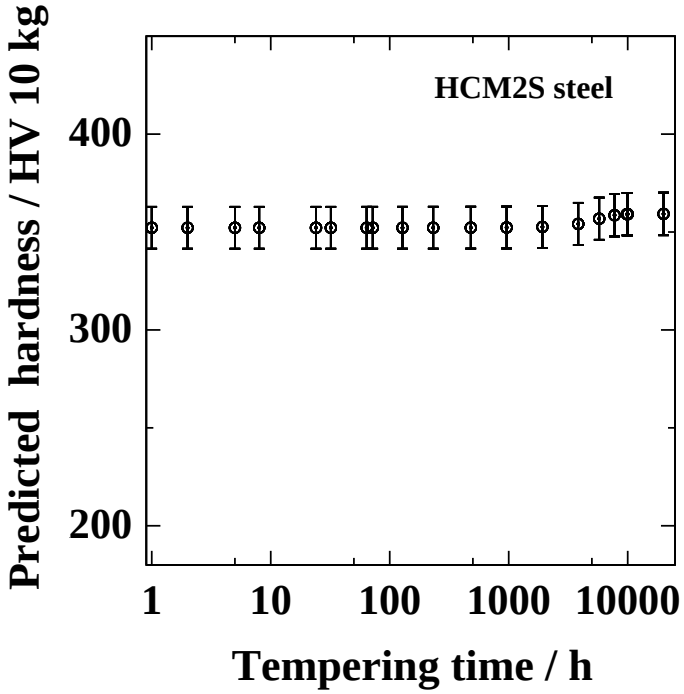

(b)

Figure 7.29: Hardness variation in HCM2S steel tempered at 500 °C, a) measured hardness b) neural network representation of hardness data.

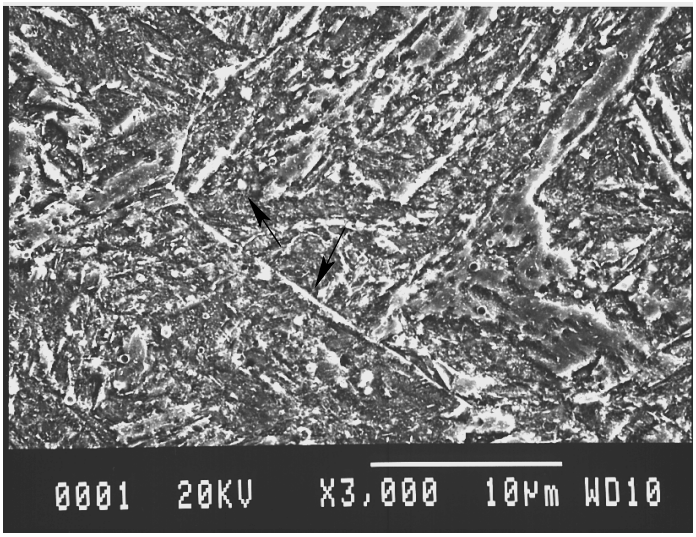

(a)

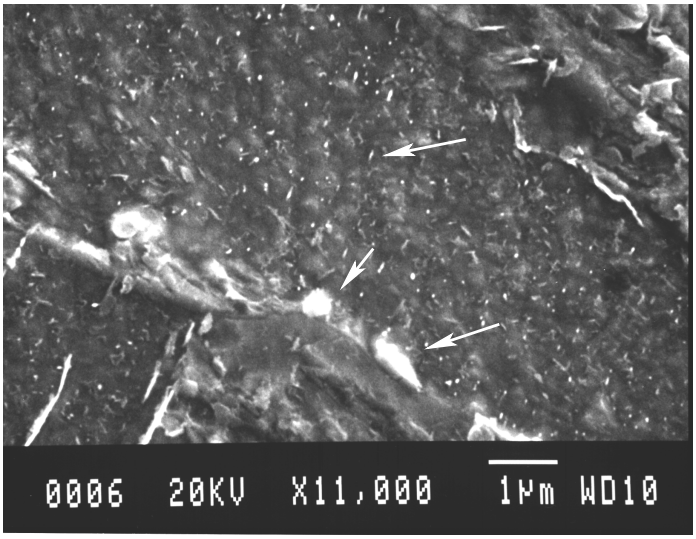

(b)

Figure 7.30: Scanning electron microscopy of HCM2S steel tempered at 500 °C for 10,000 h, a) arrows pointing to precipitates at grain boundary and within the grain b) fine precipitates within grains and coarse precipitates at grain boundaries.

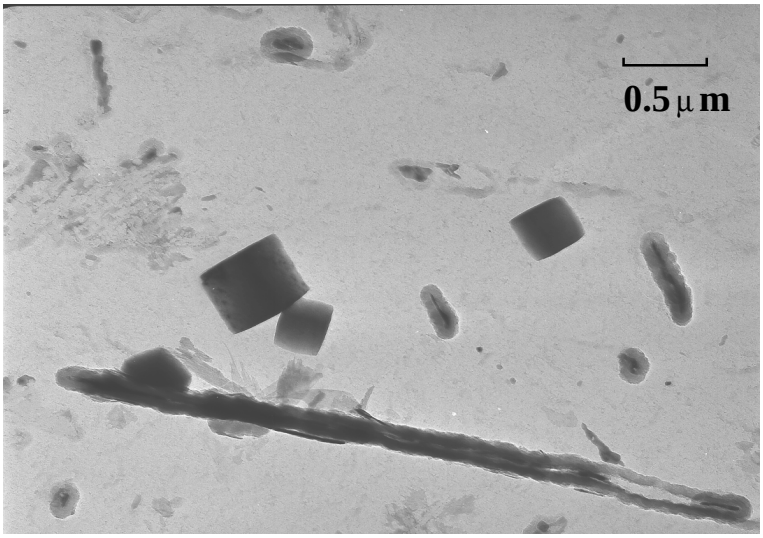

(a)

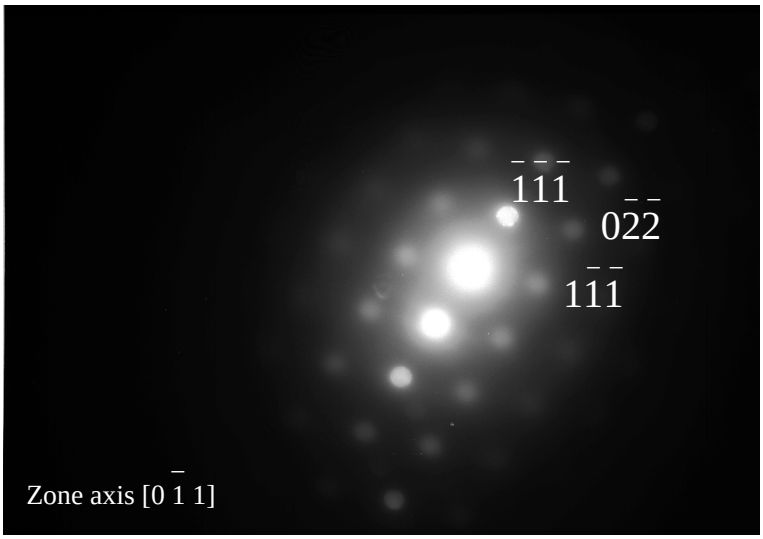

(b)

Figure 7.31: a) Various precipitates found in HCM2S steel tempered at 500 °C for 960 h, a) carbon replica b) electron diffraction pattern from V_4C_3.

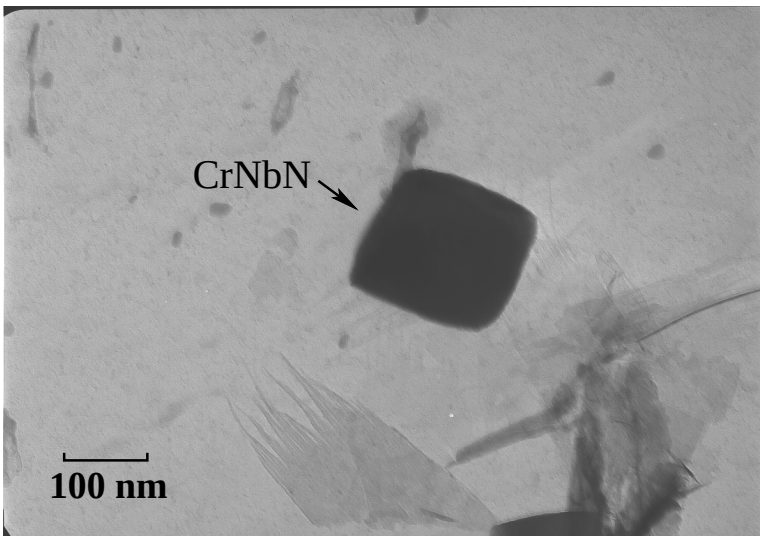

(a)

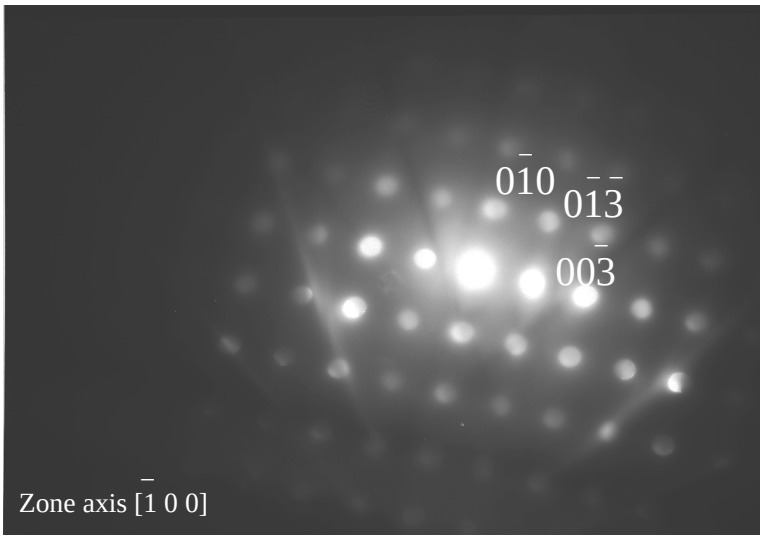

(b)

Figure 7.32: Precipitate CrNbN found in HCM2S steel after tempering at 500 °C for 960 h, a) carbon replica b) electron diffraction pattern from CrNbN.

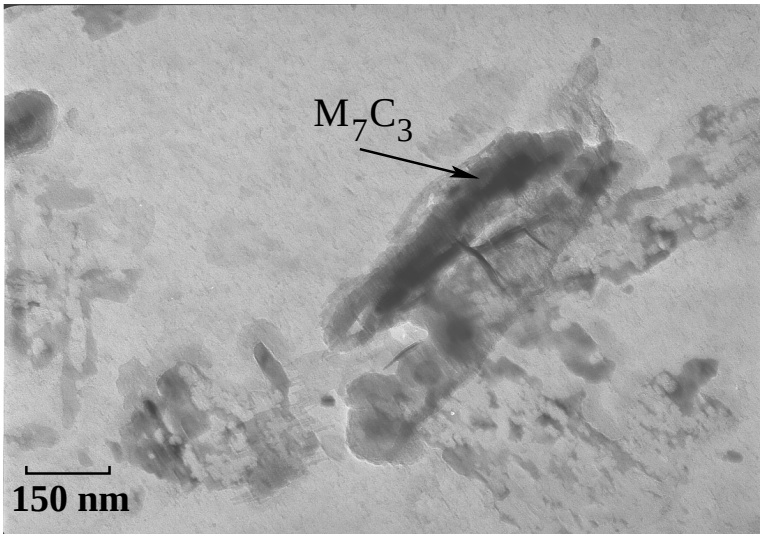

(a)

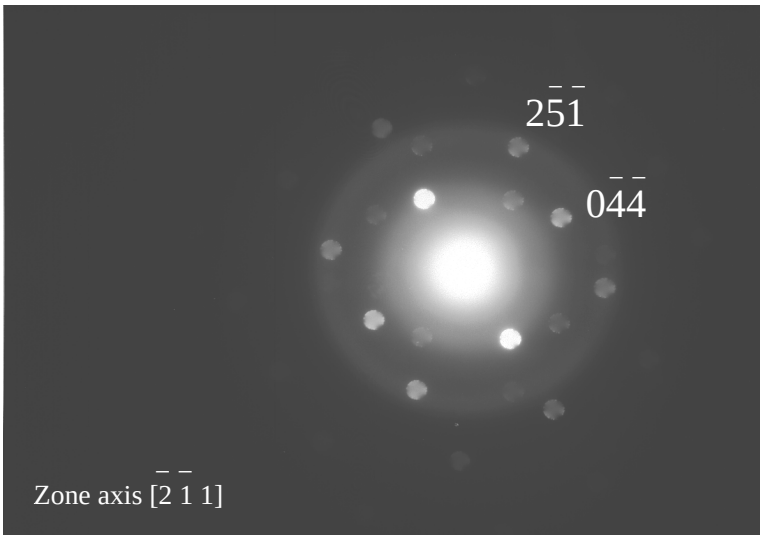

(b)

Figure 7.33: Precipitate M_7C_3 found in HCM2S steel tempered at 500 °C for 960 h, a) carbon replica b) electron diffraction pattern from M_7C_3.

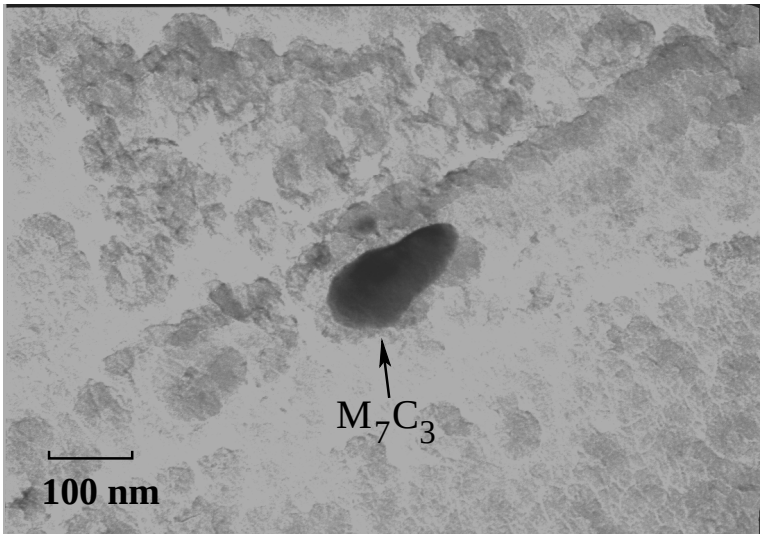

(a)

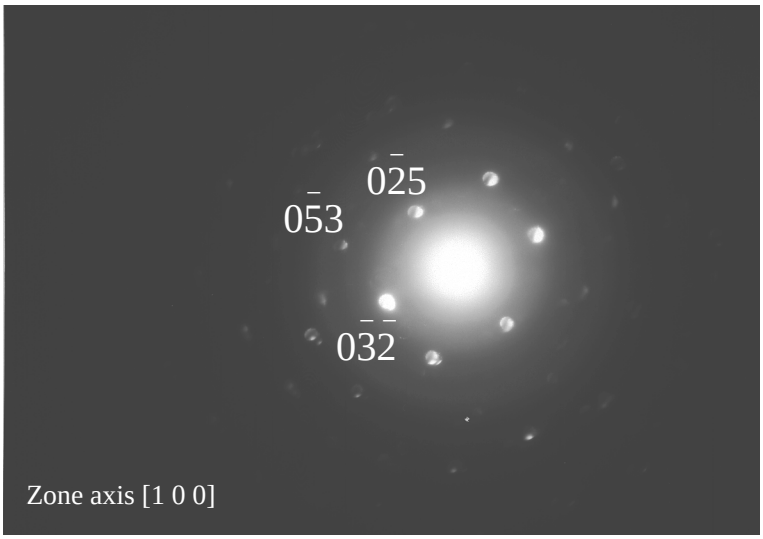

(b)

Figure 7.34: Precipitate M_7C_3 found in HCM2S steel tempered at 500 °C for 10,000 h, a) carbon replica b) electron diffraction pattern from M_7C_3.

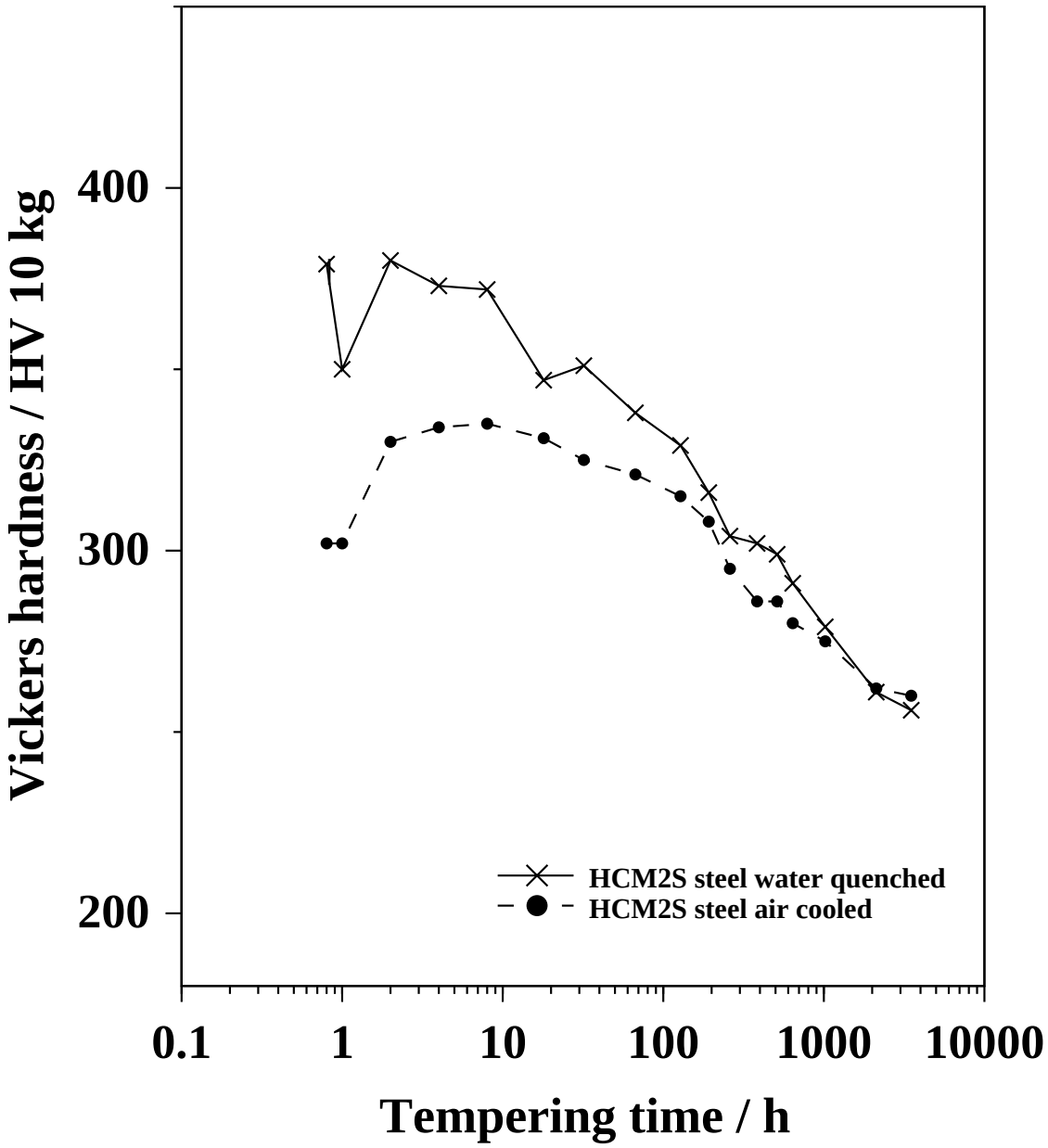

Figure 7.35: Hardness variation in HCM2S steel water quenched and air cooled from 1100 °C and tempered at 600 °C upto 3,500 h.

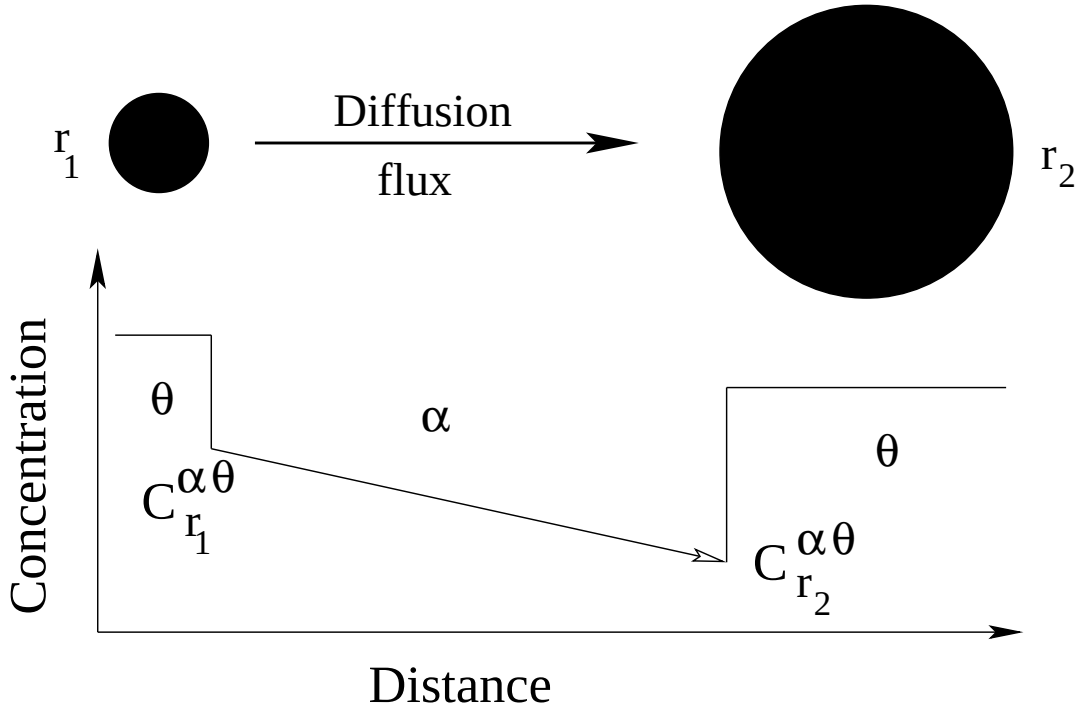

Figure 7.36: Schematic illustration of coarsening of precipitates [142]. α is the matrix, θ is the precipitate, $C^{\alpha\theta}$ is the solute concentration in matrix α and r_1 and r_2 are radii of small and large precipitates respectively.

Chapter 8

Summary and Suggestions for Further Work

The complexity of welding alloys has in the past prevented the development of generalised models capable of giving quantitative estimates of anything other than the most simple mechanical properties. It has been possible, using a neural network technique within a Bayesian framework, to develop a set of models dealing with the yield strength, ultimate tensile strength, ductility and impact toughness of weld metals as a function of the chemical composition and heat treatment. The models are based on a vast quantity of published experimental data which were all digitised and assessed for model development.

Neural networks are used in circumstances where the complexity is difficult to deal with using scientific principles. For this same reason, the trained networks cannot ever be fully tested since it is hard to imagine how multi–fold interactions between the inputs can affect the outcome. Nevertheless, an attempt was made to assess whether the networks reproduced the known physical metallurgy. For example, the effect of carbon and manganese on the yield strength of low–alloy weld deposits. In almost all cases considered, the networks could be shown to recognise known trends, taking into account the error estimates.

However, in some cases, such as when considering the effect of tungsten on the strength of low–alloy steel welds, it was evident that the models lacked knowledge to such an extent as to make the predictions unphysical. The situation was corrected by adapting steel data to represent welds, and the resulting model was demonstrated to behave properly. This example illustrates that the networks should not be used blindly but rather as an aid to design.

The combined set of models, together with experience from physical metallurgy, were then used to propose a new tungsten–containing welding alloy which can be used in circumstances where post–weld heat treatments are not practical. This proved to be successful at the first attempt; subsequently, the models have been used successfully by others in a similar way, to invent welding alloys without doing experiments.

The tempering resistance of the tungsten–containing weld has been studied experimentally and compared with that of a number of alloys. This work indicates that the replacement of molybdenum by tungsten in creep–resistant alloys leads to a lower as–deposited hardness which can be exploited to eliminate post–weld heat treatments. The creep strength can nevertheless (probably) be maintained by the use of vanadium.

The models developed here contain the chemical composition, welding heat input and heat treatment as inputs. These inputs effectively contain information about the microstructure. However, it would be useful to include microstructure directly. There are insufficient experimental data available to create a large enough dataset for analysis. Nevertheless, there are now physical models which can provide estimates of microstructure, at least for the so–called carbon–manganese alloys. In future work it would be useful to include *calculated* microstructural parameters, as well as chemical composition *etc.* as inputs in the neural network models in order to find relationships which are more physically meaningful.

Future work could focus on the development of a quantitative tempering theory since it is not yet possible to predict, using physical models, the tensile properties as a function of heat treatment following the deposition of the weld. This really is surprising given the enormous amount of published research on welds.

Appendix A

Estimation of Mechanical Properties of C–Mn Weld Metals, Avoiding Systematic Errors

In Chapters 4 and 5 essential mechanical properties of ferritic steel welds were modelled using neural network technique within a Bayesian framework. The data were collected from the published literature. As such the data originated from many different laboratories and possibly contained a variety of sources of experimental errors. By contrast, the data exploited here were on carbon–manganese and low–alloy steel welds from a single source (Evans [54]). It should therefore be possible to avoid unspecified systematic errors of the kind associated with a particular laboratory.

A.1 The Electrode Production

To study the effect of an element on the mechanical properties of weld metal requires high purity electrodes with accurate compositional control. It is very difficult to reproducibly maintain the transfer of alloying elements with conventional electrodes. The data used in the present work came from electrodes are specially manufactured with great care to detail. Rimmed steel with an average chemical composition shown in Table A.1 was selected as the core wire of an electrode. The flux contains 25% iron powder is selected and systematically mixed with other minerals to add microalloying elements which are to be studied and to keep some alloying elements such as Al, B, Nb, V and Ti below 0.0005 wt% in the final weld metal [2]. The multirun weld metal was made with three passes per layer, keeping dilution with the base metal to a minimum.

A.2 The Database

Around 720 individual experimental data of carbon–manganese multipass steel welds were compiled. The process used was shielded (manual) metal arc welding. The heat input was

Element	
Carbon (wt%)	0.07
Manganese (wt%)	0.50
Silicon (wt%)	0.008
Sulphur (wt%)	0.006
Phosphorus (wt%)	0.008
Titanium (p.p.m.)	4
Boron (p.p.m.)	2
Aluminum (p.p.m.)	15
Nitrogen (p.p.m.)	25
Oxygen (p.p.m.)	200
Chromium (wt%)	0.02
Nickel (wt%)	0.03
Molybdenum (wt%)	0.003
Vanadium (p.p.m.)	5
Copper (wt%)	0.02
Niobium (p.p.m.)	5

Table A.1: The average chemical composition of the core wire used to manufacture the electrode used in the present study. 'p.p.m.' corresponds to parts per million.

1.0 kJ mm^{-1} and the interpass temperature was 200 °C. With the exception of the Charpy impact toughness test samples, all of the other weld samples were given hydrogen removal heat treatments (200 °C for 14 h). All these experiments were done under identical conditions and data were measured by Evans [54]. The chosen input variables are tabulated in Table A.2; other variables such as heat input did not vary and hence were not included in the analysis. The input set was identical for all six models yield strength (YS), ultimate tensile strength (UTS), elongation, reduction in area and the Charpy impact toughness transition temperature at 100 J (T_{100J}) and 28 J (T_{28J}). Table A.2 shows the range, mean and standard deviation of all variables involved in model development.

The data distribution of each individual element with respect to yield strength are graphically represented in Figs A.1 and A.2. The output parameters UTS, elongation, reduction in area, T_{100J} and T_{28J} were plotted against YS in Fig. A.2. As discussed in Section 5.1.1, it was found that the difference in UTS and YS is constant. The higher strength welds will have a lower ductility. This can be found in elongation and reduction in area plots (Fig. A.2); it can be seen that the increase in yield strength leads to reduction in ductility.

Input element	Minimum	Maximum	Mean	Standard deviation
Carbon (wt%)	0.035	0.152	0.071	0.012
Manganese (wt%)	0.23	2.10	1.27	0.40
Silicon (wt%)	0.01	1.11	0.348	0.112
Sulphur (wt%)	0.003	0.046	0.0065	0.003
Phosphorus (wt%)	0.003	0.040	0.008	0.0027
Titanium (p.p.m.)	2.0	1000	105.7	142.62
Boron (p.p.m.)	1.0	200.0	16.5	39.4
Aluminum (p.p.m.)	1.0	680.0	38.7	108.0
Nitrogen (p.p.m.)	35.0	270.0	92.9	47.4
Oxygen (p.p.m.)	217.0	1180.0	398.1	90.1
Chromium (wt%)	0.03	3.5	0.166	0.50
Nickel (wt%)	0.03	5.48	0.34	1.05
Molybdenum (wt%)	0.005	1.16	0.068	0.228
Vanadium (p.p.m.)	3.0	2873.0	60.93	270.3
Copper (wt%)	0.02	2.04	0.076	0.251
Niobium (p.p.m.)	3.0	980.0	23.8	98.2
Yield strength (MPa)	350	1026	517.0	89.8
Ultimate tensile strength (MPa)	404	1123	588.9	90.0
Elongation (%)	10.5	35.8	25.6	3.9
Reduction in area (%)	21	87.8	75.3	5.3
Temperature (T_{100J}) at 100 J ($^\circ$C)	-89	45	-42.0	23.3
Temperature (T_{28J}) at 28 J ($^\circ$C)	-114	53	-67.3	20.9

Table A.2: The weld metal chemical composition used as input parameters and output variables to develop models. 'p.p.m.' corresponds to parts per million.

A.3 The Models

Six individual committee models for YS, UTS, elongation, reduction in area, T_{100J} and T_{28J} were developed. The committee model development procedure is similar for all these mechanical properties (Chapter 3). As the number of hidden units increases, the perceived level of noise σ_ν reduces, Fig A.3. It is interesting to note that the noise level is much lower than that of the levels found in the previously developed models (Chapter 4 and 5). This is because of the database comes from a single source. The other characteristics (log predictive error and test error) are shown in Fig. A.3. The details of the development of the neural network models are excluded for clarity, the procedure used is explained in Chapter 3.

A.4 The Analysis

The relevant input variables used to study the trends are shown in Table A.3. When the carbon concentration in weld metal is increased from 0.01 wt% to 0.07 wt%, there is an improvement

Input variable	
Carbon (wt%)	0.07
Manganese (wt%)	1.50
Silicon (wt%)	0.50
Sulphur (wt%)	0.006
Phosphorus (wt%)	0.008
Titanium (p.p.m.)	2.0
Boron (p.p.m.)	1.0
Aluminum (p.p.m.)	1.0
Nitrogen (p.p.m.)	80.0
Oxygen (p.p.m.)	300.0
Chromium (wt%)	0.03
Nickel (wt%)	0.03
Molybdenum (wt%)	0.005
Vanadium (p.p.m.)	3.0
Copper (wt%)	0.02
Niobium (p.p.m.)	3.0

Table A.3: Relevant inputs used to analyse mechanical properties of carbon–manganese weld metal. 'p.p.m.' corresponds to parts per million.

in mechanical properties, this is due to an initial improvement in microstructure [144]. In this range carbon promotes desirable acicular ferrite microstructure content at the expense of allotriomorphic ferrite and Widmanstätten ferrite. At higher carbon levels there is a decrease in toughness due to an increase in strength without improvement in microstructure. The effect of increasing carbon content is shown in Fig. A.13, as expected, carbon increases the strength and decreases the ductility of the weld metal. The amount of increase depends on other acicular ferrite promoting alloying elements such as manganese, molybdenum, nickel and chromium. Fig. A.14 shows that manganese improves toughness in the initial stages by decreasing the transition temperature, as well as increasing strength. The combined effects of carbon and manganese are shown in Fig. A.15. It is interesting to note that there is a gradual decrease in toughness and then an increase with increasing in carbon and manganese content. This is because, that at higher carbon and manganese levels, the acicular ferrite fraction increases, this is shown in Table A.4. These calculations were done using a published semi–empirical model [90], which enables us to calculate microstructural fractions in multirun welds. Here it can be noticed that the acicular ferrite and bainite microstructural fractions increased from 0.31 to 0.72 as the carbon content changed from 0.04 wt% to 0.14 wt% in 2.0 wt% manganese weld metal, even though there was an increase in strength. On the other hand, in 0.5 wt% manganese the amount

of acicular ferrite and bainitic microstructure is less than in 2.0 wt% manganese.

Carbon (wt%)	Manganese (wt%)	Allotriomorphic ferrite	Widmanstätten ferrite	Acicular ferrite and Bainite	Yield strength (MPa)
0.04	0.5	0.73	0.19	0.08	397
0.14	0.5	0.30	0.11	0.52	440
0.04	2.0	0.41	0.27	0.31	523
0.14	2.0	0.14	0.03	0.72	587

Table A.4: The microstructural fractions in carbon–manganese weld metal calculated using physical model [90].

It is well known fact that nickel improves low temperature toughness by increasing the stacking fault energy and making flow of dislocations easier, thereby discouraging cleavage fracture. In Section 5.2 it was found that nickel improves low–temperature toughness at lower manganese concentrations only. This was predicted by this model, Fig. A.16 shows that at lower manganese levels both the strength and toughness are increasing. When comparing the effect of nickel in 0.5 wt% and 1.5 wt% manganese welds (Fig. A.17) at the same strength, an increase in nickel concentration causes deterioration in toughness at higher manganese contents, whereas at lower manganese content it improves toughness.

A comparative analysis was done between the predictions made by a previously Charpy impact toughness model (Section 5.2) and the present carbon–manganese models. Figs A.18 and A.19 show that at lower manganese contents nickel is effective in improving the low–temperature toughness. Here the error bars cannot be compared as their units are different. This has shown that even though the Charpy impact toughness model was developed on a wide variety of weld metals, it is able to fit a non–linear function for a particular system of weld metals without affecting predictions over other classes of weld metals.

In weld metal, titanium forms oxides and protects boron (if added) from atmospheric oxygen [145, 95]. These oxides act as nucleation sites for the formation of acicular ferrite. Titanium being a strong carbide former, increases the strength by precipitation hardening. Fig. A.20 shows the expected trends, toughness was improved with initial small additions of titanium.

Oxygen forms oxide inclusions in weld metal, at low levels of oxygen in weld metal these inclusions are beneficial in promoting acicular ferrite in the presence of oxide forming elements such as titanium. At higher levels of oxygen, the increased density of oxides assists fast propagation of cracks, thereby reducing the overall ductility. Acicular ferrite microstructure offers more resistance to crack propagation, therefore the crack has to travel a greater distance before it reaches the critical length which leads to fracture. The effect of titanium in presence of varying amounts of oxygen is shown in Fig. A.21. Initial small additions of titanium promote acicular

ferrite, thus increasing toughness.

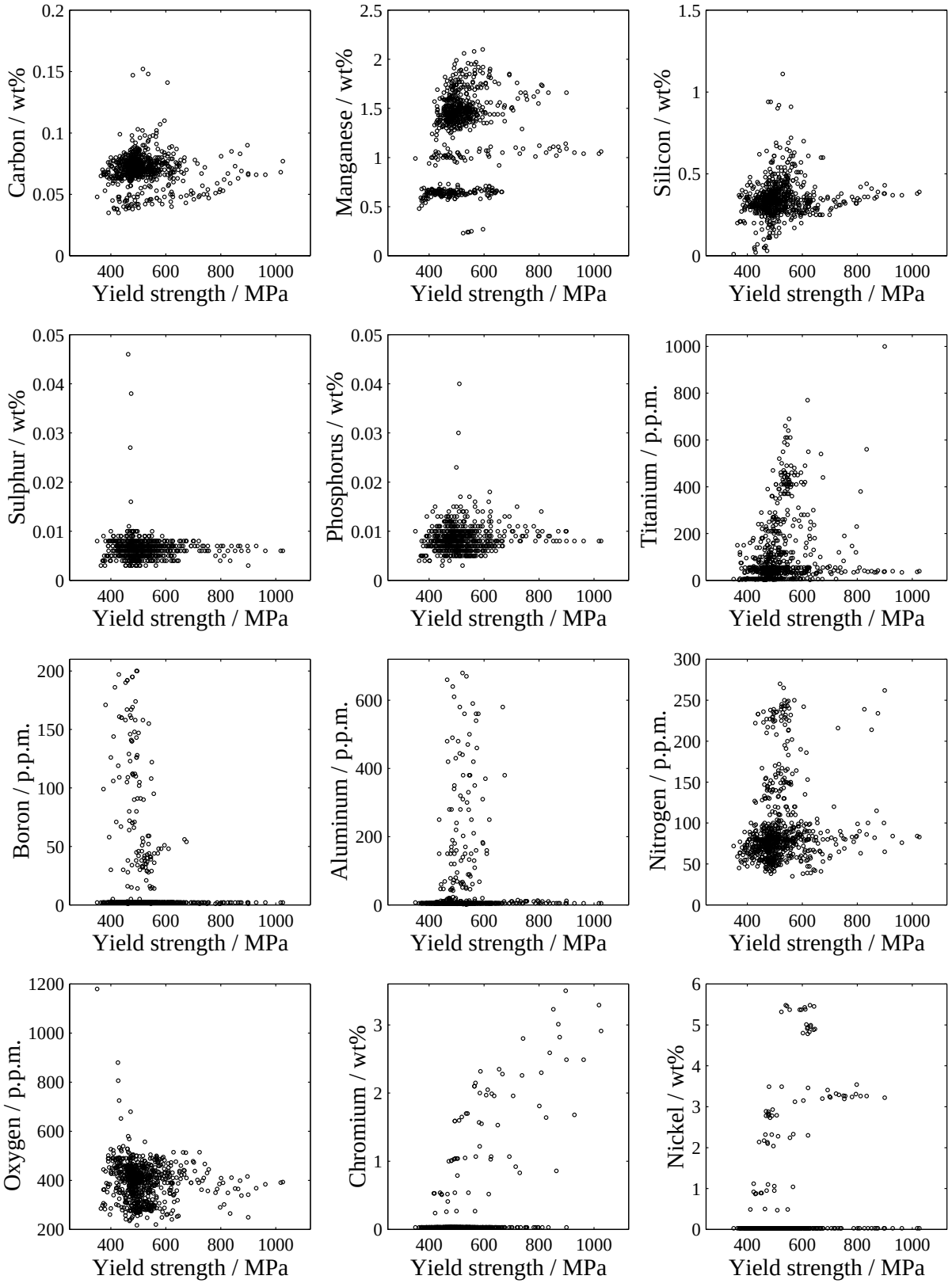

Figure A.1: The data distribution plotted against yield strength. 'p.p.m.' corresponds to parts per million by weight.

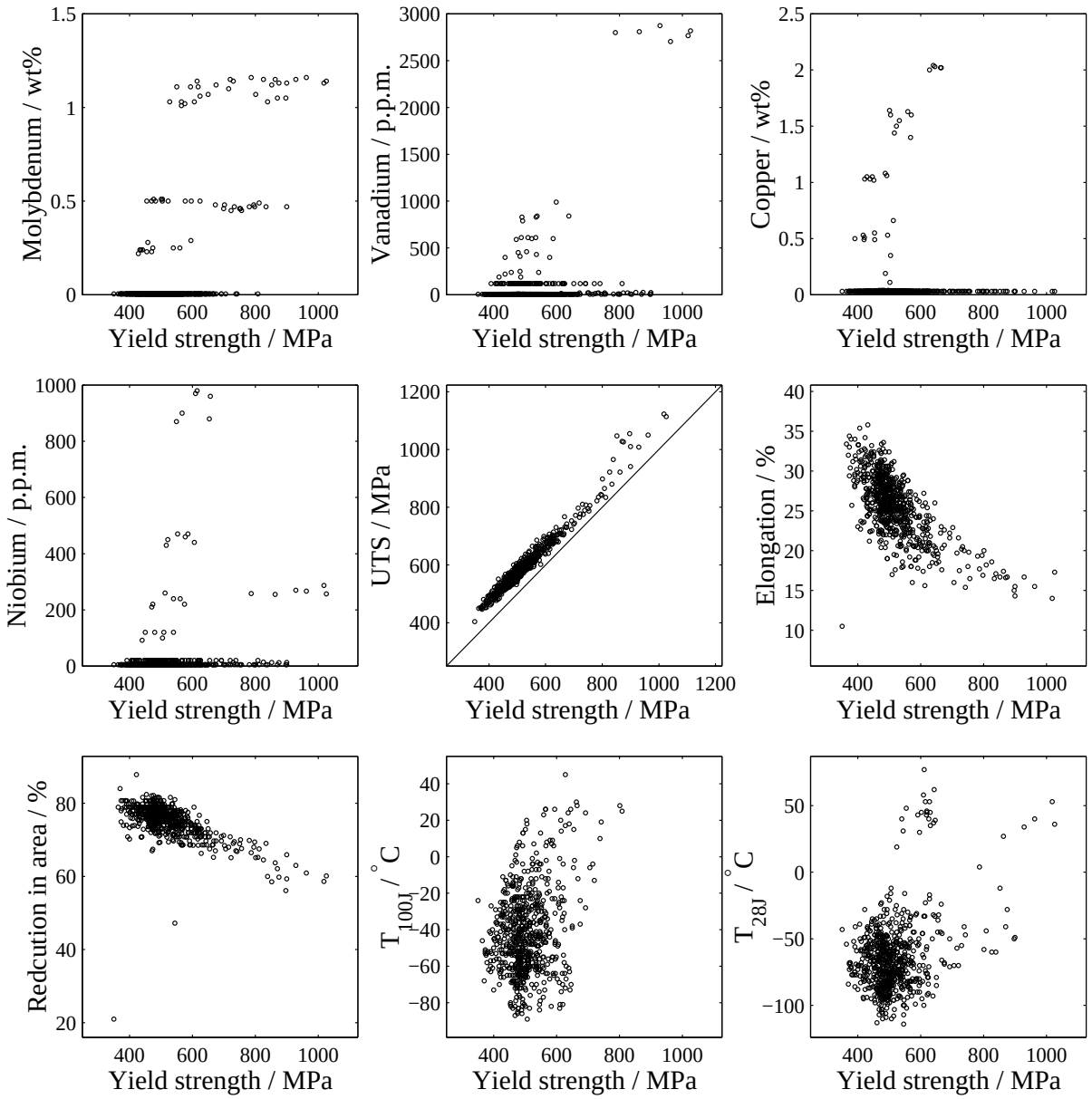

Figure A.2: Distribution of molybdenum, vanadium, copper, niobium against yield strength. The spread of UTS, elongation, reduction in area, T_{100J} and T_{28J} plotted against yield strength. 'p.p.m.' corresponds to parts per million by weight.

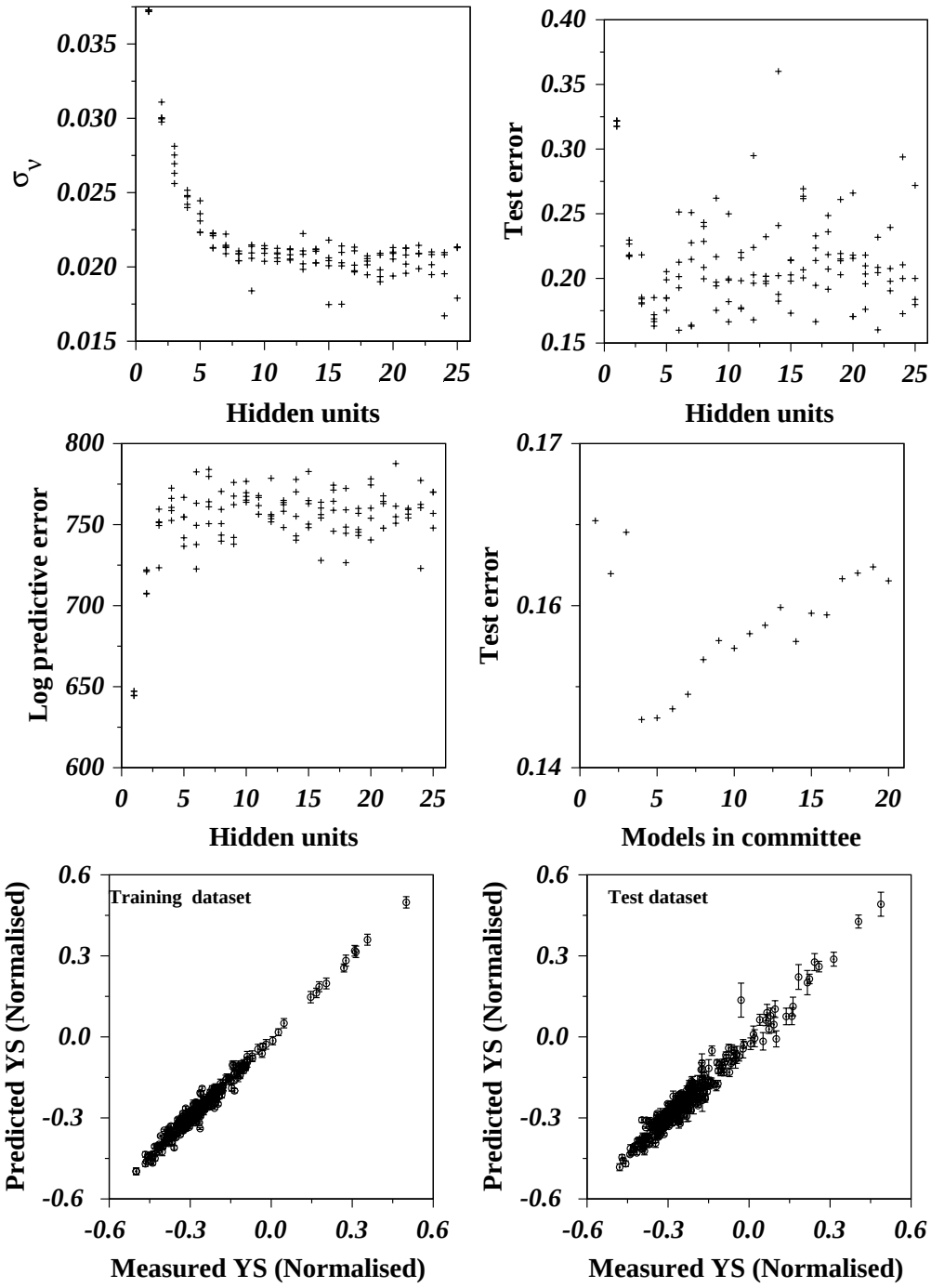

Figure A.3: Characteristics of the yield strength model.

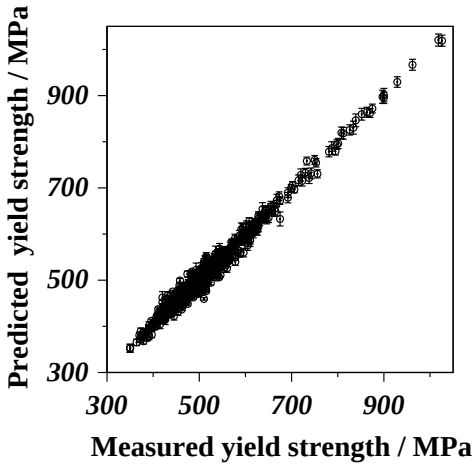

Figure A.4: Characteristics of the yield strength model.

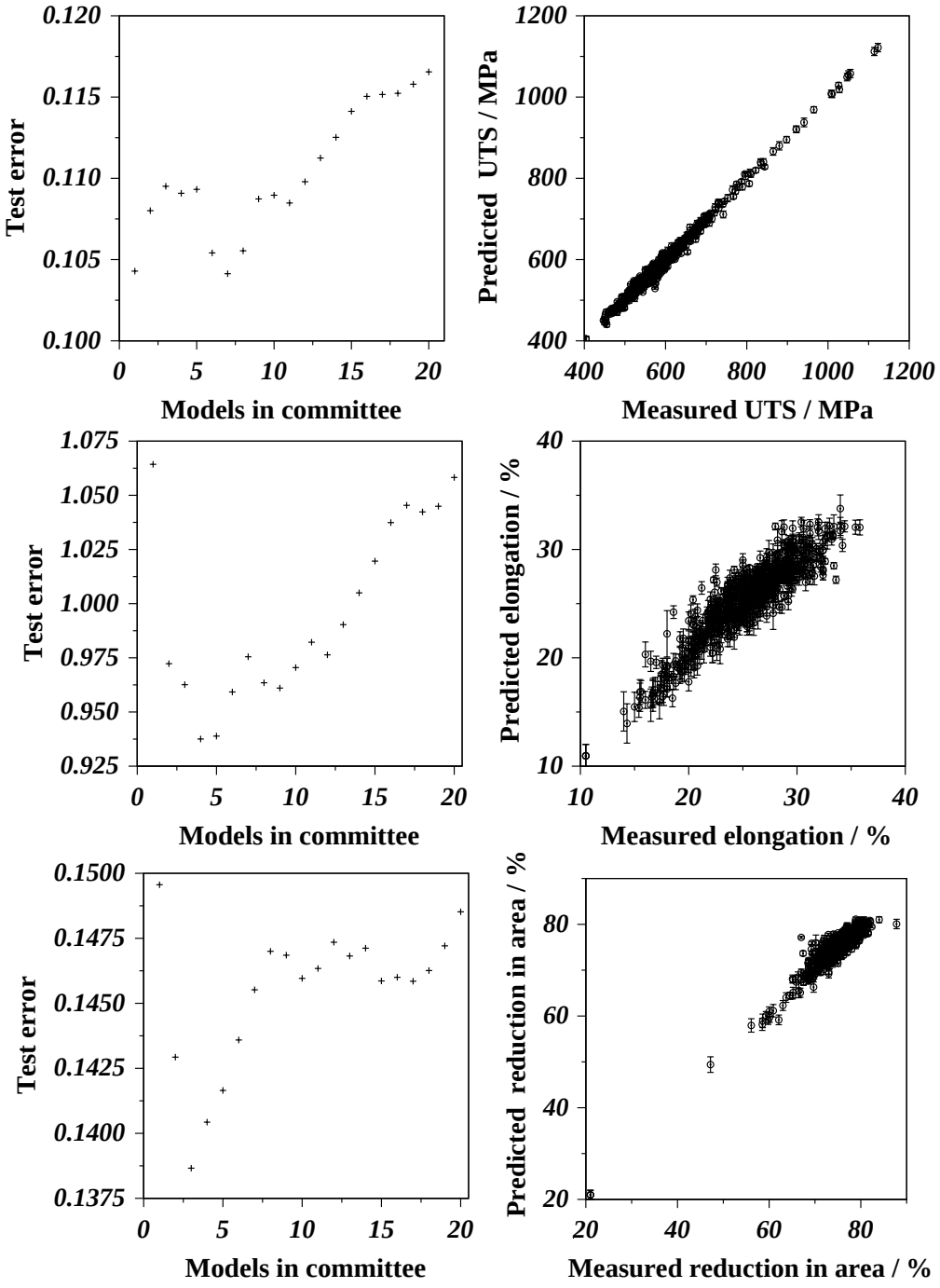

Figure A.5: Characteristics of the ultimate tensile strength, elongation and reduction in area models.

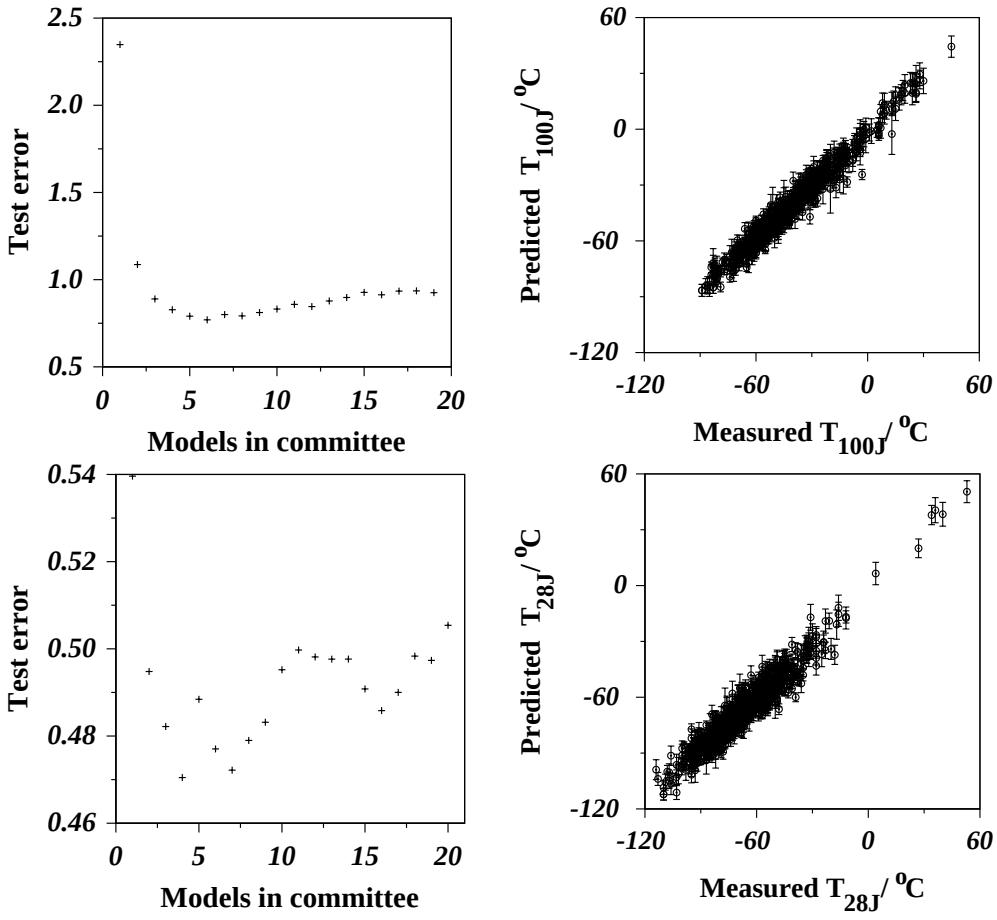

Figure A.6: Characteristics of toughness models, transition temperatures at 100J and 28J of Charpy toughness.

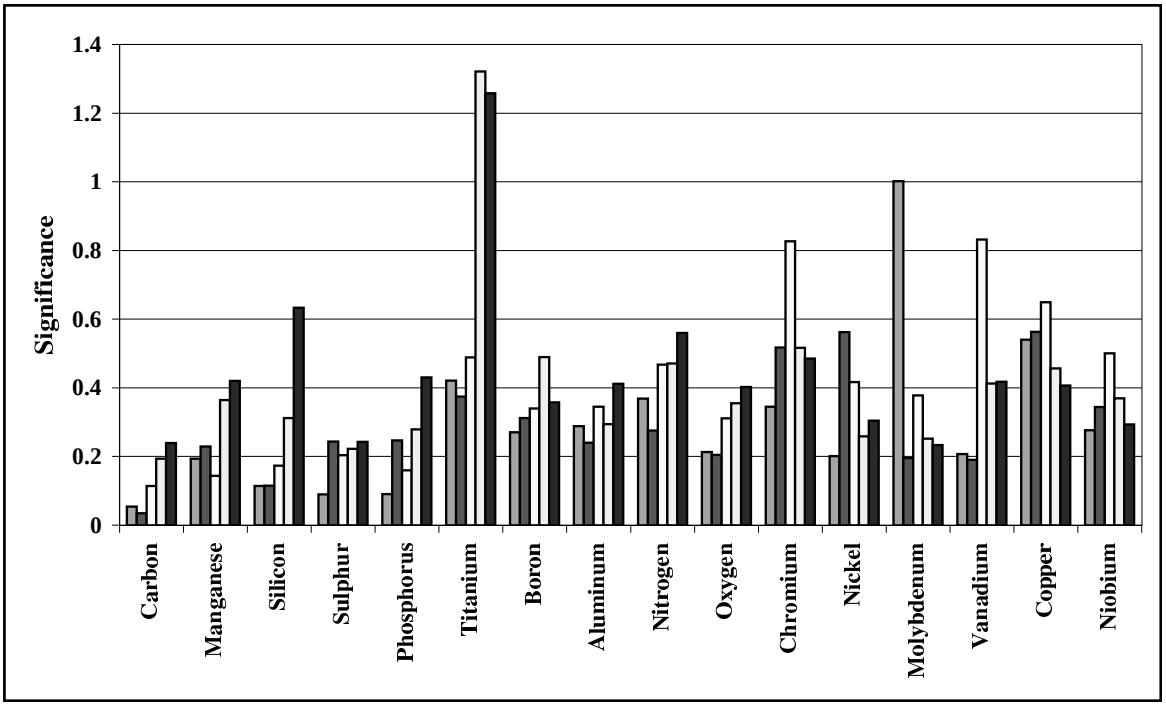

Figure A.7: The perceived significance σ_w values of yield strength committee models for each of the inputs.

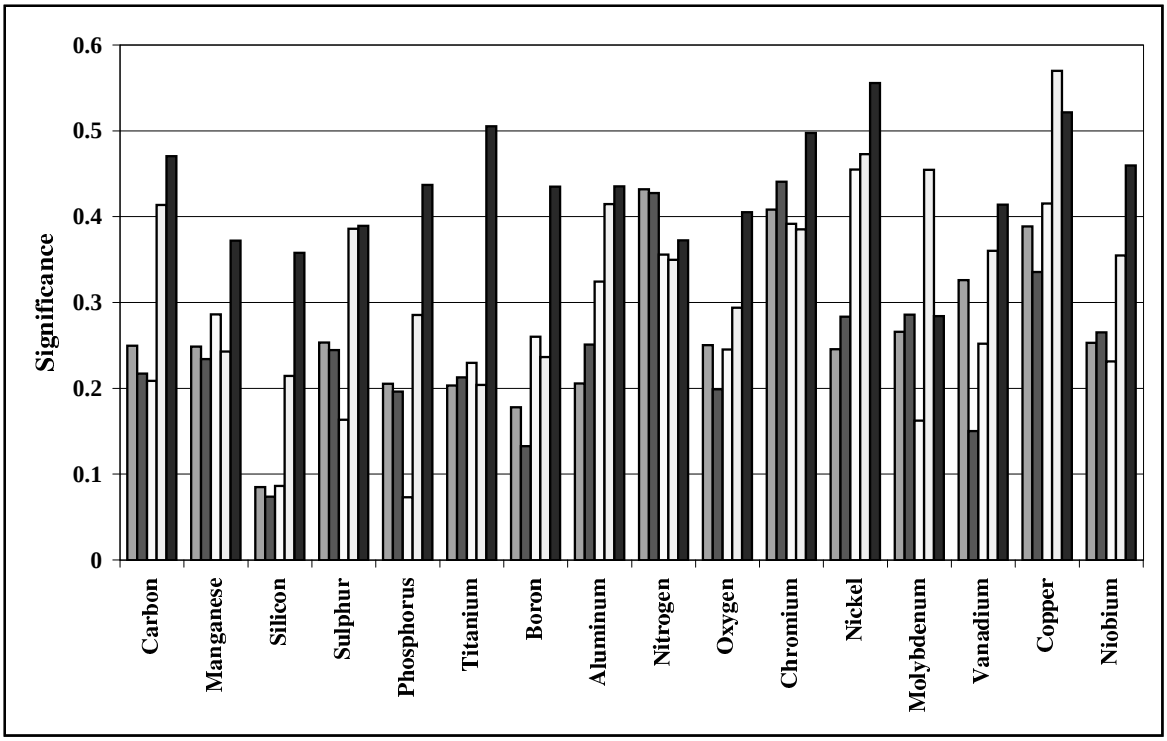

Figure A.8: The perceived significance σ_w values of ultimate tensile strength committee models for each of the inputs.

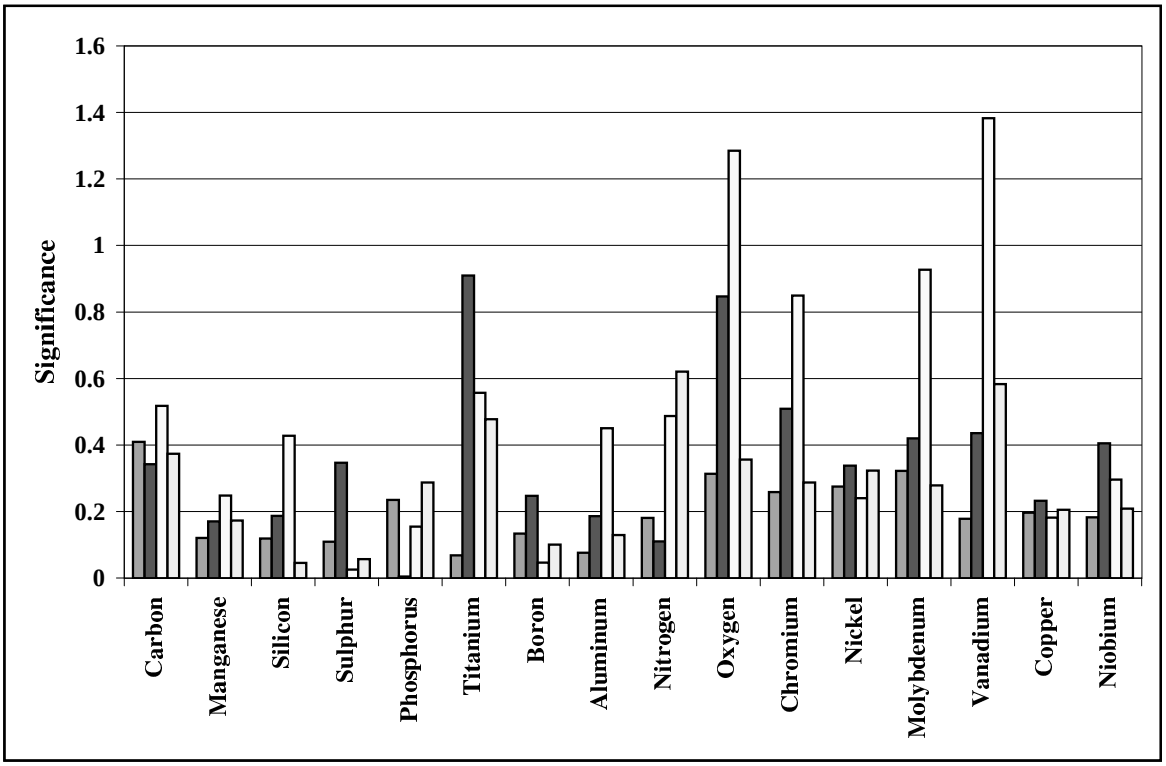

Figure A.9: The perceived significance σ_w values of elongation committee models for each of the inputs.

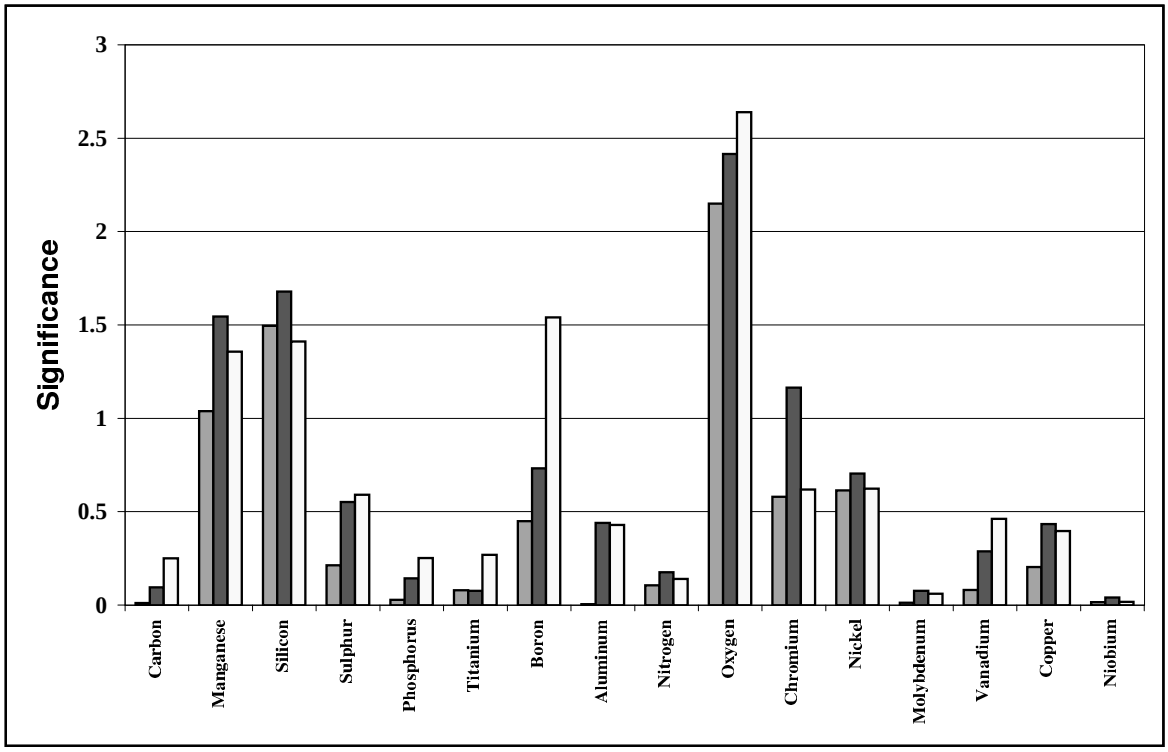

Figure A.10: The perceived significance σ_w values of reduction in area committee models for each of the inputs.

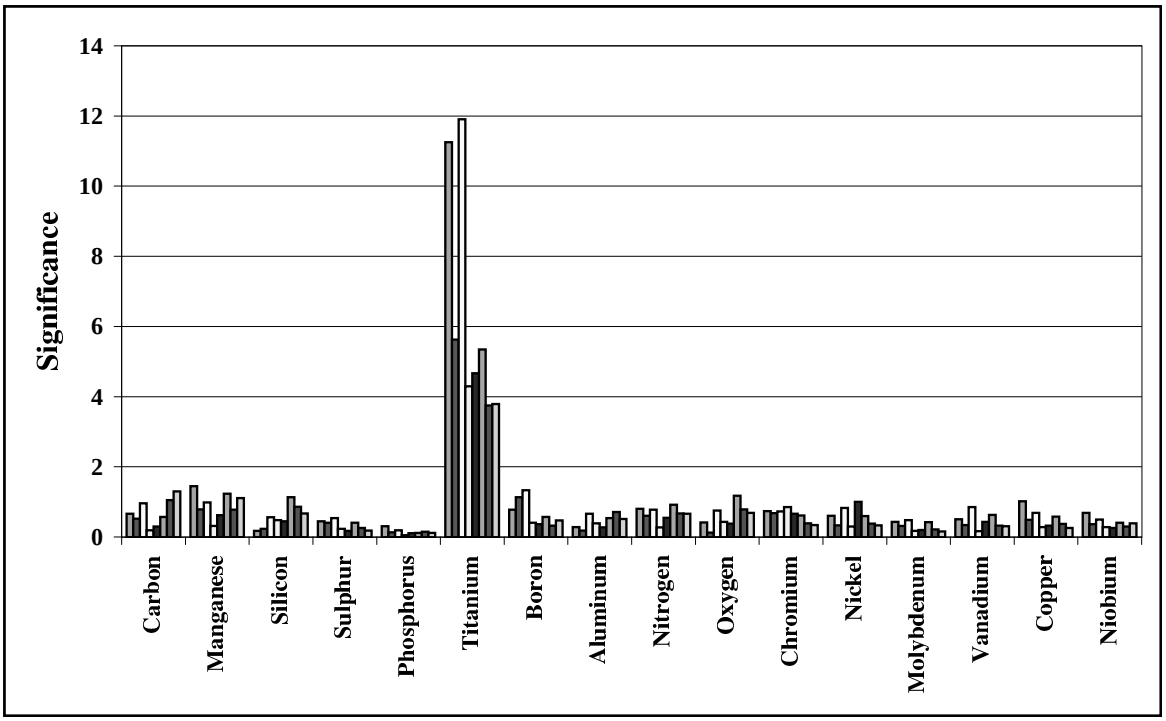

Figure A.11: The perceived significance σ_w values of T_{100J} committee models for each of the inputs.

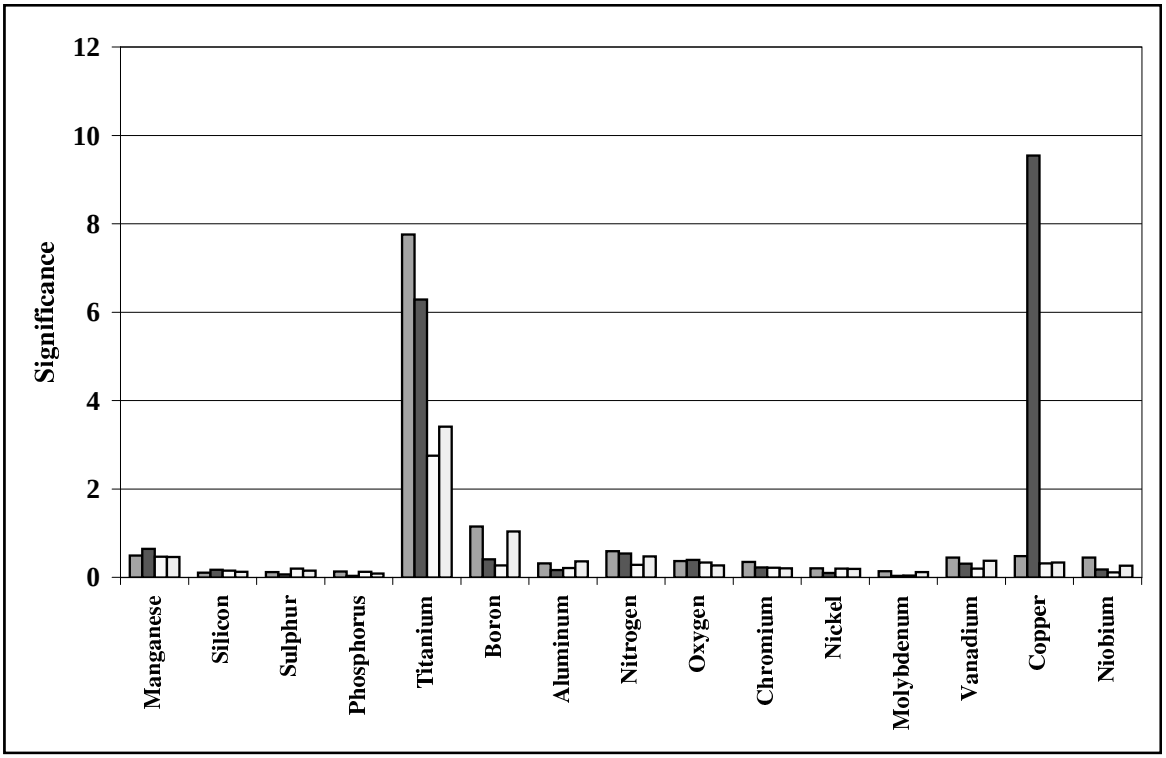

Figure A.12: The perceived significance σ_w values of T_{28J} committee models for each of the inputs.

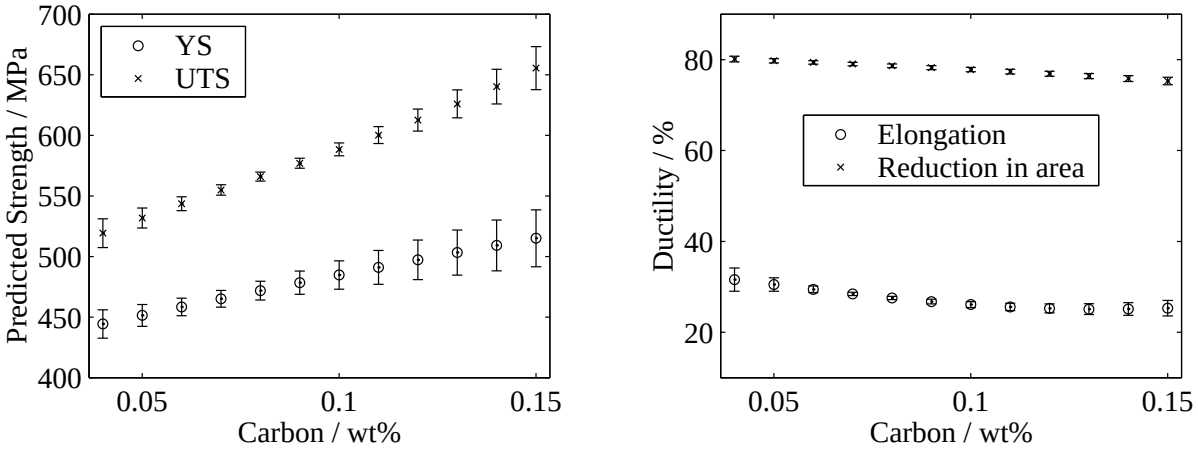

Figure A.13: The calculated effect of carbon on strength and ductility.

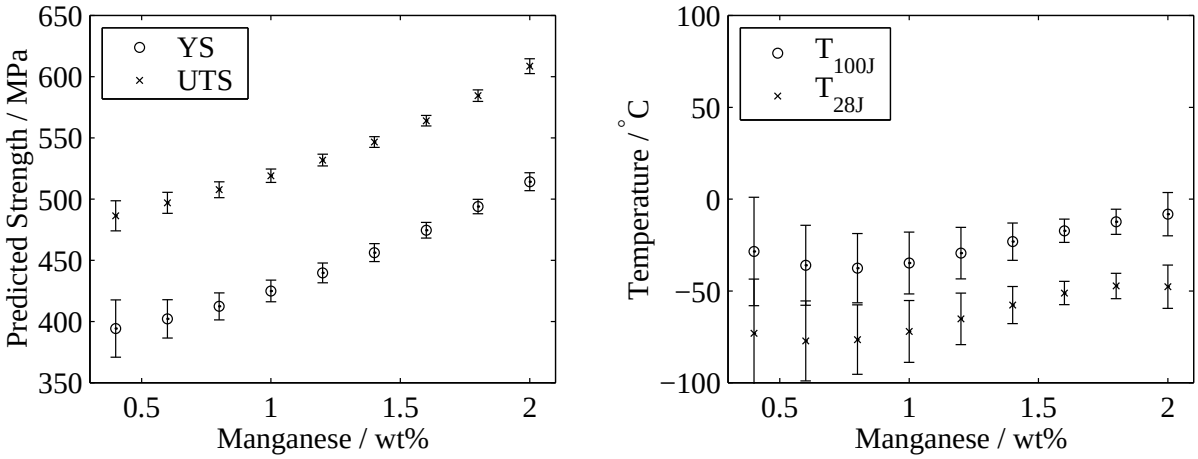

Figure A.14: The effect of manganese on strength and toughness.

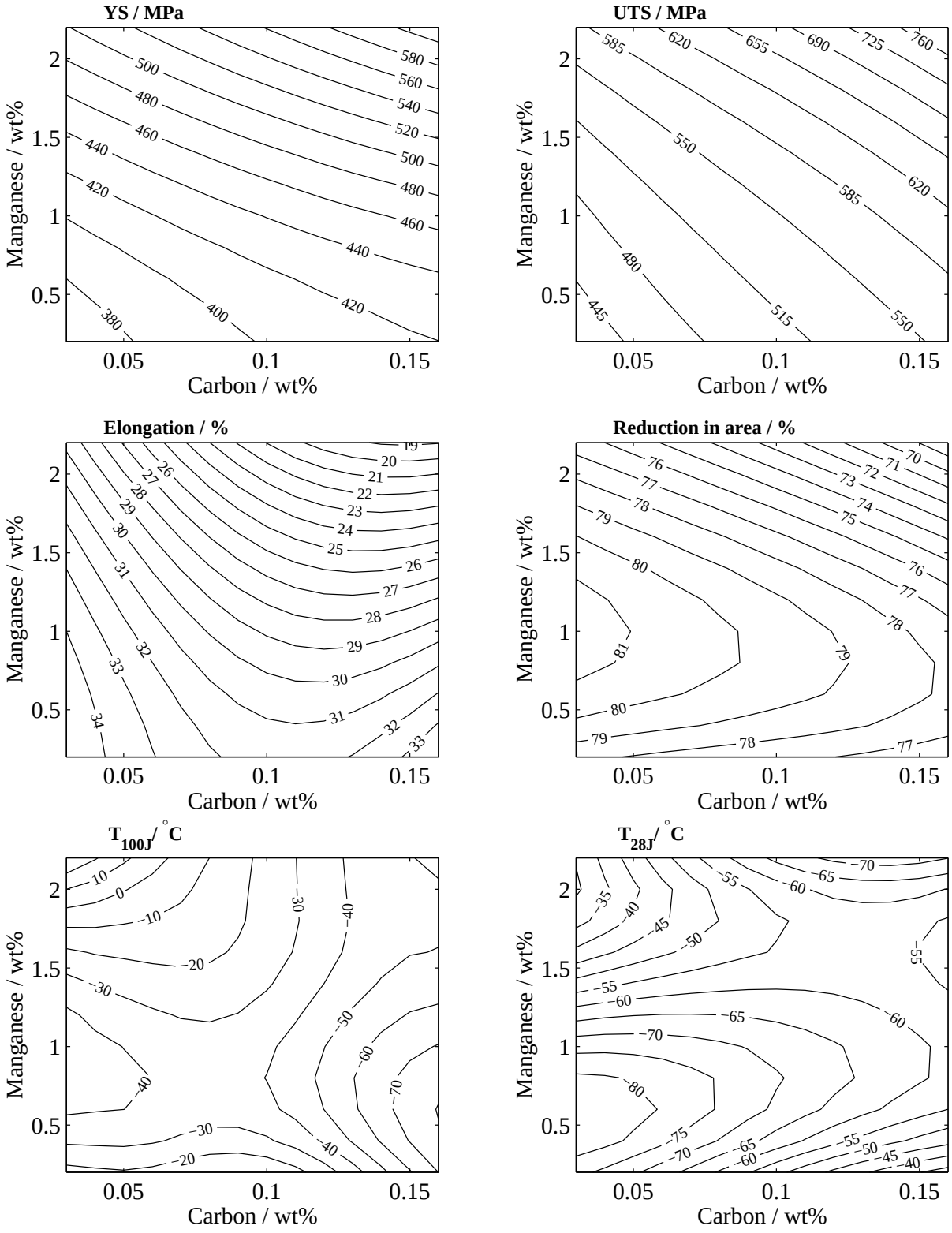

Figure A.15: The combined effect of carbon and manganese on mechanical properties of C–Mn weld metals.

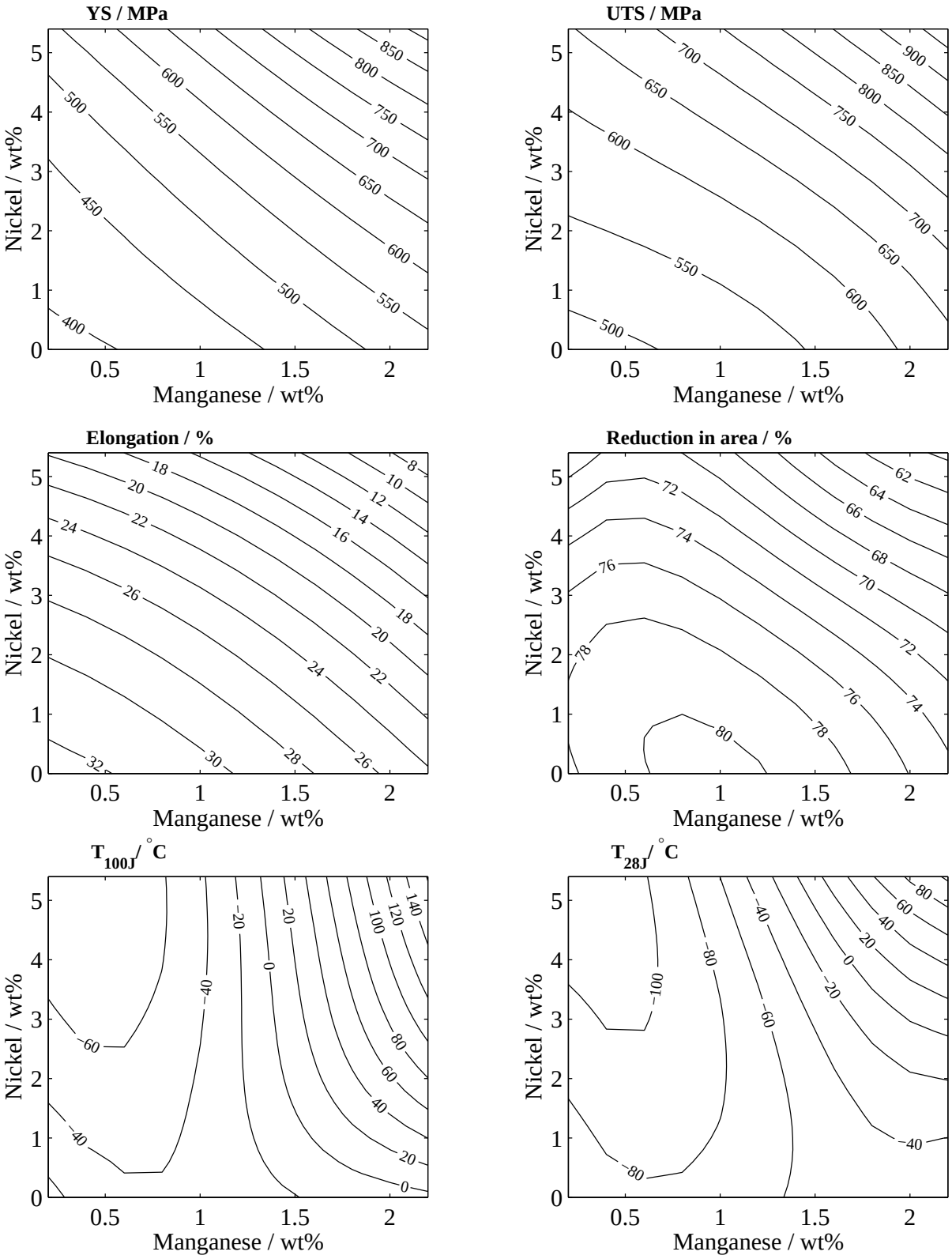

Figure A.16: Calculated mechanical properties of welds with respect to change in nickel and manganese.

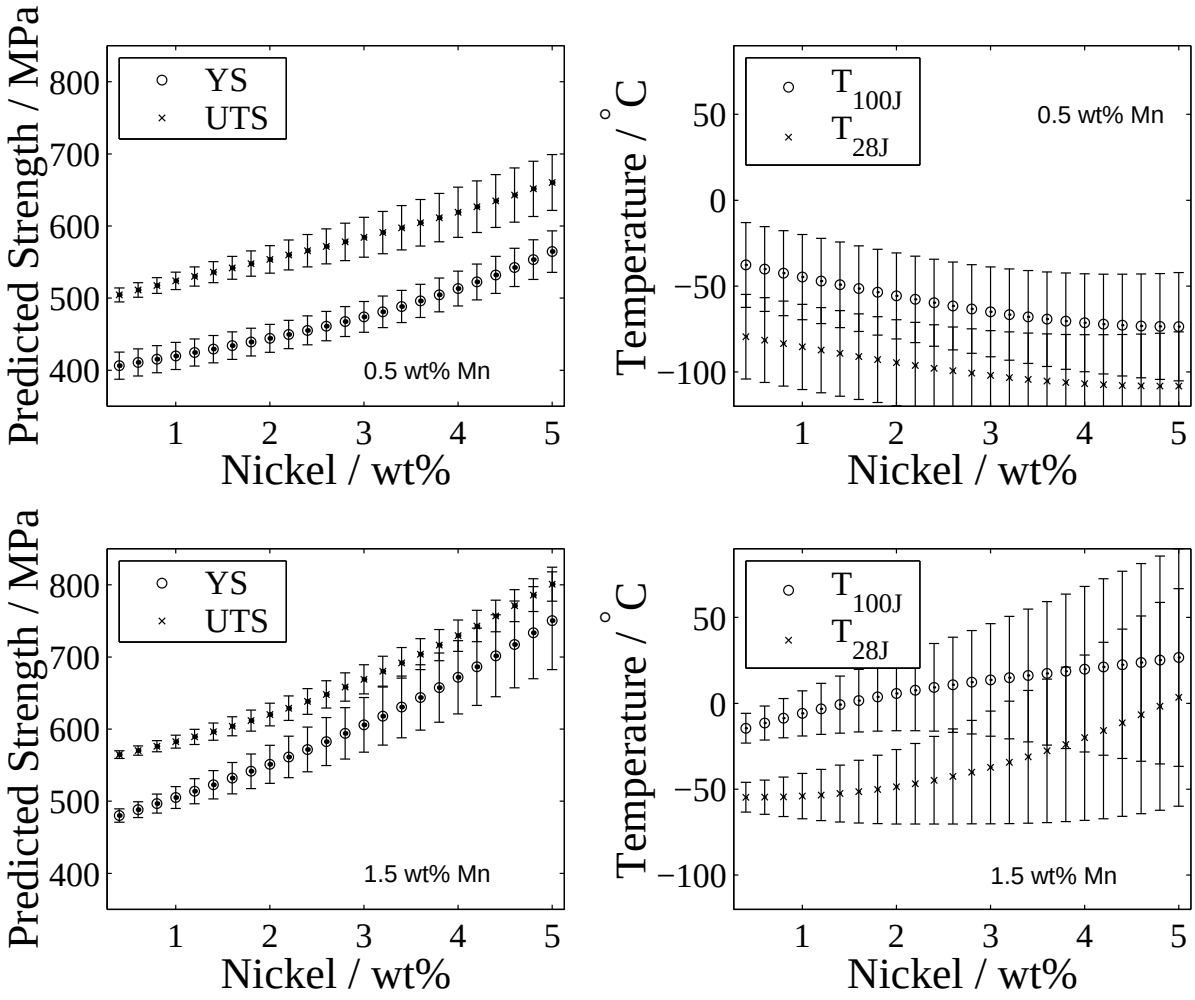

Figure A.17: Calculated strength and transition temperature in 0.5 wt% and 1.5 wt% manganese weld metal.

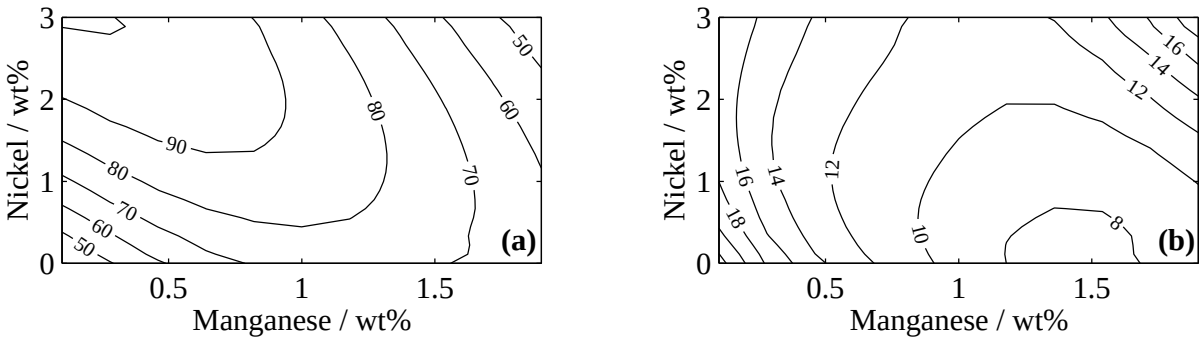

Figure A.18: Calculated Charpy impact toughness of welds with respect to change in nickel and manganese using Charpy impact toughness model (Section 5.2) a) Charpy toughness in Joule, b) the corresponding error bars in Joule.

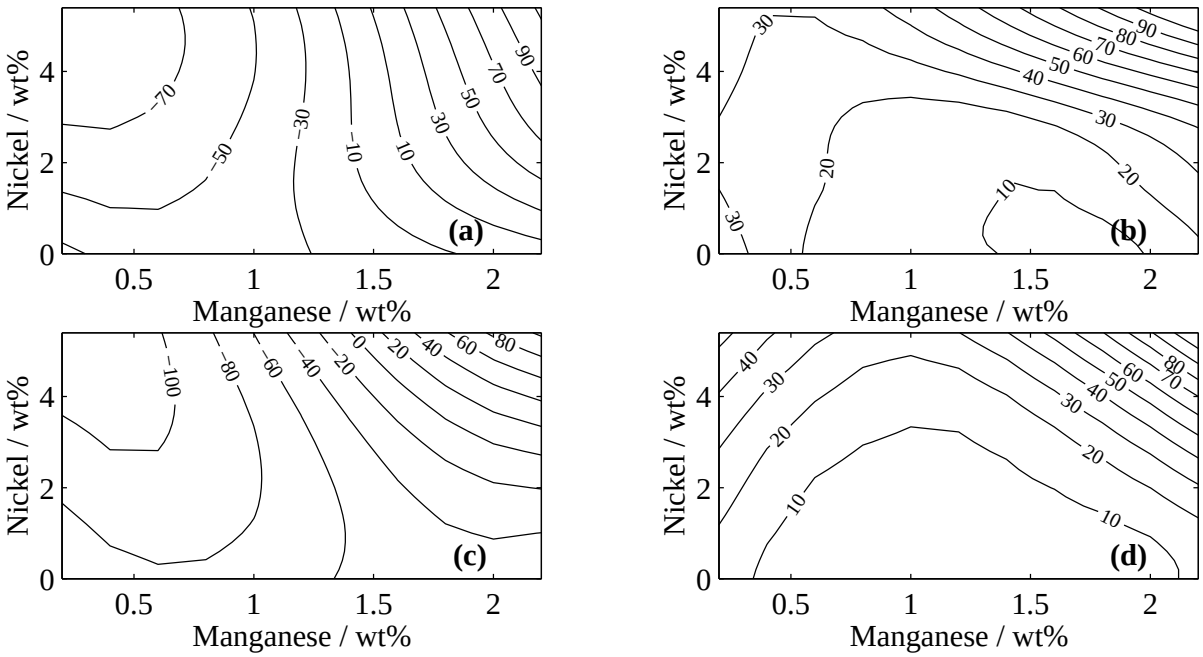

Figure A.19: Calculated Charpy impact toughness transition temperature of welds with respect to change in nickel and manganese using Carbon–Manganese weld metals model, a) transition temperature in °C at 100 J, b) the corresponding error bars in °C and c) transition temperature in °C at 28 J, d) the corresponding error bars in °C.

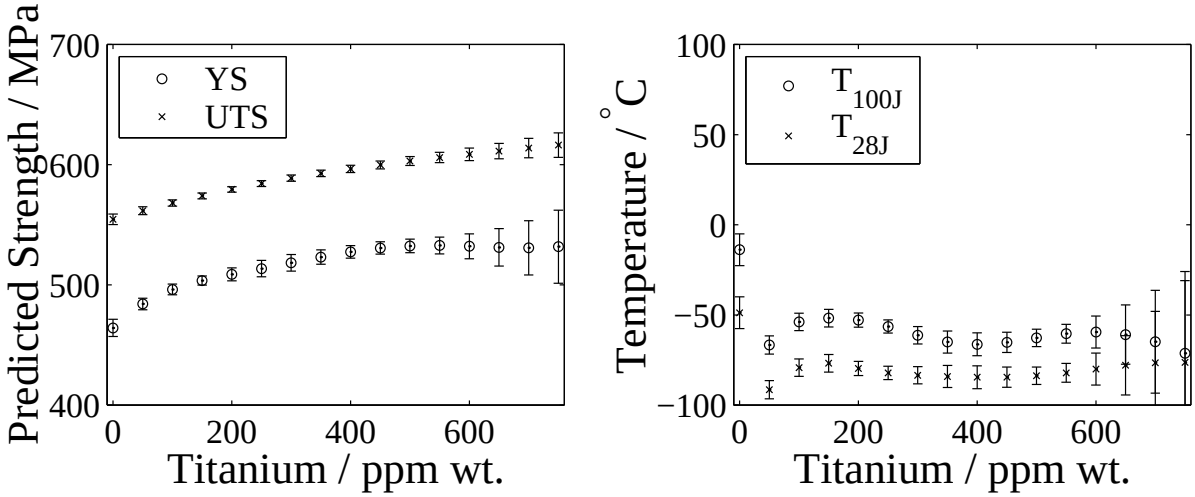

Figure A.20: Calculated mechanical properties of welds with respect to change in titanium content in weld metal.The contour plot curves represents impact toughness in J.

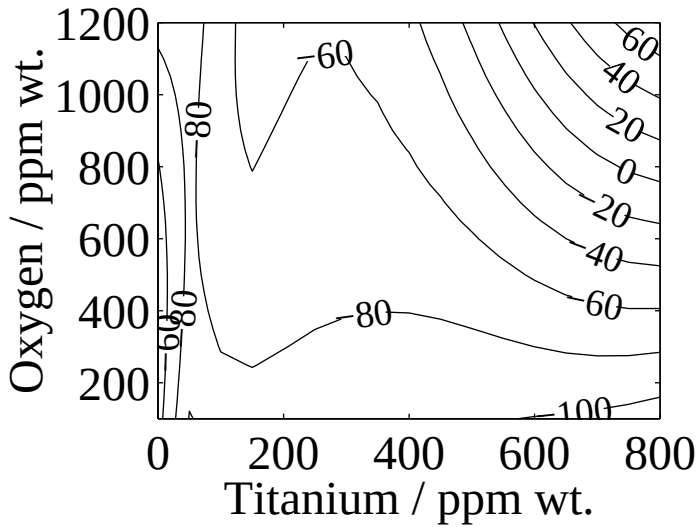

Figure A.21: Combined effect of oxygen and titanium on transition temperature at Charpy impact toughness of 28 J. The contour plot curves represents temperature in °C.

Appendix B

Design of Novel Weld Metals

A variety of commercial and experimental weld metals have been designed using the models developed in the present work. This appendix shows two examples of alloys developed using the models described in the thesis.

B.1 New Weld Design in Nippon Steel

The Nippon Steel Welding Company was able to develop novel high strength welding alloys in response to customer demands, by calculating the effect of molybdenum on the strength of welds and without doing any prior experiments. Kazutoshi Ichikawa (Nippon Steel, Japan) had the task to develop weld metal for the manual metal arc welding (MMAW) and submerged arc welding (SAW) processes for thick plates (upto 80 mm).

He demonstrated first that the models could predict the ultimate tensile strength of existing alloys already marketed by his company to great accuracy, Fig. B.1. He needed to raise the UTS to around 750 MPa so he chose to increase the molybdenum to 0.6 wt%. When the actual weld was made, (Table B.1) and the results matched predictions. Thus Nippon Steel Welding Products and Engineering Co. Ltd. was then able to commercialise and patent the new electrode.

B.2 Further Applications

Scientists at ESAB AB (Sweden) have been searching for strong and tough weld metals for submarine applications. Marimuthu [146] had designed welds for this purpose using the models described in this thesis. The expected and actual results are tabulated in Table B.2. It is heartening to find that the models are able to extrapolate to 9 wt% nickel even though the maximum nickel concentration in the database used to create the models is 4.8 wt% (Table 4.1).

As a result of this work, an interaction has been discovered between manganese and nickel which leads to a remarkable improvement in toughness. This has been demonstrated experi-

Input variable	MMAW
C (wt%)	0.078
Si (wt%)	0.38
Mn (wt%)	1.37
S (wt%)	0.003
P (wt%)	0.011
Ni (wt%)	0.64
Cr (wt%)	0.03
Mo (wt%)	0.57
V (wt%)	0.004
Cu (wt%)	0.012
Co (wt%)	0.0
W (wt%)	0.0
O (p.p.m.)	247
Ti (wt%)	150
B (p.p.m.)	$\leq$3
Nb (p.p.m.)	30
Heat input(kJ mm^{-1})	1.85
Interpass temperature ($^{\circ}$C)	100
Tempering temperature ($^{\circ}$C)	20
Tempering time (h)	0.0
Predicted UTS(MPa)	760
Measured UTS (MPa)	771

Table B.1: Comparison between the designed and experimental results of new weld metal designed for Nippon Steels, Japan.

mentally but the details cannot be described here for commercial reasons.

B.3 Software

All the models and programs developed can be accessed on the world wide web;

YS and UTS models:

http://www.msm.cam.ac.uk/map/neural/programs/weldmetalyu-b.html

Elongation and Charpy impact toughness models:

http://www.msm.cam.ac.uk/map/neural/programs/weldmetalec.html

27 J Charpy toughness transition temperature model:

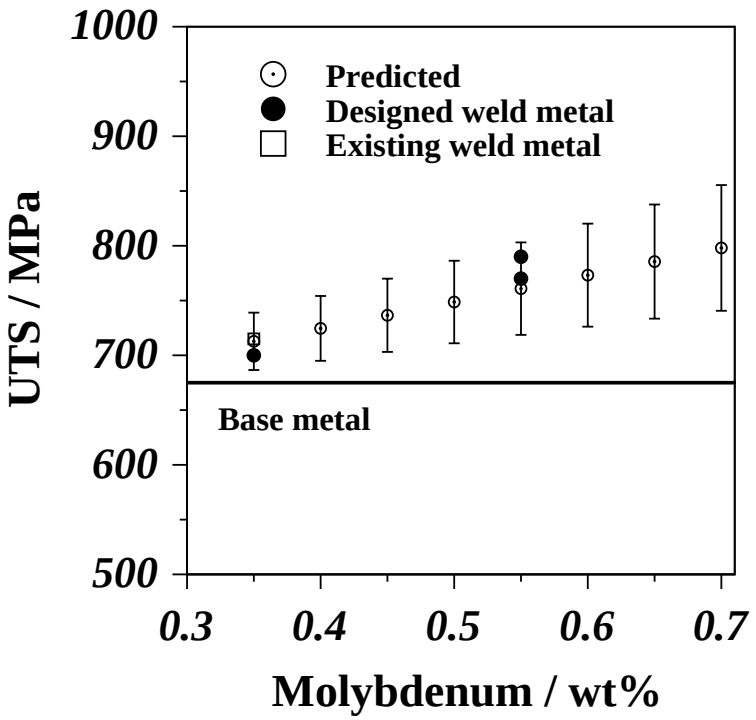

Figure B.1: Effect of molybdenum on ultimate tensile strength.

http://www.msm.cam.ac.uk/map/neural/programs/weldmetalT27J.html

Temper embrittlement model:

http://www.msm.cam.ac.uk/map/neural/programs/weldmetalEmb.html

Analysis of electron diffraction patterns program:

http://www.msm.cam.ac.uk/map/crystal/programs/crystal2.html

□

Input variable	Proposed	Actual
C (wt%)	0.030	0.030
Si (wt%)	0.29	0.35
Mn (wt%)	2.09	2.18
S (wt%)	0.012	0.007
P (wt%)	0.005	0.010
Ni (wt%)	7	7.2
Cr (wt%)	0.43	0.34
Mo (wt%)	0.59	0.63
V (wt%)	0.019	0.13
Cu (wt%)	0.03	0.03
Co (wt%)	0.0	0.009
W (wt%)	0.0	0.004
O (p.p.m.)	267	370
Ti (wt%)	0.014	0.013
B (p.p.m.)	0.0005	0.0006
Nb (p.p.m.)	0.0	10
Heat input(kJ mm^{-1})	1.0	1.14
Interpass temperature ($^{\circ}$C)	200	200
Tempering temperature ($^{\circ}$C)	250	250
Tempering time (h)	14	14
YS (MPa)	814 ± 179	789

Table B.2: Comparison between the proposed and actual properties of C–Mn–Ni weld metal. 'p.p.m.' corresponds to parts per million by weight.

References

[1] Bhadeshia, H. K. D. H., in *Mathematical Modelling of Weld Phenomena-3*, edited by H. Cerjak and H. K. D. H. Bhadeshia (The Institute of Materials, London, UK, 1997), pp. 229–284.

[2] Evans, G. M. and Bailey, N., *Metallurgy of Basic Weld Metal* (Abington Publishing, Cambridge, UK, 1997).

[3] Bhadeshia, H. K. D. H., *Modelling of steel welds*, Materials Science and Technology **8**, 123 (1992).

[4] Young, C. H. and Bhadeshia, H. K. D. H., *Strength of mixtures of bainite and martensite*, Materials Science and Technology **10**, 209 (1994).

[5] Sugden, A. A. B. and Bhadeshia, H. K. D. H., in *Proccedings of the 2nd International conference on trends in welding research, International trends in welding Science and Technology*, edited by S. A. David and J. M. Vitek (ASM International, Materials Park, Ohio, USA, 1989), pp. 745–748.

[6] MacKay, D. J. C., in *Mathematical Modelling of Weld Phenomena-3*, edited by H. Cerjak and H. K. D. H. Bhadeshia (The Institute of Materials, London, UK, 1997), pp. 359–389.

[7] Robert Honeycombe and Bhadeshia, H. K. D. H., *Steels, Microstructure and properties* (Edward Arnold, London, 1995).

[8] Bhadeshia, H. K. D. H., Svensson, L.–E and Gretoft, B., *The influence of alloying elements of the formation of allotriomorphic ferrite in low–alloy steel weld deposits*, Journal of Materials Science Letters **4**, 305 (1985).

[9] Levine, E. and Hill, D. C., *Toughness in HSLA steel weldments*, Metal Construction 346 (1997).

[10] Garland, J. G. and Kirkwood, P. R., *Towards improved sumberged arc weld metal*, Metal Construction 275 (1975).

[11] Bain, E. C. and Paxton, H. W., *Alloying Elements in Steel* (American Society for Metals, Metals Park, Ohio, USA, 1966).

[12] Leslie, W. C., *Iron and its dilute substitutional solid solutions*, Metallurgical transactions **3**, 5 (1972).

[13] Buchi, G. J. P., Page, J. H. R. and Sideys, M. P., *Creep properties and precipitation characteristics of 1%*Cr–Mo–V *steels*, Journal of the Iron and Steel Institute 291 (1965).

[14] Irvine, K. J., Crowe, D. J. and Pickering, F. B., *The physical metallurgy of 12% chromium steels*, Journal of the Iron and Steel Institute 386 (1960).

[15] Ridley, N., Maropolous, S. and Paul, J.D.H., *Effects of heat treatment on microstrucutre and mechanical properties of* Cr–Mo–$3.5Ni$–V *steel*, Materials Science and Technology **10**, 229 (1994).

[16] AWS, *American Welding Society hand book, Section 4, 6th edition* (American Welding Society, Miami, Florida, USA, 1972).

[17] George E. Dieter, *Mechanical Metallurgy* (McGraw–Hill Book Company, London, UK, 1988).

[18] Knott, J .F., *Fundamentals of Fracture Mechanics* (Butterworths, London, U.K., 1973).

[19] Abiko, K, Scientific American (Jap. edition) **23**, 20 (1993).

[20] Pickering, F. B., *Physical Metallurgy and the Design of Steels* (Applied Science Publishers Ltd., London, 1978).

[21] Petch, N. J., *The clevage strength of poly crystals*, Journal of Iron and Steel Institute **174**, 25 (1953).

[22] Knot, J. F., *Fundamentals of Fracture Mechanics* (Butterworths, London, UK, 1988).

[23] Baker, R. G. and Nutting, L., *The tempering of* $2\frac{1}{4}Cr$–$1Mo$ *steel after quenching and normalizing*, Journal of the Iron and Steel Institute **192**, 257 (1959).

[24] Nutting, J., in *Advanced heat resistant steels for power generation*, edited by R. Viswanathan and J. Nutting (IOM Communications Ltd, London, 1998), pp. 12–30.

[25] Sugden, A. A. B. and Bhadeshia, H. K. D. H., *A model for the strength of as–deposited regions of steel weld metals*, Metallurgical Transactions **19A**, 1597 (1988).

[26] Winchel, P. G. and Cohen, M., Trans. ASM **55**, 347 (1962).

[27] Cool, T., Bhadeshia, H. K. D. H. and MacKay, D. J. C., *The yield and ultimate tensile strength of steel welds*, Materials Science and Engineering **A223**, 186 (1997).

[28] Evans, G. M., Welding Research Supplement 447s (1992).

[29] Abson, D. J. and Evans, G. M., in *An international conference on The effect of residual, impurity, and microalloying elements on weldability and weld properties*, edited by R. Dolby and D. McKeown (The Welding Institute, Cambridge, UK, 1984), pp. 44.1–44.16.

[30] Alekseev, A. A., Shevchenko, G. A., Pokhodnya, I. K. and Yurlov, B. V., *Effect of Copper on Structure and Properties of Multilayer C–Mn–Ni Weld Metal*, Doc II-A-845-91 Kiev, USS Academy of Sciences, USSR National Welding Commitee (1991).

[31] Blondeau, R., Boulisset, R., Ramson, L., Kaplan, D. and Roesch, L., in *Proceedings of the 5th International Conference on Pressure Vessel Technology* (ASME, San Francisco, USA, 1984), Vol. 2, pp. 1257–1289.

[32] Batte, A. D. and Murphy, M. C., *Reheat cracking in 2.25Cr–Mo weld metal: influence of residual elements and microstructure*, Metals Technology 62 (1979).

[33] Chandel, R. S., Orr, R. F., Gianetto, J. A., McGrath, J. T., Patchett, B. M. and Bicknell, A. C., *The microstructure and mechanical properties of narrow gap welds in 2.25Cr1Mo steel*, Physical Metallurgy Research Laboratories, Canmet. Report: ERP/PMRL 85-16(OP–J) (1985).

[34] Cunha, P. C. R., Pope, A. M. and Nobrega, A. F., in *Second International Conference on Offshore Welded Structures* (TWI, Cambridge, UK, 1982).

[35] Dittrich, S. and Große-Wordemann, J., *$2\frac{1}{4}$Cr–1Mo filler metals with high toughness properties after step cooling*, Thyssen Schweißtecknik GMBH report (1986).

[36] De Rissone, N. M. R., DE S. Bott I, Jorge, J. C. F., Corvalan, P. and Surian, E., *ANSI/AWS A5.1-91 E6013 rutile electrodes: The effect of wollastonite*, Welding Research Supplement **76**, 489s (1997).

[37] Dunne, D. J. and Pollard, G., in *Proccedings of the 2nd International conference on trends in welding research, International trends in welding Science and Technology*, edited by S. A. David and J. M. Vitek (ASM International, Materials Park, Ohio, USA, 1989), pp. 269–272.

[38] Es–Souni, M., Beaven, P. A. and Evans, G. M., Oerlikon Schweißmitteilungen **48**, 15 (1990).

[39] Es-Souni, M, Beaven, P.A. and Evans, G.M., in *Proccedings of the 2nd international conference on trends in welding research, International trends in welding Science and Technology*, edited by S. A. David and J. M. Viteck (ASM International, Materials Park, Ohio, USA, 1989), pp. 769–773.

[40] Evans, G. M., Oerlikon Schweißmitteilungen **36**, 4 (1978).

[41] Evans, G. M., Oerlikon Schweißmitteilungen **37**, 17 (1979).

[42] Evans, G. M., Oerlikon Schweißmitteilungen **38**, 20 (1980).

[43] Evans, G. M., Oerlikon Schweißmitteilungen **40**, 25 (1982).

[44] Evans, G. M., Oerlikon Schweißmitteilungen **41**, 15 (1983).

[45] Evans, G. M., *The effect of chromium on the microstructure and properties of* C–M*n all–weld–metal deposits*, Welding and Metal Fabrication 346 (1989).

[46] Evans, G. M., Oerlikon Schweißmitteilungen **48**, 18 (1990).

[47] Evans, G. M., Oerlikon Schweißmitteilungen **48**, 15 (1990).

[48] Evans, G. M., Oerlikon Schweißmitteilungen **49**, 18 (1991).

[49] Evans, G. M., Oerlikon Schweißmitteilungen **49**, 24 (1991).

[50] Evans, G. M., Oerlikon Schweißmitteilungen **50**, 19 (1992).

[51] Evans, G. M., Oerlikon Schweißmitteilungen **52**, 21 (1994).

[52] ESAB, *Report RC81033*, Internal Report (1981).

[53] ESAB, *Report RR82011*, Internal Report (1982).

[54] Evans, G. M., Personal communication to H. K. D. H. Bhadeshia. (1995).

[55] Evans, G. M., *Effect of boron on modified 9Cr1Mo weld metal*, Report, Oerlikon **52**, 21 (1994).

[56] Fox, A .G., Eakes, M. W. and Franke, G. L., *The effect of small changes in flux basicity on the acicular ferrite content and mechanical properties of submerged arc weld metal of navy HY–100 steel*, Welding Research Supplement 330s (1996).

[57] Garland, J. G. and Kirkwood, P. R., *Report GS/PROD/643/1/75/C*, British Steel Corp., Rotherham (1975).

[58] Green, R. S. et al., in *Proccedings of the 3rd International conference on trends in welding research, International trends in welding Science and Technology*, edited by S. A. David and J. M. Vitek (ASM International, Materials Park, Ohio, USA, 1992), pp. 359–364.

[59] Gonzalez, J.C. de Vedia, L.A,. et al., *Effect of carbon content on the characteristics of as–welded and step-cooled* AWS E–8018B2 *type weld metal*, Canadian Metallurgical Quaterly **30**, 187 (1991).

[60] Ichikawa, K., Horii, Y., Sueda, A. and Kobayashi, J., *Toughness and creep strength of modified* $2\frac{1}{4}$*Cr–1Mo steel weld metal*, Welding Research Supplement **74**, 230s (1995).

[61] Jose Vercesi and *Ė*stela Surian, *The effect of welding parameters on high strength SMAW all weld metal. Part 1: AWS E11018–M*, Welding Research Supplement **75**, 191s (1996).

[62] Klueh, R. L., *The effect of carbon on* $2\frac{1}{4}$*Cr–1Mo steel*, Journal of Nuclear Materials **54**, 41 (1974).

[63] Klueh, R. L. and Alexander, D. J., *Embrittlement of Cr–Mo steels after low fluence irradiation in HFIR*, Journal of Nuclear Materials **212–215**, 569 (1994).

[64] Klueh, R. L., Ji-Jung Kai and Alexander, D. J., *Microstructure-mechanical properties correlation of irradiated conventional and reduced-activation martensitic steels*, Journal of Nuclear Materials **225**, 175 (1995).

[65] Klueh, R. L., Alexander, D. J. and Kenik, E. A., *Development of low–chromium, chromium–tungsten steels for fusion*, Journal of Nuclear Materials **227**, 11 (1995).

[66] Lundin, C. D. and Liu, P., *Development of W–bearing low carbon Cr–Mo filler metal for Cr–Mo vessel and piping repairs*, Techincal report: Materials joining research, Materials science and Engg., Univerisity of Tennessee, Knoxville (1997).

[67] Dunne, D. J. and Pollard, G., in *Proccedings of the 2nd International conference on trends in welding research, International trends in welding Science and Technology*, edited by S. A. David and J. M. Vitek (ASM International, Materials Park, Ohio, USA, 1989), pp. 575–580.

[68] Dunne, D. J. and Pollard, G., in *Proccedings of the 2nd International conference on trends in welding research, International trends in welding Science and Technology*, edited by S. A. David and J. M. Vitek (ASM International, Materials Park, Ohio, USA, 1989), pp. 793–798.

[69] Raiter, V. and Gonzalez, J.C., *Influence of molybdenum on the microstructure and properties of weld metal with different manganese contents*, Canadian Metallurgical Quaterly **2**, 28, 179 (1989).

[70] Siemens Power Generation, Newcastle upon Tyne, Personal communication to H. K. D. H. Bhadeshia. (1998).

[71] Sumitomo Metal Industries Ltd., Japan, *Properties after service exposure of HCM2S steel tubes in a power plant*, Technical report, 1996.

[72] Smith, N. J., McGrath, J. T., Bowker, J. T. and Gianetto, J. A., in *International Conference on the metallurgy, welding and qualification of microalloyed (*HSLA*) steel weldments, Miami, Florida*, edited by H. D. G. Hickey, J. T. and M. D. Randall (American Welding Society, Miami, Florida, USA, 1990), pp. 306–324.

[73] Zhang, Z. and Farrar, R. A., *Influence of Mn and Ni on the microstructure of C–Mn-Ni weld metal*, Welding Research Supplement 183 (1997).

[74] Haigh, R. H., *Ph.D. thesis*, Univeristy of Birmingham, UK (1996).

[75] Hunt, A. C., Kluken, A. O. and Edwards, G. R., Welding Research Supplement **73**, 9s (1994).

[76] Ichikawa, K., Horii, Y., Sueda, A. and Kobayashi, J., *Report*, Nippon Steel Corp., Tokyo, Japan (1992).

[77] Inagaki, M., Okane, I. and Nakajima, M., *Influence of heat treatment on creep rupture strength of welded joint of $2\frac{1}{4}$Cr1Mo steel*, Transactions of National Research Institute for Metals **8**, 34 (1966).

[78] Jorge, J. C. F., Rebello, J. M. A. and Evans, G. M., *Microstructure and toughness relationship in C–Mn–Cr all-weld metal deposits*, IIW Document II-A-880-93, Roissy (1993).

[79] Kikutake, T., Okamoto, K., Yamanaka, K., Nakao, H., Horii, Y. and Sugioka, I., in *Proceedings of the 5th International Conference on Pressure Vessel Technology,* (ASME, San Francisco, USA, 1984), Vol. 2, pp. 1188–1209.

[80] Kluken, A. O., Siewert, T. A. and Smith, R., *Effects of copper, nickel and boron on mechanical properties of low alloy steel weld metals deposited at high heat input*, Welding Research Supplement **74**, 193s (1994).

[81] Koçak, M. , Petrovski, B. I., Richter, E. and Evans, G. M., *Influence of titanium and nitrogen on the fracture properties of weld metals*, Offshore Mechanics and Arctic Engineering, Materials Engineering, ASME **3**, 277 (1994).

[82] Natsume, S., *Effects of chemical compositions on tensile properties of weld metals for modified 2.25Cr-1Mo steels.*, Proc. 5th Int. Symp. of the Japan Welding Society, Tokyo 639 (1990).

[83] Panton–kent, R., *Members report No. 429 : Weld metal toughness of MMA electron beam welded modified 9%Cr1%Mo steel*, The Welding Institute, Cambridge 3 (1990).

[84] Park, S. and Svensson, L.–E., *Report CML 89023: Estimation of the Microstructure and the Strength of Low-Alloy Cored Wire Weld Deposits, Using a Computer Model*, ESAB (1990).

[85] Patterson, J. D., in *Joining of Metals, Material and Practice*, edited by A. Sugden (TWI, Cambridge, UK, 1981), pp. 227–244.

[86] Still, J. R. and Rogerson, J. H., *The effect of Ti and B additions to multipass submerged arc welds in 50D plate*, Metal Construction **10**, 339 (1978).

[87] Surian, E., Trotti, J., Herrera, R. and de Vedia, L. A., *Influence of carbon on mechanical properties and microstructure of weld metal from a high strength SMA electrode*, Welding Research Supplement **70**, 133s (1991).

[88] Svensson, L–E. and Gretoft, B., *Microstructure and impact toughness of CMn weld metals*, Welding Research Supplement **69**, 454s (1990).

[89] Dolby, R. E., *The effects of V and Nb on weld metal properties*, Metal Science 302 (1983).

[90] Bhadeshia, H. K. D. H. and Sevensson, L.–E., in *Mathematical Modelling of Weld Phenomena-1*, edited by H. Cerjak and K. Easterling (The Institute of Materials, London, UK, 1993), pp. 109–180.

[91] Sugden, A. A. B. and Bhadeshia, H. K. D. H., Journal of Materials Science **25**, 613 (1989).

[92] Unwin, W C., Proc. Inst. Civil. Eng. **55**, 170 (1903).

[93] Widgery, D. J., Welding Research Supplement **55**, 57s (1976).

[94] Cottrell, A. H., *50 years on the shelf*, Int. J. Pressure Vessels Piping **64**, 171 (1995).

[95] Evans, G. M., *The effect of titanium in SMA* C–M*n steel multipass deposits*, Welding Research Supplement **71**, 447s (1992).

[96] Masahiko Hamada, et al., *Microstructure and precipitation behavior in heat affected zone of* C–M*n microalloyed steel containing Nb, V and Ti*, ISIJ International **10**, 35, 1196 (1995).

[97] Spink, G. M., *Fretting fatigue of a* $2\frac{1}{2}$*%NiCrMoV low pressure turbine shaft steel – The effect of differerent contact pad materials and of variables slip amplitude*, Wear **136**, 281 (1990).

[98] Swift, R. A. and Rogers, H. C., *Embrittlement of 2.25Cr-1Mo steel weld metal by postweld heat treatment.*, Welding Research Supplement **52**, 145s (1973).

[99] Watson, M. N., Harrison, P. L. and Farrar, R. A., *How niobium influences SA mild steel weld metals*, Welding and Metal Fabrication **49**, 101 (1981).

[100] Wolstenholme, D. A., *Report R/M/N746: Hardness and strength of 2Cr1Mo manual metal arc weld metals*, Marchwood Engineering Laboratories, UK 698 (1974).

[101] Johnson, M. Q., Frederickson, G. L., Liu, S. and Edwards, G. R., in *Proccedings of the 3rd International conference on trends in welding research, International trends in welding Science and Technology*, edited by S. A. David and J. M. Vitek (ASM International, Materials Park, Ohio, USA, 1992), pp. 353–358.

[102] St–Lauerent, S. and L'Esperance, G., in *Proccedings of the 3rd International conference on trends in welding research, International trends in welding Science and Technology*, edited by S. A. David and J. M. Vitek (ASM International, Materials Park, Ohio, USA, 1992), pp. 527–531.

[103] Kluken, A. O. and Grong, Ø., in *Proccedings of the 3rd International conference on trends in welding research, International trends in welding Science and Technology*, edited by S. A. David and J. M. Vitek (ASM International, Materials Park, Ohio, USA, 1992), pp. 569–574.

[104] Gianetto, J.A., McGratth, J.T., Skith, N.J.G. and Orr, R.F., in *Proccedings of the 2nd international conference on trends in welding research, International trends in welding Science and Technology*, edited by S. A. David and J. M. Viteck (ASM International, Materials Park, Ohio, USA, 1989), pp. 805–809.

[105] Krishnadev, M.R. et al., in *Proccedings of the 2nd international conference on trends in welding research, International trends in welding Science and Technology*, edited by S. A. David and J. M. Viteck (ASM International, Materials Park, Ohio, USA, 1989), Vol. 799–803.

[106] Roy, L. E., Embury, J. D., Edwards, G. and Ashby, M. F., Acta Metall. **29**, 1509 (1981).

[107] Kluken, A. O. and Grong, Ø., *Mechanisms of inclusion formation in Al-Ti-Si-Mn deosidized steel weld metals*, Metallurgical Transactions **20A**, 1335 (1989).

[108] Singh, S.B., Bhadeshia, H. K. D. H., MacKay, D. J. C. Carey, H. and Martin, I., *Neural network analysis of steel plate processing*, Ironmaking and Steelmaking **5**, 25, 355 (1998).

[109] Bhadeshia, H. K. D. H. , MacKay, D. J. C. and Svensson, L.–E., *Impact toughness of C–Mn steel arc welds– Bayesian neural network analysis,*, Materials Science and Technology **11**, 1046 (1995).

[110] Leslie, W. C., *The Physical Metallurgy of Steels* (McGraw–Hill, London, 1982).

[111] French, I. E., *A simple method for estimating low temperature impact properties of multi–pass welds*, Australasian Welding Journal **44**, second quarter, 42 (1999).

[112] Robert Bruscato, *Temper Embrittlement and creep embrittlement of* $2\frac{1}{4}$ *Cr–1 Mo shielded metal–arc weld deposits*, Welding Research Supplement **35**, 148s (1970).

[113] Powers, A. E., *The influence of molybdenum and tungsten on temper embrittlement*, Trans. ASM **48**, 149 (1956).

[114] Grabke, H. J., Hennesen, K., Möller, R. and Wei, W., *Effects of manganese on the grain boundary segregation, bulk and grain boundary diffusivity of P in ferrite*, Scripta Metallurgica **21**, 1329 (1987).

[115] Smith, J. F., Reynolds, J. H. and Southworth, H. N., *The role of Mn in the temper embrittlement of A 3.5Ni–Cr–Mo–V steel*, Acta Metallurgica **28**, 1555 (1980).

[116] Bhadeshia, H. K. D. H., *Bainite in Steels* (The Institute of Materials, London, UK, 1992).

[117] Sumitomo Metal Industries Ltd., Japan, *Development of high strength 2.25Cr–1.6W–V–Nb steel tube (HCM2S) for boiler application*, Technical report **903 F–No. 2666**, (1993).

[118] Sumitomo Metal Industries Ltd., Japan, *Development of high strength 2.25Cr–1.6W–V–Nb, large diameter steel pipe (HCM2S) for boiler application*, Technical report (1996).

[119] Sumitomo Metal Industries Ltd. and Sumikin Welding Industries Ltd., Japan, *Welding materials for HCM2S steel*, Technical report (1995).

[120] Kaori Miyata, Masaaki Igarashi and Yoshiatsu Sawaragi, *Effect of trace elements on creep properties of 0.06C–2.25Cr–1.6W–0.1Mo–0.25V–0.05Nb steel*, ISIJ International **39**, 947 (1999).

[121] Komai, N. and Masuyama, F., *The effects of cooling rate after austenitizing on creep rupture strength of low 2.25Cr–1.6W–V–Nb steel*, ISIJ International **11**, 432 (1998).

[122] Masuyama, F., in *Advanced heat resistant steels for power generation*, edited by R. Viswanathan and J. Nutting (IOM Communications Ltd, London, 1998), pp. 33–48.

[123] Cool, T. and Bhadeshia, H. K. D. H., *Austenite formation in 9Cr–1Mo type power plant steels*, Science and Technology of Welding and Joining **2(1)**, 36 (1997).

[124] MTDATA, *Metallurgical and Thermochemical Databank* (National Physical Laboratory, Teddington, U.K., 1989).

[125] Abe, A., Araki, H. and Noda, T., *Microstructural evolution in bainite, martensite and δ–ferrite of low activation Cr–2W ferritic steels*, Materials Science and Technology **6**, 714 (1990).

[126] Klueh, R. L. and Alexander, D. J., *Effect of vanadium and titanium on mechanical properties of chromium–tungsten steels*, Journal of Nuclear Materials **212-215**, 569 (1994).

[127] Klueh, R. L., Alexander, D. J. and Maziasz, *Bainitic chromium–tungsten steels with 3% chromium*, Metallurgical and Materials Transactions **28A**, 335 (1997).

[128] Cahoon, J. R., Broughton, W. H. and Kutzak, A. R., *The determination of yield strength from hardness measurements*, Matallurgical Transactions **2**, 1979 (1971).

[129] Harrison, P. L., Watson, M. N. and Farrar, R. A., *How niobium influences* SA *mild steel weld metals*, Welding and Metal Fabrication 161 (1981).

[130] Cole, D., Martin-Moran, C., Sheard, A. G., Bhadeshia, H. K. D. H. and MacKay, D. J. C., *Modelling creep rupture strength of ferritic steel welds*, Science and Technology of Welding and Joining **5**, 81 (2000).

[131] Yoshiatsu Sawaragi and Atsuro Iseda and Satomi Yamamoto and Fujimitsu Masuyama, *Development of high strength 2%Cr steel tubes HCM2S for boilers*, The Sumitomo Search, Japan **59**, (1997).

[132] David B. Williams and C. Barry Carter, *Transmission Electron Microscopy II: Diffraction* (Plenum Press, New York, 1996).

[133] Barret, C.S. and Massalski, T.B., *Structure of Metals and Alloys* (McGraw–Hill, New York, 1968).

[134] Bhadeshia, H. K. D. H., *MAP CRYSTAL PROGRAM*, http:// www.msm.cam.ac.uk/ map/ mapmain.html (1999).

[135] Bhadeshia, H. K. D. H., *Worked Examples in the Geometry of Crystals* (The Institute of Materials, London, 1987).

[136] Data book, *Selected Powder Diffraction Data for Metals and Alloys* (JCPDS International Center for Diffraction Data, Pennsylvania, USA, 1978).

[137] Pitch, W. and Schrader, A., Archiv fuer das Eisenhuttenwesen **29**, 715 (1958).

[138] Davenport, A. T. and Honeycombe, R. W. K., *The secondary hardening of tungsten steels*, Metal Science **9**, 201 (1975).

[139] Kwon, H., Lee, K. B., Yang, H. R. and Kim, Y. S., *Secondary hardening and fracture behavior in alloy steels containing Mo, W and Cr*, Metallurgical Transactions **28A**, 775 (1997).

[140] Robson, J. D. and Bhadeshia, H. K. D. H., *Modelling precipitation sequences in power plant steels*, Materials Science and Technology **13**, 631 (1997).

[141] Martin, J. W. and Doherty, R. D., *Stability of Microstructure in Metallic Systems*, second edition ed. (Cambridge University Press, Cambridge, UK, 1997).

[142] Bhadeshia, H. K. D. H., in *The Royal Society Parsons Memorial Lecture. The Parsons 2000 Conference* (The Institution of Mechanical Engineers, to be published, 2000).

[143] Venugopalan, D. and Kirkadly, J. S., in *Hardenability Concepts with Applications to Steels*, edited by D. Doane and J. Kirkadly (TMS–AIME, Warrendale, Pennsylvania, USA, 1978), pp. 249–267.

[144] Evans, G. M., *The effect of carbon on the microstructure and properties of C–Mn all–weld metal deposits*, Welding Research Supplement **62**, 313s (1983).

[145] Evans, G. M., *The effect of titanium in manganese–containing SMA weld depostis*, Welding Research Supplement **72**, 123s (March, 1993).

[146] Marimuthu, M., *Dissertation for the Certificate of Postgraduate Studies in Natural sciences, Design of Welding Alloys: Creep and Toughness* (University of Cambridge, Cambridge, UK, 2000).